Dynamics of complex coacervate core micelles

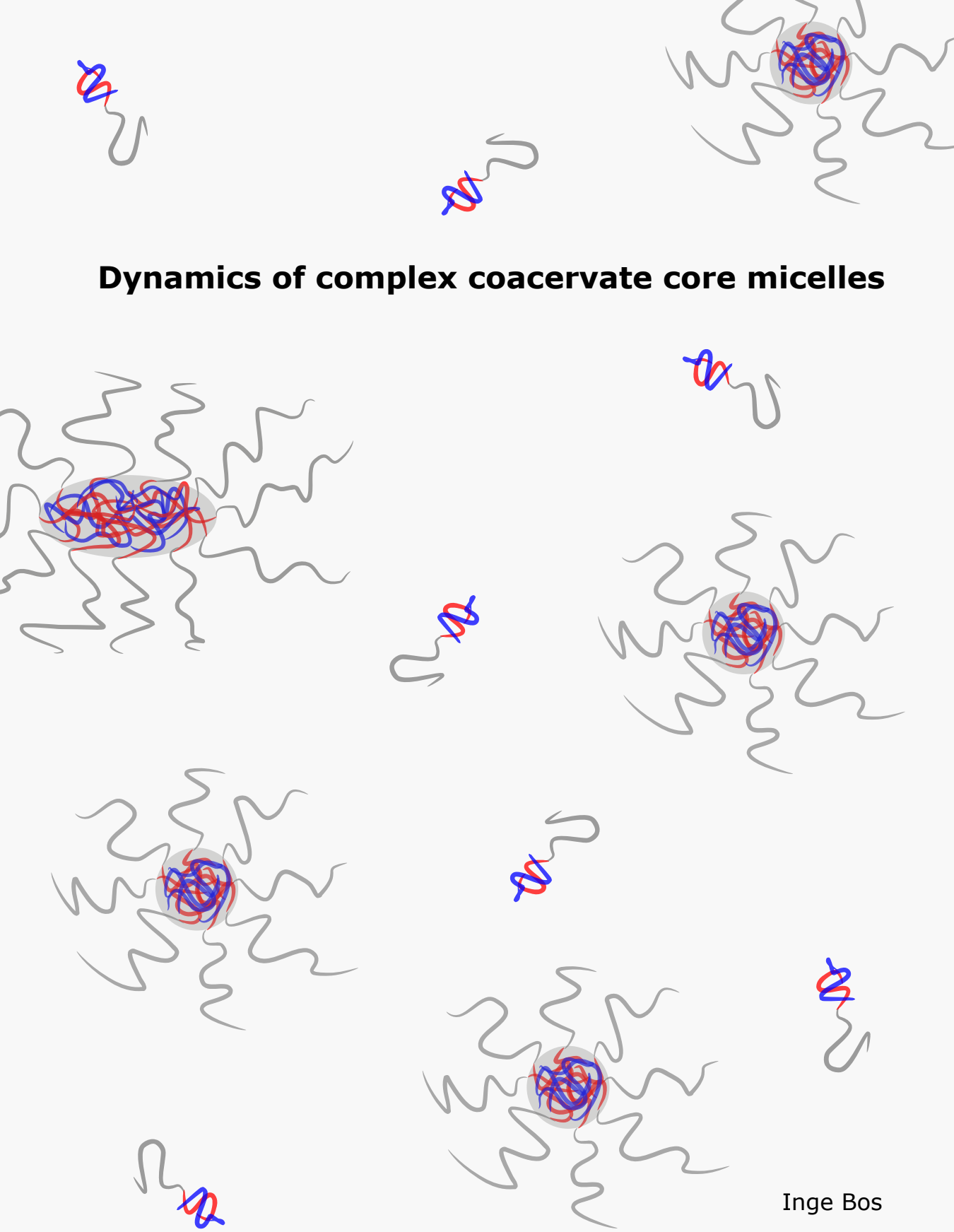

Inge Bos

Propositions

1. Combining the polymerisation reaction and micelle assembly in one network prevents kinetic trapping of certain complex coacervate core micelles.
   (this thesis)

2. Fitting FRET-based micelle exchange experiments with a simple exponential function results in an overestimation of the exchange rate.
   (this thesis)

3. Mathematics opens (so-called) black boxes in artificial intelligence.

4. Cycling enhances scientific progress.

5. Mind-wandering works better than mindfulness.

6. Thaw will always remain the only cure against “natuurijskoorts” (natural ice fever).

Propositions belonging to the thesis, entitled

Dynamics of complex coacervate core micelles

Inge Bos

Wageningen, 13 May 2022

Dynamics of complex coacervate core micelles

Inge Bos

Thesis committee

Promotor

Prof. Dr J.H.B. Sprakel
Personal chair, Laboratory of Biochemistry
Wageningen University & Research

Other members

Prof. Dr C.G.P.H. Schroën, Wageningen University & Research
Prof. Dr M.M.G. Kamperman, University of Groningen
Prof. Dr I.K. Voets, Eindhoven University of Technology
Dr S. Schmid, Wageningen University & Research

This research was conducted under the auspices of Graduate School VLAG
(Advanced studies in Food Technology, Agrobiotechnology, Nutrition and Health Sciences).

Dynamics of complex coacervate core micelles

Inge Bos

Thesis
submitted in fulfillment of the requirements for the degree of doctor
at Wageningen University
by the authority of the Rector Magnificus,
Prof. Dr A.P. J. Mol,
in the presence of the
Thesis Committee appointed by the Academic Board,
to be defended in public
on Friday 13 May 2022
at 4 p.m. in the Aula.

Inge Bos
Dynamics of complex coacervate core micelles
201 pages

PhD thesis, Wageningen University, Wageningen, The Netherlands (2022)
With references, with summary in English

ISBN: 978-94-6447-137-3
DOI: https://doi.org/10.18174/566231

Contents

Chapter 1

General introduction

1.1 Electrostatic (nano)structures

Oppositely charged compounds attract each other. When these compounds contain a sufficient number of charged groups, they can bind together for a long time and form larger structures. In nature, there are many macromolecules that contain multiple charges. As a result, many electrostatic (nano)structures can be found in nature. For example, the formation of viruses,[1,2] membraneless organelles[3,4] and sand castle worm glue[5] are all largely based on electrostatic attraction (Fig. 1.1a-c). Now, also many synthetic materials consist of electrostatic structures. Examples are under water adhesives,[5] filtration membranes,[6,7] saloplastic materials[8] and responsive colloidal gels[9] (Fig. 1.1d-g).

The binding of oppositely charged compounds can be tuned by the salt concentration and in some cases also the pH. At higher salt concentrations, the Coulomb interaction between the charged compounds becomes more screened. This results in a weaker attraction between the oppositely charged components. At certain point, the screening is so large that the electrostatic attraction is too weak to keep the components together and the structures fall apart. Some charged compounds get their charge from acidic or basic groups. For these compounds, a change in pH can alter the number of charged groups and thus the electrostatic interaction.

The assembly and disassembly of electrostatic structures is thus highly sensitive to a variety of environmental parameters. In some cases, this is a disadvantage, as it restricts the environments in which the intact electrostatic structures can be used. However, in many other cases, the ability to respond to environmental changes offers a major advantage,[10] for example in sensor systems[11] or drug delivery applications.[12]

1.2 Complex coacervates

A large part of the electrostatic structures, both in nature and in synthetic materials, consists of complexes of oppositely charged polyelectrolytes. The repeating charged units of the polyelectrolytes easily provide the multivalency that is essential to form stable electrostatic structures. When solutions of oppositely charged polyelectrolytes are mixed, the polyelectrolytes attract each other and together they can form a separate phase, which is called the polyelectrolyte complex. To accomplish this associative phase separation, both the positive and negative charges have to be present in sufficient amounts: often, the polyelectrolyte complexes form only around equal charge stoichiometry.[13–15] Because of this sensitivity to the charge ratio, changes in pH often affect the polyelectrolyte complexes: a change in pH can affect the degree of (de)protonation of one of the two polyelectrolytes and in this way alter the charge stoichiometry and thus the complex formation.[15]

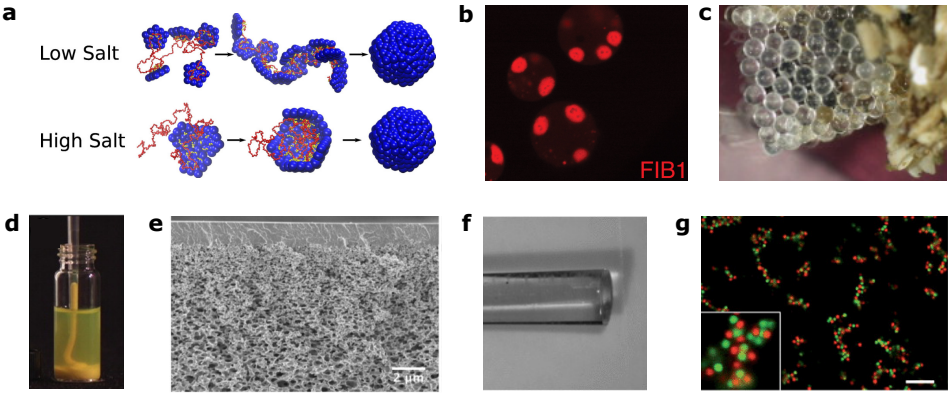

Figure 1.1. Examples of (nano)structures based on electrostatic attraction.(a) Virus assembly largely depends on electrostatic attraction between the negatively charged nucleic acid (red) and the positively charged capsid proteins (blue). Reprinted from Ref. 1 with permission from Elsevier. (b) Membraneless organelles can form based on associative phase separation of oppositely charged polyelectrolytes. In this example, the dense red regions indicate the membraneless organelles that are composed of fibrillarin protein (FIB1) and nucleid acids. Reprinted from Ref. 3 with permission form Elsevier. (c) The sand castle worm builds it sand castle by using glue that consists of pH-responsive oppositely charged polyelectrolytes. In this case, the sand grains were replaced by glass beads. (d) Under water glue can also be formed from synthetic oppositely charged polyelectrolytes. (c) and (d) are reprinted from Ref. 5 with permission from Elsevier. (e) Complexes of oppositely charged polyelectrolytes can form a porous material and in this way serve as filtration membrane. Reprinted with permission from Ref. 6. Copyright 2019 American Chemical Society. (f) Saloplastic materials can be formed by complexation of oppositely charged polyelectrolytes and subsequent water extrusion. Reprinted with permission from Ref. 8. (g) Salt-responsive colloidal gels can be formed by mixing oppositely charged hairy colloids (fluorescently coloured with red (positively charged colloids) or green (negatively charged colloids) fluorophores. Reprinted with permission of the Royal Society of Chemistry from Ref. 9.

The electrostatic nature of the polyelectrolyte complexes makes them also highly sensitive to the ionic strength: increasing the salt concentration of the solution can change the polyelectrolyte complexes from solid-like to liquid-like and at even higher salt concentrations, the polyelectrolyte complexes completely dissolve and the polyelectrolytes no longer form a separate phase from the rest of the solution (Fig.1.2a).[16] Especially the liquid-like polyelectrolyte complexes have often been studied.[17–19] These polyelectrolyte complexes that are formed by liquid-liquid phase separation are often called complex coacervates.

Not all the oppositely charged polyelectrolyte pairs form solid complexes at low salt concentrations: in some cases, the complex coacervates are already observed at the lowest salt concentrations. In addition, not every complex coacervate dissolves at the same salt concentration. The phase behaviour of the polyelectrolyte complexes thus does not only depend on the charge stoichiometry and ionic strength, but also depends on other parameters: the length of the polyelectrolyte chains[20–22] and the polylectrolyte type[17,22–26] can also play a role. Longer polyelectrolytes increase the stability of the complex coacervate phase, resulting in a higher critical ionic strength at which the coacervate dissolves (Fig. 1.2b). Different polyelectrolyte types can differ in their charge density,[25] charge patterning[26] and non-electrostatic interactions[22–24] and all these differences might affect the polyelectrolyte complex formation.

1.2.1 Voorn-Overbeek theory for complex coacervation

Traditionally, the complex coacervation has been described by the Voorn-Overbeek theory,[27,28], which describes the free energy of a solution with oppositely charged polyelectrolytes. Phase separation into

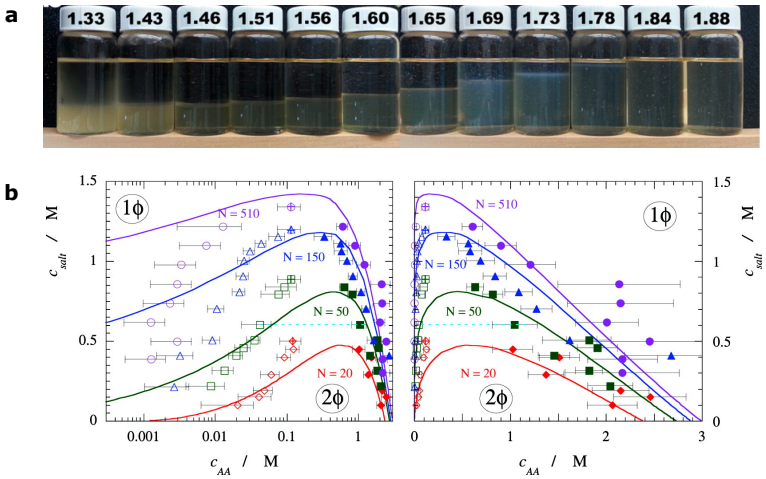

Figure 1.2. Phase behaviour of oppositely charged polyelectrolyte complexes. (a) Polyelectrolyte complexes formed from negatively charged poly(4-styrenesulfonic acid) and positively charged poly(diallyldimethylammonium chloride) transition from solid-like to liquid-like and finally completely disassemble with increasing salt concentrations (salt concentrations in mole per liter KBr are indicated by the numbers at the top). Reprinted with permission from Ref. 16. (b) Phase diagram of the complex coacervation of oppositely charged poly(acrylic acid) (PAA) and poly(N,N-dimethylaminoethyl methacrylate) (PDMAEMA) with the monomer concentration c_{AA} on a logarithmic (left) or linear (right) scale. 1ϕ indicates a one phase system and 2ϕ indicates a two phase system. Filled symbols indicate the composition of the coacervate phase and open symbols indicate the composition of the coexisting dilute phase. N indicates the length of the polyelectrolytes. Reprinted with permission from Ref. 20. Copyright 2010 American Chemical Society.

a polyelectrolyte rich and a polyelectrolyte poor phase will occur when the free energy of the two coexisting phases is lower than the free energy of the homogeneous mixture of all the components. In the Voorn-Overbeek theory, the free energy F of the system is given by a combination of electrostatic attraction, mixing entropy and non-electrostatic interactions:

$$\frac{l^3 F}{V k_B T} = -\alpha \left(\sum_i \sigma_i \phi_i \right)^{3/2} + \sum_i \frac{\phi_i}{N_i} \ln \phi_i + \frac{1}{2} \sum_i \sum_{j<i} \chi_{ij} \phi_i \phi_j \tag{1.1}$$

where l is the lattice size and corresponds to the size of a monomer, V is the total volume, α is the electrostatic interaction parameter ($\alpha = \frac{2}{3}\sqrt{\pi}(\frac{l_B}{l})^{3/2}$ where l_B the Bjerrum length, which is $\sim 0.7\,\mathrm{nm}$ in water at room temperature), σ_i is the charge density, ϕ_i is the volume fraction and N_i is the chain length of component i and χ_{ij} is the interaction parameter between component i and j. Usually, only the symmetric case is considered, where the positive polyelectrolyte has the same length and volume fraction as the negative polyelectrolyte. The salt dependence of the complex coacervation is captured in the first term, which describes electrostatic interaction energy based on the Debye Hückel theory. The chain length dependence arises from the second term. This term describes the mixing entropy based on the Flory-Huggins theory for the mixing of polymers. Longer chains have a lower mixing entropy and therefore systems with longer polymers separate more easily in two different phases. Finally, often also some enthalpic interaction parameter is included (the last term), to describe the non-electrostatic interaction between the oppositely charged polyelectrolytes.

Although the Voorn-Overbeek model seems to describe the experimental data well [14,20,29,30] (Fig. 1.2b), its underlying assumptions are questioned. [18,19,31,32] For example, in the Voorn-Overbeek theory,

the complex formation is an enthalpic process driven by electrostatic interactions, while isothermal calorimetry measurements have shown that complex coacervation is often mainly driven by an entropy increase and in some cases the enthalpy change upon complex formation can even be unfavourable.[31] This large difference between theory and experiments might be explained by the charge connectivity,[32,33] which is completely neglected in the Voorn-Overbeek theory. The Voorn-Overbeek theory does not only neglect the charge connectivity, it also neglects the volume interactions of the charged species, while in some cases the charged species can take up more than 10% of the complex coacervate volume[20] and their volume effect is thus non-negligible. Furthermore, the Voorn-Overbeek theory is based on the Debye-Hückel approximation, which is only valid at very low salt concentrations (up to 5 mM),[34] while the Voorn-Overbeek theory has been used for much higher salt concentrations (above 1 M).[20,29,30]

1.2.2 Other complex coacervation models

To overcome the limitations of the Voorn-Overbeek model, multiple new models have been developed (Fig. 1.3).[18,19] The different models work in different charge density limits and differ in their description of the driving force for the complexation. In the models for the low charge density limit, the complexation is driven by fluctuation induced opposite-charge attractions: chain connectivity results in regions with a certain charge, which can collocate with regions with an opposite charge and in this way can generate a larger amount of favourable Coulomb interactions than for unconnected charges. In the models for the high charge density limit, the complexation is driven by counter ion condensation and release (Fig. 1.3c): the release of counter ions upon complexation results in a large entropy increase of the counter ions, while the charge connectivity makes the corresponding entropy decrease of polyelectrolytes binding together relatively small. The different origins for complexations in the different charge density limits are supported by a combination of Monte Carlo and molecular dynamics simulations that showed that for high charge density polyelectrolytes the complexation is dominated by an entropy increase caused by counter-ion release, while for polyelectrolytes with low charge densities the enthalpic contributions become dominant.[35,36]

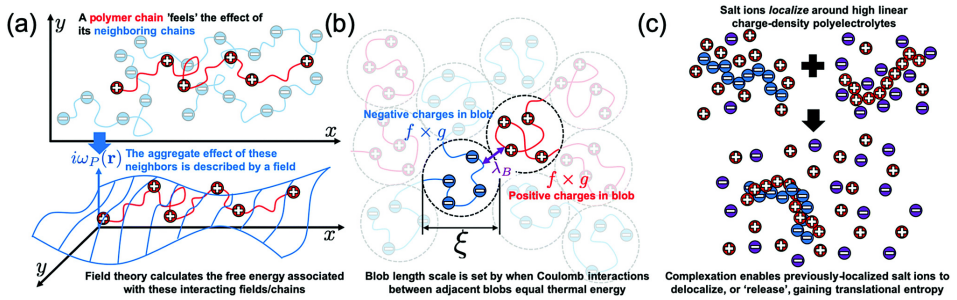

Figure 1.3. Overview of the underlying principles of the different coacervation models. (a) Field theory calculates the free energy of polyelectrolytes in a field with small charge fluctuations. (b) Scaling models divide the coacervate in densely packed blobs of size ξ. The Coulomb interaction between two neighbouring blobs is on the order of the thermal energy. (c) Models based on counter ion condensation and release assume that many counter ions are bound to the free polyelectrolytes, which are released and gain translational entropy upon complexation of the polyelectrolytes. Reprinted with permission of the Royal Society of Chemistry from Ref. 19.

In the low charge density limit, only a small part of the monomer groups are charged. Examples of such complex coacervates are complexes of weak polyelectrolytes at a pH at which the polyelectrolytes are only partly charged. In this limit, the complex coacervates can be described with a modified mean field model that includes small charge fluctuations (Fig. 1.3a). This approach is known as the random phase approximation (RPA)[37–40] and resembles to the traditional Voorn-Overbeek approach. In fact, the Voorn-Overbeek model is a simple case of RPA model.[38] The introduction of chain connectivity in

electrostatic interactions in the RPA model results in an increased stability against salt and a lower minimum charge density to form complexes as compared to the traditional Voorn-Overbeek theory.[38] Another way to describe the complexation in the low charge density limit is a scaling model.[41–43] In this approach, the coacervate is divided in densely packed blobs where the Coulomb interaction between two neighbouring blobs is on the order of the thermal energy ($\sim k_BT$) (Fig. 1.3b). The size of a blob ξ can depend on the charge fraction f, solvent selectivity and salt concentration.[43] Because of the fluctuation induced attraction, there is a larger probability that the neighbouring blob is oppositely charged than equally charged. The electrostatic blobs thus have a favourable interaction energy with their neighbouring blobs on the order of $\sim k_BT$. Blobs at the edge of the coacervate phase lack this favourable interaction, which gives rise to a interfacial tension γ on the order of $\gamma \simeq k_BT/\xi^2$. The relations for the blob size and interfacial tension obtained with this scaling approach usually agree well with the results obtained by the RPA model, although sometimes there are some small differences.[39,43] The scaling model is especially useful to predict the local structures of the coacervate complexes,[42,43] while the RPA model can be more useful to understand the underlying interactions of the complex coacervation.[39]

In the high charge density limit, nearly every monomer is charged ($f \approx 1$). Complexes formed by oppositely charged strong polyelectrolytes are usually in the high charge density limit. To describe the complexation in the high charge density limit, the chain connectivity can be introduced implicitly by describing the counterion condensation.[44] However, this implicit approach cannot describe the effect of charge patterning. An explicit description of the charge connectivity is computationally more challenging, but has been done recently.[32,33,45,46] In one of the approaches, the three-dimensional complex coacervate is mapped to a one-dimensional adsorption model.[33,45,46] For a given test polymer, every monomer is an adsorption site to which a counter ion, a new oppositely charged polymer or the same oppositely charged polymer as for the previous site can bind. This is used to calculated the partition function of the test polymer, from which the interaction free energy is calculated. The total free energy is a combination of this interaction free energy, the entropy of mixing and excluded volume effects of the non-water species. The model predicts an increase in free salt ions with an increase of the polymer volume fraction, which supports the presence of a counterion condensation and release effect.[33] This approach is especially useful to describe the effect of polymer chain architecture[45] and charge density patterning.[46]

In conclusion, starting from the Voorn-Overbeek theory, the models on complex coacervation have become more and more advanced over the past years. The current models not only try to describe the effect of ionic strength, charge stoichiometry, charge density and polyelectrolyte length, but also try to include other effects like salt partitioning,[21,32,47] non-electrostatic interactions,[23,24] charge patterning,[26,40,46] polymer architecture,[48,49] chain flexibility[50,51] and solvent quality.[43] At this moment, the models of complex coacervation are still being further developed and complex coacervation is intensively studied both experimentally and theoretically.

1.3 Complex coacervate core micelles (C3Ms)

In general, oppositely charged homopolyelectrolytes tend to phase separate on a macroscopic scale, although in some cases it can take a long time before small polyelectrolyte complexes combine into one macroscopic phase. When a neutral hydrophilic block is attached to at least one of the two polyelectrolyte types, this macroscopic phase separation can be prevented. The repulsive excluded volume interactions of the neutral blocks limit the size of the formed structures and prevent coalescence with other structures. As a result, stable micellar nanostructures are formed where the polyelectrolyte complex forms the core and the neutral blocks form the outer shell, known as the micelle corona (Fig. 1.4a). Often, this micellar structure is called a complex coacervate core micelle,[52] abbreviated as C3M. In some cases, the name C3M is even used when polyelectrolyte complex phase is not liquid-like,

although strictly speaking this name is thus incorrect in these cases. Other names that are used for these micellar structures are polyelectrolyte complex micelles (PCMs), polyion complex (PIC) micelles, block ionomer complexes (BIC) and inter polyelectrolyte complex (IPEC) micelles. In this thesis, we will mainly use the name complex coacervate core micellles (sometimes, we also use it to refer to micelles with a solid-like polyelectrolyte complex core).

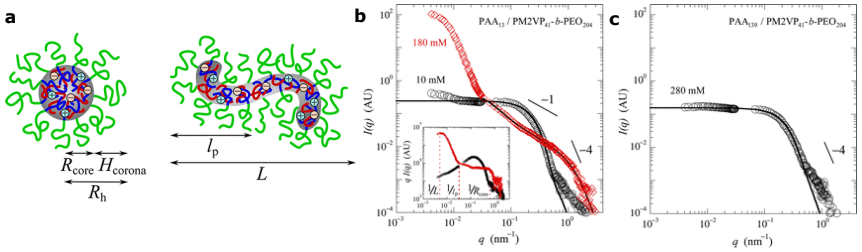

Figure 1.4. The morphology of complex coacervate core micelles (C3Ms). (a) Schematic representation of C3Ms. The oppositely charged polyelectrolytes (red and blue) form the core of the micelle and the neutral blocks (green) form the micelle corona. The C3Ms can have different morphologies, like spherical (left) or wormlike (right). (b) Angular dependent light and X-ray scattering measurements show that the transition from a spherical to wormlike morphology can be induced by an increase in the salt concentration: at low salt concentrations (black) the scattering data of the C3Ms can be fitted with a polydisperse core-shell sphere model, while at higher salt concentrations (red) the data can be fitted with a polydisperse cylinder model. (c) Not all the C3Ms show the transition to the wormlike morphology. C3Ms with a longer homopolyelectrolyte (PAA) length still have a spherical morphology at high salt concentration. All three sub figures are reprinted with permission from Ref. 53.

To form C3Ms, the length ratio of the neutral and ionic block of the diblock copolymer has to be chosen well. When the neutral blocks are much larger than the ionic blocks, the repulsive interactions between the neutral blocks will be stronger than the driving force for the coacervation and instead of micelles, only free dimers will be formed, that contain only one or two neutral blocks. On the other hand, when the neutral blocks are too short compared to the ionic blocks, macroscopic phase separation is not prevented and precipitates are formed.[52]

When C3Ms are formed, the excluded volume repulsion of the neutral blocks limits the number of copolymers that can be incorporated in one C3M to typically $\sim 10 - 250$ copolymers.[52] As a result, the micelle size is often in the order of 10 nm to 100 nm. The precise micelle aggregation number and size also depend on parameters like the salt concentration and the ionic block size.[53,54] When the salt concentration is increased, some of the C3Ms rearrange from spherical to larger wormlike objects (Fig. 1.4b), although others do not show this rearrangement (Fig. 1.4c). Rumyantsev *et al.* have shown that, at least in the weak charge density limit, this transition depends on the block lengths and the ionisation degree: they have adapted the coacervate scaling models (Section 1.2.2) to include the effect of the neutral block.[55] In this way, they could predict the C3M morphology as function of the ionic strength, ionisation degree and block lengths and found a region where the C3Ms can transition from spherical to wormlike/cylindrical with increasing salt concentration.

The neutral corona around the micelle core results in a repulsive interaction between the C3Ms: when two micelle aproach each other, the corona blocks can be slightly compressed, until the micelle intearction becomes similar to a hard sphere interaction and the micelles cannot approach any further.[56] In this way, the corona blocks prevent that the micelle core coalesce and therefore macroscopic phase separation does not occur.

The neutral blocks do not only limit the size of the C3Ms and prevent the cores from coalescing, they also form a protective layer around their core. This protective property and their ability to respond to salt and pH changes, make the C3Ms useful for a broad range of applications.[52,57] They can for example be used as drug delivery devices,[58–60] (bio)imaging tools,[61,62] nanoreactors,[63,64] synthesis

templates[65,66] and anti-fouling coatings.[67,68] Many of these applications make use of the encapsulating capability of the C3Ms, which will be the focus of the next section.

1.3.1 Complex coacervate core micelles as encapsulators

Charged compounds can usually be easily encapsulated in complex coacervate core micelles by making the compounds part of the complex coacervate phase. Often, the C3Ms spontaneously form by mixing the desired charged compounds with oppositely charged ionic-neutral copolymers. However, in some cases the desired charged compounds do not have the required properties to drive the C3M formation. For example, their charge density might be too low or their length too short to form coacervates (see also Section 1.2). In that case, additional compounds can be added to facilitate the encapsulation of the desired compound in a complex coacercate core micelle. For example, the additional compounds can crosslink different charged compounds to increase the coacervate stability. Alternatively, the additional compounds can be strongly charged to increase the charge density. Now, the encapsulation of many different compounds in C3Ms have been reported ranging from relatively large compounds like proteins,[69–72] DNA,[54,73–77] and RNA[78–81] to relatively small compounds like lanthanide ions[62] and small charged drugs.[82,83]

Every encapsulation application has its specific requirements on the micelle properties and thus requires a specific C3M type. For most applications, the encapsulation needs to last for a long time. Therefore, the C3M sensitivity to salts can be a disadvantage. For example, some C3Ms quickly disassemble at the physiological salt concentration which limits their use as drug delivery tool or bio-imaging agent. To overcome the dissociation problems, the core is sometimes stabilised by covalent cross-links[63,76] or hydrophobic modifications.[81,84] However, by increasing the stability of the core, the release of the encapsulated cargo also becomes more difficult. This release is especially important for drug delivery applications. Therefore, many studies focus on C3Ms that are not stabilised by irreversible modifications. Even for these micelles, the triggered release is very challenging. First, the micelles need to stay intact until they reach their target site and only then fall apart. In addition, the C3Ms are usually taken up by the cell via endosomal pathway and their cargo thus has to be able to escape from the endosome. In some cases, relatively simple C3Ms already show promising results.[78] Yet, often more advanced switches need to be incorporated to facilitate both triggered micelle disassembly and endosomal escape.[60] For example, in some cases, special polycations are used that become more protonated in the acididic environment of the endosome and in this way can disrupt the endosome membrane[79] (Fig. 1.5). Another example is the introduction of acid-labile bonds in the C3M that are cleaved in the endosome and in this way facilitate micelle disassembly and endosomal escape.[80]

To design new C3Ms based on the broad variety of existing C3Ms, it helps to know the underlying parameters that determine specific micelle properties. Hence, multiple studies have systematically investigated the effect of a specific parameter on a specific micelle property, like the effect of block length on micelle size,[53,54] salt concentration on critical micelle concentration[85] and block length ratio on micelle stability.[52,67]

1.3.2 The dynamics of C3Ms affects their encapsulating properties

Up to now, most of the experimental and theoretical studies on C3M have focused on their average static properties and how these properties change in response to environmental changes. Only a few studies have focused on the C3M dynamics[86–101] (Table 1.1), while this can largely affect the micelle encapsulation properties. First, the exchange dynamics determines how often a part of the micellar components is expelled from the micelle and thus the rate at which part of the cargo might be exposed to the surroundings. In this way, the exchange dynamics affects the level of protection that the micelle gives. In addition, the structure of the C3Ms sometimes depends on their preparation

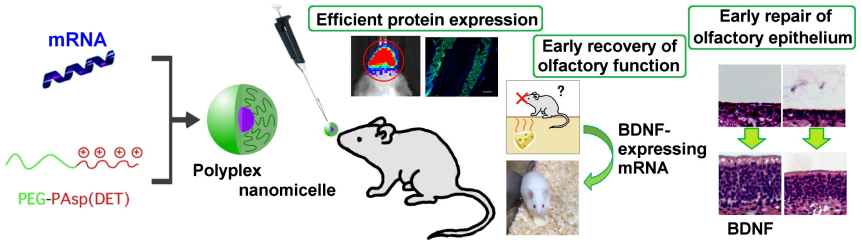

Figure 1.5. Example of C3Ms as responsive drug encapsulators: the C3Ms are formed by the neutral-ionic poly(ethylene glycol)-poly(N'-(N-(2-aminoethyl)-2-aminoethyl) aspartamide) diblock copolymer (PEG-PAsp(DET)) and the negatively charged messenger RNA (mRNA). Additional protonation of the positively charged PAsp(DET) block in the endosome facilitates micelle dissassembly and escape from the endosome. In this way, the mRNA can be delivered to the cell cytoplasm. In this case, the mRNA expresses the brain-derived neutrophic factor (BNDF) protein. Successful mRNA delivery is shown by injections of these C3Ms in mice that have an olfactory dysfunction. After the injections, the BNDF proteins are expressed, which confirms the mRNA delivery. The BNDF expression results in repair of the olfactory epithelium and recovery of the olfactory function. Reprinted from Ref. 79 with permission from Elsevier.

pathway.[72,77,102–104] Kinetic effects thus can govern the structure of the micelles and in this way their encapsulation properties. For the rational design of new C3M encapsulators it is thus essential to understand both their micellisation kinetics and their equilibrium exchange. Therefore, we aim to unravel both of these aspects of the C3M dynamics in this thesis.

Table 1.1. Overview of earlier studies that have focused on the underlying mechanisms of the dynamics of complex coacervate core micelles (NMR = nuclear magnetic resonance, SEC = size exclusion chromatography, TEM = transmission electron microscopy, SEM = scanning electron microscopy, DLS = dynamic light scattering, SLS = static light scattering, AFM = atomic force microscopy, SAXS = small angle X-ray scattering, FRET = Förster resonance energy transfer).

Stage	Technique	References
Formation (polymerisation induced assembly)	NMR, SEC, ζ potential, TEM, SEM, AFM, light microscopy, DLS, SLS*	87–93
Formation (assembly after polymerisation)	SLS	94,95
	SAXS	96,97
	FRET	98
Equilibrium	FRET	98,99
	Fluorescence quenching	100
Dissociation	SLS	95
	SAXS	101

* The mentioned techniques for formation by polymerisation induced assembly have mainly been used to characterise the end-structures and therefore only give little information on the underlying formation mechanisms.

Even though the dynamics of C3Ms themselves is not often studied, already some predictions on their dynamics can be made based on studies on related systems. For example, the exchange mechanisms of another micelle type, amphiphilic diblock copolymer micelles, have thoroughly been investigated. Insights from these studies might also be used to interpret the C3M dynamics. In addition, the dynamics of polyelectrolyte complexes, which form the core of the C3Ms, can also provide important insights into the C3M dynamics. Therefore, before discussing the few studies on the dynamics of C3Ms themselves (Section 1.6), we first focus on the dynamics of amphiphilic diblock copolymer micelles (Section 1.4) and the dynamics of polyelectrolyte complexes (Section 1.5).

1.4 Dynamics of amphiphilic diblock copolymer micelles

Amphiphilic diblock copolymer micelles consist of copolymers with an insoluble block and a soluble block. The insoluble blocks form the core of the micelle and the soluble blocks form the micelle corona. For these micelles, the importance of their dynamic properties has been widely recognised and their exchange has been extensively studied.

Often, two different exchange mechanisms are considered to interpret the dynamics of amphiphilic diblock copolymer micelles. The first mechanism is called expulsion/insertion and is based on the exchange of single polymers: one polymer (or a few polymers) splits off and is inserted in another micelle (Fig. 1.6a). The second mechanism is called fission/fusion. In this case, the micelle splits in two parts of both substantial size. These parts can fuse with other micelles to form a new micelle (Fig. 1.6b) For the fission, both parts that are formed still have a corona structure. For the expulsion however, the expelled part contains only one or two soluble blocks, which is not enough to form a micelle corona. This difference in corona makes the rate-limiting step of the two exchange mechanisms different. As a result, both mechanisms depend differently on the system parameters.

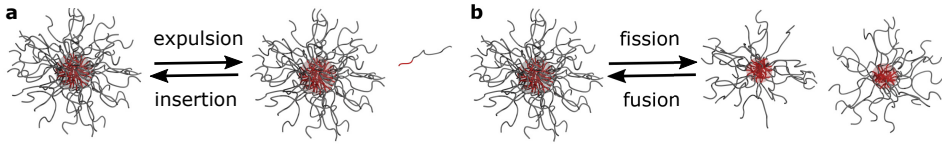

Figure 1.6. Schematic overview of the two mechanisms by which micelle exchange can occur. (a) Only one or a few polymers are expelled from the micelle and inserted into another micelle. (b) The micelle splits in two parts of both substantial sizes (fission), which can combine with other micelles to form a new micelle (fusion).

For insertion/expulsion, the expulsion step is thought to be rate limiting. The expulsion is usually described by an activated process where the energy barrier E_a is given by the increase in surface energy of the expelled core block:

$$k_{\text{exp}} \simeq \tau_{\text{un}}^{-1} \exp\left(-\frac{E_a}{k_B T}\right) \simeq \tau_{\text{un}}^{-1} \exp\left(-\frac{(N_A)^{2/3} b^2 \gamma}{k_B T}\right) \tag{1.2}$$

Here, N_A is core block length, b is monomer size and γ is the interfacial tension. Often, it is assumed that the core block is expelled as a blob, where only the outer monomers contribute to the surface energy. This gives the $N_A^{2/3}$ dependence of the activation energy E_a. However, for small core blocks, the activation energy sometimes seems to depend linearly on the number of core blocks: $E_a \sim N_A b^2 \gamma$ and therefore this linear dependence is also used sometimes to describe the micelle exchange.[105] The prefactor τ_{un} can depend on the corona block length N_B,[105–109] the core block length N_A [107,110] or the micelle aggregation number Q.[106]

For fission/fusion, the fusion is thought to be rate limiting because this requires substantial restructuring of the corona blocks. The fusion rate is less studied than the expulsion rate, but Dormidontova has proposed to describe this fusion also as an activated process with an energy barrier caused by the stretching of the corona blocks.[106] This energy barrier depends on the aggregation numbers of the two fusing micelles Q_1 and Q_2:

$$k_{\text{fus}} \simeq \tau_{\text{mic}}^{-1} \exp\left(-\frac{Q_1 \sqrt{Q_2}}{k_B T}\right) \tag{1.3}$$

This equation applies to the case where $Q_1 \leq Q_2$: the total stretching energy of a micelle with an aggregation number Q_2 is given by $Q_2^{3/2}$ [111] and therefore the stretching energy per chain is given by

$\sqrt{Q_2}$. Insertion of a (much) smaller micelle with aggregation number Q_1, thus requires a stretching energy of approximately Q_1 times the stretching energy of one chain $\sqrt{Q_2}$, which gives the $Q_1\sqrt{Q_2}$ dependence in the energy barrier. Again, the prefactor τ_{mic} can depend on the corona block length, like this was the case for the insertion/expulsion. However, the fusion rate does not depend on the core block length, while the expulsion rate strongly depends on it. Another difference between the exchange mechanisms is that for the fission/fusion the merging step is probably rate limiting, while for the expulsion/insertion the splitting step is probably rate limiting. The merging rate increases with increasing micelle concentration, while the splitting rate does not depend on the micelle concentration. Therefore, often the concentration dependence of the exchange rate is studied to distinguish between the two exchange mechanisms.

Both exchange mechanisms might occur during the formation of amphiphilic diblock copolymer micelles. According to the theoretical work of Dormindontova, micelle fusion occurs mainly at the start of the micellisation, after the initial fast coupling of the polymers. The fusion rate strongly decreases when the micelles grow further in size. During the final stage of the micellisation, the insertion/expulsion rates are much faster than the fusion/fission rates and the micelle growth is thus mainly caused by the insertion/expulsion mechanism.[106] Indeed both the fission/fusion mechanism and the insertion/expulsion mechanism have been observed in some experiments and computer simulations.[112–114] However, in another experiment only insertion/expulsion was observed.[115] This might be explained by the relatively long time that was needed to record the first data point. The fusion dominated stage might have occurred during this time. Alternatively, the differences in exchange mechanism might also have been caused by differences in composition of the block copolymers in the different studies, like differences in the length ratio between the soluble and insoluble block.

The dynamics of amphiphilic diblock copolymer micelles has not only been measured when the micelles are forming, but also when the micelles are equilibrated. This equilibrium dynamics can be more difficult to measure because the average static properties do not change once the micelles are equilibrated and therefore these properties cannot be used to follow the micelle exchange. Still, it is possible to measure the micelle exchange by labelling the polymers. For amphiphilic diblock copolymer micelles, polymers have often been labelled by specific hydrogen/deuterium isotope compositions. In this way, the micelle exchange can be followed by time-resolved small angle neutron scattering (TR-SANS) (Fig. 1.7). The neutron scattering by hydrogen isotopes is different from the scattering by deuterium isotopes. The micellar neutron scattering is at its minimum when the micellar hydrogen/deuterium isotope composition is equal to the solvent hydrogen/deuterium isotope composition. When micelles with hydrogen isotopes in their core and micelles with deuterium isotopes in their core are mixed in a hydrogen/deuterium solvent, the scattering contrast will thus decrease upon exchange of the polymer chains until the hydrogen and deuterium isotope polymers are homogeneously mixed and the neutron scattering contrast is at its minimum. In this way, TR-SANS can be used to measure the exchange of equilibrated micelles.

The TR-SANS measurements have shown that micelle exchange in equilibrium occurs mainly via the expulsion/insertion mechanism,[110,116–118] although computer simulations have suggested that in some cases still some fission/fusion might occur.[105,119] The first equilibrium exchange measurements of amphiphilic diblock copolymer micelles showed a broad range of time scales: a logarithmic relaxation was observed in TR-SANS measurements,[116,120] while for a single exchange rate, exponential relaxation is expected. Later on, this logarithmic exchange has been explained by a modest polydispersity of the core blocks in combination with a strong dependence of the expulsion rate on the core block length.[117,121] The expulsion from the core is described as an activated process with an Rouse type of relaxation included in the prefactor:

$$k_{\text{exp}} \simeq \frac{6\pi^2 k_B T}{N_A^2 b^2 \zeta} \exp\left(-\frac{\alpha \chi N_A}{k_B T}\right) \tag{1.4}$$

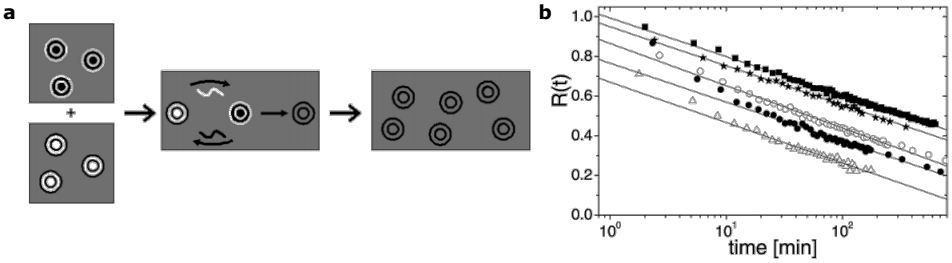

Figure 1.7. Measurement of the equilibrium exchange of amphiphilic diblock copolymer micelles by using time-resolved small angle neutorn scattering (TR-SANS). (a) To measure the exchange, micelles with deuterated (black) and hydrogenated (white) cores are mixed at time $t = 0$. When the micelles exchange, their hydrogen/deuterium isotope composition becomes similar to the solvent and the scattering contrast decreases. (b) The relaxation function R is calculated from the neutron scattering intensity I measured during the exchange experiment: $R(t) = \sqrt{\frac{I(t)-I(\infty)}{I(0)-I(\infty)}}$ and thus decreases when the micelles exchange. The exchange seems to follow a logarithmic relaxation. The different plots correspond to different temperatures. Both sub figures are reprinted with permission from Ref. 116. Copyright 2006 American Chemical Society.

where b is the monomer size, ζ is the monomeric friction factor, χ is the interaction parameter and α is a prefactor of order 1. In this description, the core block length N_A is both part of the prefactor and of the energy barrier and therefore the expulsion rate strongly depends on the core block length. As a result, already for a small core block polydiserpsity, the range of exchange times can be broad.

The core block length thus has a major effect on the equilibrium exchange of amphiphilic diblock copolymer micelles, but it is not the only factor that determines the overall exchange rate. For example, also the corona block length,[105,108,109] interfacial tension,[116] solvent selectivity[122], polymer chain architecture[123–125] and polymer stifness[119] can affect the micelle equilibrium exchange dynamics.

1.5 Dynamics of polyelectrolyte complexes

Although amphiphilic diblock copolymer micelles and C3Ms often form very similar nanostructures, they also have some fundamental differences. For example, the formation of amphiphilic diblock copolymer micelles is based on segregative phase separation of the insoluble core blocks, while the formation of C3Ms is based on associative phase separation of oppositely charged macromolecular species that are both well soluble in water. As a result, the interfacial tension of the core of C3Ms is often much lower, especially at higher salt concentrations.[29,116,126,127] In addition, the C3Ms have additional tuning parameters: the size of both oppositely charged core components can be varied independently from each other. Moreover, since only one of the charged species needs to contain a neutral block, the other macromolecular species can have much broader size range.[52,53] These differences can affect the micelle dynamics, but they are not included the current theories because these are mainly based on amphiphilic diblock copolymer micelles. This gap can be partly filled by earlier studies on the dynamics of polyelectrolyte complexes as these complexes form the core of the C3Ms.

The dynamics of polyelectrolyte complexes is often described by the sticky Rouse model.[128–130] This Rouse model is mainly used for dense polymer systems where hydrodynamic effects can be neglected. It assumes that every monomer has its own independent friction coefficient and therefore the friction coefficient of the polymer scales linearly with the polymer length. For ideal chains, the characteristic time τ_R in which the polymer diffuses a distance of the order of its own size, then scales with the square of the polymer length:[131]

$$\tau_R = \tau_0 N^2 \tag{1.5}$$

where τ_0 is the monomer relaxation time. In the sticky Rouse model, some of the monomers have attractive interactions with each other and in this way slow down the overall polymer dynamics.[132] These monomers with attractive interactions are referred to as stickers or sticky points. For polymers well above the overlap concentration, the characteristic time of a sticky polymer scales with the square of the number of stickers per chain f:

$$\tau_R = \tau_B f^2 \tag{1.6}$$

where τ_B is the (renormalized) lifetime of a bond between two sticky points, which is typically much longer than the normal monomer relaxation time τ_0.

The relaxation times of the individual polymers are difficult to measure directly, but can be determined in indirect ways. For example, the stress relaxation modulus $G(t)$ of a polymeric material can be linked to the dynamics of its polymers. The stress relaxation modulus describes how the stress $\sigma(t)$ in a material evolves as function of time t when a constant strain γ_0 is applied starting at $t = 0$: $G(t) = \sigma(t)/\gamma_0$. For the Rouse model, this stress relaxation modulus depends on the characteristic relaxation times τ_0 and τ_R as described by the following approximation:[131]

$$G(t) \approx \frac{k_B T}{b^3}\phi\left(\frac{t}{\tau_0}\right)^{-1/2}\exp(-t/\tau_R) \tag{1.7}$$

for $t > \tau_0$. Here b is the monomer size and ϕ is the volume fraction. For the sticky Rouse model, a similar relation applies, only τ_0 has to be replaced by τ_B.

The use of the sticky Rouse model to describe the dynamics of oppositely charged polyelectrolyte complexes is based on multiple observations. First, the stress relaxation modulus $G(t)$ shows the $-1/2$ power law dependence at intermediate times that is typical for Rouse relaxation (Equation 1.7) (Fig. 1.8b). In addition, the typical relaxation times are much slower than for polymers without attractive interactions, which can be explained by the ionic bonds that can act as sticky points (Fig. 1.8a). Furthermore, the relaxation time of the polyelectrolytes show the expect length dependence: since the number of stickers per chain is proportional to the polyelectrolyte length, the relaxation time should scale with the square of the polyelectrolyte chain length. The relaxation time of polyelectrolyte complexes with matched chain lengths seems to give this expected N^2 dependence (Fig. 1.8c).[128] Moreover, their diffusion coefficient scales with linearly with the polymer length,[133] as predicted by the sticky Rouse model. However, for polyelectrolyte complexes with unmatched chain lengths, the length effect is nontrivial. Sometimes, the dynamics is governed by only one of the two species and changing the length of the other species leaves the dynamics unaffected.[23,128] At this moment, the origin of this difference between the two species is not known. It might be related to their different effects on the polyelectrolyte concentration in the complex.[23] Alternatively, for weak ionic bonds, differences in charge densities between the two species might play a role.[134]

The dynamics of polyelectrolyte complexes can be largely increased by increasing the ionic strength. Often, this effect is explained by describing the rupture of the ionic bonds as an activated process where the energy barrier decreases linearly with the square root of the salt concentration:[135,136]

$$\frac{E_a}{k_B T} = -\frac{\sqrt{2000 N_A}e^3}{2\pi(\epsilon_r\epsilon_0 k_B T)^{3/2}}\sqrt{c_s} + \frac{e^2}{2\pi\epsilon_r\epsilon_0 k_B T d} \tag{1.8}$$

where E_a is the activation energy, N_A is Avogadro's constant, e is the elementary charge, ϵ_r is the relative permittivity, ϵ_0 is the vacuum permittivity, c_s is the salt concentration and d is the contact distance of the charged groups in an ion-ion pair. The first term is a Debye-Hückel approximation of the energy of the unbound ion pairs and gives the square root salt dependence. The second term corresponds to the Coulomb energy of the bound ion pairs. This approach uses similar simplifications as the Voorn-Overbeek theory that is used to describe the coacervate phase behaviour (Section 1.2.1): it

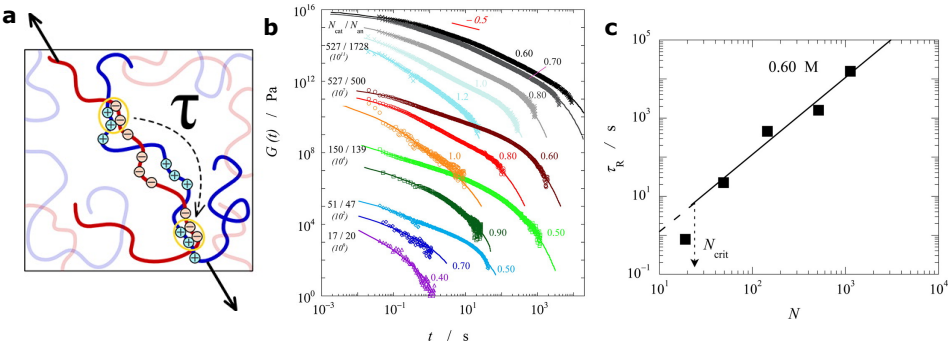

Figure 1.8. The dynamics of polyelectrolyte complexes is often described by the sticky Rouse model. (a) Schematic representation of the dynamics showing that the ionic bonds between the oppositely charged polyelectrolytes act as sticky points that slow down the movements of the polymers. (b) The stress relaxation modulus of PDMAEMA/PAA complex coacervates at different salt concentrations (numbers at the right) and for different polymer chain lengths (numbers at the left $N_{\text{cation}}/N_{\text{anion}}$). The data is vertically shifted. At intermediate times, the stress relaxation modulus show a $-1/2$ power law dependence, which is typical for Rouse relaxation (Equation 1.7). (c) The polymer characteristic relaxation time τ_R increases with increases chain length N. The solid line is a power law fit with a slope of 2.0 ± 0.3, suggesting that $\tau_R \sim N^2$. All three sub figures are reprinted with permission from Ref. 128. Copyright 2013 American Chemical Society.

neglects the connectivity of charges and uses the Debye-Hückle approximation also for higher salt concentrations. Despite these simplifications, multiple experiments seem to support the predicted square root salt concentration dependence[128,135–138], although in another case the dynamics depended more strongly on the salt concentration.[139] This stronger dependence on the salt concentration might be related to the aforementioned simplifications, but also other factors might have played a role. For example, the salt concentration can also affect the polyelectrolyte concentration in the complex (Fig. 1.2b) and in this way affect the viscoelastic properties.[23,140] In addition, binding of counter ions to the monomers might also decrease the number of sticky points per polyelectrolyte[141] and thus change the polyelectrolyte complex dynamics.

In conclusion, the studies on polyelectrolyte complexes suggest that the C3M dynamics can be affected by both the length of the core macromolecular species and by the salt concentration. The dynamics of complexes with matched chain lengths seems to be described well by the sticky Rouse model. However, for complexes with unmatched chain lengths, the effect on the dynamics can be nontrivial and the underlying mechanisms are not resolved yet. This nontrivial length effect also implies that not all the findings from amphiphilic diblock copolymer micelles dynamics can be directly applied to describe the dynamics of C3Ms.

1.6 Dynamics of complex coacervate core micelles

The studies on amphiphilic diblock copolymer micelles dynamics and polyelectrolyte complexes dynamics together provide an important foundation, but are insufficient to completely understand and predict the C3M dynamics. As already mentioned in the previous section, the amphiphilic diblock copolymer micelle cores consist of only one macromolecular species instead of two and therefore have less parameters to tune their dynamics compared to the C3Ms. Also the polyelectrolyte complexes have less tuning parameters compared to C3Ms because they lack the neutral corona block that usually affects the micelle dynamics. In addition, the results on polyelectrolyte complex dynamics are mostly obtained from their macroscopic bulk properties, while the individual dynamics of polyelectrolytes confined in the small micellar core might be different. It is thus important to study also the dynamics of C3Ms

themselves. As mentioned before, a few studies have already focused on the C3M dynamics (Table 1.1), which we will discuss below. Afterwards (Section 1.7), we will describe how this thesis expands these earlier findings on the dynamics of C3Ms, amphiphilic diblock copolymers and polyelectrolyte complexes to further unravel the C3M dynamics.

1.6.1 Formation and dissociation of complex coacervate core micelles

In some cases, the micellisation pathway of C3Ms can affect their properties.[72,77,102–104] This particular effect is used in polymerisation-induced electrostatic self-assembly (PIESA) where new micellisation pathways are obtained by combining a polymerisation reaction with the C3M assembly (Fig. 1.9). In this way, new nanostructures can be formed.[87–93] Up to now, studies on PIESA have mainly focused on the end structures that are formed at a given set of conditions. Little attention has been paid to the underlying micellisation pathways, while these are essential to tune the structure formation.

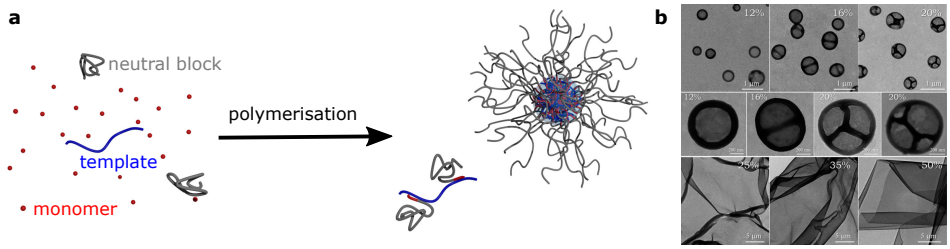

Figure 1.9. Polymerisation induced electrostatic self-assembly (PIESA) can result in the formation of new electrostatic nanostructures. (a) Schematic overview of PIESA: polymerisation of charged monomers occurs in the presence of an oppositely charged template. The polymerisation occurs at the end of a neutral polymer, resulting in the growth of a neutral-ionic diblock copolymer. When the ionic block grows sufficiently long, the interaction with the oppositely charged template becomes strong enough to induce the assembly into larger structures. Which structures are formed depend on the reaction conditions. (b) Examples of nanostructures formed at different weight concentrations (% w/w solids) by PIESA. In this case, the positively charged N-2-aminoethylacrylamide hydrochloride monomer was polymerised at the end of a neutral poly(2-hydroxypropylmethacrylamide) polymer in the presence of a negatively charged poly(2-acrylamido-2-methylpropanesulfonate) template. Reprinted with permission from Ref. 88.

The combination of the C3M assembly process with a reaction process can largely expand the number of possible micellisation pathways, but even for the micelle assembly from presynthesized macromolecuar components already different mechanisms exist. In some cases, first larger nano aggregates are formed, that slowly rearrange to smaller micelles.[94,96] In other cases, only an increase in micelle size is observed during the micellisation.[95,97] At the moment, the reasons for this difference is not known. In addition, the underlying mechanism of the continuous micelle growth has not been resolved yet. Some results support a fusion-like mechanism,[95] while other results are in favour of a expulsion/insertion based growth.[97]

The C3Ms can fall apart in response to an environmental trigger, like a salt-jump. This trigger has to make the micelle formation thermodynamically unfavourable, which results in the dissociation of the micelles. The dissociation rate can be much slower than the formation rate.[95] Recently, a SAXS study combined with theoretical modelling has shown that this dissociation process is probably a two step process where the micelles first swell and then fall apart into smaller micelles by a fission mechanism.[101]

1.6.2 Equilibrium exchange of complex coacervate core micelles

The exchange of equilibrated C3Ms can be followed by labelling the macromolecular components, like this is done for the exchange of equilibrated amphiphilic diblock copolymer micelles. To follow

the equilibrium exchange of C3Ms, fluorescent labels have been used:[98,99] one micelle population was labelled with donor fluorophores and the other micelle population was labelled with acceptor fluorophores. When the micelles exchange, the donor and acceptor fluorophores become part of the same micelle core. At this point, Förster resonance energy transfer (FRET) can occur, where an excited donor fluorophore transfers its energy to a close by acceptor fluorophore. This FRET is strongly distance dependent, with the FRET efficiency E given by:

$$E = \frac{1}{1 + (r/R_F)^6} \tag{1.9}$$

where r is the distance between the donor and acceptor fluorophore and R_F is the Förster radius, which depends on the fluorophore pair and is typically a few nanometers. Because of this strong distance dependence, FRET will occur only when the donor and acceptor fluorophore are part of the same micelle core. In this way, the increase in FRET efficiency is a measure for the micelle exchange rate (Fig. 1.10).

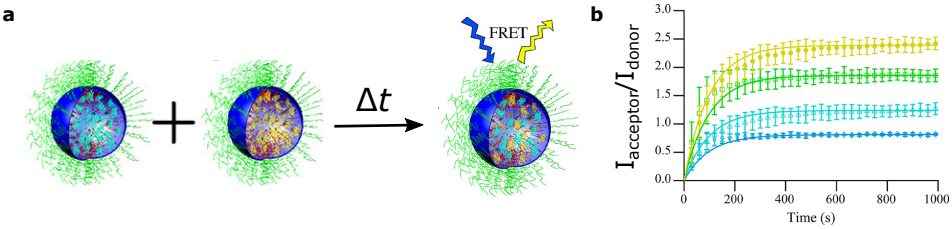

Figure 1.10. FRET can be used to measure the equilibrium exchange of C3Ms. (a) Schematic overview of the measurement of the C3M equilibrium exchange dynamics by using FRET. In this case, the fluorescent proteins mTurquoise2 (cyan) and SYFP2 (yellow) are used as the donor and acceptor fluorophores respectively. (b) Measured acceptor fluorescence intensity I_{acceptor} divided by the measured donor fluorescence intensity I_{donor} as function of time after mixing. The C3M exchange results in an increase in FRET efficiency and thus an increase in acceptor fluorescence intensity. At certain point, $I_{\text{acceptor}}/I_{\text{donor}}$ reaches a plateau because the micelles are completely mixed. The different plots correspond to different fluorophore labelling degrees increasing from bottom (blue) to top (yellow). For lower label percentages, less fluorophores are present within one core and the average distance between the fluorophores is thus larger. This results in a lower average FRET efficiency and thus a lower $I_{\text{acceptor}}/I_{\text{donor}}$ plateau. Both sub figures are adapted with permission from Ref. 98.

Fluorescent labelling has been used to measure the equilibrium exchange of both protein containing C3Ms[98] and C3Ms consisting of only synthetic polymers.[99] A large difference in exchange rate has been observed: the protein containing C3Ms exchanged within a few minutes, while the C3Ms composed of only synthetic polymers needed multiple hours to exchange completely. For these C3Ms, it was hypothesised that the observed micelle exchange was a combination of both expulsion/insertion and fission/fusion, while for the protein C3Ms it was suggested that exchange was based on only expulsion/insertion. In both cases, the hypothesis was not experimentally checked.

The first attempt to probe the dynamcis of the polyelectrolytes in the C3M core was also based on fluorescence.[100] In this case, fluorescence quenching was used: a negatively charged homopolyelectrolyte was labelled with a fluorophore (umbelliferone), whose fluorescence could be quenched by the positive block (poly-[3,5-bis(trimethylammoniummethyl)-4-hydroxystyrene iodide]) of the added diblock copolymer. The authors claimed that a decrease in the fluorescence lifetime could only occur if the positive block monomers or iodide ions collide with the fluorophore in the excited state and that the observed decrease in fluorescence lifetime thus indicate that the polyelectrolytes within the core are mobile. Yet, they did not further quantify this mobility. In addition, this study was only performed on one C3M system and it is therefore not clear whether the observations are particular for this C3M type or that this also occurs in other C3M systems.

1.7 Outline of this thesis

The dynamics of C3Ms largely affects their encapsulation properties. Yet, to date, their dynamics is still poorly understood. Although earlier studies on the dynamics of amphiphilic diblock copolymers, polyelectrolyte complex and C3Ms themselves have provided a good starting point to explain the C3M dynamics, still many open questions remain, as pointed out in the previous sections. In this thesis we therefore aim to further unravel the C3M dynamics. We start from their formation kinetics and gradually transition to their equilibrium exchange. In Chapter 2, we study how the C3M formation can be altered by combining the covalent polymerisation reaction of one of the micellar building blocks and the supramolecular assembly in one network. We show that there is chemical feedback between the reaction and the assembly and that the polymerisation rate can be used to tune the C3M structure.

In Chapter 3, we continue to study the dynamics during the micelle formation and we use coarse-grained Langevin dynamics simulations to determine the molecular exchange mechanisms during the initial micellisation of charged-neutral diblock copolymers and oppositely charged homopolymers. Although we follow the exchange during the initial micellisation, our observations can also help to better understand the the molecular exchange once the C3Ms are equilibrated.

In Chapter 4, we study the molecular exchange of equilibrated C3Ms by making use of Förster resonance energy transfer. We show that the exchange occurs mainly via the expulsion/insertion mechanism. In addition, we observe a broad range of exchange rates and hypothesise that this caused by chain polydispersity, with every chain length having its own exchange rate.

We test this polydispersity hypothesis in Chapter 5 and measure the molecular exchange of C3Ms consisting of monodisperse single stranded DNA (ssDNA) and polydisperse poly(ethyleneglycol)-*b*-poly(L-lysine) (PEG-pLL) diblock copolymer. The monodisperse ssDNA exchanges with only two or three exchange rates, while the polydisperse PEG-pLL diblock copolymer again shows a broad range of exchange times, suggesting that chain length polydispersity is indeed the main factor underlying the broad range of exchange rates. To further study this chain length effect on the dynamics, we vary both the ssDNA and the poly(L-lysine) chain length and determine the effect on both the C3M molecular exchange rate and the DNA diffusion in complex coacervates.

In Chapter 6, we aim to probe the sub-chain dynamics in a polyelectrolyte complex, which might also help to better understand the dynamics inside the C3M core. Unfortunately, we have not managed yet to measure this sub-chain dynamics in a polyelectrolyte complex, but we have developed a strategy that might allow to measure this sub-chain dynamics in the future.

In the general discussion (Chapter 7), we combine the main results of the other chapters to formulate general design rules to obtain C3Ms that have minimal exchange. In addition, we discuss how the research in this thesis can be continued, not only to learn more about C3M dynamics in particular, but also about the dynamics of other systems.

References

[1] Perlmutter, J. D.; Perkett, M. R.; Hagan, M. F. Pathways for virus assembly around nucleic acids. *J. Mol. Biol.* **2014**, *426*, 3148–3165.

[2] van der Schoot, P.; Bruinsma, R. Electrostatics and the assembly of an RNA virus. *Phys. Rev. E* **2005**, *71*, 061928.

[3] Feric, M.; Vaidya, N.; Harmon, T. S.; Mitrea, D. M.; Zhu, L.; Richardson, T. M.; Kriwacki, R. W.; Pappu, R. V.; Brangwynne, C. P. Coexisting liquid phases underlie nucleolar subcompartments. *Cell* **2016**, *165*, 1686–1697.

[4] Banani, S. F.; Lee, H. O.; Hyman, A. A.; Rosen, M. K. Biomolecular condensates: organizers of cellular biochemistry. *Nat. Rev. Mol. Cell Biol.* **2017**, *18*, 285–298.

[5] Stewart, R. J.; Wang, C. S.; Shao, H. Complex coacervates as a foundation for synthetic underwater adhesives. *Adv. Colloid Interface Sci.* **2011**, *167*, 85–93.

[6] Sadman, K.; Delgado, D. E.; Won, Y.; Wang, Q.; Gray, K. A.; Shull, K. R. Versatile and high-throughput polyelectrolyte complex membranes via phase inversion. *ACS Appl. Mater. Interfaces* **2019**, *11*, 16018–16026.

[7] de Grooth, J.; Haakmeester, B.; Wever, C.; Potreck, J.; de Vos, W. M.; Nijmeijer, K. Long term physical and chemical stability of polyelectrolyte multilayer membranes. *J. Membr. Sci.* **2015**, *489*, 153–159.

[8] Shamoun, R. F.; Reisch, A.; Schlenoff, J. B. Extruded saloplastic polyelectrolyte complexes. *Adv. Funct. Mater.* **2012**, *22*, 1923–1931.

[9] Spruijt, E.; Bakker, H. E.; Kodger, T. E.; Sprakel, J.; Cohen Stuart, M. A.; van der Gucht, J. Reversible assembly of oppositely charged hairy colloids in water. *Soft Matter* **2011**, *7*, 8281–8290.

[10] Blocher, W. C.; Perry, S. L. Complex coacervate-based materials for biomedicine. *Wiley Interdiscip. Rev. Nanomed. Nanobiotechnol.* **2017**, *9*, e1442.

[11] Fan, Y.; Tang, S.; Thomas, E. L.; Olsen, B. D. Responsive block copolymer photonics triggered by protein–polyelectrolyte coacervation. *ACS Nano* **2014**, *8*, 11467–11473.

[12] Deng, L.; Dong, H.; Dong, A.; Zhang, J. A strategy for oral chemotherapy via dual pH-sensitive polyelectrolyte complex nanoparticles to achieve gastric survivability, intestinal permeability, hemodynamic stability and intracellular activity. *Eur. J. Pharm. Biopharm.* **2015**, *97*, 107–117.

[13] Chollakup, R.; Smitthipong, W.; Eisenbach, C. D.; Tirrell, M. Phase behavior and coacervation of aqueous poly (acrylic acid)- poly (allylamine) solutions. *Macromolecules* **2010**, *43*, 2518–2528.

[14] Priftis, D.; Xia, X.; Margossian, K. O.; Perry, S. L.; Leon, L.; Qin, J.; de Pablo, J. J.; Tirrell, M. Ternary, tunable polyelectrolyte complex fluids driven by complex coacervation. *Macromolecules* **2014**, *47*, 3076–3085.

[15] Perry, S. L.; Li, Y.; Priftis, D.; Leon, L.; Tirrell, M. The effect of salt on the complex coacervation of vinyl polyelectrolytes. *Polymers* **2014**, *6*, 1756–1772.

[16] Wang, Q.; Schlenoff, J. B. The polyelectrolyte complex/coacervate continuum. *Macromolecules* **2014**, *47*, 3108–3116.

[17] Van der Gucht, J.; Spruijt, E.; Lemmers, M.; Cohen Stuart, M. A. Polyelectrolyte complexes: Bulk phases and colloidal systems. *J. Colloid Interface Sci.* **2011**, *361*, 407–422.

[18] Sing, C. E. Development of the modern theory of polymeric complex coacervation. *Adv. Colloid Interface Sci.* **2017**, *239*, 2–16.

[19] Sing, C. E.; Perry, S. L. Recent progress in the science of complex coacervation. *Soft Matter* **2020**, *16*, 2885–2914.

[20] Spruijt, E.; Westphal, A. H.; Borst, J. W.; Cohen Stuart, M. A.; van der Gucht, J. Binodal compositions of polyelectrolyte complexes. *Macromolecules* **2010**, *43*, 6476–6484.

[21] Li, L.; Srivastava, S.; Andreev, M.; Marciel, A. B.; de Pablo, J. J.; Tirrell, M. V. Phase behavior and salt partitioning in polyelectrolyte complex coacervates. *Macromolecules* **2018**, *51*, 2988–2995.

[22] Marras, A. E.; Vieregg, J. R.; Ting, J. M.; Rubien, J. D.; Tirrell, M. V. Polyelectrolyte complexation of oligonucleotides by charged hydrophobic—neutral hydrophilic block copolymers. *Polymers* **2019**, *11*, 83.

[23] Liu, Y.; Santa Chalarca, C. F.; Carmean, R. N.; Olson, R. A.; Madinya, J.; Sumerlin, B. S.; Sing, C. E.; Emrick, T.; Perry, S. L. Effect of polymer chemistry on the linear viscoelasticity of complex coacervates. *Macromolecules* **2020**, *53*, 7851–7864.

[24] Li, L.; Srivastava, S.; Meng, S.; Ting, J. M.; Tirrell, M. V. Effects of Non-Electrostatic Intermolecular Interactions on the Phase Behavior of pH-Sensitive Polyelectrolyte Complexes. *Macromolecules* **2020**, *53*, 7835–7844.

[25] Huang, J.; Morin, F. J.; Laaser, J. E. Charge-density-dominated phase behavior and viscoelasticity of polyelectrolyte complex coacervates. *Macromolecules* **2019**, *52*, 4957–4967.

[26] Chang, L.-W.; Lytle, T. K.; Radhakrishna, M.; Madinya, J. J.; Vélez, J.; Sing, C. E.; Perry, S. L. Sequence and entropy-based control of complex coacervates. *Nat. Commun.* **2017**, *8*, 1–8.

[27] Overbeek, J. T. G.; Voorn, M. Phase separation in polyelectrolyte solutions. Theory of complex coacervation. *J. Cell Comp. Phys.* **1957**, *49*, 7–26.

[28] Michaeli, I.; Overbeek, J. T. G.; Voorn, M. Phase separation of polyelectrolyte solutions. *J. Polym. Sci.* **1957**, *23*, 443–450.

[29] Spruijt, E.; Sprakel, J.; Cohen Stuart, M. A.; van der Gucht, J. Interfacial tension between a complex coacervate phase and its coexisting aqueous phase. *Soft Matter* **2010**, *6*, 172–178.

[30] Qin, J.; Priftis, D.; Farina, R.; Perry, S. L.; Leon, L.; Whitmer, J.; Hoffmann, K.; Tirrell, M.; De Pablo, J. J. Interfacial tension of polyelectrolyte complex coacervate phases. *ACS Macro Lett.* **2014**, *3*, 565–568.

[31] Fu, J.; Schlenoff, J. B. Driving forces for oppositely charged polyion association in aqueous solutions: enthalpic, entropic, but not electrostatic. *J. Am. Chem. Soc.* **2016**, *138*, 980–990.

[32] Perry, S. L.; Sing, C. E. Prism-based theory of complex coacervation: Excluded volume versus chain correlation. *Macromolecules* **2015**, *48*, 5040–5053.

[33] Lytle, T. K.; Sing, C. E. Transfer matrix theory of polymer complex coacervation. *Soft Matter* **2017**, *13*, 7001–7012.

[34] McQuarrie, D. Statistical mechanics university science books. *Sausalito, CA* **2000**, 222–223.

[35] Rathee, V. S.; Sidky, H.; Sikora, B. J.; Whitmer, J. K. Role of associative charging in the entropy–energy balance of polyelectrolyte complexes. *J. Am. Chem. Soc.* **2018**, *140*, 15319–15328.

[36] Ou, Z.; Muthukumar, M. Entropy and enthalpy of polyelectrolyte complexation: Langevin dynamics simulations. *J. Chem. Phys.* **2006**, *124*, 154902.

[37] Borue, V. Y.; Erukhimovich, I. Y. A statistical theory of globular polyelectrolyte complexes. *Macromolecules* **1990**, *23*, 3625–3632.

[38] Qin, J.; de Pablo, J. J. Criticality and connectivity in macromolecular charge complexation. *Macromolecules* **2016**, *49*, 8789–8800.

[39] Rumyantsev, A. M.; Potemkin, I. I. Explicit description of complexation between oppositely charged polyelectrolytes as an advantage of the random phase approximation over the scaling approach. *Phys. Chem. Chem. Phys.* **2017**, *19*, 27580–27592.

[40] Rumyantsev, A. M.; Jackson, N. E.; Yu, B.; Ting, J. M.; Chen, W.; Tirrell, M. V.; De Pablo, J. J. Controlling complex coacervation via random polyelectrolyte sequences. *ACS Macro Lett.* **2019**, *8*, 1296–1302.

[41] Shusharina, N.; Zhulina, E.; Dobrynin, A.; Rubinstein, M. Scaling theory of diblock polyampholyte solutions. *Macromolecules* **2005**, *38*, 8870–8881.

[42] Rubinstein, M.; Liao, Q.; Panyukov, S. Structure of liquid coacervates formed by oppositely charged polyelectrolytes. *Macromolecules* **2018**, *51*, 9572–9588.

[43] Rumyantsev, A. M.; Zhulina, E. B.; Borisov, O. V. Complex coacervate of weakly charged polyelectrolytes: Diagram of states. *Macromolecules* **2018**, *51*, 3788–3801.

[44] Salehi, A.; Larson, R. G. A molecular thermodynamic model of complexation in mixtures of oppositely charged polyelectrolytes with explicit account of charge association/dissociation. *Macromolecules* **2016**, *49*, 9706–9719.

[45] Lytle, T. K.; Sing, C. E. Tuning chain interaction entropy in complex coacervation using polymer stiffness, architecture, and salt valency. *Mol. Sys. Des. Eng.* **2018**, *3*, 183–196.

[46] Lytle, T. K.; Chang, L.-W.; Markiewicz, N.; Perry, S. L.; Sing, C. E. Designing electrostatic interactions via polyelectrolyte monomer sequence. *ACS Cent. Sci.* **2019**, *5*, 709–718.

[47] Schlenoff, J. B.; Yang, M.; Digby, Z. A.; Wang, Q. Ion Content of Polyelectrolyte Complex Coacervates and the Donnan Equilibrium. *Macromolecules* **2019**, *52*, 9149–9159.

[48] Johnston, B. M.; Johnston, C. W.; Letteri, R. A.; Lytle, T. K.; Sing, C. E.; Emrick, T.; Perry, S. L. The effect of comb architecture on complex coacervation. *Org. Biomol. Chem.* **2017**, *15*, 7630–7642.

[49] Madinya, J. J.; Chang, L.-W.; Perry, S. L.; Sing, C. E. Sequence-dependent self-coacervation in high charge-density polyampholytes. *Mol. Syst. Des. Eng.* **2020**, *5*, 632–644.

[50] Shakya, A.; King, J. T. DNA local-flexibility-dependent assembly of phase-separated liquid droplets. *Biophys. J.* **2018**, *115*, 1840–1847.

[51] Shakya, A.; Girard, M.; King, J. T.; Olvera de la Cruz, M. Role of Chain Flexibility in Asymmetric Polyelectrolyte Complexation in Salt Solutions. *Macromolecules* **2020**, *53*, 1258–1269.

[52] Voets, I. K.; De Keizer, A.; Cohen Stuart, M. A. Complex coacervate core micelles. *Adv. Colloid Interface Sci.* **2009**, *147*, 300–318.

[53] van der Kooij, H. M.; Spruijt, E.; Voets, I. K.; Fokkink, R.; Cohen Stuart, M. A.; van der Gucht, J. On the stability and morphology of complex coacervate core micelles: From spherical to wormlike micelles. *Langmuir* **2012**, *28*, 14180–14191.

[54] Lueckheide, M.; Vieregg, J. R.; Bologna, A. J.; Leon, L.; Tirrell, M. V. Structure–property relationships of oligonucleotide polyelectrolyte complex micelles. *Nano Lett.* **2018**, *18*, 7111–7117.

[55] Rumyantsev, A. M.; Zhulina, E. B.; Borisov, O. V. Scaling theory of complex coacervate core micelles. *Acs Macro Lett.* **2018**, *7*, 811–816.

[56] Wu, H.; Ting, J. M.; Weiss, T. M.; Tirrell, M. V. Interparticle interactions in dilute solutions of polyelectrolyte complex micelles. *ACS Macro Lett.* **2019**, *8*, 819–825.

[57] Magana, J. R.; Sproncken, C.; Voets, I. K. On Complex Coacervate Core Micelles: Structure-Function Perspectives. *Polymers* **2020**, *12*, 1953.

[58] Lee, Y.; Kataoka, K. Biosignal-sensitive polyion complex micelles for the delivery of biopharmaceuticals. *Soft Matter* **2009**, *5*, 3810–3817.

[59] Kakizawa, Y.; Kataoka, K. Block copolymer micelles for delivery of gene and related compounds. *Adv. Drug Deliv. Rev.* **2002**, *54*, 203–222.

[60] Cabral, H.; Miyata, K.; Osada, K.; Kataoka, K. Block copolymer micelles in nanomedicine applications. *Chem. Rev.* **2018**, *118*, 6844–6892.

[61] Berret, J.-F.; Schonbeck, N.; Gazeau, F.; El Kharrat, D.; Sandre, O.; Vacher, A.; Airiau, M. Controlled clustering of superparamagnetic nanoparticles using block copolymers: design of new contrast agents for magnetic resonance imaging. *J. Am. Chem. Soc.* **2006**, *128*, 1755–1761.

[62] Wang, J.; Velders, A. H.; Gianolio, E.; Aime, S.; Vergeldt, F. J.; Van As, H.; Yan, Y.; Drechsler, M.; De Keizer, A.; Cohen Stuart, M. A.; Van der Gucht, J. Controlled mixing of lanthanide (III) ions in coacervate core micelles. *Chem. Commun.* **2013**, *49*, 3736–3738.

[63] Jaturanpinyo, M.; Harada, A.; Yuan, X.; Kataoka, K. Preparation of bionanoreactor based on core- shell structured polyion complex micelles entrapping trypsin in the core cross-linked with glutaraldehyde. *Bioconjugate Chem.* **2004**, *15*, 344–348.

[64] Kawamura, A.; Harada, A.; Kono, K.; Kataoka, K. Self-assembled nano-bioreactor from block ionomers with elevated and stabilized enzymatic function. *Bioconjugate Chem.* **2007**, *18*, 1555–1559.

[65] Seo, E.; Lee, S.-H.; Lee, S.; Choi, S.-H.; Hawker, C. J.; Kim, B.-S. Highly stable Au nanoparticles with double hydrophilic block copolymer templates: correlation between structure and stability. *Polym. Chem.* **2017**, *8*, 4528–4537.

[66] Maggi, F.; Ciccarelli, S.; Diociaiuti, M.; Casciardi, S.; Masci, G. Chitosan nanogels by template chemical cross-linking in polyion complex micelle nanoreactors. *Biomacromolecules* **2011**, *12*, 3499–3507.

[67] van der Burgh, S.; Fokkink, R.; de Keizer, A.; Cohen Stuart, M. A. Complex coacervation core micelles as anti-fouling agents on silica and polystyrene surfaces. *Colloid. Surface. Physicochem. Eng. Aspect.* **2004**, *242*, 167–174.

[68] Voets, I. K.; De Vos, W. M.; Hofs, B.; De Keizer, A.; Cohen Stuart, M. A.; Steitz, R.; Lott, D. Internal structure of a thin film of mixed polymeric micelles on a solid/liquid interface. *J. Phys. Chem. B* **2008**, *112*, 6937–6945.

[69] Kembaren, R.; Fokkink, R.; Westphal, A. H.; Kamperman, M.; Kleijn, J. M.; Borst, J. W. Balancing Enzyme Encapsulation Efficiency and Stability in Complex Coacervate Core Micelles. *Langmuir* **2020**, *36*, 8494–8502.

[70] Nolles, A.; Westphal, A. H.; de Hoop, J. A.; Fokkink, R. G.; Kleijn, J. M.; van Berkel, W. J.; Borst, J. W. Encapsulation of GFP in complex coacervate core micelles. *Biomacromolecules* **2015**, *16*, 1542–1549.

[71] Lindhoud, S.; de Vries, R.; Norde, W.; Cohen Stuart, M. A. Structure and stability of complex coacervate core micelles with lysozyme. *Biomacromolecules* **2007**, *8*, 2219–2227.

[72] Lindhoud, S.; Norde, W.; Cohen Stuart, M. A. Reversibility and relaxation behavior of polyelectrolyte complex micelle formation. *J. Phys. Chem. B* **2009**, *113*, 5431–5439.

[73] Harada-Shiba, M.; Yamauchi, K.; Harada, A.; Takamisawa, I.; Shimokado, K.; Kataoka, K. Polyion complex micelles as vectors in gene therapy–pharmacokinetics and in vivo gene transfer. *Gene Ther.* **2002**, *9*, 407–414.

[74] Itaka, K.; Yamauchi, K.; Harada, A.; Nakamura, K.; Kawaguchi, H.; Kataoka, K. Polyion complex micelles from plasmid DNA and poly (ethylene glycol)–poly (l-lysine) block copolymer as serum-tolerable polyplex system: physicochemical properties of micelles relevant to gene transfection efficiency. *Biomaterials* **2003**, *24*, 4495–4506.

[75] Ogris, M.; Brunner, S.; Schüller, S.; Kircheis, R.; Wagner, E. PEGylated DNA/transferrin–PEI complexes: reduced interaction with blood components, extended circulation in blood and potential for systemic gene delivery. *Gene Ther.* **1999**, *6*, 595–605.

[76] Miyata, K.; Kakizawa, Y.; Nishiyama, N.; Harada, A.; Yamasaki, Y.; Koyama, H.; Kataoka, K. Block catiomer polyplexes with regulated densities of charge and disulfide cross-linking directed to enhance gene expression. *J. Am. Chem. Soc.* **2004**, *126*, 2355–2361.

[77] Oupický, D.; Koňák, Č.; Ulbrich, K.; Wolfert, M.; Seymour, L. DNA delivery systems based on complexes of DNA with synthetic polycations and their copolymers. *J. Control. Release* **2000**, *65*, 149–171.

[78] Kuo, C.-H.; Leon, L.; Chung, E. J.; Huang, R.-T.; Sontag, T. J.; Reardon, C. A.; Getz, G. S.; Tirrell, M.; Fang, Y. Inhibition of atherosclerosis-promoting microRNAs via targeted polyelectrolyte complex micelles. *J. Mater. Chem. B* **2014**, *2*, 8142–8153.

[79] Baba, M.; Itaka, K.; Kondo, K.; Yamasoba, T.; Kataoka, K. Treatment of neurological disorders by introducing mRNA in vivo using polyplex nanomicelles. *J. Control. Release* **2015**, *201*, 41–48.

[80] Oishi, M.; Nagasaki, Y.; Itaka, K.; Nishiyama, N.; Kataoka, K. Lactosylated poly (ethylene glycol)-siRNA conjugate through acid-labile β-thiopropionate linkage to construct pH-sensitive polyion complex micelles achieving enhanced gene silencing in hepatoma cells. *J. Am. Chem. Soc.* **2005**, *127*, 1624–1625.

[81] Kim, H. J.; Ishii, A.; Miyata, K.; Lee, Y.; Wu, S.; Oba, M.; Nishiyama, N.; Kataoka, K. Introduction of stearoyl moieties into a biocompatible cationic polyaspartamide derivative, PAsp (DET), with endosomal escaping function for enhanced siRNA-mediated gene knockdown. *J. Control. Release* **2010**, *145*, 141–148.

[82] Du, Y.; Yan, W.; Lian, H.; Xiang, C.; Duan, L.; Xiao, C. 2, 2'-Dithiodisuccinic acid-stabilized polyion complex micelles for pH and reduction dual-responsive drug delivery. *J. Colloid Interface Sci.* **2018**, *522*, 74–81.

[83] Li, Y.; Ikeda, S.; Nakashima, K.; Nakamura, H. Nanoaggregate formation of poly (ethylene oxide)-b-polymethacrylate copolymer induced by cationic anesthetics binding. *Colloid Polym. Sci.* **2003**, *281*, 562–568.

[84] Voets, I. K.; de Keizer, A.; Cohen Stuart, M. A.; Justynska, J.; Schlaad, H. Irreversible structural transitions in mixed micelles of oppositely charged diblock copolymers in aqueous solution. *Macromolecules* **2007**, *40*, 2158–2164.

[85] Yan, Y.; de Keizer, A.; Cohen Stuart, M. A.; Drechsler, M.; Besseling, N. A. Stability of complex coacervate core micelles containing metal coordination polymer. *J. Phys. Chem. B* **2008**, *112*, 10908–10914.

[86] Spruncken, C. C.; Magana, J. R.; Voets, I. K. 100th Anniversary of Macromolecular Science Viewpoint: Attractive Soft Matter: Association Kinetics, Dynamics, and Pathway Complexity in Electrostatically Coassembled Micelles. *ACS Macro Lett.* **2021**, *10*, 167–179.

[87] Yu, Q.; Ding, Y.; Cao, H.; Lu, X.; Cai, Y. Use of polyion complexation for polymerization-induced self-assembly in water under visible light irradiation at 25 C. *ACS Macro Lett.* **2015**, *4*, 1293–1296.

[88] Ding, Y.; Cai, M.; Cui, Z.; Huang, L.; Wang, L.; Lu, X.; Cai, Y. Synthesis of low-dimensional polyion complex nanomaterials via polymerization-induced electrostatic self-assembly. *Angew. Chem.* **2018**, *130*, 1065–1068.

[89] Cai, M.; Ding, Y.; Wang, L.; Huang, L.; Lu, X.; Cai, Y. Synthesis of one-component nanostructured polyion complexes via polymerization-induced electrostatic self-assembly. *ACS Macro Lett.* **2018**, *7*, 208–212.

[90] Ding, Y.; Zhao, Q.; Wang, L.; Huang, L.; Liu, Q.; Lu, X.; Cai, Y. Polymerization-Induced Self-Assembly Promoted by Liquid–Liquid Phase Separation. *ACS Macro Lett.* **2019**, *8*, 943–946.

[91] Liu, Q.; Wang, X.; Ma, L.; Yu, K.; Xiong, W.; Lu, X.; Cai, Y. Polymerization-Induced Hierarchical Electrostatic Self-Assembly: Scalable Synthesis of Multicompartment Polyion Complex Micelles and Their Monolayer Colloidal Nanosheets and Nanocages. *ACS Macro Lett.* **2020**, *9*, 454–458.

[92] Zhao, Q.; Liu, Q.; Li, C.; Cao, L.; Ma, L.; Wang, X.; Cai, Y. Noncovalent structural locking of thermoresponsive polyion complex micelles, nanowires, and vesicles via polymerization-induced electrostatic self-assembly using an arginine-like monomer. *Chem. Commun.* **2020**, *56*, 4954–4957.

[93] Shen, L.; Li, Y.; Lu, Q.; Qi, X.; Wu, X.; Zhou, Z.; Shen, J. Directed arrangement of siRNA via polymerization-induced electrostatic self-assembly. *Chem. Commun.* **2020**, *56*, 2411–2414.

[94] Cohen Stuart, M.; Besseling, N.; Fokkink, R. Formation of micelles with complex coacervate cores. *Langmuir* **1998**, *14*, 6846–6849.

[95] Zhang, J.; Chen, S.; Zhu, Z.; Liu, S. Stopped-flow kinetic studies of the formation and disintegration of polyion complex micelles in aqueous solution. *Phys. Chem. Chem. Phys.* **2014**, *16*, 117–127.

[96] Amann, M.; Diget, J. S.; Lyngsø, J.; Pedersen, J. S.; Narayanan, T.; Lund, R. Kinetic pathways for polyelectrolyte coacervate micelle formation revealed by time-resolved synchrotron SAXS. *Macromolecules* **2019**, *52*, 8227–8237.

[97] Wu, H.; Ting, J. M.; Yu, B.; Jackson, N. E.; Meng, S.; de Pablo, J. J.; Tirrell, M. V. Spatiotemporal Formation and Growth Kinetics of Polyelectrolyte Complex Micelles with Millisecond Resolution. *ACS Macro Lett.* **2020**, *9*, 1674–1680.

[98] Nolles, A.; Hooiveld, E.; Westphal, A. H.; van Berkel, W. J.; Kleijn, J. M.; Borst, J. W. FRET Reveals the Formation and Exchange Dynamics of Protein-Containing Complex Coacervate Core Micelles. *Langmuir* **2018**, *34*, 12083–12092.

[99] Holappa, S.; Kantonen, L.; Andersson, T.; Winnik, F.; Tenhu, H. Overcharging of polyelectrolyte complexes by the guest polyelectrolyte studied by fluorescence spectroscopy. *Langmuir* **2005**, *21*, 11431–11438.

[100] Murmiliuk, A.; Matějíček, P.; Filippov, S. K.; Janata, M.; Šlouf, M.; Pispas, S.; Štěpánek, M. Formation of core/corona nanoparticles with interpolyelectrolyte complex cores in aqueous solution: insight into chain dynamics in the complex from fluorescence quenching. *Soft Matter* **2018**, *14*, 7578–7585.

[101] Wu, H.; Ting, J. M.; Tirrell, M. V. Mechanism of Dissociation Kinetics in Polyelectrolyte Complex Micelles. *Macromolecules* **2020**, *53*, 102–111.

[102] Berret, J.-F.; Cristobal, G.; Hervé, P.; Oberdisse, J.; Grillo, I. Structure of colloidal complexes obtained from neutral/poly-electrolyte copolymers and oppositely charged surfactants. *Eur. Phys. J. E* **2002**, *9*, 301–311.

[103] Wu, H.; Ting, J. M.; Werba, O.; Meng, S.; Tirrell, M. V. Non-equilibrium phenomena and kinetic pathways in self-assembled polyelectrolyte complexes. *J. Chem. Phys.* **2018**, *149*, 163330.

[104] Hofs, B.; De Keizer, A.; Cohen Stuart, M. On the stability of (highly aggregated) polyelectrolyte complexes containing a charged-block-neutral diblock copolymer. *J. Phys. Chem. B* **2007**, *111*, 5621–5627.

[105] Li, Z.; Dormidontova, E. E. Equilibrium chain exchange kinetics in block copolymer micelle solutions by dissipative particle dynamics simulations. *Soft Matter* **2011**, *7*, 4179–4188.

[106] Dormidontova, E. E. Micellization kinetics in block copolymer solutions: Scaling model. *Macromolecules* **1999**, *32*, 7630–7644.

[107] Halperin, A.; Alexander, S. Polymeric micelles: their relaxation kinetics. *Macromolecules* **1989**, *22*, 2403–2412.

[108] Zinn, T.; Willner, L.; Pipich, V.; Richter, D.; Lund, R. Molecular exchange kinetics of micelles: corona chain length dependence. *ACS Macro Lett.* **2016**, *5*, 884–888.

[109] Wang, E.; Lu, J.; Bates, F. S.; Lodge, T. P. Effect of corona block length on the structure and chain exchange kinetics of block copolymer micelles. *Macromolecules* **2018**, *51*, 3563–3571.

[110] Choi, S.-H.; Bates, F. S.; Lodge, T. P. Molecular exchange in ordered diblock copolymer micelles. *Macromolecules* **2011**, *44*, 3594–3604.

[111] Halperin, A. Polymeric micelles: a star model. *Macromolecules* **1987**, *20*, 2943–2946.

[112] Kalkowski, J.; Liu, C.; Leon-Plata, P.; Szymusiak, M.; Zhang, P.; Irving, T.; Shang, W.; Bilsel, O.; Liu, Y. In Situ Measurements of Polymer Micellization Kinetics with Millisecond Temporal Resolution. *Macromolecules* **2019**, *52*, 3151–3157.

[113] Parent, L. R.; Bakalis, E.; Ramírez-Hernández, A.; Kammeyer, J. K.; Park, C.; De Pablo, J.; Zerbetto, F.; Patterson, J. P.; Gianneschi, N. C. Directly observing micelle fusion and growth in solution by liquid-cell transmission electron microscopy. *J. Am. Chem. Soc* **2017**, *139*, 17140–17151.

[114] Li, Z.; Dormidontova, E. E. Kinetics of diblock copolymer micellization by dissipative particle dynamics. *Macromolecules* **2010**, *43*, 3521–3531.

[115] Lund, R.; Willner, L.; Monkenbusch, M.; Panine, P.; Narayanan, T.; Colmenero, J.; Richter, D. Structural observation and kinetic pathway in the formation of polymeric micelles. *Phys. Rev. Lett.* **2009**, *102*, 188301.

[116] Lund, R.; Willner, L.; Richter, D.; Dormidontova, E. E. Equilibrium chain exchange kinetics of diblock copolymer micelles: Tuning and logarithmic relaxation. *Macromolecules* **2006**, *39*, 4566–4575.

[117] Choi, S.-H.; Lodge, T. P.; Bates, F. S. Mechanism of molecular exchange in diblock copolymer micelles: hypersensitivity to core chain length. *Phys. Rev. Lett.* **2010**, *104*, 047802.

[118] Lu, J.; Bates, F.; Lodge, T. Chain exchange in binary copolymer micelles at equilibrium: confirmation of the independent chain hypothesis. *ACS Macro Lett.* **2013**, *2*, 451–455.

[119] Prhashanna, A.; Khan, S. A.; Chen, S. B. Kinetics of chain exchange between diblock copolymer micelles. *Macromol. Theory Simul.* **2016**, *25*, 383–391.

[120] Lund, R.; Willner, L.; Stellbrink, J.; Lindner, P.; Richter, D. Logarithmic chain-exchange kinetics of diblock copolymer micelles. *Phys. Rev. Lett.* **2006**, *96*, 068302.

[121] Zinn, T.; Willner, L.; Lund, R.; Pipich, V.; Richter, D. Equilibrium exchange kinetics in n-alkyl–PEO polymeric micelles: single exponential relaxation and chain length dependence. *Soft Matter* **2012**, *8*, 623–626.

[122] Wang, E.; Zhu, J.; Zhao, D.; Xie, S.; Bates, F. S.; Lodge, T. P. Effect of solvent selectivity on chain exchange kinetics in block copolymer micelles. *Macromolecules* **2020**, *53*, 417–426.

[123] Rharbi, Y. Fusion and fragmentation dynamics at equilibrium in triblock copolymer micelles. *Macromolecules* **2012**, *45*, 9823–9826.

[124] Peters, A. J.; Lodge, T. P. Chain Exchange Kinetics of Asymmetric B1AB2 Linear Triblock and AB1B2 Branched Triblock Copolymers. *Macromolecules* **2017**, *50*, 6303–6313.

[125] König, N.; Willner, L.; Pipich, V.; Mahmoudi, N.; Lund, R. Tale of Two Tails: Molecular Exchange Kinetics of Telechelic Polymer Micelles. *Phys. Rev. Lett.* **2020**, *124*, 197801.

[126] Priftis, D.; Farina, R.; Tirrell, M. Interfacial energy of polypeptide complex coacervates measured via capillary adhesion. *Langmuir* **2012**, *28*, 8721–8729.

[127] Jho, Y.; Yoo, H. Y.; Lin, Y.; Han, S.; Hwang, D. S. Molecular and structural basis of low interfacial energy of complex coacervates in water. *Adv. Colloid Interface Sci.* **2017**, *239*, 61–73.

[128] Spruijt, E.; Cohen Stuart, M. A.; van der Gucht, J. Linear viscoelasticity of polyelectrolyte complex coacervates. *Macromolecules* **2013**, *46*, 1633–1641.

[129] Liu, Y.; Winter, H. H.; Perry, S. L. Linear viscoelasticity of complex coacervates. *Adv. Colloid Interface Sci.* **2017**, *239*, 46–60.

[130] Larson, R. G.; Liu, Y.; Li, H. Linear viscoelasticity and time-temperature-salt and other superpositions in polyelectrolyte coacervates. *J. Rheol.* **2021**, *65*, 77–102.

[131] Rubinstein, M.; Colby, R. H. *Polymer Physics*; Oxford University Press New York, 2003.

[132] Rubinstein, M.; Semenov, A. N. Dynamics of entangled solutions of associating polymers. *Macromolecules* **2001**, *34*, 1058–1068.

[133] Xu, L.; Selin, V.; Zhuk, A.; Ankner, J. F.; Sukhishvili, S. A. Molecular weight dependence of polymer chain mobility within multilayer films. *ACS Macro Lett.* **2013**, *2*, 865–868.

[134] Aponte-Rivera, C.; Rubinstein, M. Dynamic coupling in unentangled liquid coacervates formed by oppositely charged polyelectrolytes. *Macromolecules* **2021**, *54*, 1783–1800.

[135] Spruijt, E.; Sprakel, J.; Lemmers, M.; Cohen Stuart, M. A.; Van Der Gucht, J. Relaxation dynamics at different time scales in electrostatic complexes: time-salt superposition. *Phys. Rev. Lett.* **2010**, *105*, 208301.

[136] Spruijt, E.; van den Berg, S. A.; Cohen Stuart, M. A.; van der Gucht, J. Direct measurement of the strength of single ionic bonds between hydrated charges. *ACS Nano* **2012**, *6*, 5297–5303.

[137] Hamad, F. G.; Chen, Q.; Colby, R. H. Linear viscoelasticity and swelling of polyelectrolyte complex coacervates. *Macromolecules* **2018**, *51*, 5547–5555.

[138] Syed, V. M.; Srivastava, S. Time–ionic strength superposition: A unified description of chain relaxation dynamics in polyelectrolyte complexes. *ACS Macro Letters* **2020**, *9*, 1067–1073.

[139] Marciel, A. B.; Srivastava, S.; Tirrell, M. V. Structure and rheology of polyelectrolyte complex coacervates. *Soft Matter* **2018**, *14*, 2454–2464.

[140] Morin, F. J.; Puppo, M. L.; Laaser, J. E. Decoupling salt-and polymer-dependent dynamics in polyelectrolyte complex coacervates via salt addition. *Soft Matter* **2021**, *17*, 1223–1231.

[141] Yang, M.; Shi, J.; Schlenoff, J. B. Control of dynamics in polyelectrolyte complexes by temperature and salt. *Macromolecules* **2019**, *52*, 1930–1941.

Chapter 2

Chemical feedback in templated reaction-assembly networks

Chemical feedback between building block synthesis and their subsequent supramolecular self-assembly into nanostructures has profound effects on assembly pathways. Nature harnesses feedback in reaction-assembly networks in a variety of scenarios including virion formation and protein folding. Also in nanomaterial synthesis, reaction-assembly networks have emerged as a promising control strategy to regulate assembly processes. Yet, how chemical feedback affects the fundamental pathways of structure formation remains unclear. Here, we unravel the pathways of a templated reaction-assembly network that couples a covalent polymerisation to an electrostatic co-assembly process. We show how the supramolecular staging of building blocks at a macromolecular template can accelerate the polymerisation reaction and prevent the formation of kinetically-trapped structures inherent to the process in the absence of feedback. Finally, we establish a predictive kinetic reaction model that quantitatively describes the pathways underlying these reaction-assembly networks. Our results shed light on the fundamental mechanisms by which chemical feedback can steer self-assembly reactions and can be used to rationally design new nanostructures.

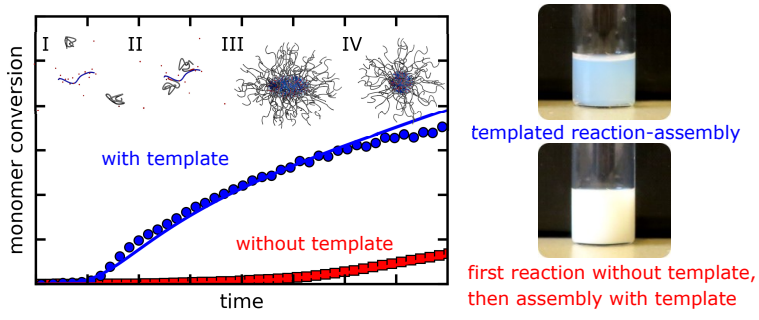

This chapter is based on: Inge Bos, Camilla Terenzi and Joris Sprakel. Chemical Feedback in Templated Reaction-Assembly Networks. *Macromolecules* **2020** *53*(23), 10675–10685.

2.1 Introduction

In nature, the biosynthesis of macromolecular building blocks and their assembly often occur simultaneously and within the same cellular compartment.[1–4] The spatiotemporal colocalisation of covalent and supramolecular reactions, involving the same molecular compounds, results in feedback between the different primary chemical reactions. Chemical feedback in these coupled reaction-assembly networks has profound effects on both the kinetics of the process and the final products that the coupled reactions yield. For example, the structure of virions is different when the translation of viral coat proteins occurs simultaneously with the DNA-templated assembly process as compared to the case when all proteins are already present at the start of the assembly.[3,5,6] Also in protein biosynthesis itself, folding of the polypeptide chain into the desired tertiary structure can be regulated by the rate of its translation.[4,7]

Supramolecular assembly strategies have become a paradigm in the creation of a plethora of synthetic nanomaterials.[8–11] However, while in nature reaction and assembly are invariably coupled, for synthetic materials the synthesis of the building blocks and their subsequent self- or co-assembly have traditionally been separated in both space and time. This facilitates experimental control on the purity and characterisation of the building blocks and of the details of the assembly process, but it also limits the structures than can be made, and the pathways by which these are reached, as the covalent reaction cannot be used to tune the assembly. In recent years, interest in the use of coupled reaction-assembly processes has emerged as a control mechanisms for creating synthetic nanomaterials. A seminal example is Polymerisation-Induced Self-Assembly (PISA), in which covalent polymerisations of amphiphilic macromolecules are coupled to the formation of micellar and vesicular structures that could not have been created using the classical spatiotemporal separation of the covalent and supramolecular processes.[12] Many examples of this strategy have now been reported.[13–15] More recently, this approach has been extended to templated assembly reactions. In Polymerisation-Induced Electrostatic Self-Assembly (PIESA), the polymerisation of a polyelectrolyte occurs in the presence of oppositely charged macroions that serve as molecular template for the assembly.[16–20] This is of particular interest, since templated assembly, in which a macromolecular template acts as a blueprint for the assembly process, is a common approach used by nature to guide multicomponent systems across their complex supramolecular energy landscapes to the desired final structure.[21–23] Yet, the control of templated assembly in the synthetic realm remains challenging.[24]

Despite the promise of these templated reaction-assembly networks, mechanistic insights into the emergence of chemical feedback in these networks remain elusive. For example, it is unclear how the kinetic pathways across underlying elementary reaction steps are affected by the coupling. Moreover, comprehensive and predictive models that capture the essence of chemical feedback in these chemical networks are lacking. Yet, these insights are crucial; not only to optimise and rationally-design synthetic reaction-assembly networks for nanomaterial fabrication, but also to provide a deeper understanding of how chemical feedback influences structure formation *in-vivo*.

In this chapter, we explore chemical feedback in a templated reaction-assembly network that couples covalent polymerisations to supramolecular electrostatic assembly on a macromolecular template. To unveil the kinetic pathways that underlie reaction progress, we perform time-resolved and *in-situ* measurements based on high-resolution NMR spectroscopy and spectrally-resolved relaxometry, complemented with light scattering studies. While classical NMR spectroscopy has been used previously to study reaction-assembly networks,[13,16–18] we extend these NMR spectroscopy measurements with spectrally-resolved NMR relaxation measurements to probe the local dynamics of the separate components, which is essential to unravel the underlying kinetic pathways of the network. Our experimental results reveal how the pre-assembly of monomers onto the oppositely charged template accelerates the covalent reaction and provides feedback to alter the supramolecular assembly process. On the basis of these experimental data, we establish a kinetic reaction-assembly model that quantitatively describes the underlying reaction pathways. These results can help both optimising the design of

synthetic reaction-assembly materials and resolving the role of chemical feedback in structure formation *in-vivo*.

2.2 Results and discussion

Our templated reaction-assembly network consists of a neutral macromolecular chain transfer agent P, positively charged monomers M as reagents and a negatively charged polyelectrolyte that forms the co-assembly template, consisting of template binding sites S (Fig. 2.1a). Specifically, we use poly(ethylene glycol methyl ether 4-cyano-4-(propylsulfanylthiocarbonyl)-sulfanylpentanoate (PEG-CTA) as macromolecular chain transfer agent, poly(sulphopropylmethacrylate) (PSPMA) with a degree of polymerisation of 47 as negative template and vinylbenzyltrimethylammonium chloride (VBTAC) as positive monomer. Reversible addition-fragmentation chain transfer (RAFT) polymerisation of the positive monomer occurs at the end of the neutral chain, resulting in the growth of the diblock copolymer $P\text{-}M_n$. In the standard case, the targeted degree of polymerisation of the positive block n is 50 and the ratio of monomer to template sites is 1:1. The reaction is performed at a potassium chloride (KCl) concentration of 35 mM. Both cationic monomer and the resulting cationic block of the diblock copolymer can bind to the template (Fig. 2.1b), as evidenced by isothermal titration calorimetry measurements (Fig. 2.A.1). When the cationic block grows sufficiently long, its binding to the anionic template induces micelle formation by complex coacervation. The complex of oppositely charged polyelectrolytes forms the micellar core and the neutral block forms its corona. These charge-driven micelles are often referred to as complex coacervate core micelles (C3Ms).[25]

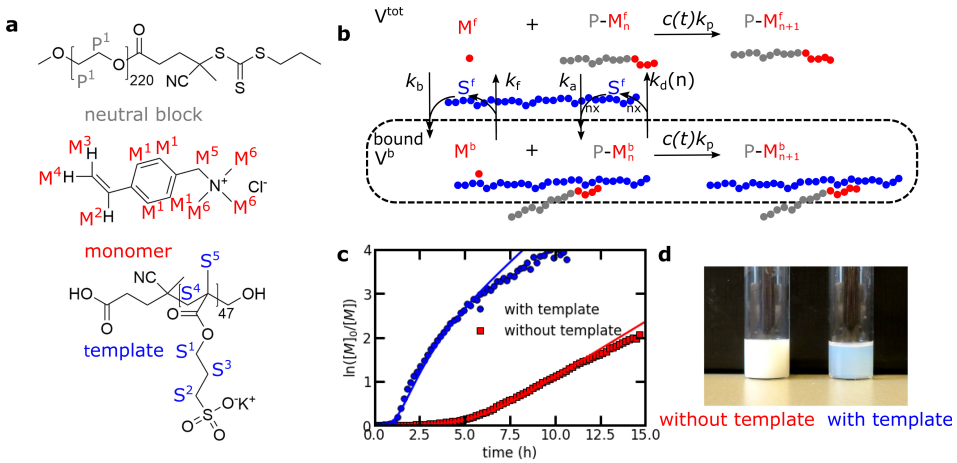

Figure 2.1. The templated reaction-assembly network. (a) The different components of the network. (b) Schematic overview of the templated reaction-assembly network and simplified representation of the kinetic model. (c) Pseudo first-order kinetics plot of the polymerisation reaction with and without template. Solid lines indicate kinetic model predictions with for the polymerisation with template $k_p = 0.36\ \mathrm{mM^{-1}h^{-1}}$, $k_b = k_a = 12\ \mathrm{mM^{-1}h^{-1}}$, $k_{bn} = 500k_b$, $k_d(n) = \omega_0 \exp(-nE_a/k_BT)$ with $\omega_0 = 3.1 \times 10^4\ \mathrm{h^{-1}}$ and $E_a = 6k_BT$, $k_f = k_d(1)$, $V^{\mathrm{tot}}/V^{\mathrm{b}} = 8$, $a = 3.0$, $t_{\mathrm{shift}} = 3.5\,\mathrm{h}$, $[M^{\mathrm{tot}}]_0 = 35$ mM, $[S^{\mathrm{tot}}]_0 = 35$ mM and $[P\text{-}M_0^{\mathrm{tot}}]_0 = 0.7$ mM. For the polymerisation without template, the same model parameters are used except for $k_b = k_a = k_f = k_d = 0$, $V^{\mathrm{tot}}/V^{\mathrm{b}} = 0$, $a = 0.9$, $t_{\mathrm{shift}} = 5.0\,\mathrm{h}$ and $[S^{\mathrm{tot}}]_0 = 0$. In both cases, the overall concentrations of the compounds, the polymerisation rate k_p, the empirical constants a and t_{shift} and the ratio between k_b and k_f follow from experiments, the values for ω_0 and E_a are based on literature values[26] and the values of $V^{\mathrm{tot}}/V^{\mathrm{b}}$ and k_{bn} are adjusted to fit the experimental data (*cf.* appendix Section 2.A.10 for further details). (d) Comparison of the end structures formed by 1) performing the polymerisation reaction without template and subsequently mixing the resulting diblock with the template at 44 °C and 2) performing the polymerisation reaction in the presence of template at 44 °C.

2.2.1 Phases in the reaction-assembly process

To unravel the kinetic pathways that underlie this templated reaction-assembly network, we use a combination of NMR spectroscopy, spectrally-resolved NMR relaxometry and light scattering. We use NMR spectroscopy to monitor the monomer conversion and NMR relaxometry to probe the chemical details of the reaction-assembly network (Fig. 2.A.2). The longitudinal relaxation time T_1 and transverse relaxation time T_2 both depend on the rotational correlation time τ_c of (part of) the molecule, with T_1 being mostly sensitive to fast molecular dynamics at the NMR measurement frequency and T_2 being mostly affected by static sources of restriction in the molecular reorientational dynamics.[27,28] Therefore, the combination of T_1 and T_2 measurements can be used to probe a wide range of mobility time scales, ranging from the fast dynamics of free monomers to the slow dynamics of polymers. The *in-situ* determination of both T_1 and T_2 is complicated by the relatively large reaction speed compared to the time needed for quantitative T_1 and T_2 measurements. To obtain both sufficient time resolution and sufficient information on the local mobility of the components, we perform only quantitative T_1 measurements during the reaction while we take the changes in a T_2-filtered intensity as measure for relative changes in T_2. We complement the ^{1}H NMR measurements with light scattering measurements: while NMR relaxation measurements probe the local dynamics of the separate components, light scattering measurements can probe the overall assembly of the different components together. Based on our experimental observations, we can distinguish four phases in the reaction-assembly process (Fig. 2.2a), which are explained below.

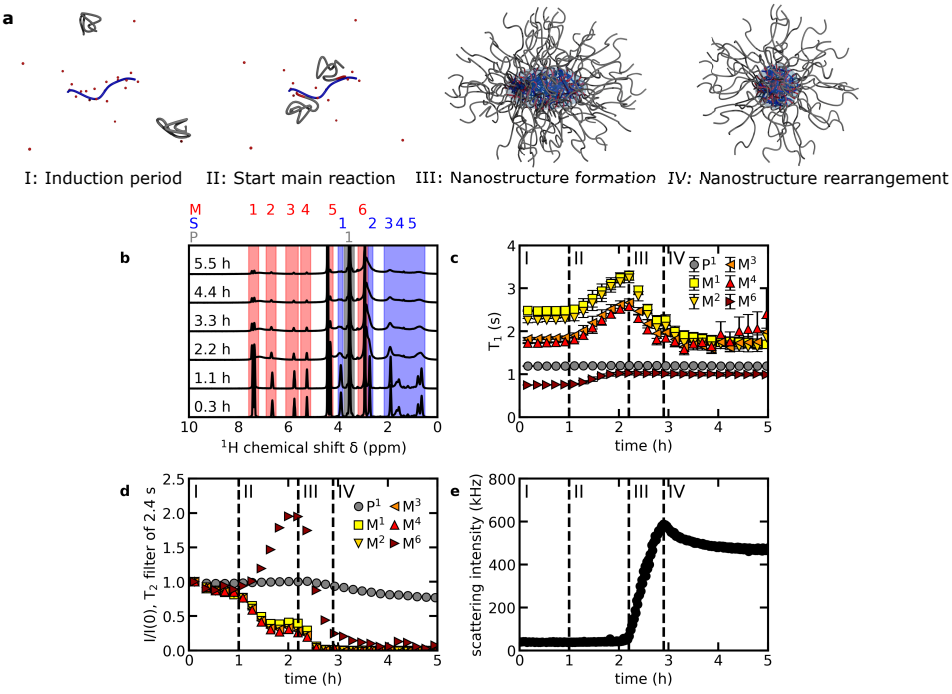

Figure 2.2. The different phases of the reaction-assembly process. (a) Schematic overview of the four different phases. At increasing reaction times of the templated reaction-assembly network: (b) ^{1}H NMR spectra; (c) T_1 values for the neutral block P and monomer M protons, with respective error bars obtained from single-exponential fitting; (d) T_2-filtered NMR spectral intensity (T_2-filter of 2.4 s) for the P and M protons, normalised to their own signal intensity at the start of the reaction; (e) Light scattering intensity.

Phase I: induction period

The reaction network is started by heating the reaction mixture which leads to thermal decomposition of the radical initiator. First, we observe an induction period (Phase I) during which the monomer conversion is slow as revealed by monitoring the monomer conversion by ^{1}H NMR spectral measurements with a 0.02 s T_2 filter (Fig. 2.1c).

Already at the start of this first phase, the situation with template differs from the one without template, in which there is no assembly and hence no chemical feedback. We observe that the longitudinal relaxation time T_1 of the monomer protons is shorter with template than without template (Table S1). For small molecules free in solution, both T_1 and T_2 decrease with increasing rotational correlation time of the molecule τ_c.[27,28] A decrease in T_1 in the presence of the template thus indicates restricted monomer mobility and can be explained by binding of monomers to the template. On the basis of T_1 measurements, we estimate that initially 50% of all monomer present binds to the oppositely charged template (Table 2.A.1). We note that differences among the T_1 values of the monomer protons are caused by differences in the intramolecular component of the dipole-dipole relaxation process. The latter process is driven by fluctuating fields generated via the interaction between two ^{1}H nuclear magnetic dipoles and its intra-molecular contribution is caused by nuclear vibrations and rotations within the molecule.[28]

The addition of the template substantially shortens the induction period (Fig. 2.1c). We hypothesise that this is due to the local accumulation of monomers at the macromolecular template, leading to a local increase of monomer concentration. To verify that a higher (local) concentration can shorten the induction phase, we performed different polymerisations without template at increasing monomer concentration, while keeping the concentration of chain transfer agent and initiator the same (Fig. 2.3a). Increasing the monomer concentration from 35 mM to 105 mM indeed shortens the induction period, while the final pseudo first-order polymerisation rate is the same in both cases (Fig. 2.3b). Further increasing the monomer concentration to 175 mM only has a moderate effect on the induction phase. This reveals that the induction period consists of two contributions, one which is sensitive to the monomer concentration and another which is not. The contribution sensitive to monomer concentration can be explained by the fact that the first monomer added to a growing chain can have a lower effective reactivity as compared to subsequently added monomers, which has also been observed in other RAFT polymerisations.[29] The contribution that is insensitive to monomer concentration is most likely due to a slow radical build-up at the reaction start, owing to the relatively low radical concentrations in our RAFT polymerisation.

Phase II: start main reaction

After the induction phase, the monomer conversion rate increases strongly, signalling the start of the main reaction (Phase II). For the polymerisation with template the polymerisation rate is strongly enhanced in this phase, as shown by the larger slope in the pseudo first-order kinetics plot of the monomer conversion (Fig. 2.1c). Also this is due to the local increase of monomer concentration near the template due to binding, and highlights the role of the template as a supramolecular staging area for the chemical reaction. We note that in another PIESA process the polymerisation with template was slower than without template.[18] We hypothesise that this difference with our system is caused by the ~17 times larger template concentration that was used in this other case, which will increase the viscosity, and thus slow down the overall polymerisation kinetics.

During Phase II, the T_1 of the monomer protons increases (Fig. 2.2c), signalling an increase in the monomer mobility. The T_2-filtered ^{1}H NMR intensity decreases for all monomer protons except M^6 (Fig. 2.2d). This trend can be explained by noticing that an increase in the T_2-filtered signal intensity can be caused by an increase either in the monomer concentration and/or in T_2. Because the monomer concentration decreases in Phase II, the behaviour of M^6 in Fig. 2.2d is due to an increase in T_2 which

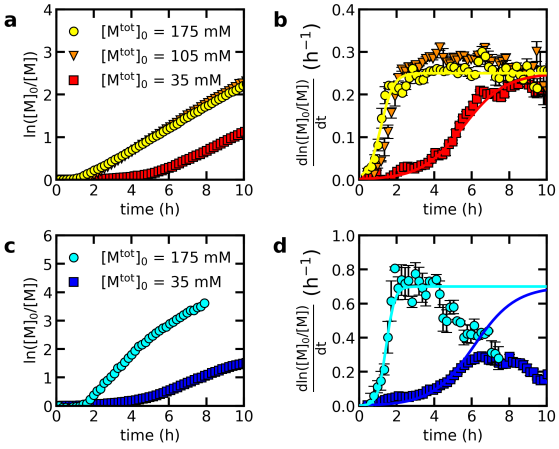

Figure 2.3. RAFT polymerisations without template at different monomer concentrations. (a,b) Polymerisation of the positive monomer (VBTAC) with the neutral block of Fig. 2.1a as chain transfer agent. (a) Pseudo first-order kinetics plot of the monomer conversion. (b) Local slope of the pseudo first-order kinetics plot of (a) as function of time. Error bars indicate uncertainty in the local slope determination. Solid lines are approximations of the experimental data based on the function $y = x(\exp(at - t_{\text{shift}})/(1 + \exp(at - t_{\text{shift}}))$ with $x = 0.25$ and $a = 0.9$ and $t_{\text{shift}} = 5.0$ (35 mM) and $a = 3.0$ and $t_{\text{shift}} = 3.5$ (175 mM). (c,d) Polymerisation of the negative monomer (KSPMA) with the neutral block of Fig. 2.4a as chain transfer agent. (c) Pseudo first-order kinetics plot of the monomer conversion. (d) Local slope of the pseudo first-order kinetics plot of (c) as function of time. Error bars indicate uncertainty in the local slope determination. Solid lines are approximations of the experimental data based on the function $y = x(\exp(at - t_{\text{shift}})/(1 + \exp(at - t_{\text{shift}}))$ with $x = 0.7$ and $a = 0.9$ and $t_{\text{shift}} = 5.5$ (35 mM) and $a = 4.5$ and $t_{\text{shift}} = 6.5$ (175 mM).

confirms the increased monomer mobility as seen by T_1. For the other monomer protons, their T_2 also presumably increases in Phase II but, because their T_2 is longer than that of M^6, the underlying intensity increase that is induced by T_2 increase becomes negligible compared to the intensity decay due to monomer consumption (appendix Section 2.A.3). These changes in T_1 and T_2 occur only for the polymerisation with template (Fig. 2.A.3) and are thus the result of chemical feedback.

The onset of faster monomer reorientational dynamics in Phase II is the result of competitive template binding between the monomer and growing diblock copolymer, which binds with a higher affinity due to multivalency. The binding of the polymerising positive blocks to the template is shown by the broadening of the template peaks in the ^{1}H NMR spectrum (Fig. 2.2b). Broader peaks indicate a smaller T_2 and therefore a decrease in template mobility. The result of the competition between monomers and polymerising blocks is that the concentration of template-bound monomer decreases, slowing down the polymerisation rate at the template, as can be seen from the decrease in the slope of the monomer conversion during Phase II (Fig. 2.1c).[18]

Phase III: nanostructure formation

In Phase III, co-assembly of the templates with growing diblock copolymers leads to the nucleation of microphase-separated objects, as revealed by an increase in scattered light intensity (Fig. 2.2e). Nanostructure formation in Phase III results in the net reduction of both T_1 and T_2 values of the monomer protons, except for M^6, suggesting that nanostructure formation somehow hinders the reorientational dynamics of the monomer (Fig. 2.2c and 2.2d). Three possible causes, and combinations thereof, can be identified to explain the observed reduction in monomer mobility: (i) the incorporation of bound

monomers within the nanostructures leads to a decrease in τ_c; (ii) an increase in the bound monomer fraction; (iii) an increase in the viscosity of the sample. The T_1 of the M^6 protons stays constant in Phase III, presumably due to that this chemical group is less affected by monomer incorporation in the nanostructure or viscosity increase, or because increasing spectral overlap with the adjacent polymer peak prevents accurate evaluation of T_1 for the M^6 peak. Another possibility is that the τ_c of the M^6 protons is around $1/(\sqrt{2}\omega_L)$ where ω_L is the Larmor frequency. At this point T_1 is less sensitive to changes in τ_c.[27,28]

Phase IV: nanostructure rearrangement

During Phase IV, continued polymerisation and equilibration lead to a decrease in light scattering intensity and apparent hydrodynamic radius (Fig. 2.2e, Fig. 2.A.4). A possible explanation for this decrease is the transition from initially elongated objects into smaller spherical micelles. It is known that weakening of the electrostatic interactions can induce a change in shape from spheres to ellipsoids, e.g. by the increase in ionic strength.[30] On the contrary here, as time progresses, the electrostatic interactions grow in strength as the length of the positive block increases which could result in the transition from initially elongated objects into smaller spherical micelles. This rearrangement occurs only for shorter template lengths, while for longer templates the light scattering intensity only increases during polymerisation with a lower final intensity and smaller apparent hydrodynamic radius than for the shorter template lengths (Fig. 2.A.5). This is in accord with literature results where the formation of ellipsoidal micelles was also observed only for shorter homopolymer lengths.[30] In fact, also for micelles formed at low concentration from the components of our system, transitions to larger nanostructures at ionic strengths above 10 mM happen only for the short template lengths (Fig. 2.A.5). Future time-resolved small-angle X-ray scatting (SAXS) measurements could help to verify whether the decrease in light scattering is indeed caused by rearrangements into smaller structures. At the moment we cannot exclude that other factors than the nanostructure size have affected the light scattering intensity, since the concentration of the reaction-assembly network is relatively high for light scattering experiments and therefore multiple-scattering events or interactions between the different scattering objects might occur, which can affect the light scattering intensity and the apparent hydrodynamic radius.

The nanostructure formation and rearrangement can also be observed from the decrease in T_2 of the neutral block(Fig. 2.2d). This decrease in T_2 agrees well with the proposed micelle formation: when the neutral block becomes integrated into a dense micellar corona its mobility is restricted, resulting in a lower T_2. The neutral block in the final equilibrium nanostructures exhibits three distinct T_2 values, while at the start of the reaction it has a single T_2 (Fig. 2.A.6). The three distinct T_2 values reveal the occurrence of three main local mobility environments for protons that might be assigned to, in order of increasing local mobility, protons close to micelle core, protons in the middle of the micelle corona and protons in the outer part of the micelle corona. This might also explain why the T_2-filtered signal decreases during Phase IV: the part of the corona close to the core becomes denser when the micelles become spherical. This means that locally the mobility of the protons close to the core gets lower, and thus the overall average T_2 decreases even though protons further away from the core can have an increase in mobility upon transition to spherical micelles and their T_2 might slightly increase. While, as expected, T_2 is sensitive to slow reorientational dynamic modes, we find that the T_1 of the neutral block is not much affected by the nanostructure formation (Fig. 2.2c). It might be that the τ_c of the neutral block is around $1/(\sqrt{2}\omega_L)$ where T_1 is less sensitive to changes in τ_c.[27,28] Similar behaviour of T_1 and T_2 of the neutral block upon C3M formation have been measured earlier at equilibrium conditions.[31]

The occurrence of these four different phases is not restricted to this particular reaction-assembly network: also for a shorter and longer template length we observe the same phases (Fig. 2.A.5), with the nanostructure reorganisation phase being absent for the longest template length, as discussed

above. This demonstrates the relative robustness of our observations. We note that variations between repetitions of the same reaction-assembly experiment (Fig. 2.A.5, Fig. 2.A.7) could be explained by small differences in the trace amount of oxygen present, which results in slightly different radical concentrations. These variations do not affect the general trends: in all these measurements the polymerisation rate in the presence of template is faster than in the absence of template and at certain point in the reaction the polymerisation rate decreases.

2.2.2 Inverted system

To further verify the robustness of our description of these templated reaction-assembly networks, we invert the system by polymerising a negatively charged block in the presence of a positively charged template (Fig. 2.4a). In this way, we change both the monomer-monomer interactions at the template (Fig. 2.A.1) and the polymerisation reactivity (Fig. 2.3c,d). The inverted system also shows a feedback-enhanced reaction rate as compared to the polymerisation without template (Fig. 2.4b). In addition, T_1 measurements show that also for the inverted system about 50% of all monomers initially binds to the oppositely charged template (Table 2.A.2). Furthermore, the inverted system undergoes the same reaction-assembly network phases: initially the monomer conversion is also slow (Fig. 2.4b). Subsequently, when the main reaction starts, the template peaks also broaden (Fig. 2.4c) and the monomer T_1 increases (Fig. 2.4d). The monomer T_1 decreases again when the nanostructure formation starts and also the T_2 of the neutral block decreases upon nanostructure formation (Fig. 2.4e). The inverted system does not show nanostructure rearrangement: the scattered light intensity only increases during the polymerisation reaction (Fig. 2.4f), similar to the reaction-assembly network with the longest negatively charged template. This is because the positively charged template is probably longer than the negatively charged template that we used for Fig. 2.2.

2.2.3 Effect of reactant stoichiometry

So far, we have focused on reaction networks with a 1:1 ratio of monomer-to-template sites. The reaction-assembly process and the underlying kinetics can be tuned by various parameters, such as the reactant stoichiometry. If we add an excess of monomer compared to the number of template sites at a 3:1 ratio, first nanostructures form and then disassemble again (Fig. 2.5a). This is similar to what has been observed for another PIESA reaction [16] and agrees with the observations that complex coacervate core micelles can be formed only around equal charge stoichiometry. [25,32]

Changing the reactant stoichiometry affects the relative polymerisation rate and the evolution of T_1 and T_2 of the monomers and neutral block during the reaction. The relative polymerisation rate is slower when we add an excess of monomer (Fig. 2.5b) because a smaller fraction of the total monomer can pre-assemble at the template, as it becomes saturated. This is reflected by the larger monomer T_1 values at the start of the reaction (Fig. 2.5c). The increase in T_1 at the start of the main reaction again indicates expulsion of the monomer from the template due to binding competition and the subsequent T_1 decrease again coincides with the start of the nanostructure formation which reduces the monomer mobility. As reaction time progresses, the point of equal charge stoichiometry is crossed, leading to an excess of positive block units as compared to template sites. This results in the disintegration of the nanostructures into soluble complexes where the excess part of the positive block is free in solution and the other part of the positive block is bound to the template, as evidenced by ^{1}H NMR spectroscopy (Fig. 2.A.8). The nanostructure disassembly results in an increase of the T_1 of the monomer protons. After 4 h, when the nanostructures are completely disassembled (Fig. 2.5a), the T_1-values of the monomers in the reaction network values have approached the T_1 values of free monomers in the absence of template (Table 2.A.1). After this point the T_1 values of the monomers remain constant. The apparent decrease of T_1 of the M^2 proton peak is probably due to partial overlap with the NMR signal of the adjacent peak of positive polymer formed during the reaction. The measured T_1 of the M^6 proton peak is not

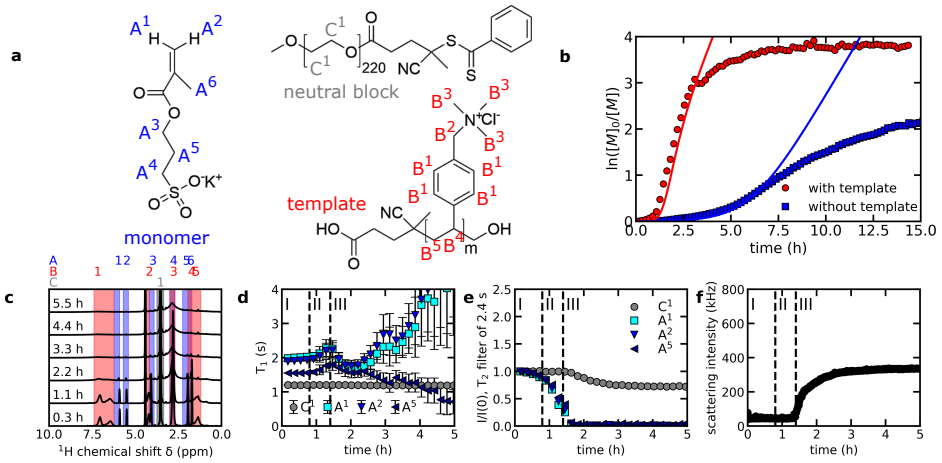

Figure 2.4. The inverted reaction-assembly network where a negatively charged block is polymerised in the presence of a positively charged template. (a) The different components of the inverted reaction-assembly network. (b) Pseudo first-order kinetics plots of the monomer conversions for reactions with template and without template. Solid lines indicate model predictions with for the polymerisation with template $k_p = 1.0\ \mathrm{mM^{-1}h^{-1}}$, $k_b = k_a = 12\ \mathrm{mM^{-1}h^{-1}}$, $k_{bn} = 500k_b$, $k_d(n) = \omega_0 \exp(-nE_a/k_BT)$ with $\omega_0 = 3.1 \times 10^4\ \mathrm{h^{-1}}$ and $E_a = 6k_BT$, $k_f = k_d(1)$, $V^{\mathrm{tot}}/V^{\mathrm{b}} = 8$, $a = 4.5$ and $t_{\mathrm{shift}} = 6.5\,\mathrm{h}$, $[M^{\mathrm{tot}}]_0 = 35$ mM, $[S^{\mathrm{tot}}]_0 = 35$ mM and $[P\text{-}M_0^{\mathrm{tot}}]_0 = 0.7$ mM. For the polymerisation without template, the same model parameters are used except for $k_b = k_a = k_f = k_d = 0$, $V^{\mathrm{tot}}/V^{\mathrm{b}} = 0$, $a = 0.9$, $t_{\mathrm{shift}} = 5.5\,\mathrm{h}$ and $[S^{\mathrm{tot}}]_0 = 0$. At increasing reaction times of the templated reaction-assembly network: (c) ^{1}H NMR spectra; (d) T_1-values for neutral block C and the monomer A protons, with respective error bars obtained from single-exponential fitting; (e) T_2-filtered NMR spectral intensity (T_2-filter of 2.4 s) for the C and A protons, normalised to their own signal intensity at the start of the reaction; (f) Light scattering intensity.

much affected by the nanostructure formation, as was also observed in the 1:1 ratio case. The T_2-filtered intensity of the monomers show similar trends as the T_1 (Fig. 2.5f), except in that it decreases after 4 h, most probably because of the concurrent effects due to variations in monomer concentration and in T_2: after 4 h the amount of monomer keeps decreasing, thus lowering the T_2-filtered intensity, while T_2 probably remains constant. The decrease and subsequent increase in T_2-filtered intensity of the neutral block reflect the nanostructure formation and subsequent disassembly.

The change in stoichiometry not only affects the reaction rate and the final structure formed, but also the (intermediate) structures that are formed at equal charge stoichiometry of both polyelectrolytes. The polyelectrolyte charge stoichiometry can be expressed by the fractional polymer charge ratio $f^+_{\mathrm{pol}} = [\mathrm{pos}]/([\mathrm{pos}]+[\mathrm{neg}])$ where [pos] and [neg] are the concentrations of monomers that are part of a polycation and polyanion respectively. At equal charge stoichiometry $f^+_{\mathrm{pol}} = 0.5$. In excess of monomer, the intermediate structures at $f^+_{\mathrm{pol}} = 0.5$ scatter more light, indicating that different structures are formed. This difference can be explained from the effect of stoichiometry on the absolute reaction rate: although the relative reaction rate is lower when the monomer is present in excess, the absolute reaction rate is still higher. This can be seen by comparing the increase of the degree of polymerisation of the positive block (Fig. 2.5e). Especially around $f^+_{\mathrm{pol}} = 0.5$ the polymerisation with excess monomer is faster. This higher absolute rate is the result of the larger overall monomer concentration.

This reveals the important role that the kinetic pathways play in structure formation: the building blocks form different structures when the rate at which they approach the point of equal charge stoichiometry is higher. This is seen by the fact that the scattering intensity is higher when the rate of polymerisation around $f^+_{\mathrm{pol}} = 0.5$ is increased. Moreover, direct mixing of pre-synthesised polymers

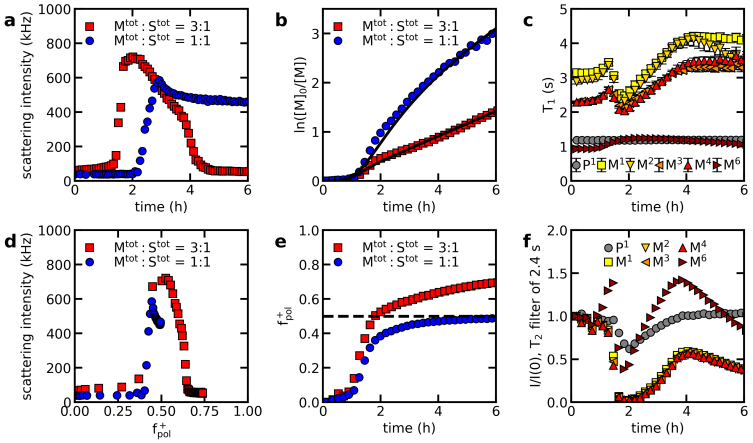

Figure 2.5. Effect of the monomer to template ratio $M^{\text{tot}} : S^{\text{tot}}$. (a) Light scattering intensity during the reaction-assembly process. (b) Pseudo first-order kinetics plot of the reaction-assembly process. Solid lines indicate model predictions with the same model parameters as in Fig. 2.1, except for the initial monomer concentration for $M^{\text{tot}} : S^{\text{tot}} = 3 : 1$, which is $[M^{\text{tot}}]_0 = 105$ mM. (c) T_1-values of P and M protons during the reaction-assembly process for $M^{\text{tot}} : S^{\text{tot}} = 3 : 1$ with respective error bars obtained from single-exponential fitting. (d) Light scattering intensity as function of fractional polymer charge ratio f^+_{pol}. (e) Positive polymer fraction f^+_{pol} during the reaction-assembly process. The dashed line indicates the point of equal charge stoichiometry of the oppositely charged polyelectrolytes. (f) Changes in the T_2-filtered NMR spectral intensity (T_2-filter of 2.4 s) for the P and M protons, normalised to their own signal intensity at the start of the reaction, for the $M^{\text{tot}} : S^{\text{tot}} = 3 : 1$ reaction-assembly process.

at $f^+_{\text{pol}} = 0.5$, where equal stoichiometry is achieved almost instantly, results in very turbid samples (Fig. 2.1d). This suggests that in this case kinetically-trapped structures are formed when building block synthesis and assembly are decoupled. Indeed, during C3M formation larger non-equilibrium clusters are sometimes observed to be formed, which can either relax to their equilibrium state [33,34] or remain trapped if equilibration is too slow. [33,35] Gradual transition across the energy landscape for co-assembly by coupling synthesis with assembly can avoid the formation of these trapped structures, without necessitating laborious protocols in which salt is gradually removed to slowly increase the interaction strength. [36]

2.2.4 Kinetic model

These data shed light on the fundamental effects that chemical feedback can have on the templated co-assembly process explored here. To obtain a quantitative grasp on these effects for a predictive understanding of reaction-assembly networks, we develop a kinetic reaction network model that captures the elementary reaction steps and their couplings. Polymerisation can take place both at the template and in solution, with a rate constant k_p. At the template, the monomer concentration is locally increased because of supramolecular binding. The factor by which the concentration is increased depends on the ratio of the volume around the template compared to the total volume $V^{\text{b}}/V^{\text{tot}}$ and the monomer fraction that is bound to the template. This fraction depends on the number of available free binding sites S^f and on the monomer binding affinity. The binding affinity is reflected in the ratio between the binding constant k_b and release constant k_f of the monomer to the template. The positive block binds stronger to the template due to multivalency: $k_d = \omega_0 \exp(-nE_a/k_BT)$, where E_a is the binding energy of a single monomer unit to the template. The diblock binds to the template with an association rate k_a, which is diffusion-limited. The positive monomers of a bound diblock can

temporarily release from the template and subsequently bind again. As long as part of the monomers of the bound diblock remain bound, this temporal release of some of the monomers will not result in the release of the diblock from the template. The release rate constant of a diblock monomer is the same as the dissociation constant for a single monomer k_f. However, we expect that the binding rate constant k_{bn} is larger than the binding constant of a single monomer k_b because the free monomers of the bound diblock remain close to the template. The different processes of the kinetic reaction network model are schematically summarised in Fig. 2.1b. For visual clarity, the reaction of the free diblock with the bound monomers, the reaction of the bound diblock with the free monomers and the exchange of the bound monomers of the bound diblock between a template bound and a free state are not shown in Fig. 2.1b.

The polymerisation rate in our kinetic model has to be corrected to account for the experimentally-observed induction period. For this we use the polymerisations without template at different monomer concentrations to obtain experimentally-derived correction functions $c(t)$ (Fig. 2.3). For the polymerisation with template we obtain the $c(t)$ from the polymerisation without template at a monomer concentration 175 mM. This is an approximation because the local monomer concentration at the template is not exactly 175 mM and the monomer concentration is only locally increased. However, at larger monomer concentrations the effect of the monomer concentration on the induction period is small compared to monomer independent induction time. Therefore, we expect that these differences only have a minor effect and the approximation will work reasonably well. The correction functions $c(t)$ follow from the local slopes of the pseudo first-order kinetics plots: for pseudo first-order polymerisation kinetics, this slope equals $k_p \sum_n [P\text{-}M_n]$ where k_p is the polymerisation rate constant per molar of polymer $\sum_n [P\text{-}M_n]$. The factor by which the local slope at time t deviates from this value, gives the correction value $c(t)$. We note that for the polymerisation of the inverted system, deviations from pseudo first-order kinetics do not happen only at the start of the reaction, but also at the end probably because of radical termination reactions (Fig. 2.3c,d). Since we expect the termination reactions to be slightly different for every polymerisation reaction, we do not include these effects in $c(t)$. In order to numerically solve the differential equations of the kinetic model we need a better time resolution than we can obtain from the NMR reaction experiments. Therefore we approximate the local slope function by the function $y = x(\exp(at - t_{\text{shift}})/(1 + \exp(at - t_{\text{shift}})) = xc(t)$ where x should equal $x = k_p \sum_n [P\text{-}M_n]$ and a and t_{shift} are empirical constants (Fig. 2.3b,d).

The covalent and supramolecular reactions together can be described by a set of differential reaction kinetics equations (Methods). Once the initial concentrations and model constants are known, this system of differential equations can be numerically solved to give the concentrations of the different components as function of the reaction time. Most rate constants are obtained from additional experiments or literature[26]; see appendix Section 2.A.10 and Fig. 2.A.10-2.A.17 for parameterisation details. We use only the ratio $V^{\text{tot}}/V^{\text{b}}$ and the binding rate of the unbound monomers of the bound diblock k_{bn} as adjustable parameters to fit the model to the experimental data. By taking $V^{\text{tot}}/V^{\text{b}} = 8$ and $k_{bn} = 500k_b$ the model prediction of the monomer conversion agrees well with the experimental data for the reaction-assembly network with the negatively charged template (Fig. 2.1c, 2.5b). In addition, it also correctly describes the time point of free monomer fraction increase (Fig. 2.6b, Fig. 2.2c,d, Fig. 2.5c,f). For the inverted reaction-assembly network, the model overestimates the reaction rate at longer reaction times (Fig. 2.4b) because we did not include the effect of radical termination in the model $c(t)$ function as explained above. The obtained value for $V^{\text{tot}}/V^{\text{b}}$ is smaller than we estimated based on estimations of the ionic bond length and polyelectrolyte blob size (Fig. 2.A.9). Possible explanations for this difference are that the bound monomers might also be further away than the ionic bond length or that neglecting the prefactors in the estimation resulted in an overestimation of the $V^{\text{tot}}/V^{\text{b}}$ ratio. In addition, viscosity effects might have slightly slowed down the polymerisation, resulting in a lower apparent $V^{\text{tot}}/V^{\text{b}}$ ratio in the experiments. The fact that k_{bn} has to be much larger than the binding rate constant of a single monomer k_b to accurately describe the data (Fig. 2.A.11)

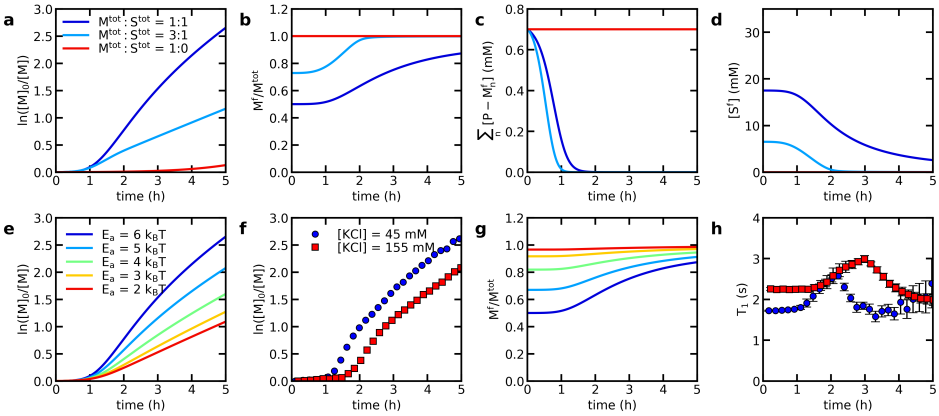

Figure 2.6. Kinetic model predictions and the effect of the monomer-template interaction strength.(a-e,g) Kinetic model predictions for (a,e) the time evolution of the monomer concentration, (b,g) free monomer fraction M^f/M^{tot}, (c) free diblock copolymer concentration $\sum_n [P\text{-}M_n^f]$ and (d) free template sites concentration. Model predictions are made for the polymerisation reaction with different monomer to template ratios (a-d) and for the polymerisation reaction with template at $M^{tot}:S^{tot} = 1:1$ with decreasing monomer binding strengths by decreasing the value of E_a (e,g), which affects both k_d and k_f. Unless otherwise indicated the model parameters are the same as in Fig. 2.1. (f,h) Experimental effects of decreasing the monomer binding strength by increasing the ionic strength (KCl concentration) in the reaction-assembly network on (f) the monomer conversion and on (h) the T_1 of the monomer proton M^4.

demonstrates once more that local enrichment can significantly increase the rate at which the process occurs.

The free diblock copolymer concentration decreases before we observe the increase in the fraction of free monomers (Fig. 2.6c). Only when the average degree of polymerisation increases sufficiently such that the binding affinity of the diblock becomes larger, the bound monomer fraction decreases. The increased binding affinity of the diblock results in a decrease in free template sites S^f (Fig. 2.6d). This decrease in S^f shifts the monomer-to-template binding equilibrium more towards the free monomers. The binding of the diblock to the template is reflected by the broadening of the template proton peaks in the ^{1}H NMR spectra (Fig. 2.2b, Fig. 2.A.8).

Within our model, the template plays an essential role by acting as staging area for the chemical reaction. By decreasing the monomer-template interactions, the template effect can be reduced: decreasing the binding energy E_a of a monomer to the template results in less monomer binding and as a result the reaction rate is decreased (Fig. 2.6e,g). In fact, for the lowest binding energies the decrease might even be larger than shown here because the induction period and thus $c(t)$ are also affected when the monomer concentration largely decreases (Fig. 2.3, Fig. 2.A.13). A way to decrease the interaction strength experimentally is to increase the ionic strength in the solution. A higher ionic strength indeed lowers the monomer binding and the reaction rate (Fig. 2.6f,h, Fig. 2.A.18). In addition, the induction period seems to lengthen at higher ionic strength, which could indicate that the decrease in local monomer concentration is large enough to affect the induction period. These effects of changing the interaction strength demonstrate that the reaction rate of the templated reaction-assembly network can be tuned, which is essential to regulate the assembly and in some cases can regulate the final structures formed, as discussed above.

2.3 Conclusions

The rational design of synthetic reaction-assembly strategies requires a deep understanding of the chemical feedback between the covalent reaction and the supramolecular assembly. Here, we have unravelled the kinetic pathways of templated reaction-assembly networks and we have shown that chemical feedback fundamentally changes both processes. Supramolecular staging of the monomers on the template strongly accelerates the polymerisation reaction. The rate at which the reaction reaches the point of self-assembly in turn affects the structures that are formed.

One of the challenges in the design of self- or co-assembling systems is to ensure they arrive at their equilibrium state and do not become trapped in a local energetic minimum. Our results highlight how the rational design of a reaction-assembly network can achieve exactly this also at relatively high concentrations, where kinetic trapping is often inevitable in conventional assembly processes.[37] These results can be easily extended to other PIESA and PISA systems where kinetic trapping is avoided or in some cases promoted to arrive at new nanostructures.[14,16,17] Also in these other reaction-assembly networks spectrally-resolved NMR relaxometry can be applied to probe the local dynamics of the separate components. Simultaneously, our kinetic model can serve as a framework to describe also these other systems after implementing some adaptations, for example including viscosity effects or replacing local enrichment at the template by local enrichment within assembled structures. It would be interesting to complement these future measurements by time-resolved SAXS measurements as the interpretation of SAXS measurements at the relatively high concentrations of the reaction-assembly networks is less ambiguous than for conventional light scattering experiments. By using this combination of NMR experiments, scattering experiments and kinetic modelling, the assembly of a wide variety of nanostructures can be linked to the corresponding reaction kinetics, facilitating the rational design of new synthetic supramolecular materials.

2.4 Methods

2.4.1 Sample preparation

A comprehensive overview of synthetic methods is provided in the appendix (Section 2.A.1). For the reaction-assembly experiment at $M^{tot} : S^{tot} = 1 : 1$, the positive monomer vinylbenzyltrimethylammonium chloride (VBTAC, 35 mM, the macroRAFT chain transfer agent poly(ethylene glycol methyl ether 4-cyano-4-(propylsulfanylthiocarbonyl)- sulfanylpentanoate (PEG-CTA, 0.7 mM), the radical initiator 2,2'-azobis[2-(2-imidazolin-2-yl)propane] dihydrochloride (VA-044, 0.14 mM), the template poly(sulphopropylmethacrylate) (PSPMA, 35 mM of SPMA units) and potassium chloride (KCl) (10 mM) were dissolved in 5 mL D_2O. The solution was degassed with N_2 for 30 min. Simultaneously a glass tube for light scattering experiments and a NMR tube both sealed with a rubber septum were also degassed for 30 min. Subsequently, circa ~ 0.8 mL was transferred to the NMR tube and ~ 3.5 mL was transferred to the glass tube.

For the polymerisation at a $M^{tot} : S^{tot} = 3 : 1$ ratio, the monomer concentration was 105 mM instead of 35 mM, for the polymerisations without template no PSPMA was added and for the polymerisation at larger ionic strength, 120 mM KCl was added instead of 10 mM.

The sample preparation protocol for the inverted reaction-assembly network was similar to the sample preparation protocol for the normal reaction-assembly network with [VBTAC] = 35 mM. Only this time, the negatively charged PSPMA template was replaced by the positively charged poly((vinylbenzyl) trimethylammoniumchloride) (PVBTA) template and the positively charged VBTAC monomer was replaced by the negatively charged 3-sulphoproyl methacrylate potassium (KSPMA) monomer. In addition, the PEG chain transfer agent was replaced by another PEG chain transfer agent, poly(ethylene glycol) 4-cyano-4-phenylcarbonothioylthio) pentanoate. For the polymerisations without template no PVBTA was added.

2.4.2 Light scattering measurements

Light scattering measurements were performed at 44 °C on ALV light-scattering apparatus equipped with an ALV/LSE-5004 light scattering electronic and multiple tau digital correlator and a HeNe-laser operating at 632.8 nm. The scattering angle was set at 90°. The scattered intensities were obtained by averaging the photon count rate over periods of 60 s. The apparent hydrodynamic radius was obtained from second-order cumulant analysis of the intensity autocorrelation function (Fig. 2.A.4).

2.4.3 NMR measurements

^{1}H NMR reaction experiments were performed at 44 °C on a Bruker 700 MHz Avance NMR equipped with a BBI probe. During the reaction, a set of four different NMR measurements was continuously repeated, consisting of: (i) single-pulse spectral acquisition; (ii) single-pulse spectral acquisition with a T_2-filter based on PROJECT pulse sequence[38] (short filter of 20 ms, Section 2.A.3 and Fig. 2.A.2); (iii) same as in (ii) but with long T_2-filter of 2.4s (Section 2.A.3); (iv) inversion recovery measurement with a PROJECT-based acquisition scheme (Section 2.A.3 and Fig. 2.A.2). Here, measurements (ii), (iii) and (iv) were used respectively to quantify the monomer conversion, to observe indirect effects of T_2 on signal intensity, and to determine T_1 relaxation rates. The length of the 90° RF pulse was readjusted at the start of every reaction and was subsequently kept constant within the reaction study. A 14 kHz spectral width was used. In each experiment the signal from two consecutive acquisitions was added to obtain sufficient signal-to-noise ratio. The receiver dead time was set to 6.5 µs. The longest T_1 was about 3-4 s during most of the reaction, thus the recycle delay was set to 21 s ($\sim 5T_1$) to obtain quantitative results while achieving the desired time resolution. Only at the end of the reactions with template at $M^{\text{tot}} : S^{\text{tot}} = 3 : 1$, and during the reactions without template, the T_1 of one M peaks (M^2) exceeded 4.2 s (Fig. 2.A.2), thus this particular result is not fully quantitative. Yet, this does not affect the data interpretation presented here. The M^5 proton peak partly overlaps with the solvent peak and the A^3, A^4 and A^6 proton peaks (partly) overlap with the template proton peaks. Therefore these protons are not included in the analysis of T_1 and of the T_2-filtered intensity. After the reaction, the measured free induction decays were Fourier transformed, phased, baseline corrected and integrated by using the Bruker NMR software TopSpin 4.0.7. Single-exponential data fitting of T_1 recovery curves was performed by using a constrained non-linear least square fit algorithm as implemented in the Python package SciPy.

2.4.4 Kinetic model

The kinetic model describes the changes in concentration of the different components with a set of differential equations. Here we give a brief overview of these equations. More details are given in the appendix (Section 2.A.10).

The change in free monomer concentration is given by:

$$\frac{d[M^f]}{dt} = -k_b[M^f][S^f] + k_f[M^b] - k_p c(t)[M^f]\left(\sum_n [P\text{-}M_n^f] + \sum_n [P\text{-}M_n^b]\right) \tag{2.1}$$

where the first two terms indicate the change of free monomer concentration due to exchange of the monomer between the free and the bound state and the last term indicates the change due to the polymerisation reaction. In a similar way we get for the bound monomer:

$$\frac{d[M^b]}{dt} = k_b[M^f][S^f] - k_f[M^b] - k_p c(t)[M^b]\left(\frac{V^{\text{tot}}}{V^b}\sum_n [P\text{-}M_n^b] + \sum_n [P\text{-}M_n^f]\right) \tag{2.2}$$

Here the factor V^{tot}/V^b accounts for the fact that the monomer concentration at the template is locally increased.

The change in concentration of a free diblock with a degree of polymerisation of the positive block n is given by:

$$\frac{d[P\text{-}M_n^f]}{dt} = -k_a[S^f][P\text{-}M_n^f] + k_d(n)[P\text{-}M_n^b] + k_p c(t)\Big([M^f] + [M^b]\Big)\Big([P\text{-}M_{n-1}^f] - [P\text{-}M_n^f]\Big) \tag{2.3}$$

Also here the first two terms correspond to exchange between the free and the bound state and the last term corresponds to the polymerisation reaction.

The change in concentration of a bound diblock with degree of polymerisation of the positive block n follows from:

$$\frac{d[P\text{-}M_n^b]}{dt} = k_a[S^f][P\text{-}M_n^f] - k_d(n)[P\text{-}M_n^b] + k_p c(t)\Big([M^f] + \frac{V^{\text{tot}}}{V^b}[M^b]\Big)\Big([P\text{-}M_{n-1}^b] - [P\text{-}M_n^b]\Big) \tag{2.4}$$

The neutral block $P\text{-}M_0$ cannot bind to the template and therefore always remains in the free state. Its concentration decreases due to the polymerisation reaction:

$$\frac{d[P\text{-}M_0^f]}{dt} = -k_p c(t)\Big([M^f] + [M^b]\Big)[P\text{-}M_0^f] \tag{2.5}$$

When a diblock with n positive monomers is bound to the template, part of the monomers can also temporarily unbind from the template and rebind again. The positive monomers of bound diblocks can thus exchange between a free and a bound state. We indicate the concentration of bound positive monomers of bound diblocks with $[n^b]$ and the concentration of free positive monomers of bound diblocks with $[n^f]$. The concentration of bound positive monomers of bound diblocks $[n^b]$ changes according to:

$$\begin{aligned}\frac{d[n^b]}{dt} =& k_{bn}[n^f][S^f] - k_d(1)[n^b] + k_a[S^f]\sum_n [P\text{-}M_n^f]n - z\sum_n k_d(n)[P\text{-}M_n^b]n + \\ & k_p c(t)\Big([M^f] + \frac{V^{\text{tot}}}{V^b}[M^b]\Big)\sum_n [P\text{-}M_n^b]\end{aligned} \tag{2.6}$$

where $z = [n^b]/([n^b] + [n^f])$ is the fraction of bound monomers of the positive block. The first two terms correspond to the exchange between the free and bound state. The third and fourth term indicate the changes in $[n^b]$ due to binding and release of the diblock respectively and the last term indicates the increase in $[n^b]$ when a bound diblock reacts with a free monomer.

The change in the concentration of free positive monomers of bound diblocks $[n^f]$ is given by:

$$\frac{d[n^f]}{dt} = -k_{bn}[n^f][S^f] + k_d(1)[n^b] - (1-z)\sum_n k_d(n)[P\text{-}M_n^b]n \tag{2.7}$$

Finally, the change of the free template site concentration is given by:

$$\begin{aligned}\frac{d[S^f]}{dt} =& -k_b[M^f][S^f] + k_f[M^b] - k_a[S^f]\sum_n [P\text{-}M_n^f]n + z\sum_n k_d(n)[P\text{-}M_n^b]n - \\ & k_{bn}[n^f][S^f] + k_d(1)[n^b] + k_p c(t)\Big([M^b]\sum_n [P\text{-}M_n^f] - [M^f]\sum_n [P\text{-}M_n^b]\Big)\end{aligned} \tag{2.8}$$

where the first two terms correspond to the binding and release of a single monomer, the third and fourth term to the binding and release of a diblock, the fifth and sixth term to the binding and release of the monomers of the bound diblocks and the last term account for changes in $[S^f]$ due to reactions of a bound monomer with a free diblock or a free monomer with a bound diblock.

We have used the Runge-Kutta fourth-order method to numerically solve this system of differential equations for different sets of model parameters (Fig. 2.A.10-2.A.17).

2.A Appendix

2.A.1 Polymer synthesis

PEG chain transfer agent synthesis

Materials

1-Propanethiol (99 %), sodium hydroxide pellets (NaOH, 98 %), carbondisulfide (99.9 %), iodine (I_2, 99%), magnesium sulfate (99 %), 4,4-azobis(4-cyanovaleric acid) (ACVA, 98%), methyl ether polyethylene glycol (mPEO, M_n = 10 000 g mol^{-1}) and *N,N*-dicyclohexylcarbodiimide (DCC, 99%) were purchased from Sigma Aldrich. Sodium thiosulfate (99%) was purchased from VWR. 4-(Dimethylamino)pyridine (DMAP, 99%) was purchased from Acros Organics. Diethyl ether, dioxane, ethyl acetate, hexane and dichloromethane were purchased from Biosolve. All materials were used as received.

Methods

The PEG chain transfer agent, poly(ethylene glycol methyl ether 4-cyano-4-(propylsulfanylthiocarbonyl)-sulfanylpentanoate, was synthesised by first synthesizing 4-cyano-4-(propylsulfanylthiocarbonyl)sulfanyl-pentanoic acid (CPP), which was subsequently coupled to polyethylene glycol methyl ether to give the PEG chain transfer agent.

The synthesis of CPP was based on a protocol described by Barlow et al.[39]: first bis(propylsulfanyl-thiocarbonyl)disulfide (BPD) was synthesised which was subsequently reacted with ACVA to give the CPP. For the BPD synthesis, 1-propanethiol (5.3 g, 70 mmol) was dissolved in 50 mL diethyl ether and the mixture was strongly stirred at room temperature. Next, 1 equivalent of aqueous NaOH was added and the mixture was stirred for 30 minutes. Subsequently, 1.1 equivalent carbondisulfide in 5 mL diethyl ether was added. Again the mixture was stirred for 30 minutes. Then the reaction mixture was diluted by adding 30 mL diethyl ether and 0.55 equivalent I_2 was slowly added. After 90 minutes, 6 mL diethyl ether was added and the mixture was washed two times with 0.25 M sodium thiosulfate solution and one time with demiwater. The organic layer was dried with magnesium sulfate and the solvent was evaporated to give the BPD product (8.18 g, 27.1 mmol, 77 % yield). Part of the BPD product (2.5 g, 8.3 mmol) was dissolved in 25 mL dioxane and reacted with ACVA (4.6 g, 16.4 mmol) under N_2 atmosphere at 70 °C for 20 h. The dioxane was evaporated to give the crude product as a viscous orange oil. The product was purified by using column chromatography on a silica gel with ethyl acetate/hexane (1/1, v/v) as mobile phase. This yielded the CPP (2.3 g, 8.1 mmol, 48 % yield).

The procedure to couple the CPP to the polyethylene glycol methyl ether was adapted from a protocol described by Xu et al.[40]: mPEO (4.0 g, 0.4 mmol), CPP (0.27 g,1.0 mmol) and DMAP (0.049 g , 0.4 mmol) were dissolved in 15 mL dichloromethane. The solution was mixed and then the reaction flask was placed in an icebath. Subsequently, DCC (0.20 g, 1.0 mmol) was added in portions. After reacting 8 h at 0 °C, the mixture was allowed to react for another 40 h at room temperature. Subsequently the precipated dicyclohexylurea was filtered off. The PEG chain transfer agent (2.46 g, 0.25 mmol, 60 % yield) was obtained by precipitating the filtrate three times in diethyl ether and drying under vacuum.

The PEG chain transfer agent (poly(ethylene glycol) 4-cyano-4-phenylcarbonothioylthio)pentanoate) of the inverted reaction-assembly network was purchased from Sigma Aldrich.

PSPMA synthesis

Materials

4,4-azobis(4-cyanovaleric acid) (ACVA, 98%), 4-Cyano-4-(phenylcarbonothioyl thio)pentanoic acid (CTA1), 3-sulphoproyl methacrylate potassium salt (KSPMA, 98%) and hydrogen peroxide (H_2O_2) 30 wt % solution were purchased from Sigma Aldrich. Dimethyl formamide (DMF) was purchased from Biosolve. All materias were used as received.

Methods

Poly(sulphopropylmethacrylate) (PSPMA) was synthesised by RAFT polymerisation. Subsequently, the RAFT end group was removed to prevent that this end group interferes with the RAFT polymerisation of the reaction-assembly network. In a typical procedure, CTA1 (10 mg, 38 µmol), KSPMA (1.11 g, 4.5 mmol) and ACVA (2.1 mg, 7.5 mmol) were added to 30 mL miliQ/DMF (4/6, v/v) solution. To obtain PSPMA with a different degree of polymerisation, the amounts of CTA1 and ACVA were adapted. The solution was degassed with N_2 for 30 minutes and then reacted at 70 °C for 14 h. Subsequently, 6 mL of the reaction mixture was taken apart to use for characterisation of the PSPMA before end group removal. The remainder of the reaction mixture was used for end group removal based on a procedure by Jesson et al..[41] First, the DMF was removed by dialysis against miliQ. Subsequently, the volume of the reaction mixture was adapted to get a CTA1 concentration of 0.63 mM. Then, 5 equivalent of H_2O_2 was added and the mixture was let to react at 24 h at 70 °C. The PSPMA samples before and after end group removal were both dialysed against miliQ and subsequently freeze dried. The PSPMA after end group removal has a much lower absorption at 300 nm compared to the PSPMA before end group removal, indicating successful end group removal.

The number-average molecular weights (M_n) and molecular weight distributions ($Đ_M$) of the PSPMA polymers were determined using an Agilent aqueous GPC equipped with a refractive index detector and using PL aquagel Mixed-M as the column. $NaNO_3$ (0.2 M)–NaH_2PO_4 (0.01 M) buffer solution (pH = 7.0) with NaN_3 (0.2 wt %) was used as the eluent at a flow rate of 0.6 mL min^{-1} at 30 °C. The column was calibrated using polymethacrylic acid standards. The M_n of the three PSPMA polymers used in this study are 6.7×10^3 g mol^{-1} (degree of polymerisation = 27, $Đ_M$ =1.2), 1.2×10^4 g mol^{-1} (degree of polymerisation = 47, $Đ_M$ =1.3) and 2.8×10^4 g mol^{-1} (degree of polymerisation = 116, $Đ_M$ =1.7).

PVBTA synthesis

Materials

4-((((2-Carboxyethyl)thio)carbonothioyl)thio)-4-cyanopentanoic acid (CTA2, 95 %), (vinylbenzyl) trimethylammoniumchloride (VBTAC, 99 %) and hydrogen peroxide (H_2O_2) 30 wt % solution were purchased from Sigma Aldrich. 2,2′-Azobis[2-(2-imidazolin-2-yl)propane]dihydrochloride (VA-044, 97 %) was purchased from WAKO chemicals. All chemicals were used as received.

Methods

Similar to the PSPMA synthesis, poly((vinylbenzyl)trimethylammoniumchloride) (PVBTA) was prepared by RAFT polymerisation followed by RAFT end group removal. CTA2 (12 mg, 38 µmol), VBTAC (0.95 g, 4.5 mmol) and VA-044 (2.4 mg, 7.5 µmol) were added to 30 mL miliQ. The solution was degassed with N_2 for 30 minutes and then reacted at 44 °C for 14 h. Subsequently, 6 mL of the reaction mixture was taken apart to use for characterisation of the PVBTA before end group removal. The remainder of the reaction mixture was used for end group removal. The volume of the reaction mixture was adapted to get a CTA2 concentration of 6.3 mM. Then, 20 equivalent of H_2O_2 was added and the mixture was let to react at 24 h at 70 °C. A larger concentration of CTA and a larger equivalent of H_2O_2 is used compared to the PSPMA RAFT end group removal. This is because CTA2 has a larger stability than

CTA1. The PVBTA samples before and after end group removal were both dialysed against miliQ and subsequently freeze dried. End group removal was again confirmed by UV-VIS absorption.

2.A.2 Isothermal titration calorimetry measurements

Isothermal calorimetry was performed with a VP-ITC (MicroCal Inc.) instrument at 25 °C. All solutions contained 10 mM KCl and were degassed at 18 °C for 5 min before each measurement. For the normal titration, a 150 mM monomer solution in a rotating (310 rpm) syringe was injected into a sample cell (1.4552 mL) filled with a 5 mM template units solution in sequential 3 µL aliquots. The time between the injection steps was 240 s. The heat flow to the sample cell to keep it at the same temperature as the reference cell was recorded as function of time. For the reversed titration, a 150 mM template units solution was added to a 5 mM monomer solution. In both cases, the measured heat was corrected for the background dilution heat by measuring the heat flow for the addition of the syringe solution to a 10 mM KCl solution. For the normal titrations, the datapoints are the average of two titration experiments corrected by the average of two dilution experiments. For the reversed titration only one titration and one dilution measurement were done because of the limited available amount of template polymers.

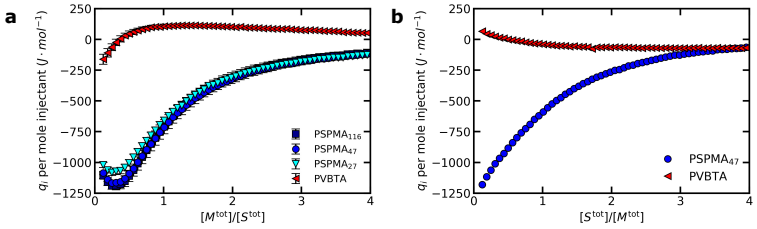

Figure 2.A.1. Isothermal titration calorimetry measurements. (a) Addition of VBTAC monomer to PSPMA template or addition of KSPMA monomer to PVBTA template. (b) Reversed titration: addition of PSPMA template to VBTAC monomer or addition of PVBTA template to KSPMA monomer.

The heat change upon VBTAC addition to the PSPMA template indicates that the monomer and template interact with each other (Fig. 2.A.1a). In this case, heat is released which means that the binding is exothermic. The heat formation is not the largest in the first addition step. Instead the heat formation increases in the first steps and then decreases again. This indicates that the monomers bound to the template interact with each other and that this interaction is also exothermic.[42] This is further supported by the slightly smaller heat formation for the shortest PSPMA template: at the end of the template the monomer can have interactions with the other monomers at one side only and therefore the contribution of monomer-monomer interaction decreases when the fraction of template ends increases. In a reversed titration, the monomer-monomer interactions at the template are the largest after the first addition step and then decrease because the number of available template sites increases. Indeed, in the reversed titration the released heat only decreases with increasing titration steps (Fig. 2.A.1b).

The addition of KSPMA to the PVBTA template is different. The binding of the monomer to the template is still exotherm. However, the monomer-monomer interactions are endotherm in this case, as shown by the heat decrease in the later titration steps.

2.A.3 ^{1}H NMR measurements during the reaction

Spectra with short T_2-filter to quantify monomer conversion

The ^{1}H NMR spectra from the single-pulse measurements indicate a decrease of monomer concentration in time. However, these spectra cannot be used to obtain the exact monomer concentration at a given

time point because after the start of reaction the PVBTA and PSPMA peaks start to broaden excessively and start to overlap with the monomer vinyl proton peaks. Spectra with narrower line shapes were obtained by a multi-pulse sequence based on spin-echo acquisition, where a PROJECT loop scheme[38] was introduced to refocus J-coupling interactions (Fig. 2.A.2a,b). An inter-pulse delay τ of 5 ms and a single loop (n=1) were used to obtain a T_2-filter duration of 20 ms, in turn much shorter than the T_2-values of the monomer vinyl protons (~ 3-4 s). Therefore, the loss of monomer signal intensities during this short T_2-filter is negligible. In this condition, the intensities of the M^4 and A^2 proton peaks can be used to calculate the monomer concentrations during conversion, respectively in the normal and inverted reaction-assembly network.

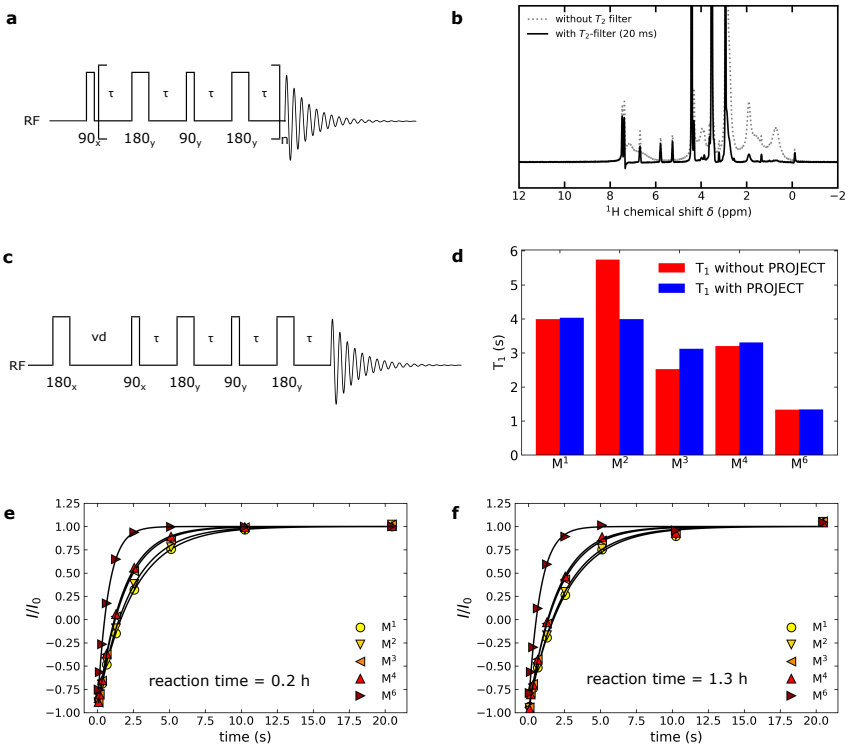

Figure 2.A.2. Overview of the different ^{1}H NMR measurements used to monitor the reaction-assembly network. (a) The PROJECT sequence.[38] (b) ^{1}H NMR spectra obtained without T_2-filter and with a T_2-filter based on the PROJECT sequence with τ = 5 ms and n = 1 (which gives a T_2-filter of 20 ms). Both spectra are measured during the reaction-assembly process of the system with $[M^{tot}]$ = 35 mM at a reaction time of 3.3 h. (c) The inversion recovery PROJECT sequence used to measure the T_1 during the reaction (vd = variable delay time). (d) Comparison of T_1 values of the VBTAC protons in a 35 mM VBTAC and 10 mM KCl solution measured without and without PROJECT sequence. (e,f) Example of T_1 measurements of the VBTAC monomer in the reaction-assembly network with $[M^{tot}]$ = 35 mM at a reaction time of (e) 0.2 h and (f) 1.3 h. Solid lines indicate the fits to the data with the function $I = I_0[1 - 2k\exp(-t/T_1)]$. In all fitting conditions, k was estimated around 1.0 ± 0.04, as expected for inversion recovery measurements.

Spectra with long T_2-filter to indirectly estimate T_2

We used a long T_2-filter to get a qualitative measure for changes in T_2. Specifically, we used the PROJECT loop scheme with 120 loops and an inter-pulse delay $\tau = 5\,\text{ms}$ to obtain a T_2 filter time of 2.4 s (Fig. 2.A.2a).[38]

Effect of a T_2 increase during the reaction

The intensity modulation due to T_2 is given by $I = I_0 \exp(-t/T_2)$ where t is the T_2-filter time. For the long PROJECT T_2-filter $t = 2.4\,\text{s}$. During the reaction the monomer amount decreases and therefore I_0 of the vinyl protons decreases. If T_2 remains the same, the T_2 -filtered intensity I would decrease as well. However, when T_2 increases, it is possible to observe an increase of the T_2-filtered monomer intensity I_B compared to a T_2 filtered monomer intensity I_A measured earlier in the reaction. This happens when $\frac{1}{T_{2,B}} < \frac{1}{T_{2,A}} + \frac{1}{t}\ln\left(\frac{I_{0,B}}{I_{0,A}}\right)$ because in that case $\frac{I_B}{I_A} > 1$. For a shorter $T_{2,A}$, the term $\frac{1}{T_{2,A}}$ is larger. This means that the $\frac{1}{t}\ln\frac{I_{0,B}}{I_{0,A}}$ term has a smaller contribution. As a result, when $T_{2,A}$ is shorter it is easier to get an increase in T_2-filtered monomer even when $\frac{I_{0,B}}{I_{0,A}} < 1$. The M^6 proton has a shorter T_2 than the other monomer protons. This explains why only the M^6 proton peak shows an increase in T_2-filtered signal during the reaction (main text, Fig. 2.2d).

Inversion recovery measurements with short T_2-filter for T_1 measurements

To measure the T_1 of the monomer we combined an inversion recovery sequence with a PROJECT-based T_2-filter of 20 ms (Fig. 2.A.2c). In this way, we remove the broad peaks from the spectrum and we can measure the T_1 of only the monomer instead of a mixture of the T_1 of the monomer and the T_1 of the polymer. Only for M^6 this is not possible, because the T_2 filter created by the PROJECT sequence is too short to completely remove the adjacent polymer peak that forms during the reaction.

We note that since the PROJECT sequence makes use of coherence transfer, the T_1 values that we obtain are mixture of the T_1 of the coupled protons (Fig. 2.A.2d). This is not a problem because we are interested only in relative changes in T_1 of the complete monomer. The J coupling constants of the protons do not change during the reaction and therefore the way that the T_1 values of the protons are mixed will remain the same. An increase of all measured T_1 for the monomer peaks thus still indicates that the T_1 of all the monomer protons has increased.

We perform the T_1 measurements while the polymerisation reaction is going on and therefore the intensity is not only modulated by T_1 but also by the ongoing reaction. To minimise the bias from the reaction, we have mixed the variable delay list (the used list is 0.08 s, 20.48 s, 0.32 s, 5.12 s, 1.28 s, 0.64 s, 2.56 s, 0.16 s, 10.24 s). Examples of the T_1 measurements both during the induction period and during the reaction are shown in Figs. 2.A.2e,f. The reaction introduces some additional noise in the T_1 measurement, but does not bias the T_1 measurement as would be the case for a continuously increasing variable delay list.

The T_1 values were obtained by fitting the data with a single-exponential function $I = I_0[1 - 2k\exp(-t/T_1)]$. For this, we used a constrained non-linear least square fit algorithm as implemented in the Python package SciPy.

2.A.4 Estimation of the initial bound monomer fraction from NMR T_1 measurements

Each measured T_1 decay was single-exponential and yielded one observed mean relaxation time, T_1^{obs}, resulting from fast exchange between the T_1's of free and bound states, as given by:

$$\frac{1}{T_1^{\text{obs}}} = \frac{x}{T_1^b} + \frac{1-x}{T_1^f} \tag{2.A.1}$$

where $x = M^b/M^{\text{tot}}$ is the bound monomer fraction and T_1^b and T_1^f are the longitudinal relaxation times of the bound and free monomer respectively. The value of T_1^f can be separately obtained from the T_1 measurement of the monomer without template. The two parameters T_1^b and x are left to be determined, and thus two equations are needed. For this, we have measured the T_1 for the templated reaction networks at two different monomer concentrations $[M^{\text{tot}}]$, namely of 35 mM and 105 mM.

Changing the monomer concentration also affects the bound monomer fraction: as a result, and as predicted by Equation 2.A.1, the T_1^{obs} values obtained for these two systems were different. By assuming that the T_1^b value for the bound monomer is independent of the monomer concentration, we obtain:

$$\frac{1}{T_1^b} = \frac{1}{x_A}\left(\frac{1}{T_{1,A}^{\text{obs}}} - \frac{1-x_A}{T_1^f}\right) = \frac{1}{x_B}\left(\frac{1}{T_{1,B}^{\text{obs}}} - \frac{1-x_B}{T_1^f}\right) \tag{2.A.2}$$

where A and B indicate the two monomer concentrations used. If we neglect the binding cooperativity effects, the bound fraction x can be directly obtained from the equilibrium constant, which is given by:

$$K = \frac{[M^b]}{[M^f][S^f]} = \frac{[M^b]}{([M^{\text{tot}}] - [M^f])([S^{\text{tot}}] - [M^b])} \tag{2.A.3}$$

Rewriting and dividing by $[M^{\text{tot}}]$ gives:

$$x = \frac{[M^b]}{[M^{\text{tot}}]} = \frac{1}{2[M^{\text{tot}}]}\left([M^{\text{tot}}] + [S^{\text{tot}}] + \frac{1}{K} \pm \sqrt{([M^{\text{tot}}] + [S^{\text{tot}}] + \frac{1}{K})^2 - 4[M^{\text{tot}}][S^{\text{tot}}]}\right) \tag{2.A.4}$$

Only the expression where the square root term is subtracted is a feasible solution for x because addition would give a bound monomer fraction that is larger than 1.

Both x_A and x_B can thus be expressed in terms of the equilibrium binding constant K, the total monomer concentration $[M_A^{\text{tot}}]$ and $[M_B^{\text{tot}}]$ respectively and the total template binding sites $[S^{\text{tot}}]$. In these equations K is the only unknown. Substitution of the expressions for x_A and x_B in Equation 2.A.2 thus gives an equation that can be numerically solved for K by using a root finding algorithm. In this case we used the bisection method. Subsequently Equation 2.A.4 can be used to calculate x_A and x_B. Next, the longitudinal relaxation time of the monomer bound to the polymer T_1^b can be calculated from Equation 2.A.2.

The equilibrium binding constant K, bound monomer fractions x_A and x_B and the longitudinal relaxation time of the bound monomer T_1^b can be calculated for different protons of the monomer (Table 2.A.1). In this way, we find for the binding of the positively charged VBTAC monomer to the negatively charged PSPMA template at a KCl concentration of 35 mM an average equilibrium constant of $K = 0.056 \pm 0.006$ mM^{-1} and average bound fractions of $x_A = 0.50 \pm 0.02$ and $x_B = 0.27 \pm 0.005$ for $[M^{\text{tot}}] = 35$ mM and $[M^{\text{tot}}] = 105$ mM respectively. For the binding of the negatively charged KSPMA monomer to the positively charged PVBTA template at a KCl concentration of 35 mM we find an average equilibrium constant of $K = 0.057 \pm 0.005$ mM^{-1} and average bound fractions of $x_A = 0.50 \pm 0.01$ and $x_B = 0.27 \pm 0.004$ for $[M^{\text{tot}}] = 35$ mM and $[M^{\text{tot}}] = 105$ mM respectively (Table 2.A.2). We note that these values are an approximation, since we have neglected cooperativity effects while the isothermal titration calorimetry measurements (Section 2.A.2) indicate that these are present. For cooperative binding the effective equilibrium constant for $[M^{\text{tot}}] = 105$ mM will be slightly lower than for $[M^{\text{tot}}] = 35$ mM, and *vice versa* for anticooperative binding.

Table 2.A.1. The observed longitudinal relaxation times for the different positively charged VBTAC monomer protons and the calculated equilibrium binding constant K, bound monomer fractions x_A en x_B and the longitudinal relaxation time of the bound monomer T_1^b. Here the subscript A indicates the start of a reaction-assembly process with $[M^{\text{tot}}]$ = 35 mM, the subscript B indicates the start of a reaction-assembly process with $[M^{\text{tot}}]$ = 105 mM and T_1^f is obtained from the start of a polymerisation reaction without template with $[M^{\text{tot}}]$ = 35 mM. In all cases, the KCl concentration is 35 mM.

proton	T_1^f (s)	$T_{1,A}^{\text{obs}}$ (s)	$T_{1,B}^{\text{obs}}$ (s)	K (mM^{-1})	x_A	x_B	T_1^b (s)
M^1	4.6	2.5	3.1	0.060	0.51	0.27	1.7
M^2	4.5	2.2	2.9	0.049	0.48	0.26	1.5
M^3	3.3	1.8	2.3	0.052	0.48	0.27	1.2
M^4	3.6	1.7	2.3	0.065	0.52	0.28	1.2
M^6	1.3	0.7	0.9	0.054	0.49	0.27	0.5

Table 2.A.2. The observed longitudinal relaxation times for the the negatively charged KSPMA monomer protons whose NMR peaks do not overlap with template PVBTA protons peaks and the calculated equilibrium binding constant K, bound monomer fractions x_A en x_B and the longitudinal relaxation time of the bound monomer T_1^b. Here the subscript A indicates a sample equivalent to the start of a reaction-assembly process with $[M^{\text{tot}}]$ = 35 mM the subscript B indicates a sample equivalent to the start of a reaction-assembly process with $[M^{\text{tot}}]$ = 105 mM and T_1^f is obtained from the start of a polymerisation reaction without template with $[M^{\text{tot}}]$ = 35 mM. In all cases, the KCl concentration is 35 mM.

proton	T_1^f (s)	$T_{1,A}^{\text{obs}}$ (s)	$T_{1,B}^{\text{obs}}$ (s)	K (mM^{-1})	x_A	x_B	T_1^b (s)
A^1	2.7	1.8	2.1	0.063	0.51	0.28	1.4
A^2	2.6	1.8	2.0	0.054	0.49	0.27	1.3
A^5	2.0	1.4	1.7	0.053	0.49	0.27	1.1

2.A.5 Polymerisation without template

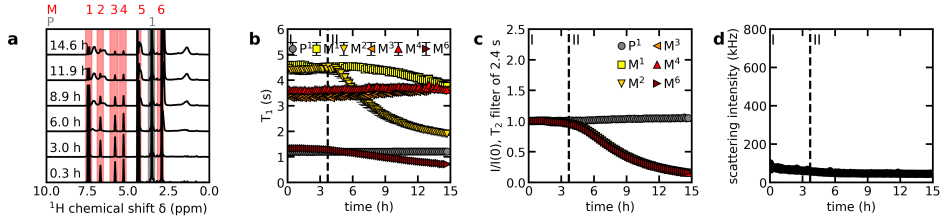

Figure 2.A.3. The polymerisation reaction without template. At increasing reaction times: (a) ^{1}H NMR spectra; (b) T_1 values for the neutral block P and monomer M protons, with respective error bars obtained from single-exponential fitting. The decrease in T_1 for M^1, M^2 and M^6 during the reaction is the result of overlap of these monomer proton peaks with the polymer proton peaks; (c) T_2-filtered NMR spectral intensity (T_2-filter of 2.4 s) for the P and M protons, normalised to their own signal intensity at the start of the reaction; (d) Light scattering intensity.

2.A.6 Light scattering: apparent hydrodynamic radius

Light scattering measurements can be used not only to obtain the average static light scattering intensity, but also to obtain information of the movements of the light scattering objects based on the fluctuations of the scattered light intensity in time. In general, these fluctuations are interpreted by making use of second order cumulant analysis of the intensity autocorrelation function. This analysis gives a characteristic decay rate Γ from which the diffusion coefficient is determined by using $\Gamma = Dq^2$ where q is the scattering wave vector. For spherical objects, the radius can be obtained from this diffusion coefficient by using Stokes-Einstein equation. Here, we use a similar approach to obtain an apparent hydrodynamic radius R_H^{app}. We refer to this radius as an apparent radius because we measure only at a single scattering angle, while to ensure that the samples indeed contain spherical objects with similar sizes we need to determine Γ at multiple scattering angles and obtain the diffusion coefficient D from the slope of the Γ versus q^2 plot. This multi-angle measurement takes too long to perform during the reaction. In addition, we measure at relatively large concentrations and therefore multiple scattering events or structure factor effects might affect the scattered light intensity and the sample might already be outside the dilute concentration regime for which the Stokes-Einstein equation is valid. The apparent hydrodynamic radius that we obtain here should thus be interpreted mainly as a first indication of the movements of the light scattering objects in the sample. Additional measurements (e.g. time-resolved SAXS) are required to verify whether this apparent radius correctly reflects the trends in movement of the objects and to obtain detailed structural information on the formed objects.

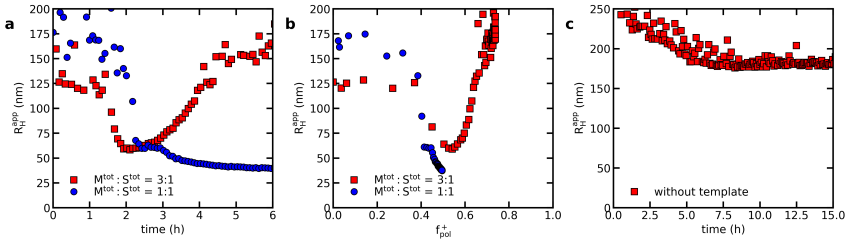

Figure 2.A.4. The apparent hydrodynamic radius during the reaction. (a) R_H^{app} as function of reaction time for the templated reaction-assembly networks at different monomer to template ratios. (b) R_H^{app} as function of polymer charge ratio f^+pol for the templated reaction-assembly networks at different monomer to template ratios. (c) R_H^{app} as function of reaction time for the polymerisation without template.

At the start of the reaction, the apparent hydrodynamic radius is about ~ 175 nm and this R_H^{app} decreases in the course of the reaction (Fig. 2.A.4). For the $M^{\text{tot}} : S^{\text{tot}} = 3 : 1$ ratio the R_H^{app} increases again when the nanostructures disassemble. These trends in R_H^{app} are opposite to what we expect based on the light scattering intensities: larger intensities indicate the formation of larger structures, but the apparent hydrodynamic radius is the smallest for the largest scattering intensities. We hypothesize that the large R_H^{app} at low scattering intensities is due to the presence of slow modes of the polymers instead of the formation of large structures. These slow modes are observed both for neutral and charged polymers in the semidilute or concentrated regime and might be the result of hindered motions of the interacting chains.[43] Especially for PEG and PEO polymers these slow modes are often observed and their origin is still under debate.[44,45] Indeed, we also observe large R_H^{app} for the polymerisation without template, where only PEG is present and no PSPMA (Fig. 2.A.4c). Since the nanostructures scatter much more light than single polymers, we expect that in the templated reaction-assembly networks the R_H^{app} at the maximum intensity mainly reflects the nanostructure movement and not the movements of the individual polymers.

2.A.7 Effect of the template length

Reaction-assembly measurements

Reaction-assembly measurements with different template lengths were performed in the same way as described in the methods section of the main text by using PSPMA of different lengths (Fig. 2.A.5). After 10 h of reaction, we performed a multi-angle light scattering measurement to determine the characteristic decay rate Γ of the intensity autocorrelation function for different scattering angles (Fig. 2.A.5e). The measurement was started at a scattering angle of 30° and every time the scattering angle was increased with 5° until the final scattering angle of 130° was reached. At every angle 10 independent runs of 20 s were recorded. The reported Γ is the average of these 10 runs. The Γ versus q^2 plots do not pass exactly through the origin. A possible explanation for this is that the formed nanostructures are not monodisperse or not spherical. Both are required to make Γ directly proportional to q^2. Alternatively, the relatively large concentrations of the samples might have resulted in deviations in the light scattering experiments. The dependence of Γ on q^2 is different for the different template length, indicating that different structures are formed. The steeper slope and smaller final apparent hydrodynamic radius (Fig. 2.A.5d) seem to suggest that the longest templates form the smallest nanostructures. Further structural analysis by SAXS or SANS measurements is required to verify whether the longest template indeed form the smallest nanostructures. We note that a decrease in apparent hydrodynamic radius with increasing template length has been observed earlier for C3Ms,[30] only they observed this template dependence only at higher ionic strengths, while in our case it seems to occur already at low ionic strengths.

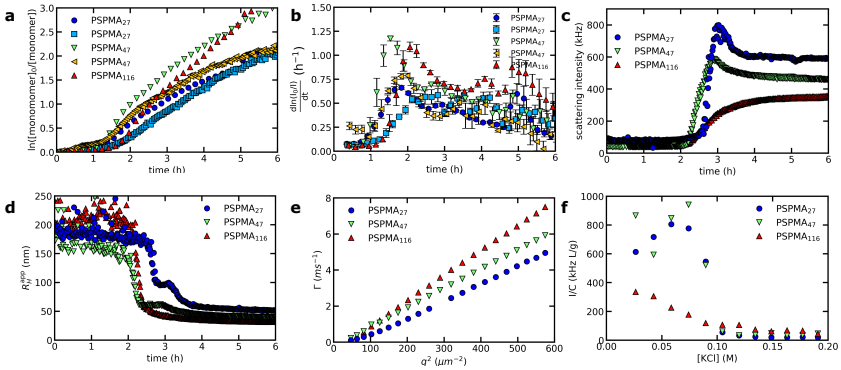

Figure 2.A.5. The effect of the template length on the reaction kinetics and nanostructure formation. (a) Pseudo first-order kinetics plot of the monomer conversion. Plots with the same template length are repetitions of the same experiment. (b) Local slope of the pseudo first-order kinetics plot of (a) as function of time. Error bars indicate uncertainty in the local slope determination. (c) Light scattering by the sample during the reaction-assembly process. (d) The apparent hydrodynamic radius obtained from the light scattering measurements during the reaction-assembly process. (e) Multi-angle measurements of the decay rate of the intensity auto correlation function as function of the squared scattering wave vector q^2. (f) Salt titrations of PEG-PVBTA/PSPMA micelles for different template lengths: light scattering intensity I corrected for the total polymer weight concentration C as function of ionic strength.

Salt titrations

Light scattering titrations were performed on an ALV instrument equipped with a 660 nm laser. The detection angle was 90°. A Schott–Geräte computer-controlled titration setup was used to regulate the addition of titrant, stirring, and delay time between additions. A 6 mL solution of PEG-PVBTAC/PSPMA micelles ([VBTAC] = [SPMA] = 1 mM) in 10 mM KCl was prepared. To this solution, a stock solution of

2 M KCl was added in steps of 0.050 mL. After a stirring and delay time of both 60 s, the light scattering intensity was recorded in 10 independent runs of 20 s. The recorded light scattering intensities I are corrected for the total polymer weight concentration C. For the two shortest PSPMA templates, this corrected light scattering intensity first increases with increasing salt concentration and afterwards decreases (Fig. 2.A.5f). The same behaviour has been observed earlier for C3Ms with short template lengths and it was shown that this increase in light scattering intensity corresponded to a micelle rearrangement from spherical to ellipsoidal.[30] We therefore expect that also here the increase in light scattering intensity corresponds to a rearrangement to ellipsoidal micelles. For the longest PSPMA this rearrangement does not occur since here the intensity only decreases with increasing salt concentration.

2.A.8 ^{1}H NMR T_2 measurements of the neutral block

To measure the T_2 of the neutral block protons we used the PROJECT sequence[38] with an inter-pulse delay time τ of 5 ms and a number of echoes that was varied from 2 to 1024 in 57 steps. For every echo number the signal from eight consecutive acquisitions was added. The receiver dead time was set to 6.5 µs. The T_1 of the protons in the neutral block is 1.2 s, thus the recycle delay of 10 s was long enough ($> 5T_1$) to obtain quantitative results. The total duration of this complete T_2 measurement was 2.2 h. To measure the T_2 of the neutral block before the reaction starts a new sample was prepared by adding the VBTAC monomer, the PSPMA template, the neutral block chain transfer agent and the KCl in the same concentration as in the reaction-assembly network with $[M^{tot}]$ = 35 mM. No initiator was added. For the T_2 measurement after the reaction the sample of the reaction-assembly process at $[M^{tot}]$ = 35 mM as described in the main text was used. Before the reaction the neutral block protons have a single T_2-relaxation time of about 0.96 s (Fig. 2.A.6a), while after the reaction the neutral block protons seem to exhibit a tri-exponential relaxation decay (Fig. 2.A.6b) as also confirmed by independent data analysis using Laplace inversion (data not shown here). Two components have a T_2 that is shorter than the initial T_2, while the third component has a longer T_2. The small fraction (~ 12%) of protons with the shortest T_2 (0.14 ± 0.02 s) presumably corresponds to the protons that are close to the core of the micelle and very restricted in their mobility due to the dense micelle corona at this position. The dominant fraction of ^{1}H signal (~ 50%) with an intermediate T_2 (0.7 ± 0.1 s) probably arises from protons in the middle of the micelle corona, where mobility is less hindered than closer to the core. Finally, the protons with the longest T_2 of 1.2 ± 0.2 s, most likely correspond to the protons in the periphery of the micelle corona, where the corona is very diluted and the protons might have gained additional mobility compared to the protons in the polymer coil configuration before reaction.

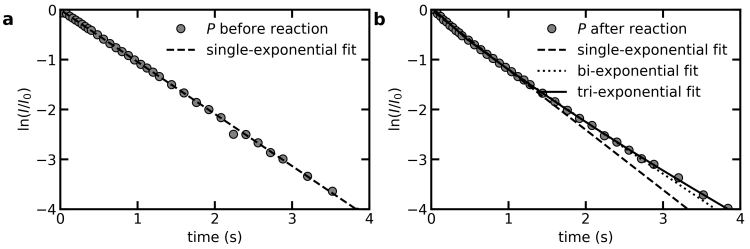

Figure 2.A.6. ^{1}H NMR T_2 measurements of the neutral block protons.(a) T_2 measurement before the reaction-assembly process. (b) T_2 measurement after the reaction assembly process. The dashed lines in (a) and (b) indicate the fits of the data to the single-exponential function $I(t) = I_0 \exp(-t/T_2)$ yielding T_2 = 0.957 ± 0.003 s and T_2 = 0.83 ± 0.01 s before and after the reaction respectively. The dotted line in (b) shows the fit to the bi-exponential function $I = I_0(x \exp(-t/T_{2,A}) + (1-x)\exp(-t/T_{2,B}))$ yielding $T_{2,A}$ = 0.23 ± 0.01 s, $T_{2,B}$ = 0.96 ± 0.008 s, x = 0.2 ± 0.009. The solid line in (b) shows the fit to the tri-exponential function $I = I_0(x_A \exp(-t/T_{2,A}) + x_B \exp(-t/T_{2,B}) + (1 - x_A - x_B)\exp(-t/T_{2,C}))$ yielding $T_{2,A}$ = 0.7 ± 0.1 s, $T_{2,B}$ = 0.14 ± 0.02 s, $T_{2,C}$ = 1.2 ± 0.2 s, x_A = 0.5 ± 0.2 and x_B = 0.12 ± 0.02.

2.A.9 Reactant stoichiometry effects

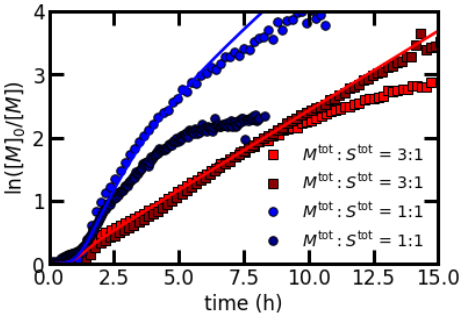

Figure 2.A.7. Pseudo first order kinetic plots of the monomer conversion for different monomer to template ratios. Plots with the same monomer to template ratios are repetitions of the same experiments. Solid lines indicate kinetic model predictions for $k_p = 0.36\ \mathrm{mM^{-1}h^{-1}}$, $k_b = k_a = 12\ \mathrm{mM^{-1}h^{-1}}$, $k_d(n) = \omega_0 \exp(-nE_a/k_BT)$ with $\omega_0 = 3.1 \times 10^4\ \mathrm{h^{-1}}$ and $E_a = 6k_BT$, $k_f = k_d(1)$, $k_{bn} = 500k_b$ $V_{\mathrm{tot}}/V_{\mathrm{b}} = 8$ and a $c(t) = \exp(at - t_{\mathrm{shift}})/(1 + \exp(at - t_{\mathrm{shift}})$ with $a = 3.0$ and $t_{\mathrm{shift}} = 3.5\,\mathrm{h}$. For $M^{\mathrm{tot}} : S^{\mathrm{tot}} = 3 : 1$ the initial concentrations are $[M^{\mathrm{tot}}] = 105$ mM, $[S^{\mathrm{tot}}] = 35$ mM and $[P\text{-}M_0^{\mathrm{tot}}] = 0.7$ mM and for $M^{\mathrm{tot}} : S^{\mathrm{tot}} = 1 : 1$ the initial concentrations are $[M^{\mathrm{tot}}] = 35$ mM, $[S^{\mathrm{tot}}] = 35$ mM and $[P\text{-}M_0^{\mathrm{tot}}] = 0.7$ mM.

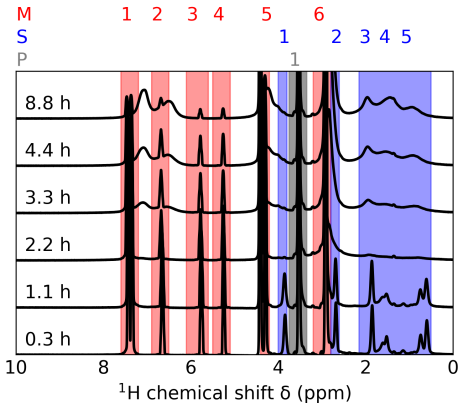

Figure 2.A.8. Example ^{1}H NMR spectra at different reaction times for the templated reaction-assembly with $M^{\mathrm{tot}} : S^{\mathrm{tot}} = 3 : 1$.

2.A.10 Kinetic model

Model equations

In our model we have free monomers M^f, bound monomers M^b, free template sites S^f, free diblocks $P\text{-}M_n^f$ and bound diblocks $P\text{-}M_n^b$. Both the free and bound diblock can have a distribution of the degree of polymerisation of the positive block n. The positive monomers of the bound diblock can exchange between a template bound and a template free state. The concentration of bound positive monomers of the bound diblock is denoted by $[n^b]$ and the concentration of free monomers of the bound diblock is denoted by $[n^f]$. The concentration of all the components can change because of the polymerisation reaction and because the components can exchange between a template bound and a free state.

In the polymerisation reaction a monomer reacts with a diblock $P\text{-}M_{n-1}$ to give a diblock $P\text{-}M_n$. The polymerisation rate constant is k_p. As explained in the main text this polymerisation rate constant has to be multiplied by a time dependent function $c(t)$ to account for the induction period. The change in local bound monomer concentration due to the polymerisation reaction with the bound diblock is thus given by:

$$\left(\frac{d[M^b]^{\text{bound}}}{dt}\right)_{\text{polymerisation}} = -k_p c(t)[M^b]^{\text{bound}} \sum_n [P\text{-}M_n^b]^{\text{bound}} \tag{2.A.5}$$

where the superscript bound refers to the local concentrations in the volume around the template. However, we observe the overall monomer concentration $[M^b]^{\text{tot}} = M^b/V^{\text{tot}}$ and not the local monomer concentration $[M^b]^{\text{bound}} = M^b/V^b = [M^b]^{\text{tot}}\frac{V^{\text{tot}}}{V^b}$. The same applies for the bound diblock concentration $[P\text{-}M_n^b]^{\text{bound}} = [P\text{-}M_n^b]^{\text{tot}}\frac{V^{\text{tot}}}{V^b}$. Substitution of the expressions for the local monomer concentration in equation 2.A.5 gives:

$$\left(\frac{d[M^b]^{\text{tot}}}{dt}\right)_{\text{polymerisation}} = -k_p c(t)\frac{V^{\text{tot}}}{V^b}[M^b]^{\text{tot}} \sum_n [P\text{-}M_n^b]^{\text{tot}} \tag{2.A.6}$$

The local polymerisation rate of the bound diblocks due to reaction with the bound monomer can be converted to the overall polymerisation rate in the same way as the for the polymerisation rate of the bound monomer. In the remainder of the text we will use only the overall concentrations and therefore we will omit the superscript 'tot' for the concentrations.

Now we have converted local concentrations to overall concentrations we can describe the changes in overall concentrations of the different components in time. The concentration of the free monomer can decrease because the free monomer binds to the template or because the monomer is used in the polymerisation reaction. The free monomer can react both with free diblocks and with bound diblocks. The free monomer concentration can increase when bound monomer releases from the template. The overall change in free monomer concentration is thus given by:

$$\frac{d[M^f]}{dt} = -k_b[M^f][S^f] + k_f[M^b] - k_p c(t)[M^f]\left(\sum_n [P\text{-}M_n^f] + \sum_n [P\text{-}M_n^b]\right) \tag{2.A.7}$$

The bound monomers can react both with the free diblocks and the bound diblocks. As explained above, the reaction rate of the bound monomer with the bound diblock is increased by a factor V^{tot}/V^b due to the locally larger concentration. This is not the case for reaction with the free diblock because the free diblock concentration is not locally increased around the template. The concentration of the bound monomers increases when a free monomer binds to the template and decreases when a bound monomer releases from the template. This gives:

$$\frac{d[M^b]}{dt} = k_b[M^f][S^f] - k_f[M^b] - k_p c(t)[M^b]\left(\frac{V^{\text{tot}}}{V^b}\sum_n [P\text{-}M_n^b] + \sum_n [P\text{-}M_n^f]\right) \tag{2.A.8}$$

The concentration of a free diblock with n positive monomers $[P\text{-}M_n^f]$ can change in different ways. First the concentration decreases when the free diblock binds to the template. The concentration increases when a bound diblock with n positive monomers releases from the template. This release rate depends on n. Here we presume that this release can be described with an Arrhenius-type of process: $k_d(n) = \omega_0 \exp(-nE_a/(k_BT))$ where E_a is the binding energy a single monomer. The association rate k_a of the diblock is diffusion limited. Since the neutral block is relatively large compared to the polymerising block, the effect of n on the diffusion rate will be relatively small and therefore we here neglect the effect of n on k_a. $[P\text{-}M_n^f]$ can also change due to polymerisation. If a free diblock with $n-1$ positive monomers reacts with a monomer the concentration of $P\text{-}M_n^f$ increases. On the other hand, if this diblock $P\text{-}M_n^f$ reacts again with another monomer, the concentration of $P\text{-}M_n^f$ decreases. For simplicity we assume that a free diblock that reacts with a bound monomer remains in a free state, i.e. the bound monomer releases from the template when it reacts with the free diblock. Since in our model the rate of diblock binding is much faster than the polymerisation rate (appendix Section 2.A.10), we expect the diblocks will reach their equilibrium distribution before the next polymerisation step and therefore this simplification will not affect the outcome of the model. The change in overall free diblock concentration with n positive monomers can thus be given by:

$$\frac{d[P\text{-}M_n^f]}{dt} = -k_a[S^f][P\text{-}M_n^f] + k_d(n)[P\text{-}M_n^b] + k_p c(t)\Big([M^f] + [M^b]\Big)\Big([P\text{-}M_{n-1}^f] - [P\text{-}M_n^f]\Big) \quad (2.A.9)$$

A neutral block with $n = 0$ cannot bind to the template and therefore always is in the free state ($[P\text{-}M_0^f] = [P\text{-}M_0^{\text{tot}}]$). Its concentration decreases due to the polymerisation reaction:

$$\frac{d[P\text{-}M_0^f]}{dt} = -k_p c(t)\Big([M^f] + [M^b]\Big)[P\text{-}M_0^f] \quad (2.A.10)$$

We can describe the changes in overall bound diblock concentration with n positive monomers in a similar way as the overall free diblock concentration. Only this time the polymerisation rate of the polymerisation with the bound monomer is increased by a factor V^{tot}/V^b. In addition, the bound diblock concentration decreases when a bound diblock releases from the template and increases when a free diblock binds to the template. This gives:

$$\frac{d[P\text{-}M_n^b]}{dt} = k_a[S^f][P\text{-}M_n^f] - k_d(n)[P\text{-}M_n^b] + k_p c(t)\Big([M^f] + \frac{V^{\text{tot}}}{V^b}[M^b]\Big)\Big([P\text{-}M_{n-1}^b] - [P\text{-}M_n^b]\Big) \quad (2.A.11)$$

The monomers of the bound diblock can exchange between a template bound and template free state. As long as part of the monomers of the bound diblock remain bound, this temporal release of some of the monomers will not result in the release of the diblock from the template. When a free diblock with degree of polymerisation n binds, the number of bound monomers of bound diblocks n^b increases by n. In addition, when a monomer reacts with a bound diblock, n^b increases by 1. Part of the monomers of the bound diblocks can temporarily release from the template and rebind again. The release decreases $[n^b]$ while the rebinding increases $[n^b]$. When a bound diblock $P\text{-}M_n^b$ completely releases from the template, the number of bound monomers is decreased by zn where $z = [n^b]/([n^b] + [n^f])$ is the fraction of bound monomers of the positive block. The change in concentration of the bound positive

monomers $[n^b]$ is thus given by:

$$\frac{d[n^b]}{dt} = k_{bn}[n^f][S^f] - k_d(1)[n^b] + k_a[S^f]\sum_n[P\text{-}M_n^f]n - z\sum_n k_d(n)[P\text{-}M_n^b]n + k_p c(t)\left([M^f] + \frac{V^{\text{tot}}}{V^b}[M^b]\right)\sum_n[P\text{-}M_n^b] \tag{2.A.12}$$

The change in the concentration of free charged monomers of bound diblocks $[n^f]$ is given by:

$$\frac{d[n^f]}{dt} = -k_{bn}[n^f][S^f] + k_d(1)[n^b] - (1-z)\sum_n k_d(n)[P\text{-}M_n^b]n \tag{2.A.13}$$

Finally we have the concentration of free template sites $[S^f]$. This concentration decreases when free monomers M^f, free monomers of a bound diblock n^f or a complete free diblock $P\text{-}M_n^f$ bind to them. A monomer occupies one template site. For a positive block with n monomers, n template sites are used. The concentration of free template sites also decreases when a bound diblock reacts with a free monomer and increases when a free diblock reacts with a bound monomer. The concentration of free template sites also increases when the bound monomer M^b, a monomer of the bound diblock n^b or a complete bound diblock release from the template.:

$$\frac{d[S^f]}{dt} = -k_b[M^f][S^f] + k_f[M^b] - k_a[S^f]\sum_n[P\text{-}M_n^f]n + z\sum_n k_d(n)[P\text{-}M_n^b]n - k_{bn}[n^f][S^f] + k_d(1)[n^b] + k_p c(t)\left([M^b]\sum_n[P\text{-}M_n^f] - [M^f]\sum_n[P\text{-}M_n^b]\right) \tag{2.A.14}$$

Equations 2.A.7 - 2.A.14 together form a system of differential equations that can be numerically solved when the rate constants, volume ratio V^{tot}/V^b and initial concentrations are known. Here we have used the Runge-Kutta fourth-order method to numerically solve these equations.

Model parameterisation

To calculate the time evolution of the concentration of the different components we need to know the initial concentrations $[M^f]$, $[M^b]$, $[S^f]$ $[P\text{-}M_0^f]$ and $[P\text{-}M_0^b]$ and the parameters k_p, $c(t)$, k_b,k_f, k_a, k_d, k_{bn} and V^{tot}/V^b. We use the last two parameters as adjustable parameters, while the other parameters are determined from experiments or literature.

The bound and free monomer concentrations follow from the total monomer concentration and the bound monomer fraction as determined by NMR (appendix Section 2.A.4). For the $M^{\text{tot}} : S^{\text{tot}} = 1:1$ case, the total monomer concentration is 35 mM and approximately 50% is bound. This gives $[M^f] = 17.5$ mM and $[M^f] = 17.5$ mM. A bound monomer occupies one template site. This means that the initial concentration of free template site is given by $[S^f] = [S^{\text{tot}}] - [M^b] = 17.5$ mM. Since the neutral block does not have any binding affinity for the template, $[P\text{-}M_0^f] = [P\text{-}M_0^{\text{tot}}] = 0.7$ mM and $[P\text{-}M_0^b] = 0$.

The polymerisation rate constant k_p and the correction functions $c(t)$ can be obtained from the polymerisation reactions without template (main text, Fig. 2.3). k_p is obtained when the final slope in the pseudo first order kinetics plot of the monomer conversion is divided by the total chain transfer agent concentration $\sum_n[P\text{-}M_n] = 0.7$ mM. This gives $k_p = 0.36$ mM^{-1}h^{-1} for the normal reaction-assembly network. For the inverted reaction-assembly network the final slope in the pseudo first-order kinetic plots is lowered by termination reactions. Therefore, we use the maximum slope that occurs during the

reaction to obtain k_p. This gives $k_p = 1.0\,\mathrm{mM^{-1}h^{-1}}$. For all polymerisations with template we use the $c(t)$ obtained from the polymerisation without template at a monomer concentration of 175 mM.

For the activation energy barrier in the expression for k_d we take $E_a = 6k_BT$. This is based on the determination of the activation energy barrier of a single ionic bond between N-methyl-2-vinylpyridinium and 3-sulfopropyl-methacrylate in a salt free solution.[26] From the same article we can obtain ω_0. For this, we use the given expression $B = f_B \ln(r_f/(\omega_0 f_B)) + f_B l_B/d$ and the given values for B (170 pN), the constant f_B (27 pN), the loading rate r_f (3×10^3 pN s^{-1}), the Bjerrum length l_B (0.71 nm) and the ionic bond distance d (0.2 nm). This gives $\omega_0 = 8.7\,\mathrm{s^{-1}} = 3.1\times10^4\,\mathrm{h^{-1}}$.

The release of a monomer is approximately the same as the release of a diblock with $n = 1$. Therefore we take $k_f = k_d(1)$. Subsequently we can estimate k_b from the initial free and bound monomer concentrations: in equilibrium the binding rate equals the release rate: $k_b[M^f][S^f] = k_f[M^b]$. This gives $k_b = k_f[M^f]([S^{\mathrm{tot}}] - [M^b])/[M^b]$.

We expect that the diblock with $n = 1$ has approximately the same binding affinity as a monomer. To get the same equilibrium binding constant we take $k_a = k_b$.

We note that the exact choice of the model parameters does not largely affect the model outcome as long as the parameters remain within a certain range as explained below. The predicted model trends are thus not affected if the estimated values for the model parameters deviate somewhat from the real values.

The model outcome is similar for a broad range of E_a (Fig. 2.A.14) and ω_0 (Fig. 2.A.15) values. Only when E_a becomes very large or ω_0 becomes very small the predicted outcomes are different. Both scenarios correspond to small dissociation and association constants because we use $k_d = \omega_0 \exp(-nE_a/(k_BT))$ and subsequently use k_d to calculate k_f, k_b and k_a (here the association constants k_b and k_a are set by the dissociation constants k_d and k_f and the experimentally observed bound monomer fraction). For these small dissociation and association constants the monomer and diblock exchange between the free and bound state is slower than the polymerisation, resulting in a different outcome. Since the association process is mainly driven by diffusion, we do not expect to have such low association constants.

In the model parameterisation we have also assumed that the association constant of the diblock k_a equals the association constant of the monomer k_b. In reality, k_a might be slightly lower than k_b because of the neutral block that is attached to the positive block. For $k_a \geq 0.05k_b$ the model trends are not affected (Fig. 2.A.16). For $k_a = 0.01k_b$ the predictions start to deviate. This is because for $k_a = 0.01k_b$ at the start of the reaction the diblock association is slower than the polymerisation rate as shown by the initial small increase in S^f (Fig. 2.A.16e): bound monomers are consumed by the reaction with the free diblock P-M_0 and therefore S^f increases. The free diblocks do not bind fast enough to compensate for this increase. Again we do not expect that the real association constant of the diblock will be so low that it is slower than the polymerisation rate.

Finally, we have used the bound monomer fraction as estimated from NMR experiments (appendix Section 2.A.4). In this estimation, we have neglected any cooperativity effects and therefore the real bound monomer fraction might slightly deviate. This does not largely affect the model predictions (Fig. 2.A.17), especially if we take into account that the estimation of the V^{tot}/V^b ratio can also be slightly adapted.

Fraction of bound monomers of bound diblocks

The choice of k_{bn} affects which fraction z of the monomers of the bound diblock is in the bound state (Fig. 2.A.11f). The smaller k_{bn}, the smaller z, until at $k_{bn} = k_b$ the monomers of the bound diblock have the same binding affinity as the free monomers and z becomes the same as the bound fraction of single monomers. For $k_{bn} = k_b$, the number of free template sites S^f and the bound monomer fraction M^b/M^{tot} remain constant during the reaction (Fig. 2.A.11c,e). In experiments S^f and M^b/M^{tot} decrease as shown by the peak broadening of the template proton peaks and the increase in T_1 of the monomer protons respectively. k_{bn} thus has to be larger than k_b. For large $k_{bn} : k_b$ ratios the model

describes the experimental reaction kinetics data the best (Fig. 2.A.11a). These large k_{bn} result in a large z and small S^f at the end of the reaction for the 1:1 monomer to template site ratio. This means that a large majority of the polyelectrolyte monomers are bound to the monomers of the oppositely charged polyelectrolyte, which agrees with the low salt doping degrees of coacervates at low ionic strengths.[46]

For an excess of monomers compared to template sites, $M^{\text{tot}} : S^{\text{tot}} > 1$, z decreases when the point of equal charge stoichiometry is crossed (Fig. 2.A.12f). After this point, the total number of monomers of the bound diblocks is larger than the total number of template sites and therefore not all the bound diblock monomers can bind to the template and z decreases. This is reflected in the ^{1}H NMR spectra where PVBTA peaks start to appear after this point (Fig. 2.A.8). The PSPMA template peaks on the other hand remain broad and therefore remain invisible in the ^{1}H NMR spectra, in agreement with the low S^f values (Fig. 2.A.12e).

Estimation of $\frac{V^{\text{tot}}}{V^b}$

The ratio between the local volume of the bound monomers and diblock V^b and the total volume V^{tot} can be estimated from the polyelectrolyte blob size ξ and the maximum distance at which a monomer is still bound to the template d (Fig. 2.A.9). The blob size of a polyelectrolyte in a good solvent in the semi-dilute regime is given by $\xi \approx \sqrt{(A^2/u)^{2/7}/(cb)}$ where A is the number of monomers between effective charges, $u = l_B/b$ with l_B the Bjerrum length and b the monomer size and c is the monomer concentration. For a polyelectrolyte in a θ solvent $\xi \approx \sqrt{(A^2/u)^{1/3}/(cb)}$ and for a polyelectrolyte in a poor solvent $\xi \approx \sqrt{(A^2/u)^{2/3}/(cb)}$.[47] The concentration c is 35 mM = 2.1×10^{25} m^{-3}. The monomer size b is approximately 0.3 Å and the Bjerrum length at 44 °C is 0.66 Å. A follows from the fraction of condensed counter ions f: $A = 1/(1-f)$. This fraction can be estimated from the Manning theory for counter ion condensation where the fraction of condensed counter ions is given by $f = 1 - 1/\Gamma$ with $\Gamma = l_B/b$. In this way we find $\xi \approx 14$ nm for a polyelectrolyte in a good solvent, $\xi \approx 14$ nm for a polyelectrolyte in a θ solvent and $\xi \approx 16$ nm for a polyelectrolyte in a poor solvent.

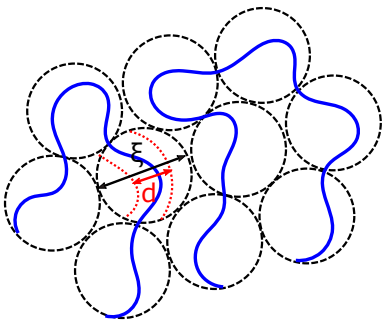

Figure 2.A.9. Estimation of the ratio between the local volume of the bound monomers and diblock V^b and the total volume V^{tot} for a polyelectrolyte template in the semi-dilute regime: $V^{\text{tot}}/V^b \approx \xi^3/(d^2\xi)$.

For d we can use the length of an ionic bond. Different ionic bond lengths exist, but often they are not larger than 0.5 nm.[48] This gives $d = 1$ nm. In this way we find for polyelectrolytes in a good solvent $V^{\text{tot}}/V^b \approx \xi^2/d^2 \approx (14/1)^2 \approx 2 \times 10^2$. This value for $V^{\text{tot}}/V^{\text{b}}$ is larger than the ratio that we used to model our experimental data. This difference might be explained by that the bound monomers might also be further away than the electrostatic bond length. In addition, we neglected any prefactors in our estimation, which might have resulted in a larger value for $V^{\text{tot}}/V^{\text{b}}$. Furthermore, viscosity effects might have resulted in a lower apparent $V^{\text{tot}}/V^{\text{b}}$ ratio in experiments.

Kinetic model predictions

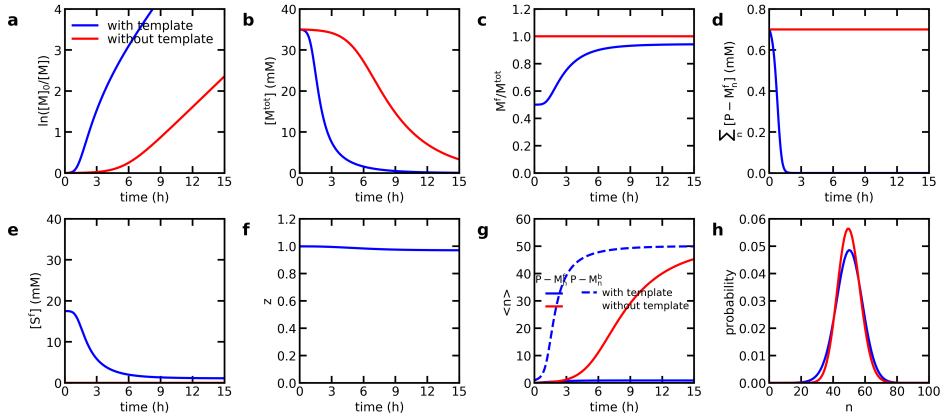

Figure 2.A.10. Kinetic model predictions for the polymerisation with and without template. At increasing reaction times: (a) Monomer conversion shown in a pseudo-first order kinetics plot; (b) Total monomer concentration (c) Free monomer fraction M^f/M^{tot}; (d) Free diblock concentration $\sum_n[P\text{-}M_n^f]$; (e) Free template site concentration $[S^f]$; (f) Bound fraction z of the monomers of the bound diblock; (g) Average degree of polymerisation of the free and bound positive block. (h) Molecular weight distribution of the positive block after a reaction time of 40 h. The standard model parameters are $k_p = 0.36\,\text{mM}^{-1}\text{h}^{-1}$, $k_b = k_a = 12\,\text{mM}^{-1}\text{h}^{-1}$, $k_{bn} = 500k_b$, $k_d(n) = \omega_0\exp(-nE_a/k_BT)$ with $\omega_0 = 3.1\times10^4\,\text{h}^{-1}$ and $E_a = 6k_BT$, $k_f = k_d(1)$, $V^{\text{tot}}/V^{\text{b}} = 8$, $a = 3.0$, $t_{\text{shift}} = 3.5\,\text{h}$, $[M^{\text{tot}}]_0 = 35$ mM, $[S^{\text{tot}}]_0 = 35$ mM and $[P\text{-}M_0^{\text{tot}}]_0 = 0.7$ mM. For the polymerisation without template $k_b = k_a = k_f = k_d = 0$, $V^{\text{tot}}/V^{\text{b}} = 0$, $a = 0.9$, $t_{\text{shift}} = 5.0\,\text{h}$ and $[S^{\text{tot}}]_0 = 0$.

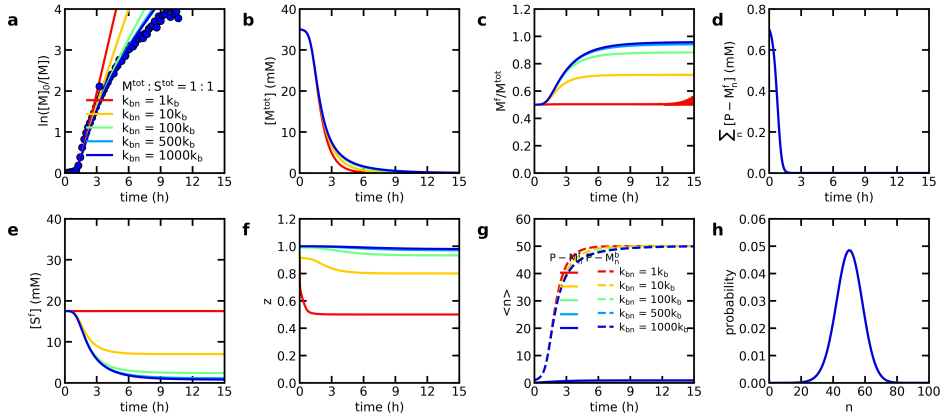

Figure 2.A.11. The effect of changing k_{bn} in the kinetic model, while keeping all the other parameters the same as the standard model parameters in Fig. 2.A.10. At increasing reaction times: (a) Monomer conversion shown in a pseudo-first order kinetics plot. Symbols indicate experimental data of the reaction-assembly network with $M^{\text{tot}} : S^{\text{tot}} = 1:1$; (b) Total monomer concentration (c) Free monomer fraction M^f/M^{tot}; (d) Free diblock concentration $\sum_n[P\text{-}M_n^f]$; (e) Free template site concentration $[S^f]$; (f) Bound fraction z of the monomers of the bound diblock; (g) Average degree of polymerisation of the free and bound positive block. (h) Molecular weight distribution of the positive block after a reaction time of 40 h.

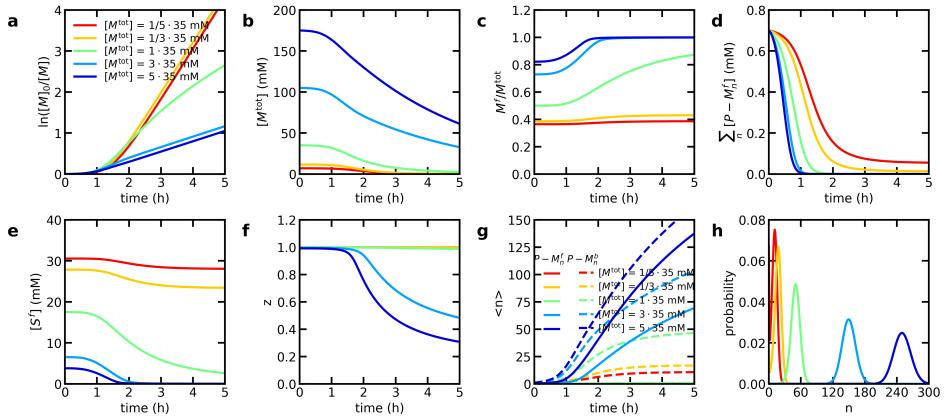

Figure 2.A.12. Effect of the monomer to template ratio. The standard model parameters of Fig. 2.A.10 are used, except for the initial monomer concentration $[M^{\text{tot}}]_0$. At increasing reaction times: (a) Monomer conversion shown in a pseudo-first order kinetics plot; (b) Total monomer concentration (c) Free monomer fraction M^f/M^{tot}; (d) Free diblock concentration $\sum_n [P\text{-}M_n^f]$; (e) Free template site concentration $[S^f]$; (f) Bound fraction z of the monomers of the bound diblock; (g) Average degree of polymerisation of the free and bound positive block. (h) Molecular weight distribution of the positive block after a reaction time of 40 h.

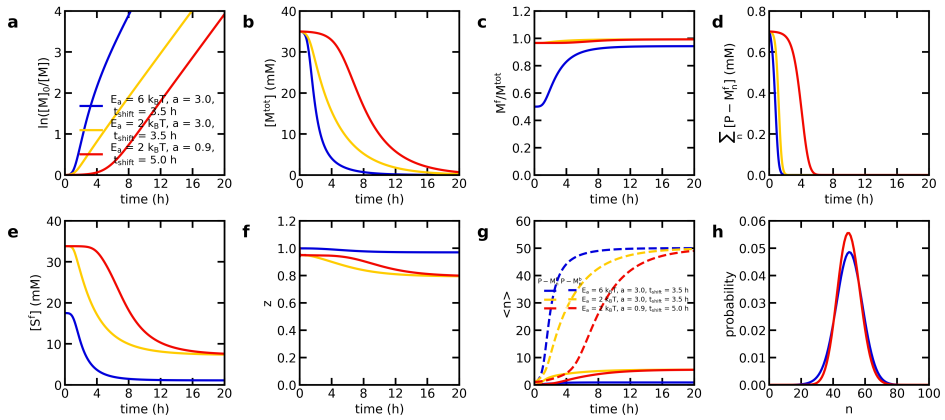

Figure 2.A.13. Effect of the monomer-template interaction strength E_a. Changing the interaction strength affects both $k_d(n)$ and k_f in the kinetic model. In addition, for $E_a = 3k_BT$ the effect of changing the $c(t)$ parameters to $a = 0.9$, $t_{\text{shift}} = 5.0\,\text{h}$ is shown. The other model parameters are the same as the standard model parameters in Fig. 2.A.10. At increasing reaction times: (a) Monomer conversion shown in a pseudo-first order kinetics plot; (b) Total monomer concentration (c) Free monomer fraction M^f/M^{tot}; (d) Free diblock concentration $\sum_n [P\text{-}M_n^f]$; (e) Free template site concentration $[S^f]$; (f) Bound fraction z of the monomers of the bound diblock; (g) Average degree of polymerisation of the free and bound positive block. (h) Molecular weight distribution of the positive block after a reaction time of 40 h. Note that the plot of '$E_a = 3k_BT$, $a = 3.0$ and $t_{\text{shift}} = 3.5h$' completely overlaps with the plot of '$E_a = 3k_BT$, $a = 0.9$ and $t_{\text{shift}} = 5.0h$' and therefore this plot is not visible.

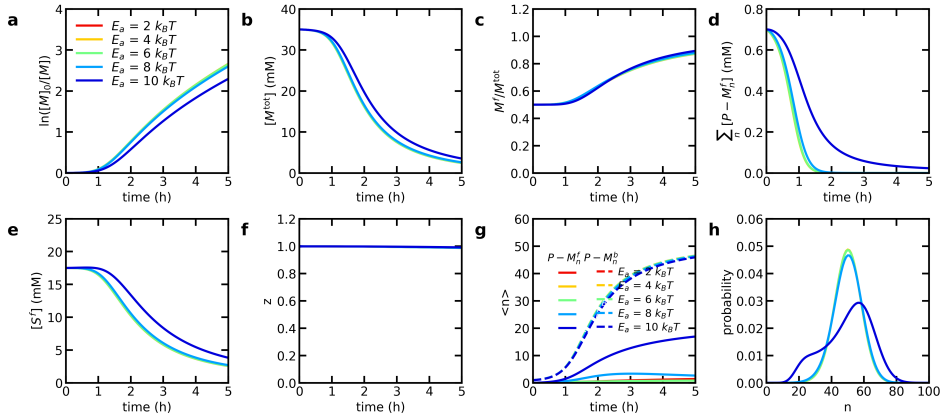

Figure 2.A.14. The effect of the choice of E_a in the kinetic model. Model parameters are the same as the standard model parameters of Fig. 2.A.10, except for the variation of E_a and corresponding changes in k_d, k_f, k_b and k_a to keep the initial bound monomer fraction at 0.5. At increasing reaction times: (a) Monomer conversion shown in a pseudo-first order kinetics plot; (b) Total monomer concentration (c) Free monomer fraction M^f/M^{tot}; (d) Free diblock concentration $\sum_n [P\text{-}M_n^f]$; (e) Free template site concentration $[S^f]$; (f) Bound fraction z of the monomers of the bound diblock; (g) Average degree of polymerisation of the free and bound positive block. (h) Molecular weight distribution of the positive block after a reaction time of 40 h.

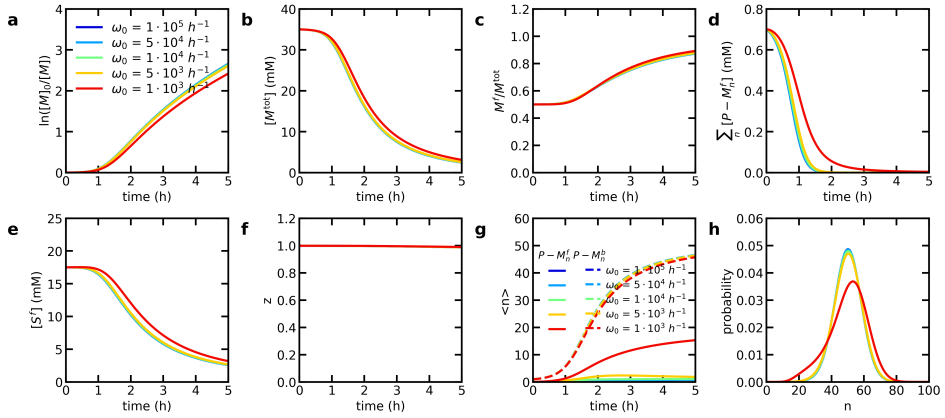

Figure 2.A.15. The effect of the choice of ω_0 in the kinetic model. Model parameters are the same as the standard model parameters of Fig. 2.A.10, except for the variation of ω_0 and corresponding changes in k_d, k_f, k_b and k_a to keep the initial bound monomer fraction at 0.5. At increasing reaction times: (a) Monomer conversion shown in a pseudo-first order kinetics plot; (b) Total monomer concentration (c) Free monomer fraction M^f/M^{tot}; (d) Free diblock concentration $\sum_n [P\text{-}M_n^f]$; (e) Free template site concentration $[S^f]$; (f) Bound fraction z of the monomers of the bound diblock; (g) Average degree of polymerisation of the free and bound positive block. (h) Molecular weight distribution of the positive block after a reaction time of 40 h.

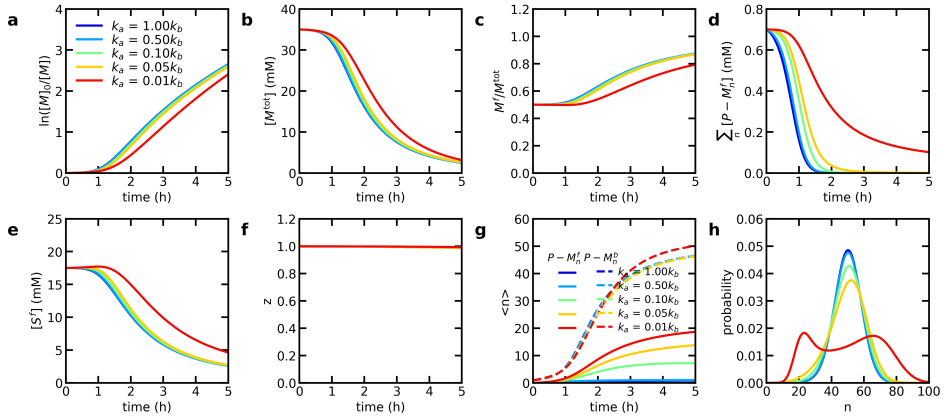

Figure 2.A.16. The effect of the choice of the diblock binding constant k_a in the kinetic model. The other model parameters are the same as the standard model parameters of Fig. 2.A.10. At increasing reaction times: (a) Monomer conversion shown in a pseudo-first order kinetics plot; (b) Total monomer concentration (c) Free monomer fraction M^f/M^{tot}; (d) Free diblock concentration $\sum_n [P\text{-}M_n^f]$; (e) Free template site concentration $[S^f]$; (f) Bound fraction z of the monomers of the bound diblock; (g) Average degree of polymerisation of the free and bound positive block. (h) Molecular weight distribution of the positive block after a reaction time of 40 h.

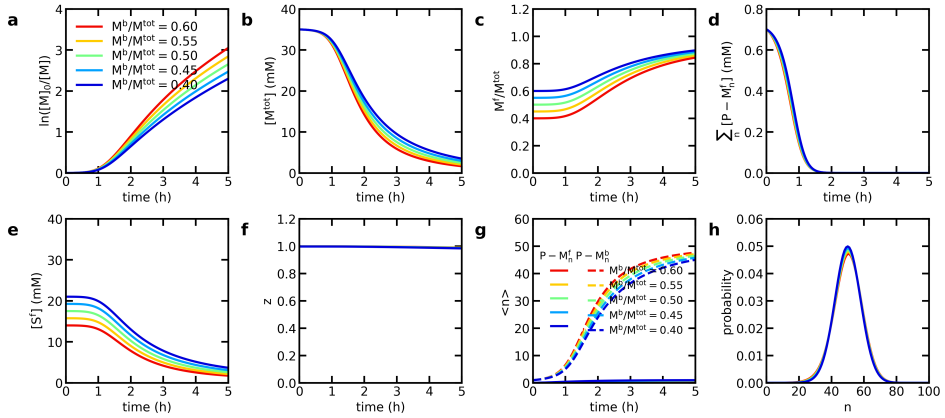

Figure 2.A.17. Kinetic model predictions for the polymerisation reaction with template with different fractions of bound monomer. Here the monomer binding constant $k_b = k_f[M^f]([S^{tot}] - [M^b])/[M^b]$ and the diblock binding constant $k_a = k_b$ are obtained from the bound monomer fraction. The other model parameters are the same as the standard model parameters in Fig. 2.A.10. At increasing reaction times: (a) Monomer conversion shown in a pseudo-first order kinetics plot; (b) Total monomer concentration (c) Free monomer fraction M^f/M^{tot}; (d) Free diblock concentration $\sum_n [P\text{-}M_n^f]$; (e) Free template site concentration $[S^f]$; (f) Bound fraction z of the monomers of the bound diblock; (g) Average degree of polymerisation of the free and bound positive block. (h) Molecular weight distribution of the positive block after a reaction time of 40 h.

2.A.11 Reaction-assembly network at 155 mM KCl

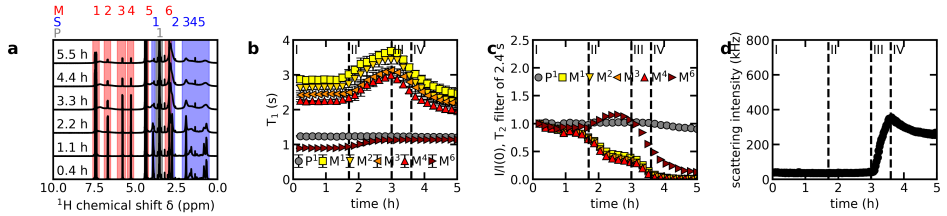

Figure 2.A.18. The reaction-assembly network at 155 mM KCl. At increasing reaction times: (a) ^{1}H NMR spectra; (b) T_1 values for all neutral block P and monomer M protons, with respective error bars obtained from single-exponential fitting; (c) T_2-filtered NMR spectral intensity (T_2-filter of 2.4 s) for the P and M protons, normalised to their own signal intensity at the start of the reaction; (d) Light scattering intensity.

References

[1] Govindarajan, S.; Nevo-Dinur, K.; Amster-Choder, O. Compartmentalization and spatiotemporal organization of macromolecules in bacteria. *FEMS Microbiol. Rev.* **2012**, *36*, 1005–1022.

[2] Zhou, H.-X.; Rivas, G.; Minton, A. P. Macromolecular crowding and confinement: biochemical, biophysical, and potential physiological consequences. *Annu. Rev. Biophys.* **2008**, *37*, 375–397.

[3] Dykeman, E. C.; Stockley, P. G.; Twarock, R. Solving a Levinthal's paradox for virus assembly identifies a unique antiviral strategy. *Proc. Natl. Acad. Sci. U.S.A.* **2014**, *111*, 5361–5366.

[4] Zhang, G.; Hubalewska, M.; Ignatova, Z. Transient ribosomal attenuation coordinates protein synthesis and co-translational folding. *Nat. Struct. Mol. Biol.* **2009**, *16*, 274.

[5] Zhdanov, V. P. Viral capsids: Kinetics of assembly under transient conditions and kinetics of disassembly. *Phys. Rev. E* **2014**, *90*, 042721.

[6] Verdier, T.; Foret, L.; Castelnovo, M. Modeling the kinetics of open self-assembly. *J. Phys. Chem. B* **2016**, *120*, 6411–6420.

[7] Komar, A. A. A pause for thought along the co-translational folding pathway. *Trends Biochem. Sci.* **2009**, *34*, 16–24.

[8] Whitesides, G. M.; Grzybowski, B. Self-assembly at all scales. *Science* **2002**, *295*, 2418–2421.

[9] Lehn, J.-M. From supramolecular chemistry towards constitutional dynamic chemistry and adaptive chemistry. *Chem. Soc. Rev.* **2007**, *36*, 151–160.

[10] Yan, X.; Wang, F.; Zheng, B.; Huang, F. Stimuli-responsive supramolecular polymeric materials. *Chem. Soc. Rev.* **2012**, *41*, 6042–6065.

[11] Chakrabarty, R.; Mukherjee, P. S.; Stang, P. J. Supramolecular coordination: self-assembly of finite two-and three-dimensional ensembles. *Chem. Rev.* **2011**, *111*, 6810–6918.

[12] Rieger, J.; Stoffelbach, F.; Bui, C.; Alaimo, D.; Jérôme, C.; Charleux, B. Amphiphilic poly (ethylene oxide) macromolecular RAFT agent as a stabilizer and control agent in ab initio batch emulsion polymerization. *Macromolecules* **2008**, *41*, 4065–4068.

[13] Warren, N. J.; Armes, S. P. Polymerization-induced self-assembly of block copolymer nano-objects via RAFT aqueous dispersion polymerization. *J. Am. Chem. Soc.* **2014**, *136*, 10174–10185.

[14] Canning, S. L.; Smith, G. N.; Armes, S. P. A critical appraisal of RAFT-mediated polymerization-induced self-assembly. *Macromolecules* **2016**, *49*, 1985–2001.

[15] Penfold, N. J. W.; Yeow, J.; Boyer, C.; Armes, S. P. Emerging Trends in Polymerization-Induced Self-Assembly. *ACS Macro Lett.* **2019**, *8*, 1029–1054.

[16] Yu, Q.; Ding, Y.; Cao, H.; Lu, X.; Cai, Y. Use of polyion complexation for polymerization-induced self-assembly in water under visible light irradiation at 25 C. *ACS Macro Lett.* **2015**, *4*, 1293–1296.

[17] Ding, Y.; Cai, M.; Cui, Z.; Huang, L.; Wang, L.; Lu, X.; Cai, Y. Synthesis of Low-Dimensional Polyion Complex Nanomaterials via Polymerization-Induced Electrostatic Self-Assembly. *Angew. Chem.* **2018**, *57*, 1053–1056.

[18] Ding, Y.; Zhao, Q.; Wang, L.; Huang, L.; Liu, Q.; Lu, X.; Cai, Y. Polymerization-Induced Self-Assembly Promoted by Liquid–Liquid Phase Separation. *ACS Macro Lett.* **2019**, *8*, 943–946.

[19] Liu, Q.; Wang, X.; Ma, L.; Yu, K.; Xiong, W.; Lu, X.; Cai, Y. Polymerization-Induced Hierarchical Electrostatic Self-Assembly: Scalable Synthesis of Multicompartment Polyion Complex Micelles and Their Monolayer Colloidal Nanosheets and Nanocages. *ACS Macro Lett.* **2020**, *9*, 454–458.

[20] Zhao, Q.; Liu, Q.; Li, C.; Cao, L.; Ma, L.; Wang, X.; Cai, Y. Noncovalent structural locking of thermoresponsive polyion complex micelles, nanowires, and vesicles via polymerization-induced electrostatic self-assembly using an arginine-like monomer. *Chem. Commun.* **2020**, *56*, 4954–4957.

[21] Klug, A. The tobacco mosaic virus particle: structure and assembly. *Phil. Trans. R. Soc. B.* **1999**, *354*, 531–535.

[22] Liang, Y.; Fotiadis, D.; Filipek, S.; Saperstein, D. A.; Palczewski, K.; Engel, A. Organization of the G protein-coupled receptors rhodopsin and opsin in native membranes. *J. Biol. Chem.* **2003**, *278*, 21655–21662.

[23] Kinoshita, M.; Field, C. M.; Coughlin, M. L.; Straight, A. F.; Mitchison, T. J. Self-and actin-templated assembly of mammalian septins. *Dev. Cell* **2002**, *3*, 791–802.

[24] Van Galen, M.; Higler, R.; Sprakel, J. Allosteric pathway selection in templated assembly. *Sci. Adv.* **2019**, *5*, eaaw3353.

[25] Voets, I. K.; de Keizer, A.; Cohen Stuart, M. A. Complex coacervate core micelles. *Adv. Colloid Interface Sci.* **2009**, *147*, 300–318.

[26] Spruijt, E.; van den Berg, S. A.; Cohen Stuart, M. A.; van der Gucht, J. Direct measurement of the strength of single ionic bonds between hydrated charges. *ACS Nano* **2012**, *6*, 5297–5303.

[27] Bloembergen, N.; Purcell, E. M.; Pound, R. V. Relaxation effects in nuclear magnetic resonance absorption. *Phys. Rev.* **1948**, *73*, 679.

[28] Levitt, M. H. *Spin dynamics: basics of nuclear magnetic resonance*; John Wiley & Sons, 2013.

[29] Drache, M.; Schmidt-Naake, G.; Buback, M.; Vana, P. Modeling RAFT polymerization kinetics via Monte Carlo methods: cumyl dithiobenzoate mediated methyl acrylate polymerization. *Polymer* **2005**, *46*, 8483–8493.

[30] van der Kooij, H. M.; Spruijt, E.; Voets, I. K.; Fokkink, R.; Cohen Stuart, M. A.; van der Gucht, J. On the stability and morphology of complex coacervate core micelles: From spherical to wormlike micelles. *Langmuir* **2012**, *28*, 14180–14191.

[31] Nakai, K.; Nishiuchi, M.; Inoue, M.; Ishihara, K.; Sanada, Y.; Sakurai, K.; Yusa, S.-i. Preparation and characterization of polyion complex micelles with phosphobetaine shells. *Langmuir* **2013**, *29*, 9651–9661.

[32] van der Burgh, S.; de Keizer, A.; Cohen Stuart, M. A. Complex coacervation core micelles. Colloidal stability and aggregation mechanism. *Langmuir* **2004**, *20*, 1073–1084.

[33] Amann, M.; Diget, J. S.; Lyngsø, J.; Pedersen, J. S.; Narayanan, T.; Lund, R. Kinetic Pathways for Polyelectrolyte Coacervate Micelle Formation Revealed by Time-Resolved Synchrotron SAXS. *Macromolecules* **2019**, *52*, 8227–8237.

[34] Cohen Stuart, M.; Besseling, N.; Fokkink, R. Formation of micelles with complex coacervate cores. *Langmuir* **1998**, *14*, 6846–6849.

[35] Lindhoud, S.; Norde, W.; Cohen Stuart, M. A. Reversibility and relaxation behavior of polyelectrolyte complex micelle formation. *J. Phys. Chem. B* **2009**, *113*, 5431–5439.

[36] Lueckheide, M.; Vieregg, J. R.; Bologna, A. J.; Leon, L.; Tirrell, M. V. Structure–property relationships of oligonucleotide polyelectrolyte complex micelles. *Nano Lett.* **2018**, *18*, 7111–7117.

[37] Pergushov, D. V.; Müller, A. H.; Schacher, F. H. Micellar interpolyelectrolyte complexes. *Chem. Soc. Rev.* **2012**, *41*, 6888–6901.

[38] Aguilar, J. A.; Nilsson, M.; Bodenhausen, G.; Morris, G. A. Spin echo NMR spectra without J modulation. *Chem. Commun.* **2012**, *48*, 811–813.

[39] Barlow, T. R.; Brendel, J. C.; Perrier, S. Poly (bromoethyl acrylate): A reactive precursor for the synthesis of functional RAFT materials. *Macromolecules* **2016**, *49*, 6203–6212.

[40] Xu, X.; Smith, A. E.; Kirkland, S. E.; McCormick, C. L. Aqueous RAFT synthesis of pH-responsive triblock copolymer mPEO- PAPMA- PDPAEMA and formation of shell cross-linked micelles. *Macromolecules* **2008**, *41*, 8429–8435.

[41] Jesson, C. P.; Pearce, C. M.; Simon, H.; Werner, A.; Cunningham, V. J.; Lovett, J. R.; Smallridge, M. J.; Warren, N. J.; Armes, S. P. H2O2 Enables Convenient Removal of RAFT End-Groups from Block Copolymer Nano-Objects Prepared via Polymerization-Induced Self-Assembly in Water. *Macromolecules* **2017**, *50*, 182–191.

[42] Velázquez-Campoy, A. Ligand binding to one-dimensional lattice-like macromolecules: analysis of the McGhee–von Hippel theory implemented in isothermal titration calorimetry. *Anal. Biochem.* **2006**, *348*, 94–104.

[43] Li, J.; Ngai, T.; Wu, C. The slow relaxation mode: from solutions to gel networks. *Polym. J.* **2010**, *42*, 609–625.

[44] Wang, J. The origin of the slow mode in dilute aqueous solutions of PEO. *Macromolecules* **2015**, *48*, 1614–1620.

[45] Koziol, M.; Fischer, K.; Seiffert, S. Origin of the low-frequency plateau and the light-scattering slow mode in semidilute poly (ethylene glycol) solutions. *Soft Matter* **2019**, *15*, 2666–2676.

[46] Ghostine, R. A.; Shamoun, R. F.; Schlenoff, J. B. Doping and Diffusion in an Extruded Saloplastic Polyelectrolyte Complex. *Macromolecules* **2013**, *46*, 4089–4094.

[47] Dobrynin, A. V.; Colby, R. H.; Rubinstein, M. Scaling theory of polyelectrolyte solutions. *Macromolecules* **1995**, *28*, 1859–1871.

[48] Kumar, S.; Nussinov, R. Relationship between ion pair geometries and electrostatic strengths in proteins. *Biophys. J.* **2002**, *83*, 1595–1612.

Chapter 3

Langevin dynamics simulations of the exchange of complex coacervate core micelles: the role of non-electrostatic attraction and polyelectrolyte length

Complex coacervate core micelles (C3Ms) are promising encapsulators for a wide variety of (bio)molecules. To protect and stabilise their cargo, it is essential to control their exchange dynamics. Yet, to date, little is known about the kinetic stability of C3Ms and the dynamic equilibrium of molecular building blocks with micellar species. Here we study the C3M exchange during the initial micellization by using Langevin dynamics simulations. In this way, we show that charge neutral heterocomplexes consisting of multiple building blocks are the primary mediator for exchange. In addition, we show that the kinetic stability of the C3Ms can be tuned not only by the electrostatic interaction, but also by the non-electrostatic attraction between the polyelectrolytes, the polyelectrolyte length ratio and the overall polyelectrolyte length. These insights offer new rational design guides to aid the development of new C3M encapsulation strategies.

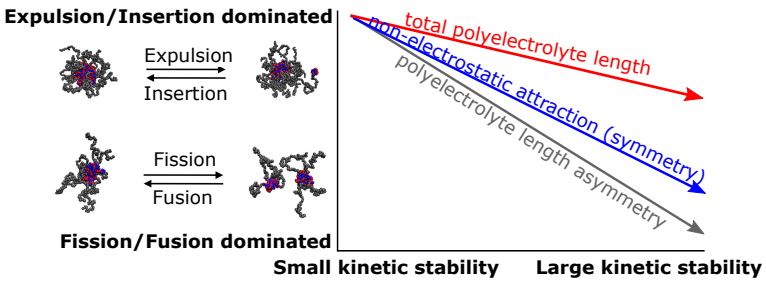

This chapter is based on: Inge Bos and Joris Sprakel. Langevin Dynamics Simulations of the Exchange of Complex Coacervate Core Micelles: The Role of Nonelectrostatic Attraction and Polyelectrolyte Length. *Macromolecules* **2019** *52*(22), 8923–8931.

3.1 Introduction

Complex coacervate core micelles (C3Ms) have a core that consists of complexes of oppositely charged polyelectrolytes and are therefore well-suited to encapsulate hydrophilic (bio)molecules. The core formation relies on the associative phase separation of the oppositely charged polyelectrolytes from the water phase. The phase rich in polyelectrolytes is called the complex coacervate. Macroscopic phase separation is prevented by a neutral, water-soluble block that is attached to at least one the two polyelectrolyte types. This neutral block forms the corona around the complex coacervate core. Molecules that prefer to go to the complex coacervate phase can be incorporated in the C3M core and can be protected from the outside by the surrounding corona. This makes the C3Ms promising encapsulators for different types of (bio)molecules. In fact, C3Ms have already been studied as encapsulators for many applications,[1] especially for drug and gene delivery.[2–4]

To design good C3M encapsulators it is essential to understand their exchange dynamics. First, the exchange dynamics between C3Ms determines the rate with which cargo in the core is exposed to the surroundings and thus the level of protection the encapsulation vehicle offers. In addition, the structure of the C3Ms sometimes depends on their preparation pathway,[5–8] which means that kinetic effects can govern the C3M structure and thus their encapsulation properties.

For amphiphilic diblock copolymer micelles the importance of exchange dynamics is widely recognised and their exchange dynamics has been thoroughly studied.[9–18] These micelles consist of a single macromolecular species featuring an soluble and an insoluble block. Often, two different mechanisms are distinguished to describe the exchange of these micelles, based on the theoretical framework developed by Dormidontova.[11] The first mechanism is unimer exchange. Here, one polymer (or a few polymers) splits off and is inserted into another micelle. The second mechanism is fission followed by fusion. In that case, the micelle splits into two parts of both substantial sizes, which can subsequently fuse with another micelle. For the fission, both parts that are formed still have a corona structure. For the expulsion however, the expelled part contains only one or two soluble blocks, which is not enough to form a micelle corona. Due to this difference in corona both mechanism have different rate limiting steps and therefore different dependencies on the system parameters. A change of one of the system parameters can thus change which of the two mechanisms dominates or whether they both occur. As a result, micelle exchange rates can have a complex dependence on system parameters like core block length,[12–16] corona block length,[12,16,17] polymer concentration,[12,14] chain flexibility[16] and interfacial tension between core and solvent.[12,14,18]

Although the theory developed for amphiphilic diblock copolymer micelle exchange provides a good starting point to describe C3M exchange, it cannot describe the C3M exchange completely. The two micelle types differ in the interactions that drive the core formation. For amphiphilic diblock copolymer micelles, the core formation is usually driven by hydrophobic attraction, while for C3Ms the core formation is the result of electrostatic attraction between the oppositely charged polyelectrolytes enabling the release of counter ions. The difference in interaction can be partly accounted for because polyelectrolyte complexes have already been thoroughly studied. For example, it has been shown that the dynamics within the complex coacervate phase depends both on the polyelectrolyte length and the salt concentration.[19] This can help to describe the relaxation within the C3M core. In addition, the interfacial tension of certain complex coacervates[20] and the strength of an ionic bond have been measured,[21] which can help to describe the release of polyelectrolytes from the C3M core. However, the fact that the core formation is based on the attraction between two different block types instead of one also introduces additional tuning parameters that are absent for amphiphilic diblock copolymer micelles. Instead of only varying the length of one core block, the block length of the negative and positive polymer block can be varied independently from each other. Furthermore, the choice to attach the corona block to both core blocks or to only one of the two can alter the micelle properties.[22] It is

thus insufficient to focus only on amphiphilic diblock copolymer micelles to understand the exchange of C3Ms.

Unfortunately, the exchange of C3Ms is much less studied and the few studies done on this subject [23,24] had an indirect way of interpreting their results. The authors mixed C3Ms labelled with a donor fluorophore with C3Ms labelled with an acceptor fluorophore and took the rate of increase in Förster Resonance Energy Transfer (FRET) as a measure for the micelle exchange rates. In this way, they found that the exchange rate depends on the polyelectrolyte length and charge stoichiometry [23] and that the exchange rate is fast for C3Ms containing proteins. [24] Subsequent interpretations on the exchange mechanisms were mainly based on the observed exchange rates and not on direct observations. Although these studies give very useful insights into the time scales at which micelle exchange can occur, they are limited in the mechanistic descriptions they can provide.

In this chapter we aim to provide insights into the molecular mechanisms of exchange in C3Ms. To this end, we exploit coarse-grained dynamics simulations. This type of simulations has already shown its value in the studies on amphiphilic diblock copolymer micelle exchange. [12,14–16] In addition, coarse-grained dynamics simulations have also been used to study complex coacervation, [25,26] the formation of a single C3M [27] and the static properties of multiple C3Ms. [28–30] We use the coarse-grained simulations to follow the initial micellization kinetics of multiple C3Ms. In this way, we obtain new mechanistic insights into the exchange of C3Ms and we identify ways to improve the kinetic stability of C3Ms. This information on the kinetic stability can complement earlier on the static C3M stability, [31–34] which is usually expressed as the critical salt concentration where the micelles fall apart. In particular, we show that also the kinetic stability of C3Ms can be improved by tuning the non-electrostatic interactions and the polyelectrolyte length ratio.

3.2 Methods

We used the Kremer-Grest bead-spring model to describe flexible chains in a good solvent and included electrostatic interactions and explicit ions to account for the electrostatic nature of the process we aim to describe. In the model, the polymers are represented by multiple beads connected with springs, while the counter ions are represented by single beads. The solvent is modelled implicitly. All beads have the same diameter σ and the same mass m. The springs represent polymer bonds and are modelled with a finitely extensible nonlinear elastic (FENE) potential with a bond stiffness k of $30k_BT/\sigma^2$ and a maximum bond extension distance r of 1.5σ. The electrostatic interactions between the beads are modelled with a Coulomb potential. Unless otherwise stated, we modelled the non-electrostatic interactions between equally and oppositely charged monomers with a Lennard Jones potential with a cut-off distance of 2.5σ. We varied the strength of the non-electrostatic attraction by changing the minimum of the Lennard Jones potential $\varepsilon_{\mathrm{LJ}}$ in the range $0.05k_BT - 0.25k_BT$. In contrast to the non-electrostatic interaction between equally and oppositely charged monomers, the non-electrostatic interaction between all other monomer-monomer, monomer-ion and ion-ion combinations was purely repulsive. For this repulsive interaction we used the Weeks-Chandler-Andersen (WCA) potential with an interaction strength $\varepsilon = 1k_BT$. An graphical overview of all used potentials can be found in the appendix (Section 3.A.1).

This coarse-grained bead-spring representation has often been used to model polyelectrolytes and can be mapped to experimentally realistic systems via the Bjerrum length l_B. The Bjerrum length sets the length scale of the electrostatic interaction. In pure water at room temperature the Bjerrum length is 0.71 nm. In our model we used a Bjerrum length of $l_B = 2.5\sigma$, which means that the bead diameter σ roughly corresponds to ~ 0.3 nm. The average polyelectrolyte bond distance is 0.97σ for the simulation parameters that we used. This means that the charge separation distance in our simulation is approximately ~ 2.8 Å, which is close to the distance between two adjacent side groups of a polymer

carbon backbone. We thus simulate polyelectrolytes where every side group is charged, such as the strongly charged polyelectrolyte polystyrene sulfonate.

The C3Ms in our simulations are formed from a combination of coarse-grained homopolymers, diblocks and counter ions. The homopolymers are negatively charged and have a length N_{neg}, where N represents the number of monomers. The diblock consists of a positively charged block with length N_{pos} and a neutral block with length N_{neu}. We varied the lengths of the negative polymer and the diblock polymer between the different simulations, but we chose the parameters such that the number of negative monomers was always equal to the number of positive monomers. In addition, we fixed the total number of charged monomers at 24000 and we kept the ratio between the positive and neutral block length at $2:5$. Similar ratios have also been used in experimental studies of C3Ms.[34,35] In our simulations this ratio ensured that the neutral block was long enough to prevent macro phase separation and on the other hand short enough to allow the formation of micelles instead of only free soluble complexes. We added only counter ions to the simulation box, no additional salt ions were added. We note that in solvents of experimental systems always some additional salt ions are present. However, since we use a periodic box size of $L = 235\sigma$ every time, the counter ion concentration is relatively large compared to for example the ion concentration of distilled water and these solvent ions thus can be neglected.

We started our simulation by placing the homopolymers, diblocks and counter ions randomly in the simulation box and then used Langevin dynamics simulations to simulate the formation of the C3Ms in time. We used $\gamma = 1m/\tau$ as drag coefficient and $\Delta t = 0.005\tau$ as simulation time step where $\tau = \sigma\sqrt{m/\varepsilon}$ is the time unit in the system. We saved the configuration of the simulation every 2500 steps.

To perform the simulations we used the GPU-optimized molecular dynamics software package HOOMD-Blue.[36–39] The Coulomb interactions were calculated by using the particle-particle particle-mesh (PPPM) Ewald summation method[38] with a real space cut off distance of 2.5σ. The neighbour lists were generated by using the linear bounding volumes hierarchies (LBVHs) method.[39] We used visual molecular dynamics (VMD)[40] to visualize the simulations.

To analyse the simulation data we first identified the micelles with the data clustering algorithm DBSCAN. In particular, we used the algorithm as implemented in the Python package scikit-learn[41] with a maximum allowable neighbourhood radius of 2σ and a minimum neighbourhood points number of three for a point to be a core point. To avoid that two near micelles were identified as a single micelle, we based the clustering algorithm on the polyelectrolyte coordinates and did not take the neutral block into account. We provided a precomputed sparse array as neighbour array for the DBSCAN algorithm. To obtain this array, we used the KDTree neighbour algorithm from scikit-learn. Since this algorithm does not take the periodic boundaries into account, we first added the surrounding periodic boundary images, used the KDTree algorithm to calculate neighbour list for the original simulation box and its periodic images together and then converted this to a periodic neighbour list for the original simulation box. We performed the micelle cluster identification for every tenth saved configuration (125τ). The intermediate saved configurations were analysed if the micelle composition changed within these ten steps.

The clustering algorithm yielded the micelle compositions for every time step and this was used to analyse the micelle exchange. A decrease in micelle size was counted as a split event and an increase in micelle size was counted as a merge event. The discrimination between expulsion and fission and between insertion and fusion was based on the size of the smallest cluster involved in the exchange event: if this cluster contained less than 5 polyelectrolytes, the cluster contained too little diblocks to form a corona structure and therefore the split event was called expulsion and the merge event was called insertion. Otherwise, the split event was called fission and the merge event was called fusion.

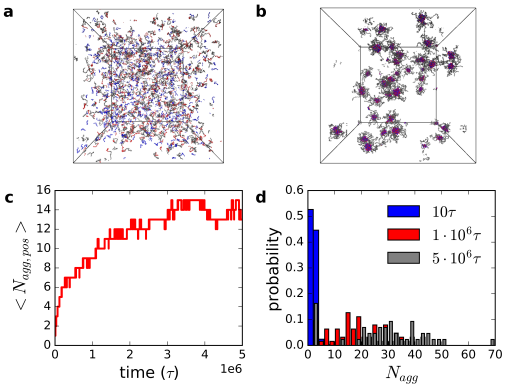

Figure 3.1. The initial micellization kinetics of C3Ms for $N_{neg} = 20$, $N_{pos} = 20$, $N_{neu} = 50$ and $\varepsilon_{LJ} = 0.15 k_B T$. a and b) Snapshots of the begin (a) and the end (b) of the simulation. Homopolymers are depicted blue, the positive block in red and the neutral block in grey. Counter ions are not shown. c) The increase of the average micelle size, expressed as the average aggregation number of positive blocks per micelle $N_{agg,pos}$, in time. d) Histograms of the C3M size distribution, expressed as total number of polymers per micelle N_{agg}, at different time points during the simulations.

3.3 Results and discussion

3.3.1 C3M formation and C3M exchange mechanisms

Complex coacervate core micelles rapidly form when we mix coarse-grained homopolymers, diblocks and counter ions together in the simulation box (Fig. 3.1). First, the polyelectrolytes have a relatively stretched configuration and are surrounded by their counter ions. The oppositely charged polyelectrolytes rapidly form complexes upon which they decrease in size and release their counter ions (appendix Section 3.A.2). At the end of the simulation, we observe clear C3M structures, where the positive and negative polymers together form the core of the micelle, while the neutral blocks form the surrounding corona (Fig. 3.1b, appendix Section 3.A.3). The initial assembly is particularly fast. Afterwards the micelle growth levels off and at the end of the simulation the average micelle size fluctuates around the same value (Fig. 3.1c).

Although the micelle growth approaches a plateau at the end of the simulation, the micelles probably do not reach complete equilibrium yet. At the end of the simulation, the micelles still have a broad size distribution that is not centred around one optimum value (Fig. 3.1d). A broad size distribution has been observed for C3Ms at large salt concentrations, but at low salt concentrations these C3Ms are more monodisperse.[34,42] At larger salt concentrations the C3Ms can form wormlike micelles where the length of the micelles can be easily varied without large changes in the free energy. At low salt concentrations the C3Ms form spherical micelles. For the spherical micelles, a change in aggregation number changes the free energy of the micelle. In equilibrium, the micelles will adapt their most favourable configuration and the micelles thus will have sizes centred around the size with the lowest free energy. Since in our simulations we did not add additional salt ions and the micelles are spherical, we expect that the equilibrium C3M size distribution will be centred around one optimal size. At the end of our simulations however, we still observe a broad size distribution with multiple maxima. Simulations of amphiphilic diblock copolymer micelles have shown that the broad size distribution can indeed evolve to a clear bimodal size distribution after longer simulation times with one size corresponding to the unimers and one to the micelles.[12] However, C3Ms sometimes need days to fully

equilibrate,[8] which would take far too long to simulate with Langevin dynamics. Therefore we focus here on the initial micellization kinetics of C3Ms and not on their equilibrium dynamics.

In addition to following the initial average micelle growth, the simulations also allow us to directly follow the individual micelle exchange (Fig. 3.2). We can observe both expulsion and insertion events and fission and fusion events. The small time and length scales make it impossible to directly observe these events in real experiments. Our simulations thus complement the experiments and can give a deeper insight into the mechanisms that underlie the C3M exchange in the early micellization stage. We note that the C3M exchange mechanisms can be different in a later stage, as is the case for amphiphilic diblock copolymer micelles.[12,43] However, since the interactions between the different monomers remain the same, our observations on the initial exchange can still help to better understand the equilibrium exchange.

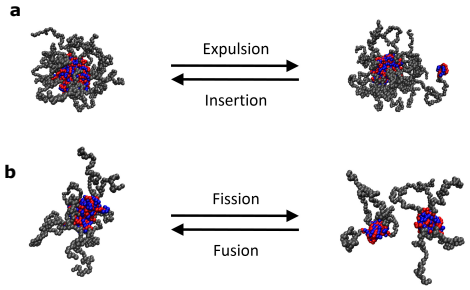

Figure 3.2. The two mechanisms by which micelle exchange occurs in the simulations. a) Only one or a few polyelectrolytes are expelled from the micelle and inserted into another micelle. b) The micelle splits in two parts of both substantial sizes (fission), which can combine with other micelles to form a new micelle (fusion). Images are snapshots from simulations with the same colour coding as in Fig. 3.1. Counter ions are not shown.

The C3M expulsion mechanism (Fig. 3.2a) is slightly different from the one of amphiphilic diblock copolymer micelles and we ascribe this difference to the difference in core interactions. In amphiphilic diblock copolymer micelles, the unfavourable interactions of the core-block with the solvent drives the core formation. For C3Ms however, the core formation is mainly driven by the electrostatic attraction between the oppositely charged core blocks. In particular, strongly and oppositely charged polyelectrolytes form complexes mainly because the entropy increases due to the release of counter ions.[26,44] This entropy increase is less when a part of the charge of the polyelectrolytes is not compensated by the oppositely charged polyelectrolytes, since in that case less counter ions are released. Neutral complexes are thus preferred. As a result, we observe that small neutral complex are expelled from C3Ms instead of the unimers that are usually expelled from amphiphilic micelles. This expulsion of neutral complexes was already predicted to describe the exchange kinetics of C3Ms loaded with fluorescent proteins[24] and is now confirmed by our simulations.

3.3.2 Effect of non-electrostatic attraction strength

Although the electrostatics plays the most important role in the formation of polyelectrolyte complexes, the non-electrostatic interactions can also have an effect. The critical salt concentration and binding strength of polyelectrolyte complexes strongly depend on the polyelectrolytes that are used.[45,46] Also for C3Ms both the critical salt concentration and their structure strongly depends on the type of polyelectrolyte.[28,34,47] This shows that apart from the number of charges on the polyelectrolyte, the polymer chemistry also plays a role in polyelectrolyte complexation. Examples of factors that increase the non-electrostatic attraction between the polyelectrolytes are the hydrophobicity of the polymers and the presence of amine groups or aromatic groups.[46]

To test whether the non-electrostatic attraction also affects the exchange kinetics of the C3Ms, we varied the non-electrostatic attraction between the polyelectrolytes by varying ε_{LJ}. An increase in ε_{LJ} results in a decrease in the repulsion between likely charged monomers at distances where the repulsion energy is close to the thermal energy (Fig. 3.A.1). For the oppositely charged monomers the change in ε_{LJ} has a more complex effect and it also changes the location of the minimum of the combined Lennard Jones and Coulomb potential (Fig. 3.A.1). The largest non-electrostatic attraction strength that we used was $\varepsilon_{LJ} = 0.25k_BT$. This is still a weak attraction and still corresponds to a polymer in good solvent: for the Lennard-Jones bead-spring model the transition to poor solvent conditions occurs at $\varepsilon_{LJ} = 0.33k_BT$.[48] Even for the largest non-electrostatic attraction strength in our simulations, the electrostatics thus remains the main driving force to form micelles and not the non-electrostatic attraction: when the electrostatic interactions are turned off the micelles fall apart (Fig. 3.A.10). In this way we ensured that we specifically studied C3Ms instead of repeating the studies on amphiphilic micelles where non-electrostatic attraction drives micelle formation.

Even a small increase in the non-electrostatic attraction largely decreases the number of exchange events, especially in the later stage of the micelle formation (Fig. 3.3). The first $10^4\tau$, the insertion and fusion rates are still comparable for the different non-electrostatic attraction strengths (Fig. 3.A.11). The non-electrostatic attraction thus does not play a large role in the early assembly. In this stage, the merge events strongly outnumber the split events. This indicates rapid micelle growth, which we indeed observed in Fig. 3.1c. The fusion outnumbers the fission longer than the insertion events outnumber the expulsion events. The fast early assembly stage is thus followed by a stage where the micelle growth occurs at the expense of smaller micelles, while the dimer population remains approximately constant (as also shown in Fig. 3.A.3 and 3.A.4). In this stage, the majority of the chains in the micelles originates from fusion events for $\varepsilon_{LJ} = 0.15k_BT$ and $\varepsilon_{LJ} = 0.25k_BT$, while for $\varepsilon_{LJ} = 0.05k_BT$ insertion remains the dominant mechanism of micelle growth (appendix section 3.A.6). The situation of the stronger non-electrostatic attractions resembles to what has been earlier observed in simulations for amphiphilic diblock copolymer micelles: these amphiphilic micelles also had a stage where their growth was mainly governed by fusion of small aggregates.[12] At the end of our simulations, both the insertion rate is similar to the expulsion rate and the fusion rate is similar to the fusion rate, indicating a slow micelle growth. In this stage, the occurrence of all exchange processes depend strongly on the non-electrostatic attraction.

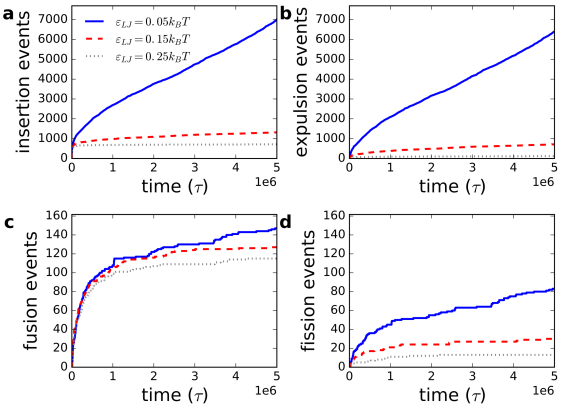

Figure 3.3. Cumulative number of insertion (a), expulsion (b), fusion (c) and fission (d) events for a non-electrostatic attraction strength between the polyelectrolytes of $\varepsilon_{LJ} = 0.05k_BT$, $\varepsilon_{LJ} = 0.15k_BT$ and $\varepsilon_{LJ} = 0.25k_BT$. In all cases, $N_{neg} = 20$, $N_{pos} = 20$ and $N_{neu} = 50$.

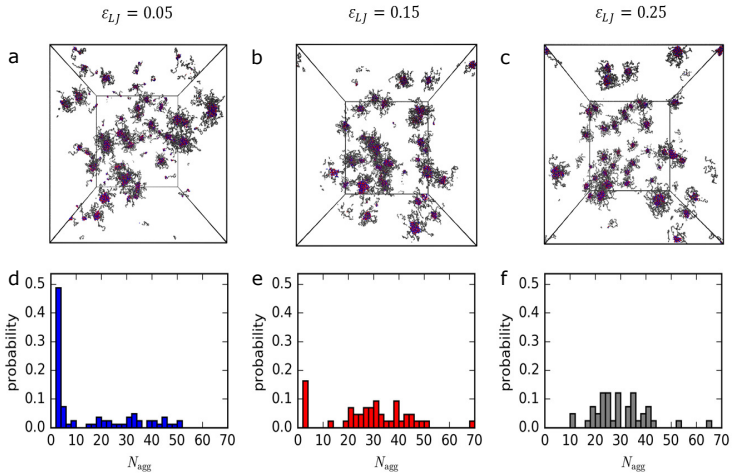

Figure 3.4. Snapshots (a,b,c) and histograms (d,e,f) of the C3M size distribution at the end of the simulation for a non-electrostatic attraction strength between the polyelectrolytes of $\varepsilon_{\mathrm{LJ}} = 0.05 k_B T$ (a,d), $\varepsilon_{\mathrm{LJ}} = 0.15 k_B T$ (b,e) and $\varepsilon_{\mathrm{LJ}} = 0.25 k_B T$ (c,f). In all cases, $N_{\mathrm{neg}} = 20$, $N_{\mathrm{pos}} = 20$ and $N_{\mathrm{neu}} = 50$. The colour coding of the simulation snapshots is the same as in Fig. 3.1. Counter ions are not shown.

For the parameter set of Fig. 3.3, the expulsion of dimers occurs often, which indicates that dimers can be easily formed. At the end of the simulation, we indeed observe a large population of dimers, which decreases with increasing non-electrostatic attraction (Fig. 3.4). A similar decrease in dimer population with increasing non-electrostatic attraction was observed by Šindelka et al.,[29] although they more strongly increased the non-electrostatic attraction and directly went from good to poor solvent conditions. Dimers can be formed because the enthalpic penalty to expel a neutrally charged dimer from a complex coacervate is small and can be counterbalanced by the entropy that the dimer gains when it is expelled from the complex coacervate. For low polyelectrolyte concentrations complex coacervation even does not occur and instead only neutral globules are formed.[49,50] As already pointed out by Šindelka et al.,[28] a stronger non-electrostatic attraction introduces another enthalpic attraction that counteracts the entropy increase when the dimer is released. In this way, the dimer formation is diminished.

Up to now, we have concluded only that a stronger non-electrostatic attraction decreases both the insertion/expulsion and fission/fusion events, but we have not yet further quantified this decrease. To make a more quantitative description, we have plotted the number of split events in the time range $2\times10^6\tau - 5\times10^6\tau$ versus the non-electrostatic attraction strength (Fig. 3.5). We selected the split events in the last part of the simulations, because these events are mainly caused by the micelle exchange kinetics. The merge events and the early split events are affected by both the micelle exchange kinetics and the micelle growth. The simultaneous occurrence of two different processes complicates the analysis and therefore we decided to focus on the later split events.

The number of expulsion events seems to decrease exponentially with increasing non-electrostatic attraction for a polyelectrolyte length of 20. This suggests a thermally activated process where the breaking of non-electrostatic attraction contributes to the energy barrier. The rate k of a thermally activated process can be described by the Arrhenius equation. To break the interactions of n monomers, the Arrhenius equation is given by $k = A\exp(-nE_a/k_BT)$, where E_a is the activation energy to break the interactions of a single monomer and A is a constant. The total number of core block monomers

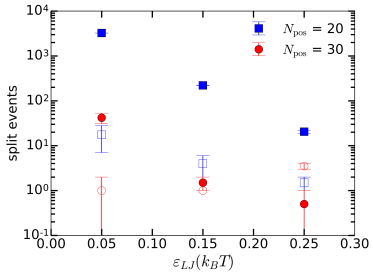

Figure 3.5. Effect of the non-electrostatic attraction strength on the expulsion events (filled symbols) and fission events (open symbols) in the time range $2 \times 10^6\tau - 5 \times 10^6\tau$, for $N_{\text{pos}} = 20, N_{\text{neg}} = 20$ and $N_{\text{neu}} = 50$ and for $N_{\text{pos}} = 30$, $N_{\text{neg}} = 30$ and $N_{\text{neu}} = 75$. Data points are the average of two simulations.

is 40 for dimers with $N_{\text{pos}} = N_{\text{neg}} = 20$. In the simplest description, all these monomers contribute to the activation energy and the non-electrostatic activation energy per monomer is just given by ε_{LJ}. This is not the case: the slope of the natural logarithm of the number of expulsion events versus the non-electrostatic attraction strength ε_{LJ} is -25.3 ± 0.51 and not -40.

Two factors can contribute to the difference between the observed slope and the slope of the simplified description. First, the activation energy per monomer is not given by ε_{LJ} but first has to be multiplied with a numerical prefactor. Not every monomer is positioned from one other monomer at exactly the distance of the minimum of the Lennard Jones potential. The distance between the monomers can deviate and a monomer might also have interactions with more than one monomer. To correct for this, the numerical prefactor is needed. This numerical prefactor was also used to describe the equilibrium exchange of amphiphilic diblock copolymer micelles.[14] Second, some of the monomers might not contribute to the activation energy barrier. For example, if the dimer is expelled as a compact globule of N monomers, only the outer $N^{2/3}$ monomers will contribute to the activation energy barrier (in the Arrhenius equation $n = N^{2/3}$). In fact, simulation snapshots of free dimers show a configuration in between a linear chain and a compact globule (Fig. 3.A.15). This would mean that N^a monomers contribute to the energy barrier with the exponent a in between $2/3$ and 1.

Increasing the polyelectrolyte lengths to 30 largely decreases the number of expulsion events. For the larger non-electrostatic attractions, the number of expulsion events in the simulations even becomes too low for reliable statistics. We note that for $\varepsilon_{\text{LJ}} = 0.05 k_BT$ the decrease in expulsion rate is much larger than we expect for a thermally activated process based on only non-electrostatic attraction. For a thermally activated process, the maximum decrease based on only non-electrostatic attraction occurs when all monomers N contribute to the activation energy barrier. In that case, based on the data for $N_{\text{pos}} = N_{\text{neg}} = 20$, the expulsion rate would depend on N as $k = A \exp(-0.63 N \varepsilon_{\text{LJ}})$. For an increase of both polyelectrolyte lengths from 20 to 30, the expected decrease factor is thus $k_{N=40}/k_{N=60} = \exp(-0.63 \cdot 40 \cdot \varepsilon_{\text{LJ}}/k_BT)/\exp(-0.63 \cdot 60 \cdot \varepsilon_{\text{LJ}}/k_BT) = 2$. In the simulations however, the expulsion rate is more than 60 times decreased. This much larger decrease could mean that the dimer expulsion is not a simple thermally activated process, although the expulsion rate seems to decrease exponentially with increasing ε_{LJ} for the polyelectrolyte lengths of 20. Alternatively, this larger decrease could also mean that apart from the non-electrostatic attraction also additional factors play a role in the dimer expulsion.

Other factors that can affect the dimer expulsion are the corona block and the electrostatic interactions. In simulations of amphiphlic diblock copolymer micelles the expulsion rate slightly decreased when the corona block:core block length ratio was increased.[12,16] The change in micelle exchange rates was ascribed to the change in micelle aggregation number that occurred by increasing the corona:core block

length ratio. Here we tried to minimise the effect of the corona block by keeping the corona:core block length ratio fixed. If the corona block length has any effect for this fixed ratio, we would expect that a longer corona block increases the expulsion rate: when the dimer is expelled the corona block gains entropy because it does not longer have to be in a stretched configuration. This entropy increase will be larger for longer corona blocks. The expected expulsion rate increase is opposite to the large decrease that we observe in simulations. This suggests that the corona block has a minor effect on the dimer expulsion. If the expulsion is indeed a thermally activated process, the large decrease thus has to be ascribed to the electrostatic interactions. The electrostatic interactions might affect the expulsion rate because the electrostatic bonds might first need to rearrange before a neutral dimer can be expelled. A larger number of monomers requires that more electrostatic bonds are rearranged and thus decreases the expulsion rate.

So far we have mainly described the expulsion. The fission requires a slightly adapted description. For example, the fission rate also decreases with increasing non-electrostatic attraction, but this decrease is smaller than for the expulsion rate. We ascribe this difference to a larger change in surface energy for the expulsion compared to fission. For both split events, the total surface increases, but for expulsion this decrease will be larger because the expelled dimer has a large surface to volume ratio. Effectively, more non-electrostatic bonds thus have to be broken for an expulsion events, resulting in a stronger dependence on non-electrostatic attraction.

The different dependencies on non-electrostatic attraction seems to result in a transition from expulsion dominated exchange to fission dominated exchange in our simulations. This transition is better visible if we correct the number of split events for the number of polymers that is involved per split event (Fig. 3.A.16). An insertion/expulsion dominant exchange was expected by Nolles et al.,[24] who studied the exchange of C3Ms loaded with fluorescent proteins. They expected that the dense corona of the C3Ms would prevent their merging. Here we see that at least in the initial micellization stage, micelle fusion can occur. For longer polyelectrolytes with a relatively large non-electrostatic attraction the fusion/fission is even the dominant exchange mechanism. However, the total number of exchange events is low in our simulations of the long polyelectrolytes with larger non-electrostatic attraction in our simulations. More events are needed to confirm that fusion/fission is really the dominant mechanism in these cases. In addition, in this initial micellization stage many small aggregates are present, which fuse more easily than the large micelles that are mainly present in equilibrium.[12,14] Domination of the fission/fusion exchange in the initial micellization period thus does not necessarily mean that this exchange mechanism is also dominant once the micelles have reached equilibrium.

3.3.3 Effect of asymmetric non-electrostatic attraction

Up to now, we have assumed that the non-electrostatic attraction is the same for all charged monomers, but this is usually not the case. The two polyelectrolyte types in the C3M always have a different polymer chemistry, otherwise they cannot be oppositely charged. This different chemistry will result in asymmetric non-electrostatic interactions: the non-electrostatic attraction between the negative polyelectrolytes can be different from the one between the positive polyelectrolytes. In addition, the non-electrostatic attraction between like-charged polyelectrolytes can differ from the non-electrostatic attraction between oppositely charged polyelectrolytes. Recently, it has been suggested that differences in the latter asymmetry might explain how the stability of C3Ms depend on the positive polyelectrolyte block: Marras et al.[34] found that micelles formed from DNA and a poly(ethylene glycole)-poly(lysine) were more stable than the micelles where the poly(lysine) was replaced by the more hydrophobic poly((vinylbenzyl) trimethylammonium). One of their explanations was that poly(lysine) might form hydrogen bonds with the DNA, while poly((vinylbenzyl) trimethylammonium) might mainly have non-electrostatic interaction with itself and not with the DNA. This would mean that non-electrostatic attraction between only the like-charged polyelectrolytes stabilises the C3Ms less than when also the oppositely charged polyelectrolytes non-electrostatically attract each other.

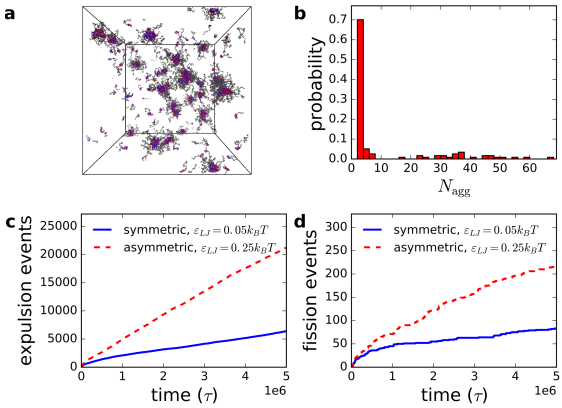

Figure 3.6. The effect of non-electrostatic attraction between only the positive polyelelectrolytes, while the other polyelectrolyte non-electrostatic attraction is purely repulsive. In all cases, $N_{neg} = 20$, $N_{pos} = 20$ and $N_{neu} = 50$. a) Snapshot and b) histogram of the micelle size distribution at the end of the simulation for a non-electrostatic positive polyelectrolyte attraction of $\varepsilon_{LJ} = 0.25k_BT$. c) Cumulative number of expulsion and d) fission events for the same non-electrostatic attraction between all polyelectrolytes of $\varepsilon_{LJ} = 0.05k_BT$ or a non-electrostatic attraction only between the positive polyelectrolytes of $\varepsilon_{LJ} = 0.25k_BT$.

We adapted our simulations to test whether a lower non-electrostatic attraction between the oppositely charged polyelectrolytes indeed results in a lower C3M stability. In addition, we aimed to see how this lower attraction affects the C3M exchange. In the adapted simulation only the positive monomers non-electrostatically attracted only the other positive monomers, while all other non-electrostatic interactions between the charged monomers were purely repulsive.

The C3Ms are largely destabilised when they lack non-electrostatic attraction between the oppositely charged polyelectrolytes and the negative polyelectrolytes (Fig. 3.6). In this asymmetric case, both the dimer population and the exchange rate are larger than for C3Ms with a completely symmetric non-electrostatic attraction of $\varepsilon_{LJ} = 0.05k_BT$, even though the non-electrostatic attraction between the positive polyelectrolytes was relatively large in the asymmetric case ($\varepsilon_{LJ} = 0.25k_BT$). A non-electrostatic attraction between only one of the polyelectrolytes is thus insufficient to stabilise the C3Ms and this might indeed explain why the micelles with the hydrophobic poly((vinylbenzyl) trimethylammonium) were less stable than the micelles with poly(lysine). In addition, this shows that it is insufficient to consider only the properties of the individual polyelectrolytes to design stable C3Ms. Instead, also the polyelectrolyte ability to non-electrostatically interact with the other polyelectrolyte has to be taken into account.

3.3.4 Effect of polyelectrolyte length asymmetry

Above we have described how the extraction of charge neutral complexes of few molecules is the main mechanism of exchange. This is facilitated when both homopolymer and charged block of the diblock are of the same length. When the block lengths are incommensurate, extracting a strictly charge neutral complex is challenging as it requires a much larger number of molecules to exit the micelle simultaneously. We thus explore how the block-length asymmetry can be used as an additional handle to tune the kinetic micelle stability. This information can complement earlier experimental studies that have shown that the length of the homopolymer (or equivalent) affects the static stability of C3Ms.[32,33]

A small change in the polyelectrolyte length ratio largely affects the expulsion rate (Fig. 3.7a-c). The expulsion rate is the largest when both polyelectrolytes have an equal length and largely decreases when the length of only the negative homopolymer is changed to give an polyelectrolyte length ratio that differs from 1. For $N_{\text{neg}}/N_{\text{pos}} = 0.75$ and $N_{\text{neg}}/N_{\text{pos}} = 1.25$, charged complexes split off (Fig. 3.A.17). This introduces an additional free energy penalty compared to the neutral complexes that can be formed for $N_{\text{neg}}/N_{\text{pos}} = 1$. As a result, the expulsion rate has a maximum at equal polyelectrolyte lengths. The maximum is the clearest for a small non-electrostatic attraction. This shows that the net charge of the expelled dimer is most important when no additional non-electrostatic attraction helps to prevent the dimer formation.

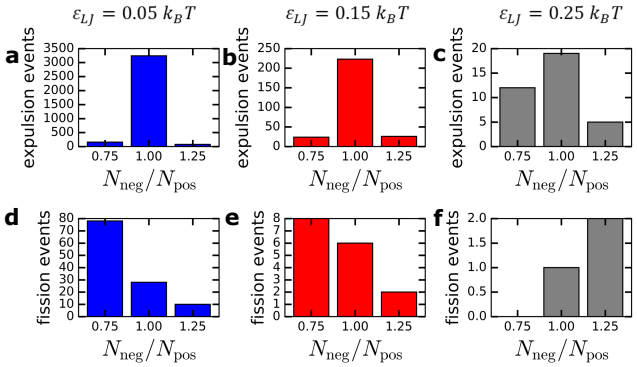

Figure 3.7. The effect of the polyelectrolyte length ratio $N_{\text{neg}}/N_{\text{neg}}$ on the expulsion (a,b,c) and fission (d,e,f) events for a non-electrostatic attraction strength of $\varepsilon_{\text{LJ}} = 0.05k_BT$ (a,d), $\varepsilon_{\text{LJ}} = 0.15k_BT$ (b,e) and $\varepsilon_{\text{LJ}} = 0.25k_BT$ (c,f). The different polyelectrolyte length ratios were obtained by fixing the positive diblock length at $N_{\text{pos}} = 20$ and varying the negative homopolymer length.

The fission is also affected by a change in the negative homopolymer length (Fig. 3.7d-f), but in a different way than the expulsion. The fission rate seem to decrease with increasing negative homopolymer length, instead of having a maximum at $N_{\text{neg}}/N_{\text{pos}} = 1$. Only for $\varepsilon_{\text{LJ}} = 0.25k_BT$ this trend is no longer visible, which is probably due to the low number number of fission events that occurred at this non-electrostatic attraction strength. The decrease in fission rate with increasing negative hompolymer length indicates that for fission the total length of the polyelectrolytes is more important than the length ratio. We can explain this by the fact that we used relatively small variations in this ratio. Therefore, neutral complexes can still be formed when multiple polyelectrolytes are combined together, which happens during fission. For shorter polyelectrolytes, the rearrangement of all the non-covalent bonds of one polyelelectrolyte is easier. As a result, we observe the fastest fission rate for the shortest negative homopolymers. For low non-electrostatic attraction, the increase in fission rate for decreasing the negative polymer length to 15 is not enough to compensate for the simultaneous decrease in expulsion rate. This shows that sometimes a counterintuitive situation can occur where a decrease of the polyelectrolyte length results in a decrease of the micelle exchange.

A small length imbalance already has a large effect on the exchange and this effect becomes even larger when we change the length ratio further to $N_{\text{pos}}/N_{\text{neg}} = 20/150$ (Fig. 3.8). In particular the expulsion rate is largely diminished. For the long homopolymer length of $N_{\text{neg}} = 150$, the expulsion can occur only when a complex with a large net charge is formed. These uncompensated charges are unfavourable and therefore the expulsion events nearly disappear. The penalty for the formation of largely charged complexes is also reflected in the micelle size distribution (Fig. 3.8a,b) where no small complexes can be observed. On the other hand, still many of the micelle sizes that we observe have a net charge (Fig. 3.A.9), since only the aggregation numbers that are a multiple of 17 correspond

to neutrally charged micelles. Also the complexes that split off all had a net charge (Fig. 3.8d). The formation of charged complexes is thus not only governed by the absolute number of charges, but also by the number of polyelectrolytes over which these charges can be distributed. If the charges can be distributed over more polyelectrolytes, the formation seems to be easier. This results in the formation of larger charged complexes and in a larger contribution of fission than of expulsion.

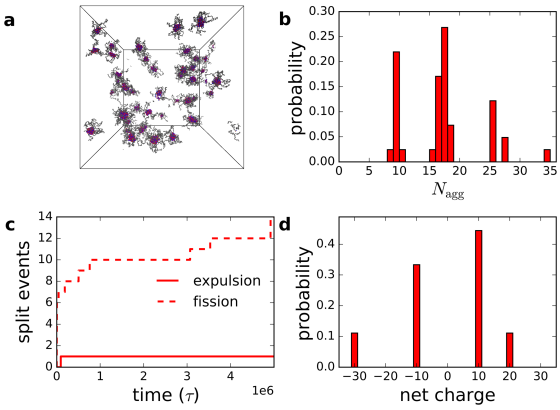

Figure 3.8. Micelle size and exchange characteristics for $N_{pos} = 20$, $N_{neg} = 150$ and $N_{neu} = 50$ and $\varepsilon_{LJ} = 0.15 k_B T$. a) Snapshot and b) histogram of the micelle size distribution at the end of the simulation. c) Cumulative number of expulsion and fission events. d) Histogram of the net charge of the smallest complex formed in a split event.

Finally, we note that the slow expulsion for the long homopolymer length shows that only the exchange times are insufficient to determine the exchange mechanisms. This way of interpretation has for example be used by Holappa et al..[23] They measured the Förster Resonance Energy Transfer (FRET) after mixing C3Ms labelled with an acceptor or a donor fluorophore for polyelectrolyte length ratios of 4.3 and 1.8. They ascribed the fast increase in FRET signal to expulsion/insertion and the slow increase to fusion/fission. However, here we observe that for a long homopolymer the expulsion/insertion is initially slower than the fission/fusion instead of the other way round. Although we expect the fusion to slow down a bit once equilibrium has been reached due to the decrease of the number of small aggregates, we do not know yet whether this decrease is large enough to become slower than the expulsion. To check whether the slowest exchange rate observed in the experiments by Holappa et al. indeed correspond to fission/fusion, additional experiments has to be performed, for example testing how the exchange rate depend on concentration.[14]

3.4 Conclusions

In conlusion, we have directly observed the C3M exchange by using Langevin dynamics simulations and we have shown that the formation of neutral complexes plays an essential role. For polyelectrolytes of equal length, neutral dimers are expelled. Although the electrostatic attraction plays the major role, also the non-electrostatic attraction between the polyelectrolytes can be used to tune the exchange. The dimer exchange can be largely diminished by slightly increasing the non-electrostatic attraction between both polyelectrolytes. Also the fission of the polyelectrolytes can be diminished in this way, but this decrease will be smaller. An increase is non-electrostatic attraction between both polyelectrolytes is thus most effective for insertion/expulsion dominated exchange. It is essential to realize that increasing the non-electrostatic attraction between only one of the two polyelectrolytes is not effective to make the C3Ms more kinetically stable. Rather than solely focusing on the single polyelectrolyte properties, new

studies should thus also pay attention to the interaction between the two polyelectrolytes. Another way to tune the C3M exchange is by changing the length of the polyelectrolytes. The expulsion rate can be easily decreased by using oppositely polyelectrolytes of unequal length, especially by making one of the polyelectrolytes very long. The fission rate can be decreased by increasing the total polyelectrolyte length. These insights into the C3M exchange can be used to develop new C3M encapsulators.

3.A Appendix

3.A.1 Interaction potentials

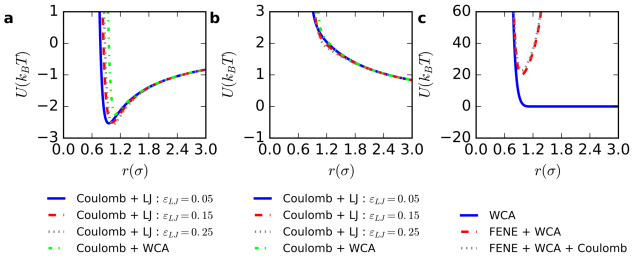

Figure 3.A.1. The interaction potentials used in the Langevin dynamics simulations. a) Coulomb potential for oppositely charged particles combined with a Lennard-Jones (LJ) potential or a Weeks-Chandler-Anders (WCA) potential b) Coulomb potential for equally charged particles combined with a Lennard-Jones (LJ) potential or a Weeks-Chandler-Anders (WCA) potential c) Weeks-Chandler-Anders (WCA) potential, a finitely extensible nonlinear elastic (FENE) potential combined with a WCA potential and a finetly extensible nonlinear elastic (FENE) potential combined with a WCA potential and a Coulomb potential.

3.A.2 C3M formation

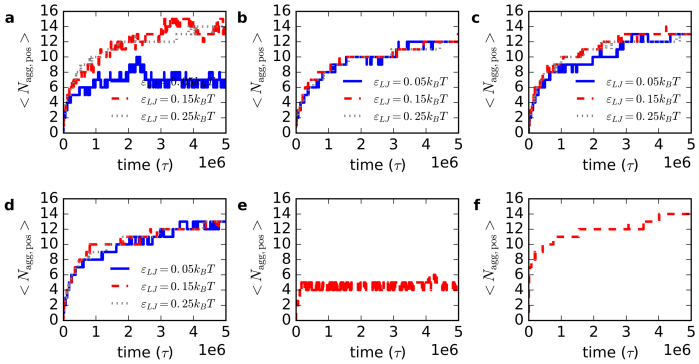

Figure 3.A.2. The increase of the average micelle size, expressed as the average aggregation number of positive blocks per micelle $N_{agg,pos}$ in time for a) $N_{pos} = N_{neg} = 20$ and $N_{neu} = 50$, b) $N_{pos} = N_{neg} = 30$ and $N_{neu} = 75$, c) $N_{pos} = 20$, $N_{neg} = 15$ and $N_{neu} = 50$, d) $N_{pos} = 20$, $N_{neg} = 25$ and $N_{neu} = 50$, e) $N_{pos} = 20$, $N_{neg} = 20$ and $N_{neu} = 50$ and only non-electrostatic attraction between the positive polyelectrolytes and f) $N_{pos} = 20$, $N_{neg} = 150$, $N_{neu} = 50$ and $\varepsilon_{LJ} = 0.15 k_BT$.

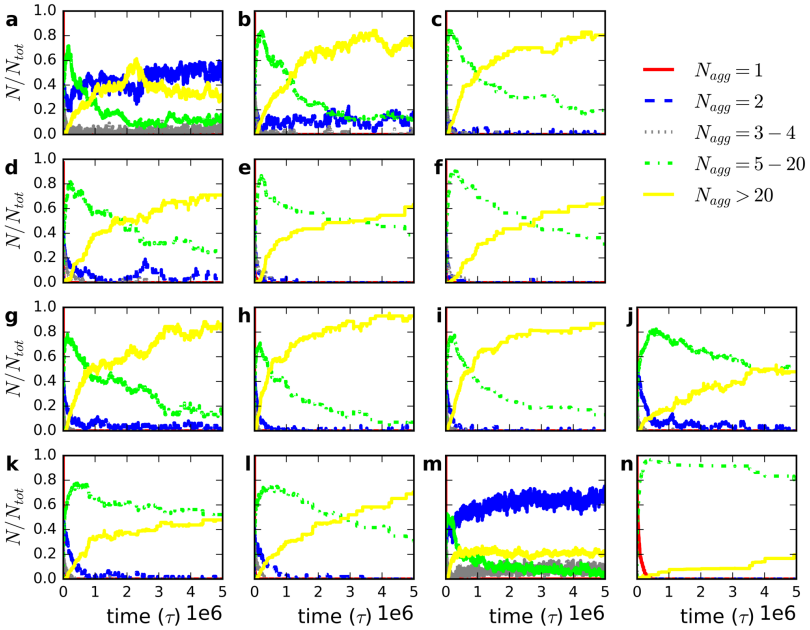

Figure 3.A.3. Time development of the number of clusters N with a certain aggregation number N_{agg} compared to the total number of clusters N_{tot} at this time step for
a,b,c) N_{pos} = 30, N_{neg} = 20 and N_{neu} = 50 and ε_{LJ} = 0.05 (a), ε_{LJ} = 0.15 (b) and ε_{LJ} = 0.25 (c),
d,e,f) N_{pos} = 30, N_{neg} = 30 and N_{neu} = 75 and ε_{LJ} = 0.05 (d), ε_{LJ} = 0.15 (e) and ε_{LJ} = 0.25 (f),
g,h,i) N_{pos} = 20, N_{neg} = 15 and N_{neu} = 50 and ε_{LJ} = 0.05 (g), ε_{LJ} = 0.15 (h) and ε_{LJ} = 0.25 (i),
j,k,l) N_{pos} = 20, N_{neg} = 25 and N_{neu} = 50 and ε_{LJ} = 0.05 (j), ε_{LJ} = 0.15 (k) and ε_{LJ} = 0.25 (l)
m) N_{pos} = 20, N_{neg} = 20 and N_{neu} = 50 and only non-electrostatic attraction between the positive polyelectrolytes and n) N_{pos} = 20, N_{neg} = 150, N_{neu} = 50 and $\varepsilon_{LJ} = 0.15 k_B T$.

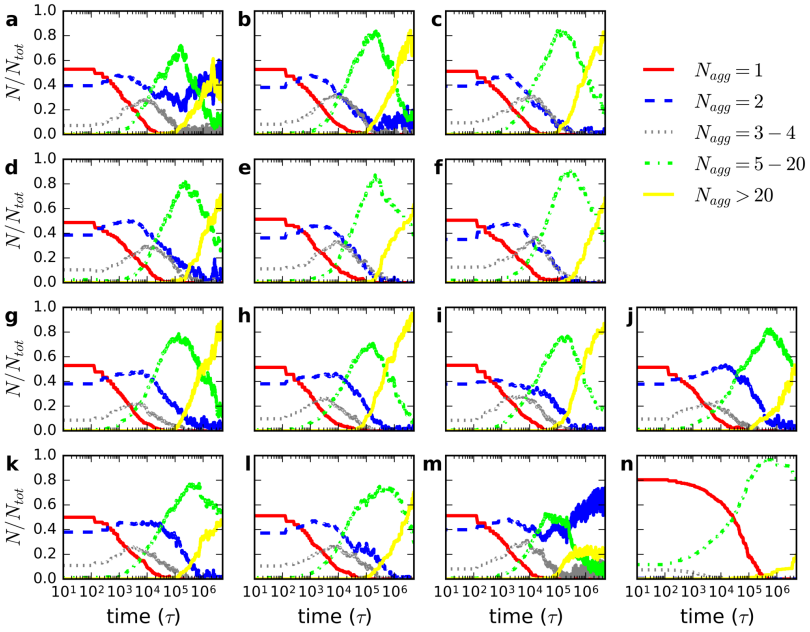

Figure 3.A.4. The same data as in Fig. 3.A.3, but now plotted with a logarithmic time axis: Time development of the number of aggregates N with a certain aggregation number N_{agg} compared to the total number of aggregates N_{tot} at this time step for
a,b,c) N_{pos} = 30, N_{neg} = 20 and N_{neu} = 50 and ε_{LJ} = 0.05 (a), ε_{LJ} = 0.15 (b) and ε_{LJ} = 0.25 (c),
d,e,f) N_{pos} = 30, N_{neg} = 30 and N_{neu} = 75 and ε_{LJ} = 0.05 (d), ε_{LJ} = 0.15 (e) and ε_{LJ} = 0.25 (f),
g,h,i) N_{pos} = 20, N_{neg} = 15 and N_{neu} = 50 and ε_{LJ} = 0.05 (g), ε_{LJ} = 0.15 (h) and ε_{LJ} = 0.25 (i),
j,k,l) N_{pos} = 20, N_{neg} = 25 and N_{neu} = 50 and ε_{LJ} = 0.05 (j), ε_{LJ} = 0.15 (k) and ε_{LJ} = 0.25 (l)
m) N_{pos} = 20, N_{neg} = 20 and N_{neu} = 50 and only non-electrostatic attraction between the positive polyelectrolytes and n) N_{pos} = 20, N_{neg} = 150, N_{neu} = 50 and $\varepsilon_{LJ} = 0.15 k_B T$.

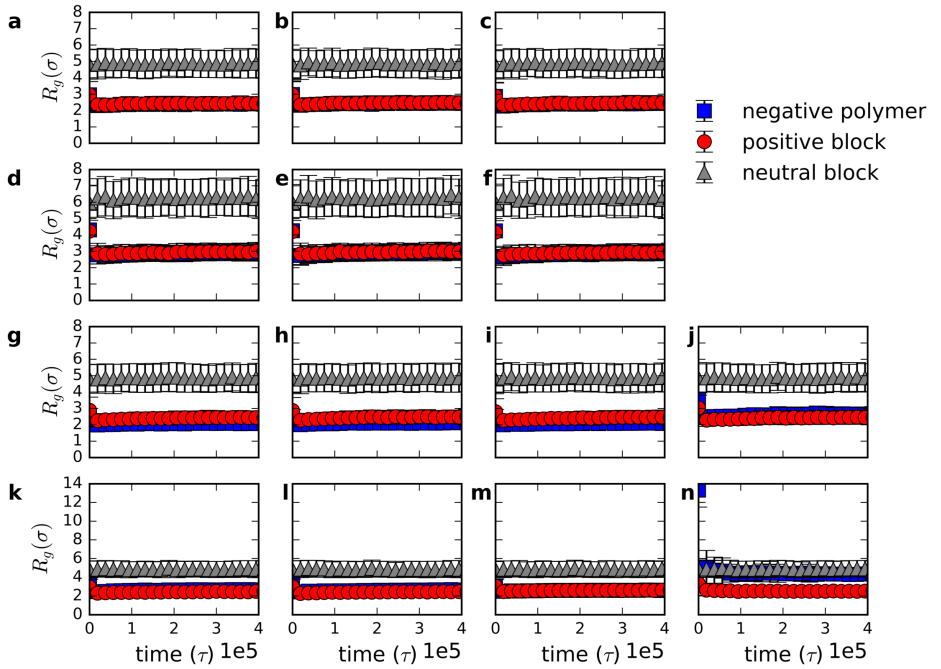

Figure 3.A.5. Early time development of the average radius of gyration R_g of the negative polymers, positive blocks and neutral blocks for
a,b,c) N_{pos} = 30, N_{neg} = 20 and N_{neu} = 50 and ε_{LJ} = 0.05 (a), ε_{LJ} = 0.15 (b) and ε_{LJ} = 0.25 (c),
d,e,f) N_{pos} = 30, N_{neg} = 30 and N_{neu} = 75 and ε_{LJ} = 0.05 (d), ε_{LJ} = 0.15 (e) and ε_{LJ} = 0.25 (f),
g,h,i) N_{pos} = 20, N_{neg} = 15 and N_{neu} = 50 and ε_{LJ} = 0.05 (g), ε_{LJ} = 0.15 (h) and ε_{LJ} = 0.25 (i),
j,k,l) N_{pos} = 20, N_{neg} = 25 and N_{neu} = 50 and ε_{LJ} = 0.05 (j), ε_{LJ} = 0.15 (k) and ε_{LJ} = 0.25 (l)
m) N_{pos} = 20, N_{neg} = 20 and N_{neu} = 50 and only non-electrostatic attraction between the positive polyelectrolytes and n) N_{pos} = 20, N_{neg} = 150, N_{neu} = 50 and $\varepsilon_{LJ} = 0.15 k_B T$.

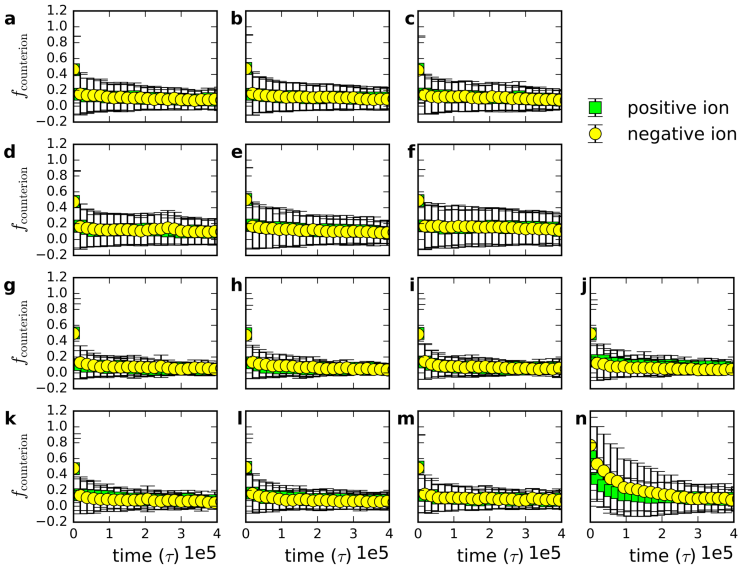

Figure 3.A.6. Early time development of the average fraction of bound counter ions $f_{\text{counter ion}}$. Here the fraction of bound counter ions is calculated by the number of counter ions present within a distance 2.5σ from the oppositely charged monomers of an cluster (single polymer or complex) divided by the total number of oppositely charged monomers in this cluster. Data points are averages over all clusters present at a time step. The data points are obtained from simulations with
a,b,c) $N_{pos} = 30$, $N_{neg} = 20$ and $N_{neu} = 50$ and $\varepsilon_{LJ} = 0.05$ (a), $\varepsilon_{LJ} = 0.15$ (b) and $\varepsilon_{LJ} = 0.25$ (c),
d,e,f) $N_{pos} = 30$, $N_{neg} = 30$ and $N_{neu} = 75$ and $\varepsilon_{LJ} = 0.05$ (d), $\varepsilon_{LJ} = 0.15$ (e) and $\varepsilon_{LJ} = 0.25$ (f),
g,h,i) $N_{pos} = 20$, $N_{neg} = 15$ and $N_{neu} = 50$ and $\varepsilon_{LJ} = 0.05$ (g), $\varepsilon_{LJ} = 0.15$ (h) and $\varepsilon_{LJ} = 0.25$ (i),
j,k,l) $N_{pos} = 20$, $N_{neg} = 25$ and $N_{neu} = 50$ and $\varepsilon_{LJ} = 0.05$ (j), $\varepsilon_{LJ} = 0.15$ (k) and $\varepsilon_{LJ} = 0.25$ (l)
m) $N_{pos} = 20$, $N_{neg} = 20$ and $N_{neu} = 50$ and only non-electrostatic attraction between the positive polyelectrolytes and n) $N_{pos} = 20$, $N_{neg} = 150$, $N_{neu} = 50$ and $\varepsilon_{LJ} = 0.15 k_B T$.

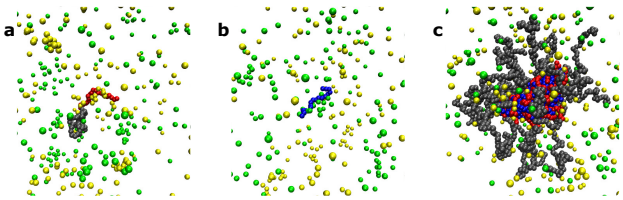

Figure 3.A.7. Example of the ion distribution around a) a diblock, b) a negative polymer and c) a C3M. Images are snapshots from the simulations at 63τ (a,b) and $5 \times 10^6 \tau$ (c). Negative homopolymers are shown in blue, the positive block in red, the neutral block in gray, the positive ions in green and the negative ions in yellow.

3.A.3 C3M configurations

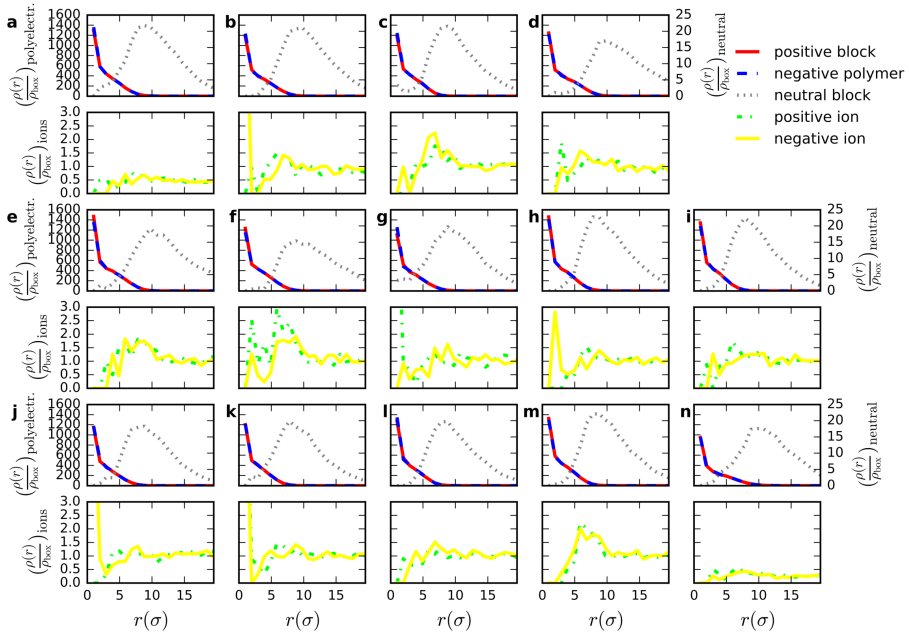

Figure 3.A.8. Normalized density profiles as function of the distance r from the mass centre of the micelle. The density profiles are averaged over all micelles present at the end of the simulation for
a,b,c) $N_{pos} = 30$, $N_{neg} = 20$ and $N_{neu} = 50$ and $\varepsilon_{LJ} = 0.05$ (a), $\varepsilon_{LJ} = 0.15$ (b) and $\varepsilon_{LJ} = 0.25$ (c),
d,e,f) $N_{pos} = 30$, $N_{neg} = 30$ and $N_{neu} = 75$ and $\varepsilon_{LJ} = 0.05$ (d), $\varepsilon_{LJ} = 0.15$ (e) and $\varepsilon_{LJ} = 0.25$ (f),
g,h,i) $N_{pos} = 20$, $N_{neg} = 15$ and $N_{neu} = 50$ and $\varepsilon_{LJ} = 0.05$ (g), $\varepsilon_{LJ} = 0.15$ (h) and $\varepsilon_{LJ} = 0.25$ (i),
j,k,l) $N_{pos} = 20$, $N_{neg} = 25$ and $N_{neu} = 50$ and $\varepsilon_{LJ} = 0.05$ (j), $\varepsilon_{LJ} = 0.15$ (k) and $\varepsilon_{LJ} = 0.25$ (l)
m) $N_{pos} = 20$, $N_{neg} = 20$ and $N_{neu} = 50$ and only non-electrostatic attraction between the positive polyelectrolytes and n) $N_{pos} = 20$, $N_{neg} = 150$, $N_{neu} = 50$ and $\varepsilon_{LJ} = 0.15 k_B T$.

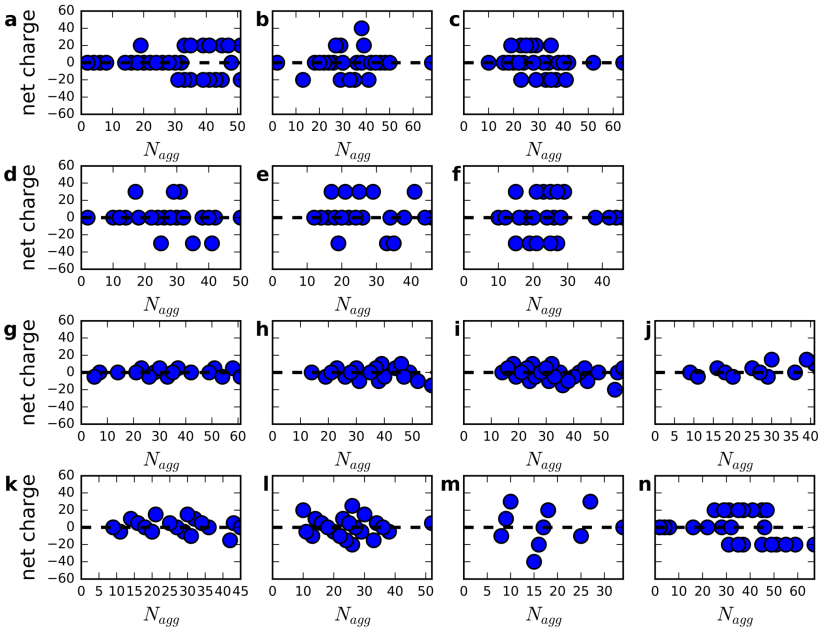

Figure 3.A.9. Net micelle charge versus micelle aggregation number for all micelles present at the end of the simulation for
a,b,c) $N_{pos} = 30$, $N_{neg} = 20$ and $N_{neu} = 50$ and $\varepsilon_{LJ} = 0.05$ (a), $\varepsilon_{LJ} = 0.15$ (b) and $\varepsilon_{LJ} = 0.25$ (c),
d,e,f) $N_{pos} = 30$, $N_{neg} = 30$ and $N_{neu} = 75$ and $\varepsilon_{LJ} = 0.05$ (d), $\varepsilon_{LJ} = 0.15$ (e) and $\varepsilon_{LJ} = 0.25$ (f),
g,h,i) $N_{pos} = 20$, $N_{neg} = 15$ and $N_{neu} = 50$ and $\varepsilon_{LJ} = 0.05$ (g), $\varepsilon_{LJ} = 0.15$ (h) and $\varepsilon_{LJ} = 0.25$ (i),
j,k,l) $N_{pos} = 20$, $N_{neg} = 25$ and $N_{neu} = 50$ and $\varepsilon_{LJ} = 0.05$ (j), $\varepsilon_{LJ} = 0.15$ (k) and $\varepsilon_{LJ} = 0.25$ (l)
m) $N_{pos} = 20$, $N_{neg} = 20$ and $N_{neu} = 50$ and only non-electrostatic attraction between the positive polyelectrolytes and n) $N_{pos} = 20$, $N_{neg} = 150$, $N_{neu} = 50$ and $\varepsilon_{LJ} = 0.15 k_B T$.

3.A.4 No electrostatic attraction

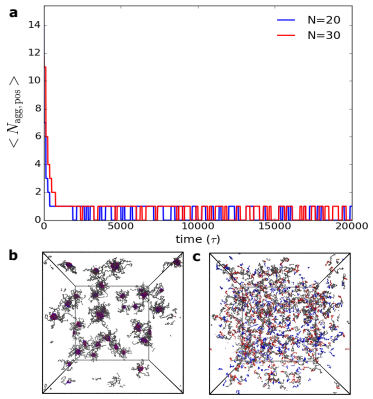

Figure 3.A.10. C3Ms fall apart when the electrostatic attraction is turned off as exemplified here for the end configurations of the simulations with the strongest non-electrostatic attraction used in this study ($\varepsilon_{LJ} = 0.25 k_B T$). a) Average aggregation number as function of time after turning off the electrostatic attraction for $N_{neg} = N_{pos} = 20$ and $N_{neu} = 50$ and for $N_{neg} = N_{pos} = 30$ and $N_{neu} = 75$. b) Configuration before electrostatic attraction is turned off (time = 0τ) for $N_{neg} = N_{pos} = 30$ and $N_{neu} = 75$. c) Configuration after turning off the electrostatic attraction (time = $1.25 \times 10^4 \tau$) for $N_{neg} = N_{pos} = 30$ and $N_{neu} = 75$.

3.A.5 Merge and split events on a logarithmic time axis

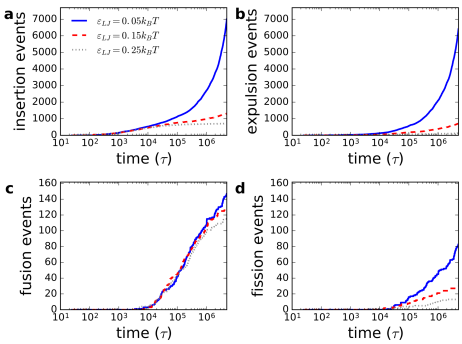

Figure 3.A.11. Cumulative number of insertion (a), expulsion (b), fusion (c) and fission (d) events for a non-electrostatic attraction strength between the polyelectrolytes of $\varepsilon_{LJ} = 0.05 k_B T$, $\varepsilon_{LJ} = 0.15 k_B T$ and $\varepsilon_{LJ} = 0.25 k_B T$. In all cases, $N_{neg} = 20$, $N_{pos} = 20$ and $N_{neu} = 50$.

3.A.6 Mechanisms of C3M growth

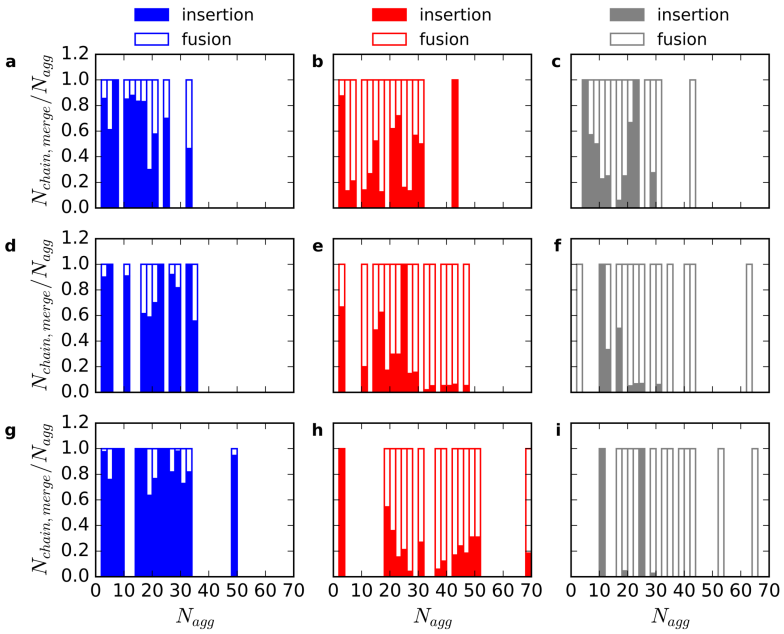

Figure 3.A.12. The fraction of chains coming from insertion and fusion as function of micelle aggregation number at the time points $5 \times 10^5 \tau$ (a,b,c), $2 \times 10^6 \tau$ (d,e,f) and $5 \times 10^6 \tau$ (g,h,i) for $N_{\text{pos}} = 20$, $N_{\text{neg}} = 20$ and $N_{\text{neu}} = 50$ with $\varepsilon_{LJ} = 0.05 k_B T$ (a,d,g), $\varepsilon_{LJ} = 0.15 k_B T$ (b,e,h) and $\varepsilon_{LJ} = 0.25 k_B T$ (c,f,i). The analysis is based on the last merging event that a chain was involved in. A chain is considered to be involved in insertion when it is part of a merging complex with a size smaller than 5. For fusion all chains of both merging complexes are considered to be involved in the fusion.

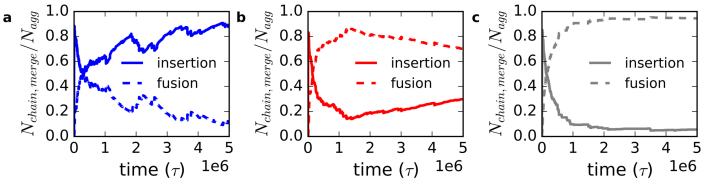

Figure 3.A.13. The fraction of chains coming from insertion and fusion as function of time for $N_{\text{pos}} = 20$, $N_{\text{neg}} = 20$ and $N_{\text{neu}} = 50$ with a) $\varepsilon_{LJ} = 0.05 k_B T$, b) $\varepsilon_{LJ} = 0.15 k_B T$ and c) $\varepsilon_{LJ} = 0.25 k_B T$.

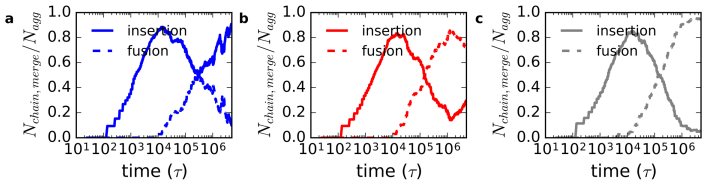

Figure 3.A.14. The same data as in Fig. 3.A.13 but now plotted on a logarithmic time axis: The fraction of chains coming from insertion and fusion as function of time on a logarithmic scale for $N_{\text{pos}} = 20$, $N_{\text{neg}} = 20$ and $N_{\text{neu}} = 50$ with a) $\varepsilon_{LJ} = 0.05 k_B T$, b) $\varepsilon_{LJ} = 0.15 k_B T$ and c) $\varepsilon_{LJ} = 0.25 k_B T$. Note that when the sum of the insertion and fusion fraction is smaller than 1 this means that some of the chains have not been involved in a merging event yet.

3.A.7 Dimer configurations

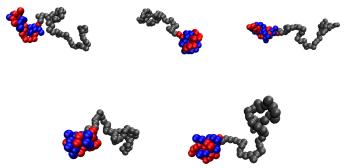

Figure 3.A.15. Examples of free dimer configurations in the last simulation step for $N_{\text{neg}} = 20$, $N_{\text{pos}} = 20$, $N_{\text{neu}} = 50$ and $\varepsilon_{\text{LJ}} = 0.15 k_B T$.

3.A.8 Split events corrected for the number of polymers involved

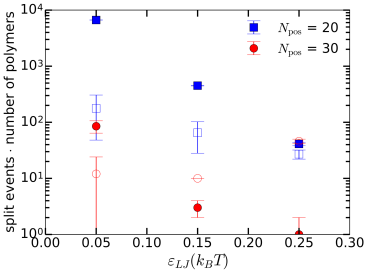

Figure 3.A.16. Number of expulsion events (filled symbols) and fission events (open symbols) corrected for the number of polymers involved per split event in the time range $2 \times 10^6 \tau - 5 \times 10^6 \tau$, for $N_{\text{pos}} = 20$, $N_{\text{neg}} = 20$ and $N_{\text{neu}} = 50$ and for $N_{\text{pos}} = 30$, $N_{\text{neg}} = 30$ and $N_{\text{neu}} = 75$.

3.A.9 Net charge histograms of expelled complexes

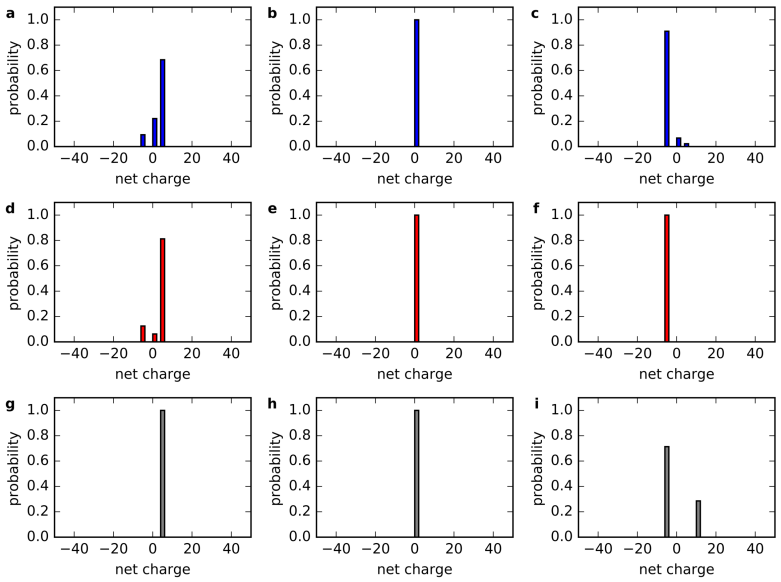

Figure 3.A.17. Histograms of the net charge of the smallest complex formed in a split event for $\varepsilon_{\mathrm{LJ}} = 0.05 k_B T$ (a,b,c), $\varepsilon_{\mathrm{LJ}} = 0.15 k_B T$ (d,e,f) and $\varepsilon_{\mathrm{LJ}} = 0.25 k_B T$ (g,h,i) and for $N_{\mathrm{neg}} = 15$ (a,d,g), $N_{\mathrm{neg}} = 20$ (b,e,h) and $N_{\mathrm{neg}} = 25$. In all cases, $N_{\mathrm{pos}} = 20$ and $N_{\mathrm{neu}} = 50$.

References

[1] Voets, I. K.; de Keizer, A.; Cohen Stuart, M. A. Complex coacervate core micelles. *Adv. Colloid Interface Sci.* **2009**, *147*, 300–318.

[2] Kakizawa, Y.; Kataoka, K. Block copolymer micelles for delivery of gene and related compounds. *Adv. Drug Deliv. Rev.* **2002**, *54*, 203–222.

[3] Harada, A.; Kataoka, K. Supramolecular assemblies of block copolymers in aqueous media as nanocontainers relevant to biological applications. *Prog. Polym. Sci.* **2006**, *31*, 949–982.

[4] Kuo, C.-H.; Leon, L.; Chung, E. J.; Huang, R.-T.; Sontag, T. J.; Reardon, C. A.; Getz, G. S.; Tirrell, M.; Fang, Y. Inhibition of atherosclerosis-promoting microRNAs via targeted polyelectrolyte complex micelles. *J. Mater. Chem. B* **2014**, *2*, 8142–8153.

[5] Berret, J.-F.; Cristobal, G.; Hervé, P.; Oberdisse, J.; Grillo, I. Structure of colloidal complexes obtained from neutral/poly-electrolyte copolymers and oppositely charged surfactants. *Eur. Phys. J. E: Soft Matter Biol. Phys.* **2002**, *9*, 301–311.

[6] Wu, H.; Ting, J. M.; Werba, O.; Meng, S.; Tirrell, M. V. Non-equilibrium phenomena and kinetic pathways in self-assembled polyelectrolyte complexes. *J. Chem. Phys.* **2018**, *149*, 163330.

[7] Hofs, B.; De Keizer, A.; Cohen Stuart, M. On the stability of (highly aggregated) polyelectrolyte complexes containing a charged-block-neutral diblock copolymer. *J. Phys. Chem. B* **2007**, *111*, 5621–5627.

[8] Lindhoud, S.; Norde, W.; Cohen Stuart, M. A. Reversibility and relaxation behavior of polyelectrolyte complex micelle formation. *J. Phys. Chem. B* **2009**, *113*, 5431–5439.

[9] Denkova, A. G.; Mendes, E.; Coppens, M.-O. Non-equilibrium dynamics of block copolymer micelles in solution: recent insights and open questions. *Soft Matter* **2010**, *6*, 2351–2357.

[10] Lund, R.; Willner, L.; Stellbrink, J.; Lindner, P.; Richter, D. Logarithmic chain-exchange kinetics of diblock copolymer micelles. *Phys. Rev. Lett.* **2006**, *96*, 068302.

[11] Dormidontova, E. E. Micellization kinetics in block copolymer solutions: Scaling model. *Macromolecules* **1999**, *32*, 7630–7644.

[12] Li, Z.; Dormidontova, E. E. Kinetics of diblock copolymer micellization by dissipative particle dynamics. *Macromolecules* **2010**, *43*, 3521–3531.

[13] Choi, S.-H.; Lodge, T. P.; Bates, F. S. Mechanism of molecular exchange in diblock copolymer micelles: hypersensitivity to core chain length. *Phys. Rev. Lett.* **2010**, *104*, 047802.

[14] Li, Z.; Dormidontova, E. E. Equilibrium chain exchange kinetics in block copolymer micelle solutions by dissipative particle dynamics simulations. *Soft Matter* **2011**, *7*, 4179–4188.

[15] Sheng, Y.-J.; Wang, T.-Y.; Chen, W. M.; Tsao, H.-K. A- B diblock copolymer micelles: Effects of soluble-block length and component compatibility. *J. Phys. Chem. B* **2007**, *111*, 10938–10945.

[16] Prhashanna, A.; Khan, S. A.; Chen, S. B. Kinetics of chain exchange between diblock copolymer micelles. *Macromol. Theory Simul.* **2016**, *25*, 383–391.

[17] Wang, E.; Lu, J.; Bates, F. S.; Lodge, T. P. Effect of Corona Block Length on the Structure and Chain Exchange Kinetics of Block Copolymer Micelles. *Macromolecules* **2018**, *51*, 3563–3571.

[18] Lund, R.; Willner, L.; Richter, D.; Dormidontova, E. E. Equilibrium chain exchange kinetics of diblock copolymer micelles: Tuning and logarithmic relaxation. *Macromolecules* **2006**, *39*, 4566–4575.

[19] Spruijt, E.; Sprakel, J.; Lemmers, M.; Cohen Stuart, M. A.; Van Der Gucht, J. Relaxation dynamics at different time scales in electrostatic complexes: time-salt superposition. *Phys. Rev. Lett.* **2010**, *105*, 208301.

[20] Spruijt, E.; Sprakel, J.; Cohen Stuart, M. A.; van der Gucht, J. Interfacial tension between a complex coacervate phase and its coexisting aqueous phase. *Soft Matter* **2010**, *6*, 172–178.

[21] Spruijt, E.; van den Berg, S. A.; Cohen Stuart, M. A.; van der Gucht, J. Direct measurement of the strength of single ionic bonds between hydrated charges. *ACS Nano* **2012**, *6*, 5297–5303.

[22] Hofs, B.; Voets, I. K.; de Keizer, A.; Cohen Stuart, M. A. Comparison of complex coacervate core micelles from two diblock copolymers or a single diblock copolymer with a polyelectrolyte. *Phys. Chem. Chem. Phys.* **2006**, *8*, 4242–4251.

[23] Holappa, S.; Kantonen, L.; Andersson, T.; Winnik, F.; Tenhu, H. Overcharging of polyelectrolyte complexes by the guest polyelectrolyte studied by fluorescence spectroscopy. *Langmuir* **2005**, *21*, 11431–11438.

[24] Nolles, A.; Hooiveld, E.; Westphal, A. H.; van Berkel, W. J.; Kleijn, J. M.; Borst, J. W. FRET Reveals the Formation and Exchange Dynamics of Protein-Containing Complex Coacervate Core Micelles. *Langmuir* **2018**, *34*, 12083–12092.

[25] Li, L.; Srivastava, S.; Andreev, M.; Marciel, A. B.; de Pablo, J. J.; Tirrell, M. V. Phase behavior and salt partitioning in polyelectrolyte complex coacervates. *Macromolecules* **2018**, *51*, 2988–2995.

[26] Ou, Z.; Muthukumar, M. Entropy and enthalpy of polyelectrolyte complexation: Langevin dynamics simulations. *J. Chem. Phys.* **2006**, *124*, 154902.

[27] Ziebarth, J.; Wang, Y. Coarse-grained molecular dynamics simulations of DNA condensation by block copolymer and formation of core- corona structures. *J. Phys. Chem. B* **2010**, *114*, 6225–6232.

[28] Šindelka, K.; Limpouchová, Z.; Lísal, M.; Procházka, K. Dissipative particle dynamics study of electrostatic self-assembly in aqueous mixtures of copolymers containing one neutral water-soluble block and one either positively or negatively charged polyelectrolyte block. *Macromolecules* **2014**, *47*, 6121–6134.

[29] Šindelka, K.; Limpouchová, Z.; Lísal, M.; Procházka, K. The electrostatic co-assembly in non-stoichiometric aqueous mixtures of copolymers composed of one neutral water-soluble and one polyelectrolyte (either positively or negatively charged) block: a dissipative particle dynamics study. *Phys. Chem. Chem. Phys.* **2016**, *18*, 16137–16151.

[30] Šindelka, K.; Limpouchová, Z.; Procházka, K. Computer study of the solubilization of polymer chains in polyelectrolyte complex cores of polymeric nanoparticles in aqueous media. *Phys. Chem. Chem. Phys.* **2018**, *20*, 29876–29888.

[31] Voets, I. K.; De Keizer, A.; Cohen Stuart, M. A.; Justynska, J.; Schlaad, H. Irreversible structural transitions in mixed micelles of oppositely charged diblock copolymers in aqueous solution. *Macromolecules* **2007**, *40*, 2158–2164.

[32] van der Kooij, H. M.; Spruijt, E.; Voets, I. K.; Fokkink, R.; Cohen Stuart, M. A.; van der Gucht, J. On the stability and morphology of complex coacervate core micelles: From spherical to wormlike micelles. *Langmuir* **2012**, *28*, 14180–14191.

[33] Wang, J.; Voets, I. K.; Fokkink, R.; van der Gucht, J.; Velders, A. H. Controlling the number of dendrimers in dendrimicelle nanoconjugates from 1 to more than 100. *Soft Matter* **2014**, *10*, 7337–7345.

[34] Marras, A.; Vieregg, J.; Ting, J.; Rubien, J.; Tirrell, M. Polyelectrolyte Complexation of Oligonucleotides by Charged Hydrophobic–Neutral Hydrophilic Block Copolymers. *Polymers* **2019**, *11*, 83.

[35] van der Burgh, S.; de Keizer, A.; Cohen Stuart, M. A. Complex coacervation core micelles. Colloidal stability and aggregation mechanism. *Langmuir* **2004**, *20*, 1073–1084.

[36] Anderson, J. A.; Lorenz, C. D.; Travesset, A. General purpose molecular dynamics simulations fully implemented on graphics processing units. *J. Comput. Phys.* **2008**, *227*, 5342–5359.

[37] Glaser, J.; Nguyen, T. D.; Anderson, J. A.; Lui, P.; Spiga, F.; Millan, J. A.; Morse, D. C.; Glotzer, S. C. Strong scaling of general-purpose molecular dynamics simulations on GPUs. *Comput. Phys. Commun.* **2015**, *192*, 97–107.

[38] LeBard, D. N.; Levine, B. G.; Mertmann, P.; Barr, S. A.; Jusufi, A.; Sanders, S.; Klein, M. L.; Panagiotopoulos, A. Z. Self-assembly of coarse-grained ionic surfactants accelerated by graphics processing units. *Soft Matter* **2012**, *8*, 2385–2397.

[39] Howard, M. P.; Anderson, J. A.; Nikoubashman, A.; Glotzer, S. C.; Panagiotopoulos, A. Z. Efficient neighbor list calculation for molecular simulation of colloidal systems using graphics processing units. *Comput. Phys. Commun.* **2016**, *203*, 45–52.

[40] Humphrey, W.; Dalke, A.; Schulten, K. VMD – Visual Molecular Dynamics. *J. Mol. Graph.* **1996**, *14*, 33–38.

[41] Pedregosa, F. et al. Scikit-learn: Machine learning in Python. *J. Mach. Learn. Res.* **2011**, *12*, 2825–2830.

[42] Yan, Y.; de Keizer, A.; Cohen Stuart, M. A.; Drechsler, M.; Besseling, N. A. Stability of complex coacervate core micelles containing metal coordination polymer. *J. Phys. Chem. B* **2008**, *112*, 10908–10914.

[43] Lund, R.; Willner, L.; Monkenbusch, M.; Panine, P.; Narayanan, T.; Colmenero, J.; Richter, D. Structural observation and kinetic pathway in the formation of polymeric micelles. *Phys. Rev. Lett.* **2009**, *102*, 188301.

[44] Fu, J.; Schlenoff, J. B. Driving forces for oppositely charged polyion association in aqueous solutions: enthalpic, entropic, but not electrostatic. *J. Am. Chem. Soc.* **2016**, *138*, 980–990.

[45] Van der Gucht, J.; Spruijt, E.; Lemmers, M.; Cohen Stuart, M. A. Polyelectrolyte complexes: bulk phases and colloidal systems. *J. Colloid Interface Sci.* **2011**, *361*, 407–422.

[46] Fu, J.; Fares, H. M.; Schlenoff, J. B. Ion-pairing strength in polyelectrolyte complexes. *Macromolecules* **2017**, *50*, 1066–1074.

[47] Ting, J. M.; Wu, H.; Herzog-Arbeitman, A.; Srivastava, S.; Tirrell, M. V. Synthesis and assembly of designer styrenic diblock polyelectrolytes. *ACS Macro Lett.* **2018**, *7*, 726–733.

[48] Grest, G. S.; Murat, M. Structure of grafted polymeric brushes in solvents of varying quality: a molecular dynamics study. *Macromolecules* **1993**, *26*, 3108–3117.

[49] Rumyantsev, A. M.; Potemkin, I. I. Explicit description of complexation between oppositely charged polyelectrolytes as an advantage of the random phase approximation over the scaling approach. *Phys. Chem. Chem. Phys.* **2017**, *19*, 27580–27592.

[50] Delaney, K. T.; Fredrickson, G. H. Theory of polyelectrolyte complexation – Complex coacervates are self-coacervates. *J. Chem. Phys.* **2017**, *146*, 224902.

Chapter 4

FRET-based determination of the exchange dynamics of complex coacervate core micelles

Complex coacervate core micelles (C3Ms) are nanoscopic structures formed by charge interactions between oppositely charged macro-ions, and used to encapsulate a wide variety of charged (bio)molecules. In most cases, C3Ms are in a dynamic equilibrium with their surroundings. Understanding the dynamics of molecular exchange reactions is essential as this determines the rate at which their cargo is exposed to the environment. Here we study the molecular exchange in C3Ms by making use of Förster resonance energy transfer (FRET) and we derive an analytical model to relate the experimentally-observed increase in FRET efficiency to the underlying macromolecular exchange rates. We show that equilibrated C3Ms have a broad distribution of exchange rates. The overall exchange rate can be strongly increased by increasing the salt concentration. In contrast, changing the unlabelled homopolymer length does not affect the exchange of the labelled homopolymers and an increase in micelle concentration only affects the FRET increase rate at low micelle concentrations. Together these results suggest that the exchange of these equilibrated C3Ms occurs mainly by expulsion and insertion where the rate limiting step is the breaking of ionic bonds to expel the chains from the core. These are important insights to further improve the encapulsation efficiency of C3Ms.

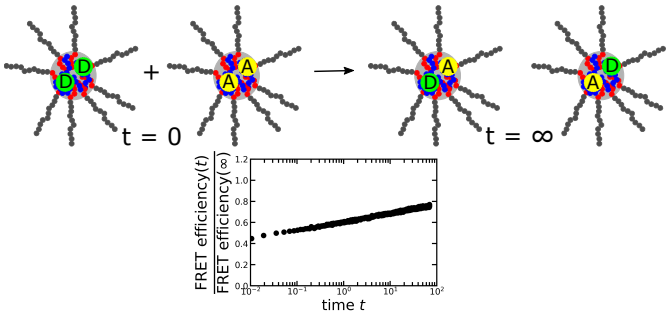

This chapter is based on: Inge Bos, Marga Timmerman and Joris Sprakel. FRET-Based Determination of the Exchange Dynamics of Complex Coacervate Core Micelles. *Macromolecules* **2021** *54*(1), 398–411.

4.1 Introduction

Complex coacervate core micelles (C3Ms) are used as encapsulators for a wide variety of (bio)molecules.[1,2] The formation of these C3Ms is based on associative liquid-liquid phase separation of oppositely charged polyelectrolytes from the water phase. Macroscopic phase separation is prevented by a neutral, hydrophilic block that is attached to at least one of the two polyelectrolytes. These neutral blocks form the corona of the micelle, while the polyelectrolytes form the micelle core. The hydrophilic environment of the core allows for incorporation of charged or hydrophilic compounds which can subsequently be protected against external compounds by the micelle corona. Since the core formation relies on electrostatic attraction, the C3Ms can respond to changes in salt concentration and in some cases also to changes in *p*H. Their protecting corona and ability to respond to external triggers make the C3Ms promising drug and gene delivery tools.[3,4]

Up to now, studies on C3Ms have mainly focused on their average static properties at varying environmental conditions like different ionic strengths and different *p*H-values. However, these average static properties do not reveal the underlying molecular exchange of the C3Ms. Even when the C3Ms are completely equilibrated and the average static properties do not change in time, the C3Ms are still a dynamic system where molecular exchange can occur continuously. Only a few studies have focused on this C3M exchange dynamics,[5–8] among which our simulations of the C3M exchange during the initial micellisation in Chapter 3, and provided some indications for the C3M exchange mechanisms and the corresponding governing parameters. Yet, to date, the exact C3M exchange mechanisms are still unresolved while their exchange dynamics can largely determine their encapsulation efficiency. After all, the exchange dynamics determines the rate at which the cargo is exposed to the surroundings and thus the level of protection that the C3M gives. Furthermore, in some cases the final structure of the C3Ms is governed by their preparation pathways, as we observed in Chapter 2 and which was also observed in other studies.[9–12] This demonstrates that kinetic effects can determine the C3M properties and thus their encapsulation efficiency.

To interpret C3M exchange experiments, the exchange mechanisms are usually divided in two main groups. The first one is the expulsion of one polymer or a small cluster of polymers followed by insertion into another micelle. In the second case, the micelle splits into two parts of both substantial size which can subsequently merge again with other micelles. This type of exchange is called fission and fusion and differs from the expulsion and insertion exchange in that all formed clusters still have a substantial micelle corona. Therefore, for fission and fusion the merging of the micelles is considered to be the rate-limiting step as this requires substantial restructuring of the micelle corona polymers, while for the expulsion and insertion case, the expulsion from the core is considered to be rate-limiting.

During the initial micellisation of C3Ms both exchange mechanisms might occur as we have shown in Chapter 3 by using Langevin dynamics simulations. We observed that for oppositely charged polyelectrolytes with matched lengths and weak non-electrostatic attraction the expulsion/insertion exchange is strongly favoured, while for unmatched chain lengths and stronger non-electrostatic interactions the fission/fusion mechanism might become more important. A recent small angle X-ray scattering (SAXS) study showed that after the very fast initial micellisation, a slower rearrangement of the micelles can occur.[7] This rearrangement was concentration independent, suggesting that the exchange during these rearrangements occurs mainly by expulsion/insertion.

The exchange mechanisms during initial C3M formation and rearrangement might deviate from the exchange of equilibrated C3Ms due to the differences in micelle size during the different stages.[13] Therefore, it is important to determine exchange dynamics of equilibrated micelles as well. Both SAXS and dynamics simulations cannot be used to study the exchange in this equilibrated state due to the absence of structural rearrangements and the relatively long equilibration times respectively. For amphiphilic diblock copolymer micelles, time-resolved small angle neutron scattering (TR-SANS) measurements have been used to follow the exchange of equilibrated micelles.[14–20] However, this

requires the synthesis of deuterated polymers and the use of advanced and not broadly available equipment. A more accessible way to follow the exchange dynamics of equilibrated micelles is to make use of Förster resonance energy transfer (FRET), which is non-radiative energy transfer from an excited donor fluorophore to a nearby acceptor fluorophore. In these experiments (Fig. 4.1a), micelles with donor fluorophores in their core are mixed with micelles with acceptor fluorophores in their core. When the micelles exchange, the donor and acceptor can become part of the same micelle core, which means that they are close enough to each other for FRET to occur. The increase in FRET efficiency over time is thus a measure for the micelle exchange rate.

This FRET approach has already been used to follow the exchange dynamics of C3Ms at different charge stoichiometry ratios[5] and to follow the formation and exchange dynamics of protein containing C3Ms.[6] Both studies took the increase in FRET efficiency normalised to the final FRET efficiency as a direct measure for the micelle exchange rate and neglected any other factors that affected the normalised FRET increase. This approach suffices to give a general idea of the exchange time scales and showed that the protein containing C3Ms exchanged much faster than the C3Ms composed of only polymers. However, to further elucidate the exchange mechanisms, more quantitative comparisons of the exchange rates are essential and in that case these other factors cannot be neglected. In fact, the FRET efficiency does not increase linearly with increasing exchanged chain fraction and also depends on parameters like the micelle core size and the acceptor and donor fluorophore properties. A more advanced description is thus needed to relate the observed normalised FRET increase to the underlying micelle exchange rates.

In this chapter, we aim to use FRET for a quantitative measure of the molecular exchange dynamics of C3Ms. We first derive an analytical model that describes the FRET increase for a given exchange rate taking into account the dependence of FRET on the micelle core size, the non-linear increase in FRET efficiency with increasing acceptor number and the variations in the number of fluorophores per micelle. In this way, we show that fitting the normalised FRET increase with a simple exponential function results in an overestimation of the micelle exchange rate. In addition, we show that in some cases the observed increase in normalised FRET efficiency does not only depend of the exchange rate but also of the initial number of fluorophores per micelle, micelle core and fluorophore size, Förster radius and micelle mixing ratio. Therefore, in the subsequent experiments, we pay special attention to characterising the fluorescence properties of the equilibrated micelles. We show that the C3M exchange can take place over a broad range of time scales. The overall exchange rate can be strongly increased by increasing the ionic strength while changing the length of the unlabelled homopolymer has little effect on the exchange of the labelled homopolymer. These observations suggest that the splitting off of one or a few polymers is the rate-limiting step for the exchange of these C3Ms. Together these results help to better understand the C3M exchange both by identifying additional important exchange parameters and by facilitating better comparison of future FRET-based C3M exchange studies.

4.2 Materials and Methods

4.2.1 Materials

The RAFT chain transfer agent 4-cyano-4-(phenylcarbonothioylthio)pentanoic acid (CTA), the coupling agents *N*-Ethyl-*N'*-(3-dimethylaminopropyl)carbodiimide hydrochloride (EDC.HCl) and 1-hydroxybenzotriazole hydrate (HOBt), the macroRAFT chain transfer agent poly(ethylene glycol) 4-cyano-4-phenylcarbonothioylthio)pentanoate M_n = 10000 g/mol (PEG-CTA), the negative monomer 3-sulfoproyl methacrylate potassium salt (KSPMA), the positive monomer 2-trimethylammonioethyl methacrylate chloride (TMAEMA) in 80 wt% aqueous solution and the radical initiator 4,4'-Azobis(4-cyanovaleric acid) (ACVA) were all purchased from Sigma Aldrich. The radical initiator 2,2'-Azobis[2-(2-imidazolin-2-yl)propane]dihydrochloride (VA-044) was purchased from WAKO chemicals. The

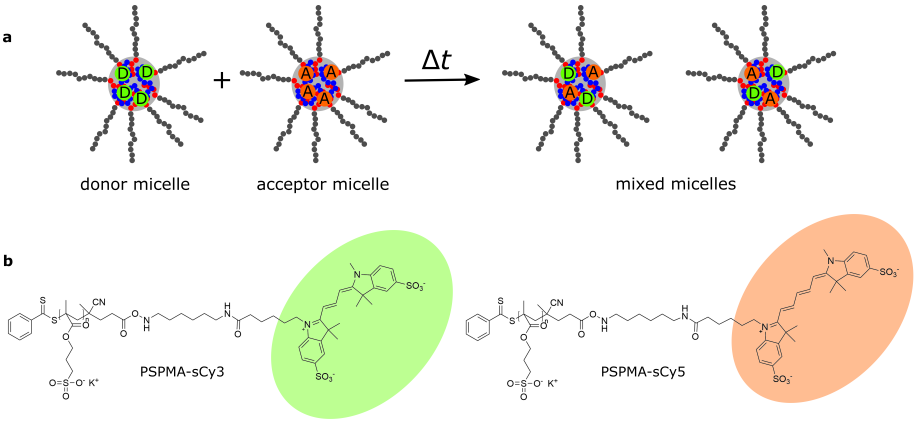

Figure 4.1. Overview of the C3M exchange experiments. (a) Schematic representation of the FRET-based micelle exchange experiment. (b) Chemical structures of the fluorescently labelled donor polymer (PSPMA-sCy3) and acceptor polymer (PSPMA-sCy5).

donor and acceptor dyes with amine linker, sulfo-cyanine3 amine and sulfo-cyanine5 amine, were purchased from Lumiprobe. The aprotic base *N,N*-Diisopropylethylamine (DIPEA) was purchased from TCI and potassium chloride (KCl) was purchased from VWR. Dimethylformamide (DMF), acetone and methanol were purchased from Biosolve. The TMAEMA monomer was run over an alumina column to remove the inhibitor. All other materials were used as received.

4.2.2 Fluorescently labelled RAFT agent synthesis

The sulfo-cyanine3 amine dye was coupled to the carboxyl group of the RAFT chain transfer agent by using EDC/HOBt coupling: sulfo-cyanine3 amine (25 mg, 35 µmol) was dissolved in 3.2 mL DMF and the CTA (15 mg, 54 µmol), EDC.HCl (13 mg, 68 µmol), HOBt (9 mg, 68 µmol) and DIPEA (12 µL, 68 µmol) were added. After 16 h of stirring at room temperature, the crude product was concentrated by rotary evaporation and purified by column chromatography on a silica gel with a mobile phase of acetone/methanol (3/1, v/v). The purified product sulfoCy3-CTA was concentrated by rotary evaporation and dried under vacuum at 40 °C (yield: 24 mg, 73 %). Functionalisation of the RAFT agent was checked by ^{1}H NMR (Fig. 4.A.1). To synthesize the sulfoCy5-CTA the same protocol was used, only the sulfo-cyanine3 amine was replaced by sulfo-cyanine5 amine (yield: 20 mg, 63 %).

4.2.3 Synthesis of the PSPMA homopolymers

For the synthesis of the negatively charged poly(3-sulfopropyl methacrylate) (PSPMA) homopolymer with the sulfo-cyanine3 dye attached to its end (Fig. 4.1b), the sulfoCy3-CTA (24 mg, 25 µmol) was dissolved in 16 mL miliQ. Subsequently, KSPMA (0.73 g, 3.0 mmol) and ACVA (1.3 mg, 5 µmol) were added. The reaction mixture was degassed with N_2 for 30 minutes and then reacted at 70 °C for 16 h. Subsequently, the reaction mixture was dialysed against miliQ and freeze dried to yield the fluorescent PSPMA-sCy3 polymer (0.51 g, 50%).

For the synthesis of the PSPMA-sCy5 polymer, the sulfoCy5-CTA (20 mg, 20 µmol) was dissolved in 16 mL of a miliQ/DMF (3/1, v/v) mixture. Subsequently, KSPMA (0.59 g, 2.4 mmol) and ACVA (1.1 mg, 4 µmol) were added. The reaction mixture was degassed with N_2 for 30 minutes and then

reacted at 70 °C for 16 h. Subsequently, the reaction mixture was dialysed against miliQ and freeze dried to yield the fluorescent PSPMA-sCy5 polymer (0.44 g, 72%).

The synthesis of the unlabelled PSPMA homopolymers is described in Chapter 2.

The number-average molecular weights (M_n) and weight-average molecular weights (M_w) of the PSPMA polymers were determined using an Agilent aqueous GPC equipped with a refractive index detector and using PL aquagel Mixed-M as the column. $NaNO_3$ (0.2 M)–NaH_2PO_4 (0.01 M) buffer solution (pH = 7.0) with NaN_3 (0.2 wt %) was used as the eluent at a flow rate of 0.6 mL min^{-1} at 30 °C. The column was calibrated using polymethacrylic acid standards. The number average molecular weights are 2.7×10^4 g mol^{-1}, 1.7×10^4 g mol^{-1}, 1.3×10^4 g mol^{-1} and 2.8×10^4 g mol^{-1} for the PSPMA-sCy3, PSPMA-sCy5, unlabelled $PSPMA_{51}$ and unlabelled $PSPMA_{132}$ respectively. The corresponding weight average molecular weights are 4.6×10^4 g mol^{-1}, 2.8×10^4 g mol^{-1}, 1.6×10^4 g mol^{-1} and 5.1×10^4 g mol^{-1}.

4.2.4 Synthesis of the PEG-*b*-PTMAEMA diblock

To synthesise the PEG-*b*-PTMAEMA diblock, the PEG-CTA (0.3 g, 30 µmol), the TMAMEA monomer (0.50 g, 2.4 mmol) and the VA-044 radical initiator (1.9 mg, 6 µmol) were dissolved in miliQ to give a final volume of 10 mL. The reaction mixture was degassed with N_2 for 30 minutes and then reacted at 44 °C for 16 h. Subsequently, the reaction mixture was dialysed against miliQ and freeze dried to yield the PEG-*b*-PTMAEMA diblock (0.65 g, 81%). Based on the ^{1}H NMR spectrum, the average degree of polymerisation of the PTMAEMA block was estimated to be 75 (Fig. 4.A.2).

4.2.5 Micelle preparation

To prepare the micelles, stock solutions of 10 mM KCl and 2 M KCl, stock solutions of the negatively charged homopolymers PSPMA-sCy3, PSPMA-sCy5, $PSPMA_{51}$ and/or $PSPMA_{132}$ and a stock solution of the positively charged diblock copolymer PEG-*b*-PTMAEMA were mixed in this order to give the micelle sample with the desired monomer and KCl concentrations. In all cases, the micelles were prepared at equal charge stoichiometry (SPMA:TMAEMA = 1:1). Unless otherwise indicated, the final KCl concentration was 100 mM and the final SPMA monomer concentration was 1 mM with 20% of these SPMA monomers being part of fluorescently labelled PSPMA (PSPMA-sCY3 and/or PSPMAsCy5) and the remaining 80% being part of the unlabelled $PSPMA_{132}$. The micelles were allowed to equilibrate for at least 24 h before they were used for fluorescence or light scattering measurements.

4.2.6 Light scattering measurements

Static light scattering measurements were performed on an ALV instrument equipped with a 660 nm laser over a detection angle range from to 30° to 120° in intervals of 2°. At every detection angle, 5 runs of 30 s were performed. The Rayleigh ratio R at each detection angle θ was calculated by:

$$R(\theta) = \frac{I_{\text{sample}}(\theta) - I_0(\theta)}{I_{\text{ref}}(\theta)} R_{\text{ref}} \left(\frac{n_0}{n_{\text{ref}}} \right)^2 \tag{4.1}$$

Here $I_{\text{sample}}(\theta)$, $I_0(\theta)$ and $I_{\text{ref}}(\theta)$ are the sample, solvent and reference scattering intensities respectively, n_0 and n_{ref} are the refractive index of the solvent and reference respectively and R_{ref} is the Rayleigh ratio of the reference. The refractive index of the solvent is $n_0 = 1.3332$. We have used toluene as reference with $n_{\text{ref}} = 1.496$ and $R_{\text{ref}} = 8.56 \times 10^{-4}$ m^{-1}.[21] To estimate the micelle molar mass from the measured Rayleigh ratio we have used Zimm analysis and Guinier analysis. According to the Zimm

approximation, the Rayleigh ratio is given by:

$$\frac{KC}{R(\theta, C)} \approx \frac{1}{M_w}\left(1 + \frac{1}{3}R_g^2 q^2\right) \tag{4.2}$$

where C is the mass concentration, M_w is the molar mass of the scattering particle, R_g is its radius of gyration, $q = (4\pi n_0/\lambda)\sin(\theta/2)$ is the scattering vector with λ the laser wavelength and K is an optical constant given by:

$$K = \frac{4\pi^2 n_0^2 (dn/dC)^2}{\lambda^4 N_{av}} \tag{4.3}$$

where N_{av} is Avogadro's number and dn/dC is the specific refractive index increment of the micelles, for which we have used a weighted average of the refractive index increments of PEG, PSPMA and PTMAEMA, which are $0.135\,\mathrm{mL\,g^{-1}}$, $0.125\,\mathrm{mL\,g^{-1}}$ and $0.158\,\mathrm{mL\,g^{-1}}$ respectively.[22–24] In the Guinier approximation, the Rayleigh ratio is given by:

$$\frac{KC}{R(\theta, C)} \approx \frac{1}{M_w}\exp\left(\frac{1}{3}R_g^2 q^2\right) \tag{4.4}$$

For the Zimm approximation the micelle molar mass M_w thus follows from the intercept when extrapolating $\frac{KC}{R(\theta,C)}$ to a zero detection angle and for the Guinier approximation the micelle molar mass follows from the intercept when extrapolating $\ln(\frac{KC}{R(\theta,C)})$ to a zero detection angle. Data points measured at angles smaller than 70° were excluded from the analysis because they showed an upturn in scattering intensity. This is presumably due to the presence of a small fraction of aggregates and was observed earlier in light scattering measurements of C3Ms.[25]. Also data points measured at a detection angle above 118° were excluded from the analysis because these data points showed a lot of scatter. The micelle molar masses that were obtained in this way and an example of a Zimm plot and a Guinier plot are given in the appendix (Table 4.A.1 and Fig. 4.A.3). Based on the molar mass of the micelles and the molar mass of the homopolymer and diblock, the number of homopolymers in the micelles can be estimated. We have used the light scattering measurements to obtain at different KCl concentrations the molar mass of donor micelles at a SPMA monomer concentration of 1 mM with all SPMA monomers being part of a PSPMA-sCy3 hompolymer (100% label percentage). Subsequently, we have used the donor micelle molar masses to estimate both the number of donors in donor micelles and the number of acceptors in acceptor micelles. This is because the acceptor micelles absorbed part of the laser light and therefore their molar mass could not be determined by light scattering measurements.

4.2.7 Fluorescence spectroscopy measurements

Fluorescence spectroscopy measurements were performed on an Agilent Cary Eclipse fluorescence spectrophotometer connected to a PCB-150 circulating water bath. All measurements were performed at 25 °C. An excitation wavelength of 530 nm was used, except for the self-quenching measurements of the acceptor micelles, for which an excitation wavelength of 620 nm was used. For the measurements of the equilibrated micelles, a single emission spectrum of the equilibrated sample was recorded. For the micelle exchange measurements, the equilibrated donor and acceptor micelles solutions were added to the cuvette in the desired ratio, mixed and placed in the spectrophotometer. Every minute an emission spectrum was recorded. For measurements that took longer than 16 h, the measurement interval was increased to five minutes after the first few hours.

To determine the FRET efficiency, the recorded spectra were first corrected for direct acceptor excitation by subtracting the spectrum of the acceptor micelles excited at 530 nm. Subsequently the spectrum was fit with a linear combination of fixed log normal functions to determine the relative contribution of the donor and acceptor emission to the overall emission spectrum (appendix Section

4.A.3). Finally, the FRET efficiency E was calculated by:

$$E = \frac{I_A}{I_A + I_D} \tag{4.5}$$

where the donor intensity I_D and acceptor intensity I_A follow from integration of the donor and acceptor part of the emission spectrum respectively.

4.3 Analytical model

To extract the micelle exchange dynamics from the observed FRET increase, we need a description how this FRET increase depends on both the micelle exchange rate and on other micelle and fluorophore properties. In this section we derive an analytical model that provides this description. We will first derive how the FRET efficiency depends on the Förster radius, micelle core size, donor size and number of fluorophores in the micelle. Subsequently, we will derive how the distribution of fluorophore numbers changes in time for a given micelle exchange rate. Finally, by combining these results we obtain an analytical description of the FRET increase in time as function of the micelle exchange rate(s) and the micelle and fluorophore properties.

The energy transfer efficiency E between a single donor and acceptor is given by

$$E = \frac{k_A}{k_A + k_D} \tag{4.6}$$

where k_D is the rate of photon emission from the donor and k_A is the rate of energy transfer to the acceptor. In the case of FRET, $k_D/k_A = (r/R_F)^6$ where r is the donor-acceptor separation distance and R_F their Förster radius. In the core of each micelle, a given donor may be surrounded by i acceptors to which the donor can transfer its excited state energy. In that case, the energy transfer efficiency per donor becomes:

$$E = \frac{\sum_i k_{A,i}}{k_D + \sum_i k_{A,i}} = \frac{\sum_i \frac{k_{A,i}}{k_D}}{1 + \sum_i \frac{k_{A,i}}{k_D}} = \frac{\sum_j n_{A,j} \left(\frac{R_F}{r_j}\right)^6}{1 + \sum_j n_{A,j} \left(\frac{R_F}{r_j}\right)^6} \tag{4.7}$$

where $n_{A,j}$ is the number of acceptors that have a distance r_j to the donor. Here we assumed that the energy transfer efficiency per donor does not depend on the number of donors in the micelle core, in other words that the energy transfer of a donor to a certain acceptor does not hinder the energy transfer of another donor to this same acceptor.

When the acceptor fluorophores distribute themselves homogeneously over the micelle core, the number of acceptors n_A at a distance r from the donor is given by $n_A = \rho_A 4\pi r^2 dr$ where ρ_a is the number density of the acceptors in the micelle core. This gives for the energy transfer efficiency per donor:

$$E = \frac{\int_{R_0}^{\infty} \rho_A 4\pi R_F^6 r^{-4} dr}{1 + \int_{R_0}^{\infty} \rho_A 4\pi R_F^6 r^{-4} dr} = \frac{\rho_A 4/3\pi R_F^6 R_0^{-3}}{1 + \rho_A 4/3\pi R_F^6 R_0^{-3}} \tag{4.8}$$

where R_0 is the size of the donor fluorophore. The acceptor number density is given by $\rho_A = n_A/(4/3\pi R_m^3)$ where R_m is the micelle core radius. The energy transfer efficiency per donor can thus also be written as:

$$E = \frac{\nu n_A}{1 + \nu n_A} \tag{4.9}$$

where we grouped different geometrical constants in a single constant $\nu = R_F^6/(R_m^3 R_0^3)$.

During the micelle exchange experiments we measure the FRET efficiency averaged over all the donors in the sample. Not all the donors will have the same FRET efficiency since not every micelle will contain exactly the same number of acceptors: initially, the micelles that started with only acceptors (the acceptor micelles) will contain much more acceptors than the micelles that started with only donors (the donor micelles). In addition, also within the donor and acceptor micelle populations the number of acceptors per micelle will vary because exchange events do not take place at exactly the same time for every micelle. The average FRET efficiency per donor in a donor micelle $< E_D >$ is given by:

$$< E_D >= \sum_{n_A} P(n_A) \frac{\nu n_A}{1 + \nu n_A} \tag{4.10}$$

where n_A is the number of acceptors in a donor micelle and $P(n_A)$ denotes the probability to find a donor micelle with n_A acceptors. Similarly, the average FRET efficiency per donor in an acceptor micelle $< E_A >$ is given by:

$$< E_A >= \sum_{m_A} P(m_A) \frac{\nu m_A}{1 + \nu m_A} \tag{4.11}$$

where we used m_A to indicate the number of acceptors in an acceptor micelle. When donor micelles contain on average $< n_D >$ donors, the total number of donors in donor micelles is given by $n_{D,\text{tot}} =< n_D > f_D q$ where f_D is the fraction of donor micelles and q is the total number of micelles. For the acceptor micelles with on average m_D donors per micelle, the total number of donors in acceptor micelles is given by $m_{D,\text{tot}} =< m_D > f_A q$ where $f_A = 1 - f_D$ is the fraction of acceptor micelles. When the donor micelles contain on average N_D donors at the start of the mixing experiment, the total number of donors in the sample is $f_D N_D q$. The FRET efficiency averaged over all donors in the sample at a certain time t is thus given by:

$$< E(t) >= \frac{f_D < n_D(t) >< E_D(t) > +(1 - f_D) < m_D(t) >< E_A(t) >}{f_D N_D} \tag{4.12}$$

To calculate the average FRET efficiency of the sample as function of time, we thus need to know the probability distributions of the number of donors and acceptors per micelle for the donor and acceptor micelles and how these distributions change in time. These changes in time are related to the exchange of the donor and acceptor fluorophores. When one fluorophore splits off from a micelle with n fluorophores, the number of micelles with n fluorophores decreases by 1 and the number of micelles with $n - 1$ fluorophores increases by 1. When one fluorophore merges with a micelle with n fluorophores, the number of micelles with n fluorophores decreases by 1 and this time the number of micelles with $n + 1$ fluorophores increases by 1.

The dissociation of fluorescently labelled chains from the micelles is a stochastic process for which we can define the average rate at which a chain splits off as k. A micelle with n fluorescently labelled chains has a n times larger chance that one fluorescently labelled chain splits off than a micelle with only one fluorescently labelled chain. The rate at which a micelle with n fluorophores goes to $n - 1$ fluorophores is thus given by nk.

The total number of splitting events of donors in a time period dt is the sum of all splitting events of the donor and acceptor micelles: $k\left(\sum_{n_D} P(n_D) n_D + \sum_{m_D} P(m_D) m_D\right) dt = k N_D dt$. In the same way, we can describe the total number of splitting events of the acceptors in a time period dt with $k\left(\sum_{n_A} P(n_A) n_A + \sum_{m_A} P(m_A) m_A\right) dt = k M_A dt$ with M_A the average number of acceptors in acceptor micelles at the start of the mixing experiment.

The average micelle size does not change in time. Therefore the total number of merge events should be equal to the total number of splitting events and is thus given by $kN dt$. Here we have used the general notation N to indicate the initial number of donors in donor micelles or the initial number of acceptors in acceptor micelles. The insertion can take place in any micelle and does not depend on the

number of fluorophores in the micelle. The probability that a fluorophore is inserted in a donor micelle of n fluorophores is thus just given by the probability to find a donor micelle with n fluorophores, which is given by $f_D P(n)$. In the same way, the probability that a fluorophore is inserted in an acceptor micelle with n fluorophores is given by $f_A P(n)$. The general notation of the merge rate thus becomes fNk where f can denote both the fraction of donor micelles and the fraction of acceptor micelles.

The expulsion rates and insertion rates together give the change in time of the probability $P(n)$ to find a micelle type with n fluorophores:

$$\frac{dP(n,t)}{dt} = fNkP(n-1,t) - (fNk + nk)P(n,t) + (n+1)kP(n+1) \tag{4.13}$$

This system of differential equations can be solved analytically (appendix Section 4.A.8) to give

$$P(n,t) = e^{-\lambda(t)} \frac{\lambda(t)^n}{n!} \tag{4.14}$$

with

$$\lambda(t) = fN(1 - e^{-kt}) \tag{4.15}$$

for the probability distribution of the number of acceptors in donor micelles and for the probability distribution of the number of donors in acceptor micelles and

$$P(n,t) = e^{-\mu(t)} \frac{\mu(t)^n}{n!} \tag{4.16}$$

with

$$\mu(t) = N(f + (1-f)e^{-kt}) \tag{4.17}$$

for the probability distribution of the number of donors in donor micelles and for the probability distribution of the number of acceptors in acceptor micelles. Equations 4.14 and 4.16 are both Poisson distributions with an average $\lambda(t)$ and $\mu(t)$ respectively. The average number of donors in acceptor micelles is thus given by $< n_D(t) >= \lambda(t) = f_D N_D(1 - e^{-kt})$ and the average number of donors in donor micelles by $< m_D(t) >= \mu(t) = N_D(f_D + (1 - f_D)e^{-kt})$.

To derive Equations 4.13 to 4.17 we have assumed that the fluorophores exchange independently from each other. This is true when micelle exchange takes place by expulsion and insertion and every chain contains maximal one fluorescent label. However, when the micelles exchange mainly by fusion and fission the chains will exchange in clusters and thus do not exchange independently. For small clusters we expect that the results will not deviate that much from independent fluorophore exchange, especially when the label fraction is low and therefore the number of fluorophores per cluster is low. For the exchange of large clusters with large fluorophore numbers Equations 4.14 to 4.17 cannot be used to describe the fluorophore exchange. Therefore, our analytical model for FRET micelle exchange experiments is limited to micelle exchange that takes place by expulsion and insertion or by fission and fusion of small clusters.

Once we know the experimental parameter ν and how the distributions of fluorophores per micelle change in time (Equations 4.14 and 4.16), we can predict how the FRET efficiency will change in time (Equation 4.12). A change in the initial number of fluoropores, the experimental constant ν, the fraction of donor micelles f_D and exchange rate k all can affect the time evolution of the FRET efficiency (Fig. 4.2). In earlier FRET exchange experiments of C3Ms[5,6] the increase in FRET efficiency has been fitted with an exponential function $E(t) = E(\infty)[1 - e^{-kt}]$ where it was assumed that the rate constant k is a direct measure for the micelle exchange rate. This exponential function gives a slower increase in FRET efficiency compared to our analytical model (Fig. 4.3). This suggests that fitting the FRET efficiency increase with a simple exponential function results in an overestimation of the micelle exchange rate. In addition, for the exponential function the increase in normalised FRET efficiency $E(t)/E(\infty)$ only

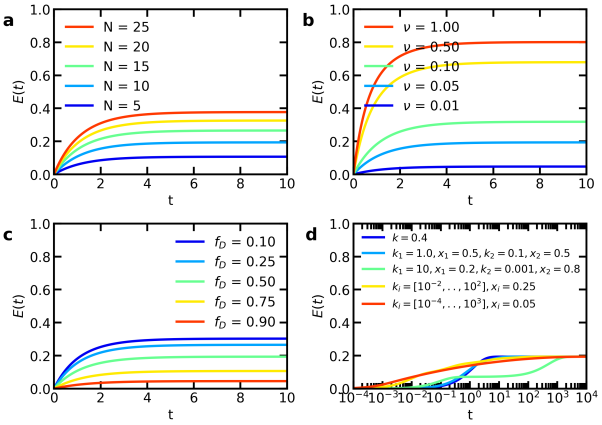

Figure 4.2. Model predictions of the FRET efficiency E as function of the time after mixing t for (a) different fluorophore numbers $N_D = N_A = N$; (b) different experimental constants ν; (c) different donor micelle fractions f_D and (d) different fluorophore types with exchange rate k_i and fraction x_i. Unless otherwise indicated, $N = 10$, $\nu = 0.05$, $f_D = 0.5$ and $k = 0.4$.

depends on the exchange rate k, while according to our analytical model this increase can be affected by changes in the initial average fluorophore number (Fig. 4.3a), the experimental constant ν (Fig. 4.3b) and the fraction of donor micelles f_D (Fig. 4.3c). These effects of N, ν and f_D occur especially for larger N and ν values (Fig. 4.4). A faster increase in normalised FRET efficiency thus does not necessarily mean that the micelle exchange is faster but might also be caused by differences in other parameters which the simple exponential fit does not take into account.

Up to now, we have considered the case of a single fluorophore type, where all fluorophores have the same exchange rate k. In reality, polydispersity of the chains and/or micelles or other sources of heterogeneity will lead to a distribution of exchange rates and we thus need to consider different fluorophore types each with their own exchange rate k_i.

To find the distribution of the total number of donor or acceptor fluorophores in a donor or acceptor micelle we make use of the fact that for random variables n_1 and n_2 with Poisson distributions with averages λ_1 and λ_2, the sum of these random variables $n = n_1 + n_2$ is also a Poisson distribution with a mean $\lambda = \lambda_1 + \lambda_2$. After summation of all fluorophore types each with their own exchange rate k_i we thus get for the number of donors in acceptor micelles and *vice versa* again a Poisson distribution $P(n,t) = e^{-\lambda(t)}\frac{\lambda(t)^n}{n!}$. This time the average of the Poisson distribution is given by:

$$\lambda(t) = \sum_i f N_i (1 - e^{-k_i t}) \tag{4.18}$$

Here N_i is the initial average number of fluorophores per micelle of fluorophore type i and is given by $N_i = x_i N$ where x_i is the fraction of this fluorophore type. For the number of donors in donor micelles and the number of acceptors in acceptor micelles we also get a Poisson distribution $P(n,t) = e^{-\mu(t)}\frac{\mu(t)^n}{n!}$ with as average:

$$\mu(t) = \sum_i N_i (f + (1-f) e^{-k_i t}) \tag{4.19}$$

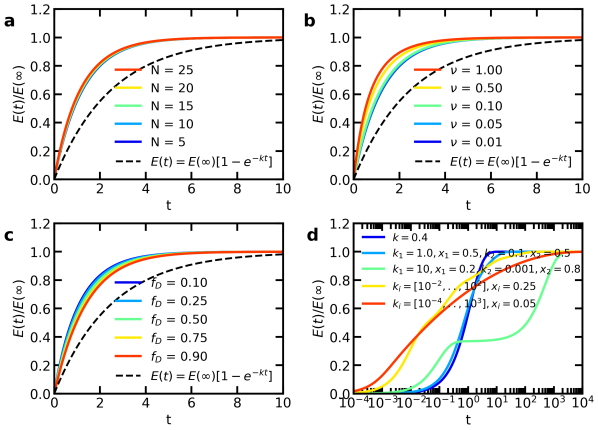

Figure 4.3. Model predictions of the normalised FRET efficiency $E(t)/E(\infty)$ as function of the time after mixing t for (a) different fluorophore numbers $N_D = N_A = N$; (b) different experimental constants ν; (c) different donor micelle fractions f_D and (d) different fluorophore types with exchange rate k_i and fraction x_i. Unless otherwise indicated, $N = 10$, $\nu = 0.05$, $f_D = 0.5$ and $k = 0.4$. Dashed lines indicate the exponential function $E(t) = E(\infty)[1 - e^{-kt}]$ with $k = 0.4$.

Equations 4.18 and 4.19 imply that for a given average fluorophore number to initial fluorophore number ratio $< n > /N$ the Poisson distribution will always will be the same irrespective of the rates at which the fluorophores exchange. This we will use later on to estimate the fraction of chains that has exchanged at a certain time.

The occurrence of multiple exchange rates can broaden the time scales over which the increase in FRET efficiency takes place (Fig. 4.2d and 4.3d). For similar exchange rates, this broadening effect is relatively small as shown by the relatively small change for the exchange with $k_1 = 1.0$ and $k_2 = 0.1$ as compared to the exchange with $k = 0.4$. For large differences in exchange rates substantial broadening of time scales occurs.

4.4 Results and Discussion

To perform the FRET-based C3M exchange experiments we have synthesised a negatively charged homopolymer with the donor or acceptor fluorophore attached to its end (Fig. 4.1b). Specifically, we have coupled a sulfo-Cyanine3 dye (donor) or a sulfo-Cyanine5 dye (acceptor) to a RAFT agent and subsequently used these fluorescently labelled RAFT agents to perform the polymerisation of 3-sulfopropyl methacrylate (SPMA) to give PSPMA-sCy3 and PSPMA-sCy5 respectively. By using this labelling protocol, we expect that the fluorophores will interfere less with the electrostatic attraction between the polyelectrolytes because we have not replaced any charged group to functionalise the polymers. Nevertheless, the introduction of these fluorophores can still affect the micelle properties by introducing additional stabilising or destabilising interactions between the fluorophores themselves or between the fluorophores and polyelectrolytes. Another advantage of our labelling protocol is that we have limited the number of fluorophores per chain to one, which increases the chance that the fluorophores exchange independently. This independent exchange is one of the assumptions that we have used to derive the analytical model. Although the number of fluorophores per chain is fixed, we still can vary the number of fluorophores per micelle by varying the ratio of labelled and unlabelled PSPMA homopolymer. We define the label fraction α as the number of SPMA monomers that are part

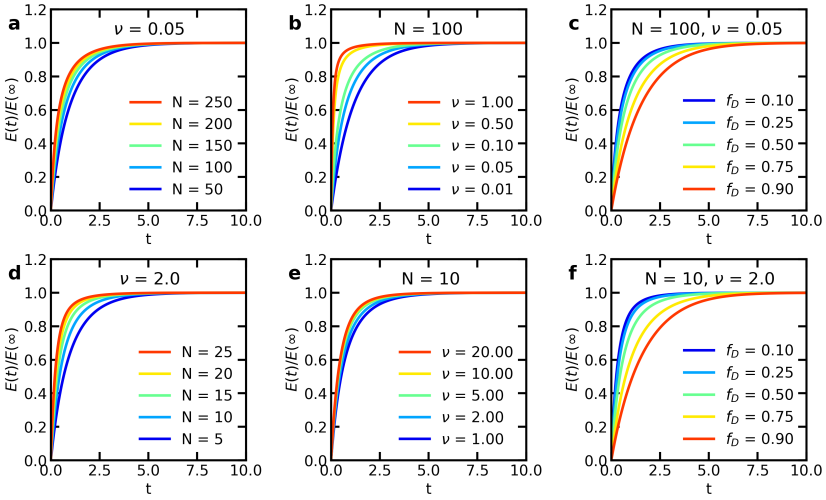

Figure 4.4. The effect of larger N or ν-values on the model predictions of the normalised FRET efficiency $E(t)/E(\infty)$ as function of the time after mixing t for (a,d) different fluorophore numbers N; (b,e) different experimental constants ν; (c,f) different donor micelle fractions f_D. For the top row (a,b,c) N is increased (unless otherwise indicated $N_D = N_A = N = 100$ and $\nu = 0.05$), while for the bottom row (d,e,f) ν is increased (unless otherwise indicated $N_D = N_A = N = 10$ and $\nu = 2.0$). The exchange rate k is 0.4. Unless otherwise indicated, $f_D = 0.5$.

of an fluorescently labelled hompolymer divided by the total number of SPMA monomers. We make the micelles by mixing the PSPMA homopolymers at a 1:1 charge ratio with the diblock copolymer PEG-*b*-PTMAEMA where PTMAEMA is the positively charged block.

4.4.1 Fluorescence of equilibrated micelles

According to the model, the micelle core size, donor size and Förster radius can have substantial effects on the increase in FRET efficiency, even when the FRET efficiency is corrected for the final FRET efficiency $E(\infty)$ of the completely mixed micelles (Fig. 4.4). Therefore, before starting the exchange experiments, we first determine the fluorescence properties of the equilibrated donor micelles, acceptor micelles and mixed micelles.

Inside the micelle, the local fluorophore concentration can be high. Hence, we first check whether self-quenching occurs. Indeed, for label fractions larger than 0.2 the fluorescence intensity does no longer increase proportionally with increasing fluorophore fraction (Fig. 4.5a,b), indicating that self-quenching takes place. The self-quenching effects are stronger for the acceptors than for the donors. The main explanation for this difference is probably the shorter length of the acceptor polymers and therefore a higher number of acceptors per micelle at equal label fractions. This difference in self-quenching will affect the measured apparent FRET efficiency. Therefore, in the micelle exchange experiments we will use a label fraction of $\alpha = 0.2$. An additional advantage of this low label fraction is that we further increase the chance that the fluorophores exchange independently.

The final FRET efficiency of the completely mixed micelles can be found by first mixing the donor and acceptor polymers and subsequently adding the oppositely charged diblock copolymer to form the micelles. Increasing the number of donor and acceptors per micelle should decrease the average distance between the fluorophores and therefore the FRET efficiency should increase. Indeed, at larger

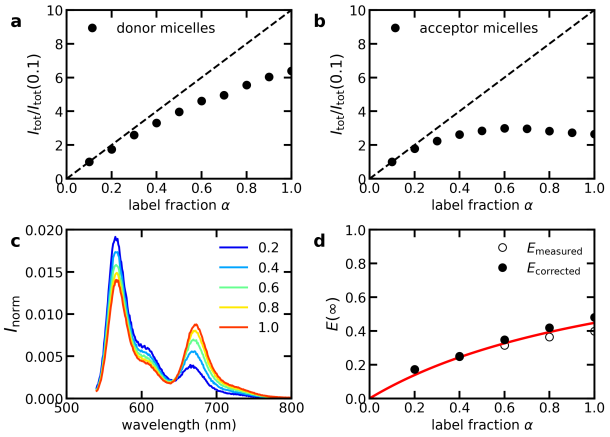

Figure 4.5. Fluorescence of the equilibrated micelles at different label fractions. (a,b) Fluorescence intensity of the donor micelles (a) and acceptor micelles (b) at different label fractions α normalised to the intensity at a label fraction $\alpha = 0.1$. The dashed lines indicate the theoretical intensity without self-quenching. (c) Normalised fluorescence spectra of the mixed micelles at different label fractions after correction for direct acceptor excitation. (d) FRET efficiency as function of label fraction α. E_{measured} is the experimentally measured FRET efficiency and $E_{\text{corrected}}$ is the FRET efficiency after correction for differences in self-quenching of the donor and acceptor. The solid red line indicates the model prediction for $N_D = 33$, $N_A = 55$ and $\nu = 0.03$.

label fractions the contribution of the donor fluorescence becomes smaller and the contribution of the acceptor fluorescences becomes larger (Fig. 4.5c).

To compare the FRET efficiencies at different label fractions with each other, the measured FRET efficiencies have to be corrected for the differences in donor and acceptor self-quenching. As a first approximation, we use the ratio between the measured intensity of the donor micelles compared to the theoretical intensity, when no self-quenching would have occurred, as correction factor for the donor intensity and do the same for the acceptor intensity. At the same label fraction, the donor micelles contain two times more donors than the end FRET micelles. The same applies for the acceptor micelles. Therefore, we have used for example the donor micelles at $\alpha = 0.5$ to calculate the correction factor for the mixed micelles at $\alpha = 1.0$. After these corrections, we can construct a plot of the FRET efficiency of the mixed micelles $E(\infty)$ as function of label fraction (Fig. 4.5d). This end FRET efficiency depends on the number of donor and acceptors per micelle and the experimental constant ν. The number of donors and acceptors per micelle at a label fraction of $\alpha = 1.0$ can be roughly estimated by using light scattering experiments (Table 4.1). By multiplying this fluorophore number by the label fraction we can also get the fluorophore numbers for other label fractions. Subsequently we can compare our data to the model predictions to roughly estimate ν (Fig. 4.5d). This gives $\nu = 0.03$.

Table 4.1. Micelle characteristics at different salt concentrations. N_D and N_A are estimated from light scattering experiments of the donor micelles with $\alpha = 1.0$. ν is estimated by comparing the experimentally measured FRET efficiency at different label fractions with the model predictions. For these model predictions, the N_D and N_A values obtained by the light scattering experiments are used.

[KCl] (mM)	N_D	N_A	ν
10	46	76	0.03
100	33	55	0.03
200	25	41	0.03
300	27	44	0.03
400	24	39	0.02

The obtained value for ν is quite low. For example, if we take a Förster radius of 5.2 nm, which is the Förster radius of the cyanine3 and cyanine5 pair in water,[26] and take a micelle core size of ~10 nm[8,27] and a donor size of ~2 nm, we would get $\nu \approx 2.5$. A possible explanation for the lower ν value is that the attachment to the polymer restricts the movement of the fluorophores, resulting in a lower Förster radius and a larger effective donor size. In addition, the Förster radius within a complex coacervate environment might differ from the Förster radius in water. Because of the third power or even sixth power dependence, small changes in R_F, R_0 and R_M can have large effects on ν.

The low ν in combination with relatively low N values would mean that the normalised FRET efficiency $E(t)/E(\infty)$ is little affected by variations around N or ν. This would make the data comparison of different experiments easier because in that case changes in $E(t)/E(\infty)$ will be mainly caused by changes in exchange rates and not by differences in N or ν. We note that although this might apply for this C3M system, this does not necessarily have to be the case for all C3Ms. For example, for protein containing C3Ms higher FRET efficiencies were found[6], indicating larger N or ν values. Indeed, the number of fluorescent proteins per micelle[28] is larger than the number of fluorescently labelled chains per micelle (Table 4.1). For these larger fluorophore numbers, variations in N and ν affect the normalised FRET increase more (Fig. 4.4a-c).

4.4.2 Micelle exchange at 100 mM KCl

Now we have characterised the fluorescence of the equilibrated C3Ms we can start to focus on their exchange. First we consider micelles at a 100 mM KCl concentration. At this salt concentration the micelles show a broad exchange time range (Fig. 4.6). The first exchange takes places within one minute, while even after 16 hours the micelles do not have reached their completely mixed state yet. This largely differs from the measured exchange of protein containing C3Ms, where the final FRET efficiency seems to be reached within five minutes.[6] On the other hand, Holappa *et al.* have also observed a broad time range for C3Ms consisting of polymers only.[5] They explained the large differences in time scales by two different processes with the expulsion and insertion being the fast process and fission and fusion being the slow process. However, this cannot be the full explanation. First, if all fluorescently labelled chains are equivalent, they can all exchange by expulsion and insertion and all chains would already have been exchanged by this mechanism before fission and fusion starts to play a role. Therefore, to observe largely different time scales, different populations of fluoroscently labelled chains should be present, where each population has its own exchange rate k_i. It might be that the slower exchanging chains indeed have a larger tendency to exchange by fission and fusion, but this is not necessarily the case. In addition, if the micelle exchange takes place by only two distinct processes as was suggested by Holappa *et al.*, the FRET efficiency would show a stepwise increase on a logarithmic time scale (Fig. 4.3d), while here the FRET efficiency seems to increase continuously. This indicates a broad distribution of different exchange rates.

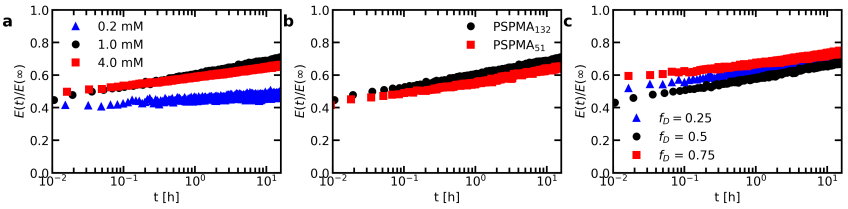

Figure 4.6. Micelle exchange experiments at 100 mM KCl: normalised FRET efficiency $E(t)/E(\infty)$ as function of time after mixing t for (a) different monomer concentrations; (b) different unlabelled homopolymer lengths and (c) different fractions of donor micelles.

A logarithmic relaxation has also been observed for amphiphilic diblock copolymer micelles.[14–16,18] Often, this logarithmic relaxation is explained by some polydispersity of the polymers in combination with a strong dependence of the exchange rate on the polymer core block length,[16–18] although computer simulations have suggested that in some cases even for monodisperse chains logarithmic relaxation might occur.[29] Also in our case, polydispersity probably has played a role, as the donor and acceptor polymer have a dispersity of 1.7 and 1.6 respectively. This is high for polymers synthesised by RAFT polymerisation and is probably caused by the fact that the polymerisation of SPMA can be prone to termination reactions as we have observed in Chapter 2 by following the reaction with ^{1}H NMR spectroscopy. To further discuss the effect that this large polydispersity might have on the exchange, we first need to know more about the exchange mechanisms. Therefore, we will first focus on these mechanisms and come back to the polydispersity effect later in this chapter.

A first step in elucidating the exchange mechanisms of micelles is to check their concentration dependence. For fission and fusion the merging is considered to be rate-limiting, which is a second order process and therefore should be concentration dependent, while for expulsion and insertion the splitting is considered to be rate limiting, which is a first order process and therefore concentration independent. In our case, only at lower concentrations an increase concentration results in a faster increase of the FRET efficiency (Fig. 4.6a). Increasing the monomer concentration above 1 mM does not increase the exchange rate any further. This indicates that at least for higher concentration no second order process is rate limiting and therefore splitting is probably the rate-limiting step. The concentration dependence at lower concentrations might mean that here the merging step is rate-limiting. Alternatively, the FRET increase might be slower because at these lower concentrations the probability of merging with the original micelle might become higher.

The rate-limiting splitting step at higher concentrations can be an expulsion process or a fission process. To determine which of these two split mechanisms prevails, we have measured the exchange for two different unlabelled homopolymer lengths (Fig. 4.6b). For fission, multiple chains split off simultaneously and we therefore expect a stronger effect of changing the unlabelled homopolymer than for expulsion. In the Langevin dynamics simulations of the initial C3M exchange we saw that decreasing the polyelectrolyte length can increase the fission rate (Chapter 3). Here we decrease the polyelectrolyte length of the majority (80%) of the homopolymers and therefore expect an increase in exchange rate if fission is rate-limiting. This is not the case: the effect of changing the homopolymer length on the exchange rate seems negligible. This suggests that the splitting occurs mainly by expulsion, where in every split step only one or two homopolymers split off.

We note that this expulsion-dominated exchange differs from the recently observed fission-dominated dissociation of micelles upon an increase in salt concentration.[8] This can be explained by the fact that we measure the exchange of equilibrated micelles, while the dissociating micelles are not in equilibrium and can gain free energy by decreasing their aggregation number with the largest gain when the micelle splits in equal sizes.[8]

The fact that the exchange rate of the labelled homopolymers is not decreased by adding longer unlabelled homopolymers also implies that, at least for this C3M system, the protection of the cargo cannot be improved by adding longer polymers that have the same charge as the cargo. This is in line with a recent study on protein containing C3Ms, where it was shown that adding a negatively charged homopolymer does not help to prevent the dissociation of the negatively charged proteins from the micelle at higher salt concentrations.[30]

In addition to changing the total micelle concentration and the length of the unlabelled polymer, we can also change the ratio at which we mix the donor and acceptor micelles (Fig. 4.6c). Rather than giving new insights into the exchange mechanisms themselves, this can give additional information on the fluorescence properties of the system. As mentioned before, these fluorescence properties are important to interpret the observed increase in normalised FRET efficiencies in terms of micelle exchange rates. The relatively low N and ν values we obtained from studying equilibrated micelles

suggest that differences in $E(t)/E(\infty)$ are mainly caused by changes in exchange rate and not by other factors. Changing the ratio of donor and acceptor micelles can help to check whether this is indeed the case: for low N and ν values, changes in the donor fraction f_D should only have little effect on the normalised FRET efficiency increase (Fig. 4.3c), while for larger N and ν this effect is larger (Fig. 4.4c,f). In this case, we observe some differences in normalised FRET increase, especially at the start of the mixing experiment. However, these differences do not follow a general trend, as the normalised FRET first seems to decrease when going from $f_D = 0.25$ to $f_D = 0.5$ and subsequently seems to increase again when going to $f_D = 0.75$. Based on our model we would expect a decrease in both $E(t)$ and $E(t)/E(\infty)$ for increasing donor fractions. For $E(t)$ this is indeed the case (Fig. 4.A.6), but the normalised FRET efficiency deviates from this prediction. Presumably, this deviation is caused by experimental uncertainties in the determination of the end FRET efficiency and the correction for direct acceptor excitation. Since we work at relatively low FRET efficiencies, small deviations might already affect the normalised FRET efficiency. This is especially the case for the highest donor fraction since this gives the lowest FRET efficiency. Due to these experimental uncertainties we cannot conclude whether the donor fraction indeed has a negligible effect on the increase in FRET efficiency. However, its effect is at least smaller than the experimental uncertainty in the determination of $E(t)/E(\infty)$.

4.4.3 Ionic strength effect

In the previous section we concluded that the chain expulsion from the core is probably the rate limiting step of the exchange. The exchange rate should thus be affected by changing the electrostatic attraction in the core. Therefore, we continue by measuring the C3M exchange at different ionic strengths. Again, we first check the fluorescence properties of equilibrated micelles before we focus on the exchange itself.

Increasing the ionic strength decreases the FRET efficiency (Fig. 4.7a). The FRET efficiency can be decreased by an increase of the fraction of fluorophores free in solution and by a decrease of fluorophore volume fraction within the micelle core. Even at 400 mM KCl, the fraction of free fluorophores is only about 2% (Fig. 4.A.7). The decrease in FRET efficiency is thus mainly the result of a decrease in fluorophore volume fraction. This means that the polyelectrolyte volume fraction in the coacervate phase decreases with increasing salt concentration, which has also been observed for the macroscopic phase separation of complex coacervates.[31,32] The decrease in FRET efficiency is accompanied by a decrease in micelle aggregation number (Table 4.1). This agrees with recent thermodynamic calculations which also showed that the equilibrium micelle aggregation number decreases with increasing salt concentration.[8]

From the measured FRET efficiencies and the estimated donor and acceptor numbers (Table 4.1), we can again estimate the experimental constant ν for the different salt concentrations. Only minor changes in ν take place (Table 4.1). The decrease in FRET efficiency is thus mainly the result of the decrease in the number of fluorophores per micelle.

The exchange rate is strongly increased by increasing the salt concentration (Fig. 4.7b). Micelles at the lowest salt concentrations have the lowest normalised FRET efficiency after the first minute and also show the slowest increase for the next 16 hours. At 400 mM KCl, the exchange is fast and within a few minutes the micelles reach the FRET efficiency of the completely mixed micelles $E(\infty)$. In fact, they even seem to reach a FRET efficiency slightly above $E(\infty)$ and subsequently their FRET efficiency slightly decreases. This might indicate that some of the fluorophores bleach, even though the majority of the fluorophores is stable against bleaching as we have shown by measuring the FRET efficiency of the mixed micelles over 16 h (Fig. 4.A.8). The fast exchange indicates that the micelles at 400 mM KCl might be less effective encapsulators than one would expect based on their static properties: their monomer concentration is well above the critical micelle concentration of ~20 μM (Fig. 4.A.7) and the salt concentration is well below the critical salt concentration of ~790 mM KCl (Fig. 4.A.4) and still all chains exchange within a few minutes.

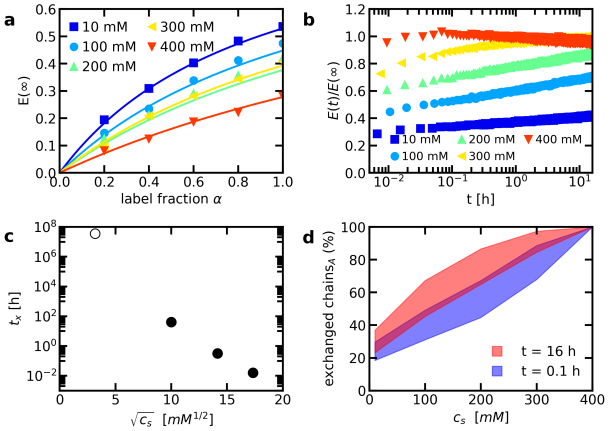

Figure 4.7. Effect of the ionic strength on the micelles. (a) FRET efficiency of the mixed micelles as function of label fraction for different salt concentrations. FRET efficiencies are corrected for differences in donor and acceptor self-quenching. Solid lines are model predictions with N_D, N_A and ν values as indicated in Table 4.1. (b) Micelle exchange experiments: normalised FRET efficiency $E(t)/E(\infty)$ as function of time after mixing t at different salt concentrations. (c) Time t_x at which $E(t_x)/E(\infty) = 0.75$, as function of the square root of the salt concentration. Filled symbols are obtained from experimental data. The open symbol is estimated from extrapolation exchange measurement of 16.7 h at $c_s = 10$ mM, assuming the same logarithmic time dependence as the final measured 3.3 hour. (d) Estimated fraction of exchanged acceptor chains at $t = 0.1$ h and $t = 16$ h as function of the salt concentration. The borders of the shaded regions correspond to the lower and upper limit of the estimated exchanged fraction.

The strong salt dependence indicates that the micelle exchange rate is largely governed by the dissociation of electrostatic bonds. This dissociation is often treated as an activated process with an energy barrier that decreases linearly with the square root of the salt concentration.[33–36] In this approach, the energy of the bound ion groups is calculated from Coulomb interactions, while the calculation of the energy of the unbound ion groups is based on the Debye-Hückel approximation. The last-mentioned gives the square root salt term in the energy barrier. To see whether the micelle exchange can also be described in this way, we compare for different salt concentrations the time t_x at which the normalised FRET efficiency equals 0.75 (Fig. 4.7c). Here, we make use of the fact that for these micelles the normalised FRET efficiency is little affected by small changes in N and ν and therefore in all cases $E(t)/E(t_x) = 0.75$ corresponds to approximately the same fraction of exchanged chains. In a first approximation, the time t_x can thus be used as a direct measure of the micelle exchange rate.

The exchange times at 100 mM, 200 mM and 300 mM KCl seem to show the expected square root salt dependence (Fig. 4.7c). However, the exchange time that is obtained from extrapolating the exchange data at 10 mM KCl deviates from this trend and is larger than expected. This might mean that the electrostatic dissociation has a stronger salt dependence, as was also suggested by Marciel *et al.*[37] Another possibility is that inaccuracies in the extrapolation resulted in an overestimation of the exchange time. We assumed that the exchange continues with the same logarithmic increase, but the exchange might also show an upturn at later times. In addition, due to the slow increase in FRET efficiency, small errors in the $E(t)/E(\infty)$ determination have a major effect on determination of t_x. To further determine the salt dependence, it would help if the exchange can be determined over a broader time range so that extrapolation is no longer necessary. A decrease of the time to measure the first data point would be especially helpful. Here, this time was set by the time needed to mix the micelle solutions and to record a full spectrum, which together took about 40 seconds. A broader time range

would also allow to determine the exchange times for different exchanged chain fractions. In this way, it would be possible to check whether the exchange of the first chains follows the same salt dependence as the later exchanging chains, which will help to determine whether all chains exchange by the same mechanism.

Although we cannot easily compare the exchange time for a given fraction of exchanged chains at all different salt concentrations, we can make the comparison the other way round and for a given time point determine which fraction of chains has exchanged. For this, we compare the experimental normalised FRET efficiency at a given time point to the model predictions of the normalised FRET efficiency for the obtained N and ν values (Table 4.1). The increase in normalised FRET efficiency differs when the donor and acceptors exchange with other rates. Since we do not know how much the donor and acceptor exchange rate differ from each other, we cannot determine the fraction of exchanged chains exactly. Instead, we estimate a lower and upper limit of the exchanged acceptor chain fraction. The acceptor chain is on average shorter. Therefore, if the donors and acceptors show any difference in exchange rate, we expect that the acceptor exchange is faster. To calculate the lower limit we thus assume that the donor and acceptor have equal exchange rates and to calculate the upper limit we set the donor exchange rate to zero and let only the acceptors exchange. Here, we make use of the fact that for a given fraction of exchanged acceptors, the distribution of acceptors in the micelles is the same irrespective of the acceptor exchange rates. The same applies for the donors. To determine the fraction of exchanged acceptor chains we can thus use arbitrary exchange rates for the model predictions. The only restriction is that the donor and acceptor rates have to be the same to determine the lower limit and the donor exchange rate has to be zero to determine the upper limit. In this way, we find that even at the lowest salt concentration at least 18% of the chains has already exchanged within 0.1 hour (Fig. 4.7d). On the other hand, more than 60% of the chains did not exchange within 16 hour. This again shows the broad time range over which the exchange takes place. Increasing the salt concentration affects both the fraction of chains that exchanges at short times and at long times. Electrostatic interactions thus play a role both for the fastest 20% of the exchanging chains and for the slower exchanging chains.

4.4.4 Comparison to literature models of exchange rates

We now return to broad range of the exchange rates and the role that the polymer polydispersity might have played in this. This requires a description how the exchange rate k depends on the polymer length W. We know that the expulsion of chains from the core is probably the rate-limiting step in the exchange and that for this expulsion electrostatic bonds have to be broken. Therefore, we compare our experimental data to three literature models predicting how the chain expulsion rate depends on the polymer length and one literature model predicting how the relaxation rate in complex coacervates depends on the polymer length.

To fit the different literature predictions to our experimental data, we first bin the exchange data in time steps that are evenly spaced on a logarithmic time scale. In this way, we give the data at short and long time scales similar weighting. Subsequently, we perform the fit. We first calculate the distribution of exchange rates k_i based on the literature model and on the polymer length W_i distribution. We approximate the experimental polymer length distribution with a Schulz-Zimm distribution. Based on GPC measurements, these distributions have a number average chain length of 110 and 71 and a weight average chain length of 189 and 115 for the donor and acceptor polymers respectively. We split the donor and acceptor polymer distribution both in hundred fractions, each fraction having the same probability of 0.01. For every fraction i, we use its median polymer length as the characteristic polymer length W_i of this fraction. Subsequently, we use the literature predictions to calculate the corresponding exchange rate k_i for every fraction. Next, we use Equations 4.18 and 4.19 to calculate the average fluorophore numbers per micelle, where every time N_i is given by $0.01N$ with N the initial average number of donors per donor micelle (N = 6.6 for 100 mM KCl) or the initial average number of acceptors per acceptor micelle (N = 11 for 100 mM KCl). Substitution of these expression in Equations

4.14 and 4.16 gives the fluorophore distributions. Finally, we use these distributions and the obtained value for ν (Table 4.1) to calculate the average FRET efficiency in time (Equation 4.12) and compare this to the experimental data. In this fit procedure, the parameters of the literature exchange rate equations are thus the only fit parameters. The other parameters are estimated from GPC measurements or are obtained from Table 4.1.

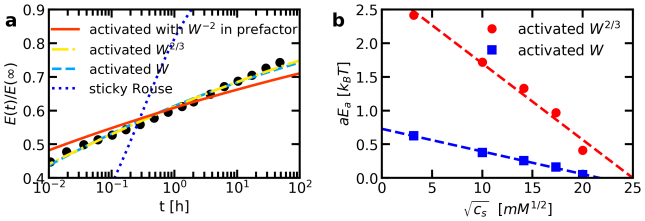

Figure 4.8. Model fits to the FRET micelle exchange data. (a) Fits of the different literature models for the exchange rate to the FRET micelle exchange data at 100 mM KCl. The obtained fit values are $\tau_0 = 1.0\,\mathrm{s}$ for the Sticky Rouse model (Equation 4.20), $\omega_0 = 3.6 \times 10^2$ Hz and $aE_a = 0.3k_BT$ for the activated process with a linear dependence of the energy barrier on the polymer length (Equation 4.21), $\omega_0 = 2.9 \times 10^5$ Hz and $aE_a = 1.6k_BT$ for the activated process with a 2/3 power dependence of the energy barrier on the polymer length (Equation 4.22) and $\alpha\chi = 0.36$ for the activated process with the polymer length included in the energy barrier and in the prefactor (Equation 4.23). (b) Fit values of the activation energy of a single monomer E_a for the activated processes (Equation 4.21 and 4.22) as function of the square-root of the salt concentration. Dashed lines are linear fits of the data.

The first model that we consider is the sticky Rouse model that was also used to describe the relaxation of complex coacervates in rheology experiments.[34] In this description, the total relaxation rate scales with W^{-2}:

$$k_i = \tau_0^{-1} W_i^{-2} \tag{4.20}$$

Here τ_0 is the relaxation time of a single monomer and is determined by the electrostatic attraction and thus the salt concentration. The sticky Rouse model cannot accurately describe the experimental data: it predicts a FRET efficiency increase over a much smaller range of time scales than for the experimental FRET efficiency increase (Fig. 4.8a). The C3M exchange can thus not be described by only a combination of sticky Rouse relaxation and chain polydispersity.

The second approach to describe the exchange rate is based on a common description for the expulsion of chains from amphiphilic diblock copolymer micelles. Here, the expulsion is treated as an activated process where the energy barrier depends on the polymer length. For short chains, the energy barrier is assumed to scale linearly with the polymer length,[38] while for longer chains the energy barrier is to assumed to scale with $W^{2/3}$ because these chains are expected to be expelled as a globule.[13] Only the interactions of the outer globule monomers have to be broken to expel the chain, which gives the $W^{2/3}$ dependence. For short chains, the exchange rate is thus given by:

$$k_i = \omega_0 \exp\left(-W_i \frac{aE_a}{k_BT}\right) \tag{4.21}$$

and for long chains by:

$$k_i = \omega_0 \exp\left(-W_i^{2/3} \frac{aE_a}{k_BT}\right) \tag{4.22}$$

Here E_a is the activation energy required to break the interaction of a single monomer, a is a numerical prefactor and ω_0 is the dissociation rate in absence of an energy barrier. Fits of these models to the experimental data give average ionic bond breaking activation energies of $aE_a = 0.3k_BT$ and $aE_a = 1.6k_BT$ for the linear and power law polymer length dependence respectively. These values are smaller than an earlier estimated bond dissociation activation energy, which was $\sim 5k_BT$ at a

100 mM ionic strength.[35] In addition, the ω_0 values are larger than earlier determined.[35] This might mean that different coacervate systems have different bond dissociation times and activation energies. Alternatively, the numerical prefactor a in C3Ms might be relatively small. Another possibility is that this activated process is actually not an accurate description of the micelle exchange rates and therefore result in apparent lower dissociation energies and shorter bond dissociation times.

Apart from evaluating the absolute value of E_a at a single ionic strength, we can also evaluate how E_a varies with ionic strength. For this, we fit these simple activated process models to the FRET micelle exchange data at different salt concentrations using ω_0 as shared fit parameter (Fig. 4.A.9). As explained in the previous section, we would expect that the activation energy E_a depends linearly on the square-root of the salt concentration for an electrostatic activated expulsion process. This indeed seems to be the case (Fig. 4.8b). A simple, purely electrostatic activated expulsion process thus seems to describe the C3M exchange data reasonably well.

The final model is based on another description of the exchange of amphiphilic diblock copolymer micelles, which was used to explain their logarithmic relaxation.[16–18] In this case, the exchange is again described as an activated process, but now with a Rouse type of relaxation included in the prefactor. The prefactor thus has a W^{-2} dependence. The energy barrier is assumed to scale linearly with W in this approach:

$$k_i = \frac{6\pi k_B T}{W_i^2 b^2 \zeta} \exp\left(-a\chi W_i\right) = B W_i^{-2} \exp\left(-a\chi W_i\right) \tag{4.23}$$

The B-term in the prefactor can be estimated based on the polymer characteristics, this gives $B \approx 1.4 \cdot 10^7$ Hz. Fitting this model to the experimental data gives a too slow increase in the normalised FRET efficiency (Fig. 4.8a). In this model, the exchange rate thus depends too strongly on the polymer length to describe the experimental data.

In summary, of the four models, the simple activated processes (Equation 4.21 and 4.22) give the best agreement with the experimental data. However, these models require an activation energy that is lower than expected for an electrostatic process, especially when the activation energy barrier depends linearly on the polymer length W. This might mean that for this complex coacervate system the energy needed to dissociate a single ionic bond is smaller than for other complex coacervate systems or that the numerical prefactor in the activation energy barrier is relatively small. Alternatively, additional factors have to be taken into account apart from the polydispersity of the homopolymer. For example, the length and polydispersity of the oppositely charged block might also play a role, giving a double polydispersity effect that is not included in one of the models. In addition, the broad range of exchange rates might not only be caused by polydispersity of the chains. Computer simulations on amphiphilic block copolymer micelles have suggested that logarithmic relaxation can even occur for monodisperse chains,[29] although in experiments with monodisperse core blocks this logarithmic relaxation has not been observed.[17,39,40] The logarithmic relaxation in the computer simulations was explained by a degeneracy of the energy states of the core blocks which is broken when the chain leaves the core. If these degeneracy effects indeed could play a role in the exchange of amphiphilic diblock copolymer micelles, they might also play a role here. For example, a homopolymer that binds to complete positive blocks only can more easily be expelled than a homopolymer that binds to only parts of different positive blocks, even though both homopolymers have the same number of ionic bonds: in the first case, only non-electrostatic interactions have to be broken, whereas the in the second case the ionic bonds first have to rearrange before expulsion can occur. It would be interesting to follow the exchange of C3Ms with less polydisperse components over a broad range of time scales to determine whether the broad distribution of exchange rates is mainly caused by the chain polydispersity or that other effects play a role as well. Protein containing C3Ms would be a good system for this, since the proteins are monodisperse and therefore only the diblocks introduce polydispersity effects in this system. However, the exchange of these protein containing C3Ms can be fast[6]. Faster measurements are thus required to determine the initial exchange as well.

4.5 Conclusions

In conclusion, we have shown that the expulsion of chains from the core is probably the rate-limiting step in the exchange of equilibrated C3Ms and that their exchange is largely governed by electrostatic interactions. This expulsion-based exchange implies that the exchange rate of C3M components of interest cannot be decreased by adding more stable components with the same charge, which is illustrated by the fact that the exchange rate of the labelled homopolymers was not decreased by replacing the shorter unlabelled homopolymers by longer ones.

We have also demonstrated that the C3M exchange can occur over a broad range of time scales. With the help of our analytical model we have shown that this broad range of time scales indicates the presence of different homopolymer types each with their own exchange rate. These different types might be polymers with different lengths. Of the four different literature models that relate the exchange rate to the polymer lengths, the two simple activated process models give the best agreement to the experimental data. However, these models do not include any other factors apart from polydispersity, while these other factors might also have played a role in the broad distribution of exchange rates. To further elucidate the exact origin of this broad distribution, further experiments are needed.

Any future FRET-based micelle exchange experiment can benefit from our analytical model as it can help to relate the observed FRET increase to the underlying micelle exchange rate. Both our experimental observations and analytical model thus help to further unravel the C3M exchange mechanisms and in this way can help to design more stable C3M encapsulators.

4.A Appendix

4.A.1 ^{1}H NMR spectra

^{1}H NMR spectra were recorded on a Bruker Avance 400 MHz NMR equipped with a BBO probe. A 20 kHz spectral width was used. For every measurement the signal from 32 consecutive acquisitions was added to obtain sufficient signal-to-noise ratio. The measured free induction decays were Fourier transformed, phased, baseline corrected and integrated by using the Bruker NMR software TopSpin 4.0.7.

Dye to chain transfer agent coupling

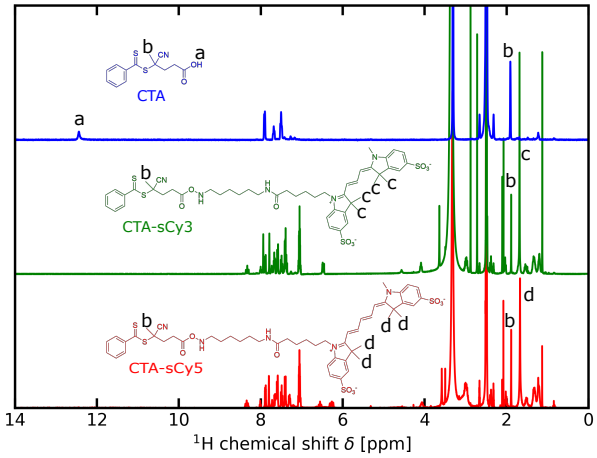

Figure 4.A.1. ^{1}H NMR spectra of the chain transfer agent (CTA), the chain transfer agent after coupling to sulfo cyanine3 (CTA-sCy3) and the chain transfer agent after coupling to sulfo cyanine5 (CTA-sCy) in deuterated DMSO. The disappearance of the proton peak a indicates successful removal of unfunctionalised CTA. The $c : b$ ratio in CTA-sCy3 is 15:3 and the $d : b$ ratio in CTA-sCy5 is 13:3. Both are slightly higher than the expected 12:3 ratio, indicating that still some free dye is present. This small dye excess does not react during the polymerisation and is removed in subsequent the dialysis step.

PEG-*b*-PTMAEMA diblock

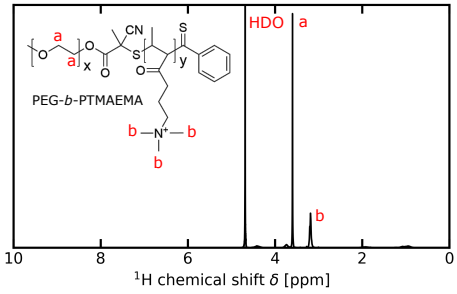

Figure 4.A.2. ^{1}H NMR spectrum of the PEG-*b*-PTMAEMA diblock in D_2O. The $a : b$ ratio is 7.2:5.5. The degree of polymerisation of the PEG block is $x = 220$. Therefore, the degree of polymerisation of the PTMAEMA block $y \approx 4x/9 \cdot 5.5/7.2 \approx 75$.

4.A.2 Light scattering experiments

Micelle molar mass estimation

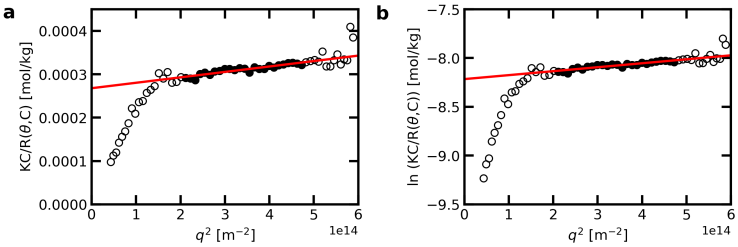

Figure 4.A.3. (a) Zimm plot and (b) Guinier plot for light scattering data of donor micelles at a label fraction $\alpha = 1.0$ and a KCl concentration of 100 mM KCl. The red line indicates the linear fit of the data from which the intercept and thus the micelle molar mass was estimated. For this fit, only the data points marked with solid symbols are used.

Table 4.A.1. Estimated molar masses M_w, micelle radius of gyaration R_g and average number of donors N_D and acceptors N_A per micelle based on Zimm and Guinier analysis of light scattering experiments of donor micelles at a label fraction of $\alpha = 1.0$ and a SPMA concentration of 1 mM for different KCl concentrations.

[KCl] [mM]	M_w [kg/mol]		R_g [nm]		N_D		N_A	
	Zimm	Guinier	Zimm	Guinier	Zimm	Guinier	Zimm	Guinier
10	5.1×10^3	5.1×10^3	35	33	46	46	76	75
100	3.7×10^3	3.7×10^3	37	35	33	33	55	55
200	2.8×10^3	2.8×10^3	43	39	25	25	41	41
300	3.0×10^3	3.0×10^3	41	37	27	27	45	44
400	2.7×10^3	2.7×10^3	42	38	24	24	39	39

Determination of the critical salt concentration

To determine the critical salt concentration at which the micelles fall apart, we stepwise increased the KCl concentration and measured the light scattering intensity after every addition step (Fig. 4.A.4). When the micelles disassemble, the scattering intensity decreases until they reach the point where all micelles are completely disintegrated. This point corresponds to the critical salt concentrations and above this concentration the light scattering per polymer remains approximately constant. In this case, the critical salt concentration is thus ~ 790 mM. We note that the increase in light scattering intensity around ~ 670 mM is probably the result of micelle rearrangement from spherical to wormlike micelles.[27] The wormlike micelles have a larger aggregation number and therefore scatter more light.

We performed the light scattering titrations on an ALV instrument equipped a 660 nm laser at a 90° detection angle. A Schott–Geräte computer-controlled titration setup was used to regulate the addition of titrant, stirring, and delay time between additions. A 6 mL solution of donor micelles ([SPMA] = 1 mM) in 10 mMKCl was prepared. To this solution, a stock solution of 2 M KCl was added in steps of 0.025 mL. After a stirring and delay time of both 60 s, the light scattering intensity was recorded in 10 independent runs of 20 s. The recorded light scattering intensities I are corrected for the total polymer weight concentration C.

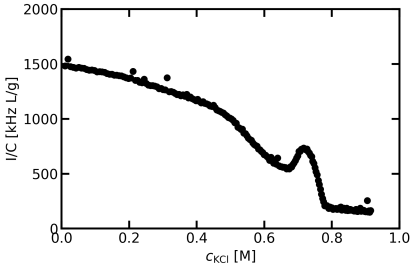

Figure 4.A.4. Light scattering salt titrations of donor micelles with a label fraction $\alpha = 1.0$ starting at a SPMA concentration of 1 mM.

4.A.3 Deconvolution of the emission spectrum

To determine the relative contributions of the donor emission and acceptor emission to the total emission spectrum, we have fit the total spectrum with a weighted sum of the separate donor and acceptor spectra:

$$I_{\text{tot}}(\lambda) = dI_D(\lambda) + aI_A(\lambda) \tag{4.A.1}$$

Here $I_{\text{tot}}(\lambda)$ it the total intensity at a wavelength λ and $I_D(\lambda)$ and $I_A(\lambda)$ are the intensity of the donor and acceptor spectrum at this wavelength respectively. The prefactors d and a give the relative contribution of the donor and acceptor. These prefactors are the fit parameters. To perform this fit, we have first approximated both the donor and acceptor emission spectrum with a sum of a two log normal functions:

$$I(\lambda) = \frac{x}{\lambda\sigma_1\sqrt{2\pi}} \exp\left(-\frac{(\ln(\lambda)-\mu_1)^2}{2\sigma_1^2}\right) + \frac{1-x}{\lambda\sigma_2\sqrt{2\pi}} \exp\left(-\frac{(\ln(\lambda)-\mu_2)^2}{2\sigma_2^2}\right) \tag{4.A.2}$$

here $I(\lambda)$ is the intensity of the donor or acceptor. For the donor spectrum, we have used $x = 0.535$, $\sigma_1 = 1.90 \times 10^{-2}$, $\mu_1 = 6.34$, $\sigma_2 = 3.99 \times 10^{-2}$ and $\mu_2 = 6.39$. For the acceptor spectrum, we have used $x = 0.678$, $\sigma_1 = 2.16 \times 10^{-2}$, $\mu_1 = 6.51$, $\sigma_2 = 5.29 \times 10^{-2}$ and $\mu_2 = 6.55$. These values were obtained by fitting Equation 4.A.2 to the donor or acceptor emission spectrum using a Monte Carlo fit algorithm.

To fit Equation 4.A.1 to the measured emission spectra, we have used the non-linear least square fit algorithm as implemented in the python package SciPy. Two fit examples are given in Fig. 4.A.5. After fitting the data, the total donor intensity and total acceptor intensity, needed to calculate the FRET efficiency, were obtained by integrating $dI_D(\lambda)$ and $aI_A(\lambda)$ over the wavelength range $\lambda = 500\,\text{nm}$ to $\lambda = 800\,\text{nm}$.

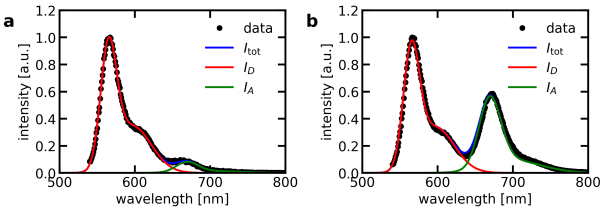

Figure 4.A.5. Fit of Equation 4.A.1 to two example emission spectra corrected for direct acceptor excitation. (a) Emission spectrum measured in an exchange measurement at 100 mM KCl, a SPMA concentration of 1 mM, a label fraction $\alpha = 0.2$ at $t = 4.0\,\text{h}$ (b) Emission spectrum of mixed micelles at 100 mM KCl, a SPMA concentration of 1 mM and a label fraction $\alpha = 1.0$.

4.A.4 FRET intensity $E(t)$ as function of time after mixing t

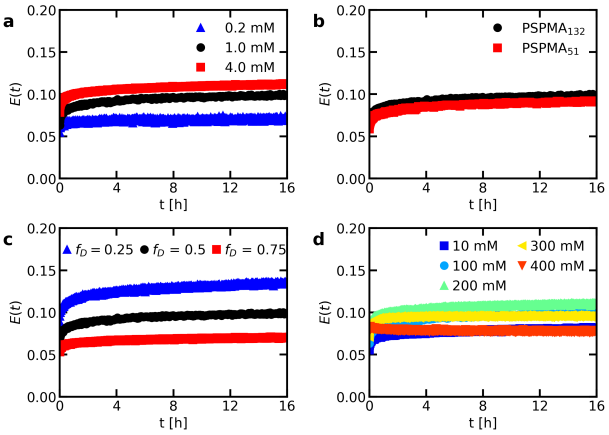

Figure 4.A.6. FRET efficiency $E(t)$ as function of time after mixing t for (a) different monomer concentrations; (b) different unlabelled homopolymer lengths; (c) different fractions of donor micelles and (d) different salt concentrations.

4.A.5 Estimation of the free polymer fraction

For all micelle concentrations, the concentration of polymers that are not part of a micelle (the free polymers) is equal to the critical micelle concentration cmc. The free polymer fraction f at a concentration c is thus given by:

$$f = \begin{cases} 1, & \text{if } c \leq cmc \\ \frac{cmc}{c}, & \text{if } c > cmc \end{cases} \tag{4.A.3}$$

Only the polymers that are part of the micelle are close enough to each other for FRET to occur and therefore only these polymers contribute to the FRET efficiency of the sample. The measured FRET efficiency will thus depend on the free polymer fraction, which decreases with increasing monomer concentration (Equation 4.A.3). We have measured an apparent FRET efficiency E^{app} at different monomer concentrations (Fig. 4.A.7). We call it an apparent FRET efficiency because we did not correct for direct acceptor excitation and differences in self-quenching. This apparent FRET efficiency can be related to the free polymer fraction by:

$$E^{\text{app}} = (1 - f)E_{\text{micelle}} + E_{\text{baseline}} \tag{4.A.4}$$

here $(1-f)$ is the fraction of polymers that are part of a micelle, E_{micelle} is the average FRET efficiency in a micelle (without correction for differences in self-quenching) and E_{baseline} is a correction term to account for direct acceptor excitation. We note that taking E_{baseline} as a constant is a simplification, as in reality the direct acceptor excitation emission will depend on whether the acceptor polymers are part of a micelle or not due to refractive index differences and differences in self-quenching. However, we do not expect that this simplification highly affects the onset of the FRET increase and thus also hardly has an effect the determination of the critical micelle concentration.

By comparing Equations 4.A.1 and 4.A.4 to the epxerimental data, we find that for 10 mM KCl the critical micelle concentration is ~ 7 μM and for 400 mM KCl the critical micelle concentration is ~ 20

μM (Fig. 4.A.7). For micelles at 400 mM KCl and a SPMA monomer concentration $c = 1$ mM, the free polymer fraction is thus $f \approx 0.02$.

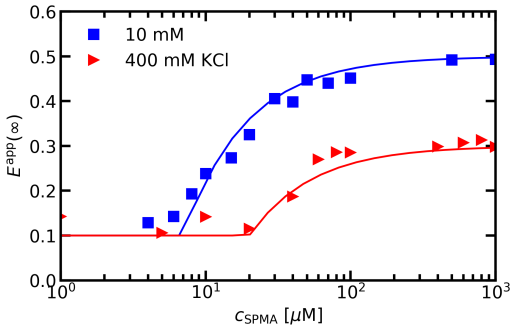

Figure 4.A.7. Apparent FRET efficiency $E^{app}(\infty)$ of mixed micelles at a label fraction $\alpha = 1.0$ as function of SPMA monomer concentration. This apparent FRET efficiency is not corrected for direct acceptor excitation and differences between donor and acceptor self-quenching. Solid lines are calculated with Equations 4.A.3 and 4.A.4 with cmc = 7 μM, $E_{micelle} = 0.40$ and $E_{baseline} = 0.10$ for 10 mM KCl and cmc = 20 μM, $E_{micelle} = 0.20$ and $E_{baseline} = 0.10$ for 400 mM KCl.

4.A.6 Bleaching test of equilibrated mixed micelles

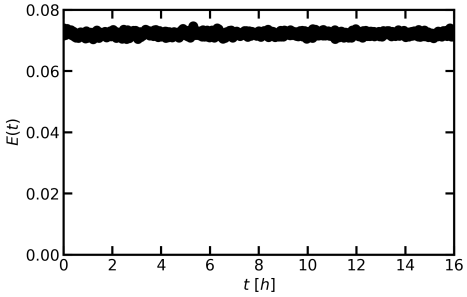

Figure 4.A.8. FRET efficiency E of mixed micelles at a label fraction $\alpha = 0.2$, a 400 mM KCl concentration and a SPMA concentration of 1.0 mM measured over 16 h.

4.A.7 Fits of the activated process models to the FRET micelle exchange data at different salt concentrations

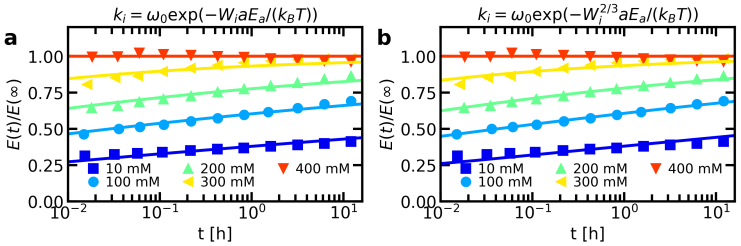

Figure 4.A.9. Fits of the activated process models to the FRET micelle exchange data at different salt concentrations using ω_0 as shared fit parameter. To ensure that the data at short and long time scales have similar weighting, the exchange data is first binned in time steps that are evenly spaced on a logarithmic time scale. The values for ν, N and the polymer length distributions are used as constants in the fit calculation. The values for ν and N are obtained from Table 4.1 of the main text and the polymer length distributions are obtained from GPC data assuming a Schulz-Zimm distribution. (a) Fit to an activated process where the total activation energy scales linearly with the polymer length ($k_i = \omega_0 \exp(-W_i E_a/(k_B T))$) yielding $\omega_0 = 9.5 \times 10^2$ Hz and $aE_a = 0.54 k_B T$, $aE_a = 0.32 k_B T$, $aE_a = 0.22 k_B T$, $aE_a = 0.14 k_B T$ and $aE_a = 0.04 k_B T$ for a salt concentration of 10 mM, 100 mM, 200 mM, 300 mM and 400 mM respectively. (b) Fit to an activated process where the total activation energy scales with the 2/3 power the polymer length ($k_i = \omega_0 \exp(-W_i^{2/3} E_a/(k_B T))$) yielding $\omega_0 = 1.2 \times 10^6$ Hz and $aE_a = 2.4 k_B T$, $aE_a = 1.7 k_B T$, $aE_a = 1.3 k_B T$, $aE_a = 0.97 k_B T$ and $aE_a = 0.42 k_B T$ for a salt concentration of 10 mM, 100 mM, 200 mM, 300 mM and 400 mM respectively.

4.A.8 Analytical solution of the differential equation for $P(n,t)$

As explained in the main text, the differential equation describing the changes in probability P to find a micelle with n fluorophores is given by:

$$\frac{dP(n,t)}{dt} = fNkP(n-1,t) - (fNk + nk)P(n,t) + (n+1)kP(n+1) \tag{4.A.5}$$

By using the generating function $G(s,t) = \sum_{n=0}^{\infty} s^n P(n,t)$ we can rewrite Equation 4.A.5 to:

$$\frac{\partial G(s,t)}{\partial t} = \sum_{n=0}^{\infty} s^n \left[fNkP(n-1,t) - (fNk + nk)P(n,t) + (n+1)kP(n+1)\right] \tag{4.A.6}$$

A change of summation variables $n \rightarrow n-1$ and $n \rightarrow n+1$ in the first and last term respectively gives:

$$\begin{aligned}
\frac{\partial G(s,t)}{\partial t} &= \sum_{n=0}^{\infty} s^{n+1} fNkP(n,t) - s^n(fNk + nk)P(n,t) + s^{n-1} nkP(n,t) \\
&= \sum_{n=0}^{\infty} fNk(s^{n+1} - s^n)P(n,t) + nk(s^{n-1} - s^n)P(n,t) \\
&= (s-1)fNk \sum_{n=0}^{\infty} s^n P(n,t) + k(s^{-1} - 1) \sum_{n=0}^{\infty} s^n nP(n,t)
\end{aligned} \tag{4.A.7}$$

The $\sum_{n=0}^{\infty} s^n nP(n,t)$ part in Equation 4.A.7 can be rewritten by making use of the property that $J(a,x) = \sum_n ax^n$ gives $x\frac{\partial J}{\partial x} = \sum_n anx^n$:

$$\begin{aligned}\frac{\partial G(s,t)}{\partial t} &= (s-1)fNk\sum_{n=0}^{\infty} s^n P(n,t) + k(s^{-1}-1)s\frac{\partial}{\partial s}\sum_{n=0}^{\infty} s^n P(n,t)\\ &= (s-1)fNkG(s,t) - k(s-1)\frac{\partial G(s,t)}{\partial s}\end{aligned} \tag{4.A.8}$$

The steady state solution of this partial differential equation at $t \to \infty$ follows from $\frac{\partial G_{st}}{\partial t} = 0$ and $G(1,t) = 1$:

$$G_{st} = e^{fN(s-1)} = e^{-fN}e^{fNs} = e^{-fN}\sum_{n=0}^{\infty}\frac{(fNs)^n}{n!} = \sum_{n=0}^{\infty} s^n e^{-fN}\frac{(fN)^n}{n!} = \sum_{n=0}^{\infty} s^n P_{st}(n) \tag{4.A.9}$$

The steady state probability distribution P_{st} is thus given by

$$P_{st}(n) = e^{-fN}\frac{(fN)^n}{n!} \tag{4.A.10}$$

This is a Poisson distribution with an average of fN.

The time-dependent solution of the partial differential equation (Equation 4.A.8) can be found by using the Lagrange method. This gives as general solution:

$$Ge^{-fNs} = F(s - 1e^{-kt}) \tag{4.A.11}$$

where F is any analytical function. The specific solution can be found from the initial condition. We distinguish two cases:

1. The number of donors in acceptor micelles and *vice versa*
2. The number of donors in donor micelles and the number of acceptors in acceptor micelles

In the first case, the initial fluorophore number is 0, therefore $P(n=0,0) = 1$ and $P(n \neq 0,0) = 0$. This gives $G(s,0) = 1$. From this initial condition we get for the first case:

$$F((s-1)e^{-kt}) = e^{-fN}e^{-fN(s-1)e^{-kt}} \tag{4.A.12}$$

Substitution of Equation 4.A.12 in Equation 4.A.11 gives the specific solution for the first case:

$$G(s,t) = e^{\lambda(t)(s-1)} \tag{4.A.13}$$

where $\lambda(t) = fN(1-e^{-kt})$. This can be rewritten to:

$$G(s,t) = e^{-\lambda(t)}\sum_{n=0}^{\infty}\frac{(\lambda(t)s)^n}{n!} = \sum_{n=0}^{\infty} s^n e^{-\lambda(t)}\frac{(\lambda(t))^n}{n!} = \sum_{n=0}^{\infty} s^n P(n,t) \tag{4.A.14}$$

The probability P at a certain time t to have a donor micelle with n acceptors or an acceptor micelle with n donors is thus given by:

$$P(n,t) = e^{-\lambda(t)}\frac{\lambda(t)^n}{n!} \tag{4.A.15}$$

For the second case we make use of the fact that the donor micelles and acceptor micelles are equilibrated when they are mixed. This means that they are in steady state. Only in this case,

no other micelle types are present and therefore $f = 1$. Their initial distribution is thus given by: $P(n,0) = e^{-N}\frac{N^n}{n!}$. This gives $G(s,0) = e^{-N}\sum_{n=0}^{\infty}\frac{(sN)^n}{n!} = e^{N(s-1)}$. In this way we get for the second case:

$$F((s-1)e^{-kt}) = e^{-fN}e^{(N-fN)(s-1)e^{-kt}} \tag{4.A.16}$$

Substitution of Equation 4.A.16 in Equation 4.A.11 gives the specific solution for the second case:

$$G(s,t) = e^{(s-1)\mu(t)} \tag{4.A.17}$$

where $\mu(t) = N(f + (1-f)e^{-kt})$. Equation 4.A.17 can again be rewritten to give the probability to find a donor micelle with n donors or an acceptor micelle with n acceptors at a time t:

$$P(n,t) = e^{-\mu(t)}\frac{\mu(t)^n}{n!} \tag{4.A.18}$$

References

[1] Magana, J. R.; Sproncken, C.; Voets, I. K. On Complex Coacervate Core Micelles: Structure-Function Perspectives. *Polymers* **2020**, *12*, 1953.

[2] Voets, I. K.; de Keizer, A.; Cohen Stuart, M. A. Complex coacervate core micelles. *Adv. Colloid Interface Sci.* **2009**, *147*, 300–318.

[3] Kakizawa, Y.; Kataoka, K. Block copolymer micelles for delivery of gene and related compounds. *Adv. Drug Deliv. Rev.* **2002**, *54*, 203–222.

[4] Harada, A.; Kataoka, K. Supramolecular assemblies of block copolymers in aqueous media as nanocontainers relevant to biological applications. *Prog. Polym. Sci.* **2006**, *31*, 949–982.

[5] Holappa, S.; Kantonen, L.; Andersson, T.; Winnik, F.; Tenhu, H. Overcharging of polyelectrolyte complexes by the guest polyelectrolyte studied by fluorescence spectroscopy. *Langmuir* **2005**, *21*, 11431–11438.

[6] Nolles, A.; Hooiveld, E.; Westphal, A. H.; van Berkel, W. J.; Kleijn, J. M.; Borst, J. W. FRET Reveals the Formation and Exchange Dynamics of Protein-Containing Complex Coacervate Core Micelles. *Langmuir* **2018**, *34*, 12083–12092.

[7] Amann, M.; Diget, J. S.; Lyngsø, J.; Pedersen, J. S.; Narayanan, T.; Lund, R. Kinetic Pathways for Polyelectrolyte Coacervate Micelle Formation Revealed by Time-Resolved Synchrotron SAXS. *Macromolecules* **2019**, *52*, 8227–8237.

[8] Wu, H.; Ting, J. M.; Tirrell, M. V. Mechanism of Dissociation Kinetics in Polyelectrolyte Complex Micelles. *Macromolecules* **2020**, *53*, 102–111.

[9] Berret, J.-F.; Cristobal, G.; Hervé, P.; Oberdisse, J.; Grillo, I. Structure of colloidal complexes obtained from neutral/poly-electrolyte copolymers and oppositely charged surfactants. *Eur. Phys. J. E* **2002**, *9*, 301–311.

[10] Wu, H.; Ting, J. M.; Werba, O.; Meng, S.; Tirrell, M. V. Non-equilibrium phenomena and kinetic pathways in self-assembled polyelectrolyte complexes. *J. Chem. Phys.* **2018**, *149*, 163330.

[11] Hofs, B.; De Keizer, A.; Cohen Stuart, M. On the stability of (highly aggregated) polyelectrolyte complexes containing a charged-block-neutral diblock copolymer. *J. Phys. Chem. B* **2007**, *111*, 5621–5627.

[12] Lindhoud, S.; Norde, W.; Cohen Stuart, M. A. Reversibility and relaxation behavior of polyelectrolyte complex micelle formation. *J. Phys. Chem. B* **2009**, *113*, 5431–5439.

[13] Dormidontova, E. E. Micellization kinetics in block copolymer solutions: Scaling model. *Macromolecules* **1999**, *32*, 7630–7644.

[14] Lund, R.; Willner, L.; Richter, D.; Dormidontova, E. E. Equilibrium chain exchange kinetics of diblock copolymer micelles: Tuning and logarithmic relaxation. *Macromolecules* **2006**, *39*, 4566–4575.

[15] Lund, R.; Willner, L.; Stellbrink, J.; Lindner, P.; Richter, D. Logarithmic chain-exchange kinetics of diblock copolymer micelles. *Phys. Rev. Lett.* **2006**, *96*, 068302.

[16] Choi, S.-H.; Lodge, T. P.; Bates, F. S. Mechanism of molecular exchange in diblock copolymer micelles: hypersensitivity to core chain length. *Phys. Rev. Lett.* **2010**, *104*, 047802.

[17] Zinn, T.; Willner, L.; Lund, R.; Pipich, V.; Richter, D. Equilibrium exchange kinetics in n-alkyl–PEO polymeric micelles: single exponential relaxation and chain length dependence. *Soft Matter* **2012**, *8*, 623–626.

[18] Lu, J.; Choi, S.; Bates, F.; Lodge, T. Molecular exchange in diblock copolymer micelles: bimodal distribution in core-block molecular weights. *ACS Macro Lett.* **2012**, *1*, 982–985.

[19] Lu, J.; Bates, F.; Lodge, T. Chain exchange in binary copolymer micelles at equilibrium: confirmation of the independent chain hypothesis. *ACS Macro Lett.* **2013**, *2*, 451–455.

[20] Wang, E.; Lu, J.; Bates, F. S.; Lodge, T. P. Effect of corona block length on the structure and chain exchange kinetics of block copolymer micelles. *Macromolecules* **2018**, *51*, 3563–3571.

[21] Wu, H. Correlations between the Rayleigh ratio and the wavelength for toluene and benzene. *Chem. Phys.* **2010**, *367*, 44–47.

[22] Polik, W. F.; Burchard, W. Static light scattering from aqueous poly (ethylene oxide) solutions in the temperature range 20-90 C. *Macromolecules* **1983**, *16*, 978–982.

[23] Mertoglu, M.; Laschewsky, A.; Skrabania, K.; Wieland, C. New water soluble agents for reversible Addition-Fragmentation chain transfer polymerization and their application in aqueous solutions. *Macromolecules* **2005**, *38*, 3601–3614.

[24] Naderi, A.; Iruthayaraj, J.; Vareikis, A.; Makuška, R.; Claesson, P. M. Surface properties of bottle-brush polyelectrolytes on mica: effects of side chain and charge densities. *Langmuir* **2007**, *23*, 12222–12232.

[25] Voets, I. K.; de Keizer, A.; Leermakers, F. A.; Debuigne, A.; Jérôme, R.; Detrembleur, C.; Cohen Stuart, M. A. Electrostatic hierarchical co-assembly in aqueous solutions of two oppositely charged double hydrophilic diblock copolymers. *Eur. Polym. J.* **2009**, *45*, 2913–2925.

[26] Olejko, L.; Bald, I. FRET efficiency and antenna effect in multi-color DNA origami-based light harvesting systems. *RSC Adv.* **2017**, *7*, 23924–23934.

[27] van der Kooij, H. M.; Spruijt, E.; Voets, I. K.; Fokkink, R.; Cohen Stuart, M. A.; van der Gucht, J. On the stability and morphology of complex coacervate core micelles: From spherical to wormlike micelles. *Langmuir* **2012**, *28*, 14180–14191.

[28] Nolles, A.; Westphal, A. H.; de Hoop, J. A.; Fokkink, R. G.; Kleijn, J. M.; van Berkel, W. J.; Borst, J. W. Encapsulation of GFP in complex coacervate core micelles. *Biomacromolecules* **2015**, *16*, 1542–1549.

[29] Daza, F. A. G.; Avalos, J. B.; Mackie, A. D. Logarithmic exchange kinetics in monodisperse copolymeric micelles. *Phys. Rev. Lett.* **2017**, *118*, 248001.

[30] Kembaren, R.; Fokkink, R.; Westphal, A. H.; Kamperman, M.; Kleijn, J. M.; Borst, J. W. Balancing Enzyme Encapsulation Efficiency and Stability in Complex Coacervate Core Micelles. *Langmuir* **2020**, *36*, 8494–8502.

[31] Spruijt, E.; Westphal, A. H.; Borst, J. W.; Cohen Stuart, M. A.; van der Gucht, J. Binodal compositions of polyelectrolyte complexes. *Macromolecules* **2010**, *43*, 6476–6484.

[32] Li, L.; Srivastava, S.; Andreev, M.; Marciel, A. B.; de Pablo, J. J.; Tirrell, M. V. Phase behavior and salt partitioning in polyelectrolyte complex coacervates. *Macromolecules* **2018**, *51*, 2988–2995.

[33] Spruijt, E.; Sprakel, J.; Lemmers, M.; Cohen Stuart, M. A.; Van Der Gucht, J. Relaxation dynamics at different time scales in electrostatic complexes: time-salt superposition. *Phys. Rev. Lett.* **2010**, *105*, 208301.

[34] Spruijt, E.; Cohen Stuart, M. A.; van der Gucht, J. Linear viscoelasticity of polyelectrolyte complex coacervates. *Macromolecules* **2013**, *46*, 1633–1641.

[35] Spruijt, E.; van den Berg, S. A.; Cohen Stuart, M. A.; van der Gucht, J. Direct measurement of the strength of single ionic bonds between hydrated charges. *ACS Nano* **2012**, *6*, 5297–5303.

[36] Syed, V. M.; Srivastava, S. Time–Ionic Strength Superposition: A Unified Description of Chain Relaxation Dynamics in Polyelectrolyte Complexes. *ACS Macro Lett.* **2020**, *9*, 1067–1073.

[37] Marciel, A. B.; Srivastava, S.; Tirrell, M. V. Structure and rheology of polyelectrolyte complex coacervates. *Soft Matter* **2018**, *14*, 2454–2464.

[38] Li, Z.; Dormidontova, E. E. Equilibrium chain exchange kinetics in block copolymer micelle solutions by dissipative particle dynamics simulations. *Soft Matter* **2011**, *7*, 4179–4188.

[39] König, N.; Willner, L.; Pipich, V.; Zinn, T.; Lund, R. Cooperativity during melting and molecular exchange in micelles with crystalline cores. *Phys. Rev. Lett.* **2019**, *122*, 078001.

[40] König, N.; Willner, L.; Pipich, V.; Mahmoudi, N.; Lund, R. Tale of Two Tails: Molecular Exchange Kinetics of Telechelic Polymer Micelles. *Phys. Rev. Lett.* **2020**, *124*, 197801.

Chapter 5

DNA dynamics in complex coacervate droplets and micelles

Dynamics plays an important role in both complex coacervates and complex coacervate core micelles (C3Ms). Yet, to date, the effect of chain length on the dynamics effect is still not fully understood. The DNA complexes provide a versatile platform to further elucidate these chain length effects because the DNA is monodisperse and its length can be easily adapted. Therefore, we study in this chapter the dynamics of fluorescently labelled ssDNA in both complex coacervate droplets and micelles. The DNA dynamics in the complex coacervate droplets is probed by fluorescence recovery after photobleaching (FRAP). We observe that the DNA diffusion coefficient depends more strongly on the DNA length than predicted by the sticky Rouse model and we show that this can be partly explained by changes in complex coacervate density, but that also other factors might play a role. We measure the molecular exchange of C3Ms by making use of Förster resonance energy transfer (FRET) and complement these measurements with Langevin dynamics simulations. We conclude that chain length polydispersity is the main cause of a broad distribution of exchange rates. We hypothesise that the different exchange rates that we observe for the monodisperse DNA are mainly caused by differences in dye interactions and show that the dye can indeed have a large effect on the C3M exchange. In addition, we show that a new description of the C3M molecular exchange is required that accounts among others for the effect of the length of the oppositely charged core species. Together our findings can help to better understand the dynamics in both specific DNA systems and in complex coacervate droplets and micelles in general.

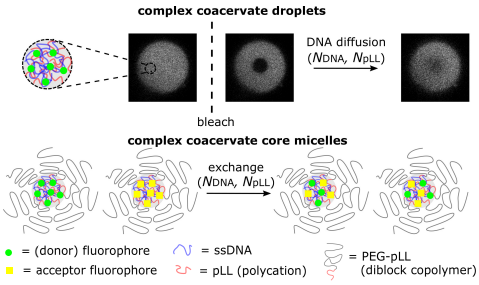

This chapter is based on: Inge Bos, Eline Brink, Lucile Michels and Joris Sprakel. DNA dynamics in complex coacervate droplets and micelles. *Soft Matter* **2022** *18*(10), 2012-2027.

5.1 Introduction

DNA is a negatively charged polyelectrolyte and can form electrostatic complexes with positively charged macro-ions. This principle underlies for example DNA condensation in chromatin where the DNA binds to positively charged histone proteins.[1,2] In addition, the formation of membraneless organelles inside cells is often based on liquid-liquid phase separation of nucleic acids with oppositely charged proteins.[3–5] This liquid-liquid phase separation also occurs for synthetic oppositely charged polyelectrolytes and the liquid phase formed by the polyelectrolyte complex is usually called a complex coacervate. Apart from their ability to phase separate, also other properties of the membraneless organelles have recently been mimicked in artificial systems using both natural and synthetic polyelectrolytes,[5] for example their ability to enhance catalysis[6,7] or their ability to form multiple phases in one complex coacervate droplet.[8,9]

When DNA is mixed with a cationic-neutral diblock copolymer, it can form complex coacervate core micelles (C3Ms) instead of complex coacervate droplets: the repulsive interactions between the neutral blocks prevent further growth of the complex coacervate and in this way thermodynamically stable nanostructures can be formed instead of the macroscopic complex coacervates that will eventually form when DNA is mixed with polycations without neutral blocks. The C3M core is formed by the DNA and the cationic blocks, while the neutral blocks form the micelle corona. The micelle corona forms a protective layer around the micelle core and prevents micelle coalescence.[10] In this way, micelles with specific polymer aggregation numbers and sizes of typically 10 to 100 nm are formed[11–13] that can protect their core components from external components. Their protective properties as well as their well-defined small size makes these DNA complex coacervate core micelles promising DNA-based medicine delivery tools.[14–17]

Studying the liquid-like DNA polyelectrolyte complexes is not only useful to better understand the formation of membraneless organelles and to improve the formation of DNA-based medicine delivery tools, but also to give fundamental insights into polyelectrolyte complexes in general. In particular, the effect of chain length and chain length polydispersity can be systemically studied with DNA because specific DNA sequences can be synthesised. This yields monodisperse DNA whose length can be systematically varied by changing the sequence. At the moment, the chain length effects on the complex coacervates and C3Ms are not completely understood. Especially the chain length effect on the coacervate dynamics is not well understood, as we will explain below.

The dynamics of complex coacervates determines the response of complex coacervate materials to deformation[18,19] and might determine their response time to dissociation triggers.[20] The chain length effect on the dynamics in complex coacervates is usually described by the sticky Rouse model[21] where the ionic bonds act as sticky points that slow down the dynamics.[18,19] In the sticky Rouse model, the overall polymer relaxation time scales with the squared number of intermolecular sticky bonds, which means for polyelectrolytes that the relaxation time should scale with the square of the polyelectrolyte length. For complex coacervates with matched chain length this description seems to work well,[18] but for complexes where the lengths of the anionic and cationic chain differ, the situation is more complex. In some cases, the dynamics seems to be solely governed by one of the two polyelectrolytes, while the length of the other polyelectrolyte does not have any effect.[18] Since only few studies have focused on polyion pairs with incommensurate lengths, an understanding of these asymmetry effects, and with that a complete description of coacervate dynamics, is lacking.

The molecular exchange dynamics of complex coacervate core micelles determines how often the core components are exposed to the surroundings and in this way the level of protection that the C3M offers to a cargo that it encapsulates. In Chapter 4 we have used Förster resonance energy transfer (FRET) to measure this molecular exchange of C3Ms and observed a broad range of exchange rates, similar to what has been observed earlier for other C3Ms.[22] We hypothesised that this large difference in exchange rates is the result of chain polydispersity. Recently, the molecular exchange of C3Ms

was also measured by small angle neutron scattering (SANS) and also here the presence of different exchange rates was explained by chain polydispersity.[23] However, this polydispersity hypothesis has not been confirmed yet, since so far only the exchange of polydisperse polymers has been measured. Measuring the exchange of C3Ms with ssDNA allows to thoroughly test this hypothesis because the DNA is monodisperse and its length can be systematically varied.

Apart from the limited knowledge on the chain lengths effect on the dynamics in both complex coacervates and C3Ms, also little is known on how the dynamics inside bulk coacervates compares to that in the nanoscopically confined interior of C3Ms, and to what extent the dynamics in bulk coacervates is predictive for the exchange dynamics in micelles. Therefore, we study in this chapter the dynamics of single stranded DNA in both complex coacervate droplets and micelles and we also compare these systems. For the complex coacervates droplets, we use fluorescence recovery after photobleaching (FRAP) to measure the diffusion coefficient of fluorescently labelled ssDNA. For the C3Ms, we use FRET-based exchange measurements to follow the exchange of both the ssDNA and the diblock copolymers and we complement these measurements with Langevin dynamics simulations. In this way, we show that both the DNA diffusion in complex coacervates and the DNA exchange of C3Ms depend on both the DNA chain length and the cationic chain length. We observe that the DNA diffusion coefficient shows a stronger dependence on the DNA length than predicted by the sticky Rouse model, which can only be partially explained by the chain length effect on coacervate density. In addition, we conclude from the comparison of the exchange of the monodisperse ssDNA and the polydisperse diblock copolymer that chain length polydispersity is indeed the main factor underlying the earlier observed broad distribution of exchange times. We hypothesise that the different exchange rates that we observe for the monodisperse DNA are mainly caused by differences in interactions of the donor and acceptor fluorophore label and show that the fluorophore can indeed have a large effect on the C3M exchange. Finally, we discuss a new description of the C3M exchange to account among others for the effect of the chain length of the oppositely charged core species on the exchange rate. Together our results can help to better understand both DNA specific systems and complex coacervates droplets and micelles in general.

5.2 Materials and methods

5.2.1 Materials

The unlabelled single stranded DNA oligonucleotides and the fluorescently labelled oligonucleotides with a donor (cyanine3 or atto488) or acceptor (cyanine5 or atto532) dye attached to the 5′ end were purchased from Integrated DNA Technologies. The oligonucleotide sequences (Table S1) were the same as described by Lueckheide *et al.*.[13] These sequences are based on a sequence complementary to human microRNA-21 and are designed in such a way that the secondary structure formation and self-dimerisation is minimised. Stock solutions of oligonucleotides were prepared by resuspending in nuclease free water at a monomer concentration of 10 mM based on the absorption measurements by the manufacturer.

The poly(L-lysine) homopolymers with number averaged lengths of 11, 55 and 234 amino acids (pLL11, pLL55 and pLL234 respectively) and the poly(ethyleneglycol)(5k)-*b*-poly(L-lysine)$_{47}$ (PEG-5k-pLL47, where 5k indicates the 5300 g/mol molecular weight of the poly(ethyleneglycol) block and 47 indicates to the number averaged amino acid length of the poly(L-lysine) block) and poly(ethyleneglycol)(20k)-*b*-poly(L-lysine)$_{212}$ (PEG-20k-pLL212) diblock copolymers were purchased from Alamanda Polymers as chloride salts. The overall polydispersities of the diblock copolymers as measured by the manufacturer were 1.06 for PEG-5k-pLL47 and 1.03 for PEG-20k-pLL212. Stock solutions of pLL homopolymers and diblock copolymers were prepared by dissolving in 1× phosphate-

buffered saline (137 mM NaCl, 2.7 mM KCl, 8 mM Na_2HPO_4, 2 mM KH_2PO_4, pH 7.4) (PBS) and subsequent sonication for 10 minutes, as recommended by the manufacturer.

Sulfo-cyanine 3 NHS ester (sCy3) and sulfo-cyanine 5 NHS ester (sCy5) dyes for PEG-5k-pLL47 labelling were purchased from Lumiprobe.

5.2.2 PEG-pLL labelling

Fluorescently labelled PEG-5k-pLL47 was obtained by using a NHS coupling reaction between the amino groups of the poly(L-lysine) block and the sCy3 or sCy5 dye. The PEG-5k-pLL47 and the sulfo-cyanine dye (either sCy3 or sCy5) were dissolved in 1X PBS to give a final lysine monomer concentration of 25 mM and a dye concentration of 0.5 mM. This corresponds to a maximum label degree of on average 1 dye per polymer chain, but the coupling efficiency is not 100% and therefore the average numbers of dyes per polymer chain is lower than 1. The reaction mixture was stirred for 4 hours at room temperature. Subsequently, the reaction mixture was dialysed for several days and afterwards the sample was freeze-dried to obtain the fluorescently labelled PEG-5k-pLL47-sCy3 and PEG-5k-pLL47-sCy5.

5.2.3 FRAP measurements

Complex coacervate samples for fluorescence recovery after photo-bleaching (FRAP) measurements were prepared by mixing stock solutions of oligonucleotides labelled with cyanine3, unlabelled oligonucleotides of the same length and poly(L-lysine) in 1X PBS. To minimise the effect of dye interactions, the fraction of labelled oligonucleotides α was only 0.002, 0.004 and 0.008 for the nt22, nt44 and nt88 nucleotides respectively. For the nt44 and nt88 nucleotides, an anionic and cationic monomer concentration of 2.5 mM was used (which corresponds to a charge ratio of 1:1). For the nt22 nucleotides, both the anionic and cationic monomer concentration was increased to 5 mM to ensure that also for these samples large enough droplets were formed to analyse the FRAP data with an infinite medium diffusion model (i.e. the droplet size is larger than 2.3 times the bleached spot size).[24] The samples were prepared directly at microscopy glass slides coated with a 5 wt % poly(vinyl alcohol) solution, sealed by gluing a cover slip on top of the slide and measured 1 h to 4 h after preparation. The FRAP measurements were performed on a Nikon C2 laser scanning confocal microscope with a 60X 1.4 NA oil-immersion objective. A 488 nm laser was used for both imaging and bleaching. The images were recorded at a 4X digital zoom and consisted of 512x512 pixels. Bleaching of a spherical region with a 3 μm diameter was performed in the middle of a coacervate droplet. The 3D spherical shape of the bleach profile, which is required for the data analysis with the 3D diffusion model,[24] was confirmed by a z-stack measurement acquired immediately after bleaching a 3 μm diameter region of a coacervate droplet of a nt88/pLL234 sample (Fig. 5.A.1a,b). Ten images were recorded before bleaching and 301 images were recorded after bleaching to follow the recovery. For the nt44 and nt88 samples, the imaging interval was 2 s and for the nt22 samples the imaging interval was 1.4 s.

Image analysis of the FRAP data was based on the method described by Taylor *et al.*[24] The fluorescence intensity concentration C inside the bleach spot was normalised according to:

$$< C > (t) = \frac{< C(r,t) > - < C(r,0) >}{< C_{\mathrm{ref}} > - < C(r,0) >} \tag{5.1}$$

where $< C(r,t) >$ is the average fluorescence intensity in the bleach spot at a time t after bleaching and C_{ref} is the average reference intensity in the bleach spot before bleaching. To account for movements of the coacervate droplets, the position of the center of the bleach spot was determined for every image in the recovery sequence separately. During the recovery, some additional bleaching occurred. Corrections for this bleaching were calculated from the intensity of a coacervate region in the image outside the bleached spot.

To obtain the characteristic diffusion time τ_D, the bleaching corrected data was fitted with a 3D diffusion model in an infinite medium:[24]

$$< C > (t) = 1 - \mathrm{erf}\left(\sqrt{\frac{\tau_D}{t}}\right) + \sqrt{\frac{t}{\pi\tau_D}}\left[3 - \exp\left(-\frac{\tau_D}{t}\right)\right] + 2\sqrt{\frac{t^3}{\pi\tau_D^3}}\left[\exp\left(-\frac{\tau_D}{t}\right) - 1\right] \qquad (5.2)$$

The diffusion coefficient D^{app} was calculated from the obtained characteristic time τ_D by $D^{\mathrm{app}} = R^2/\tau_D$ where R is the radius of the bleach region. The reported diffusion coefficients are the average of the diffusion coefficient of FRAP measurements at five different positions in the sample. For all fits, we observed a small systematic deviation between the fit and the data at the start of the recovery curve with the fit showing a slightly faster recovery than the data. This is probably because the bleaching by the laser was not perfect and also some molecules outside the bleach spot were bleached, as shown by a slight decrease in intensity outside the bleach spot directly after bleaching compared to the same position directly before bleaching (Fig. 5.A.1). In the article of Taylor *et al.*,[24] they have tried to correct for this by introducing a shift factor in the fit of the bleach profile that accounts both for imperfect bleaching by a laser with Gaussian profile and for recovery during the bleaching. However, in this case the bleach profile is not Gaussian and cannot be fitted by simply introducing a shift factor (Fig. 5.A.1c) and therefore we have not used this correction method. Because of the imperfect bleaching, the values of the reported apparent diffusion coefficients might slightly deviate from the real diffusion coefficients, but since we have used the same bleaching method for the different DNA and pLL lengths, we do not expect large deviations in the ratios of the diffusion coefficient.

5.2.4 Sample preparation for complex coacervate microviscosity measurements

The microviscosity inside the complex coacervate droplets was probed by measuring the fluorescence lifetime of a sulfonated boron-dipyrromethene (sulfo-BODIPY) molecular rotor in these droplets. The synthesis of this sulfo-BODIPY molecular rotor is described elsewhere.[25] Complex coacervate droplets containing sulfo-BODIPY molecular rotors were prepared by mixing water, concentrated PBS, oligonucleotides, poly(L-lysine) and sulfo-BODIPY stock solution (1 g/L in water) to reach in a 1X PBS solution a cationic and anionic monomer concentration of 2.5 mM (corresponding to a charge ratio of 1:1) and a sulfo-BODIPY concentration of 10 μM. The samples were prepared directly at microscopy glass slides coated with a 5 wt % poly(vinyl alcohol) solution, sealed by gluing a cover slip on top of the slide and measured 1 h to 3 h after preparation (Subsection 5.2.6).

5.2.5 Sample preparation for FRET-FLIM measurements

Complex coacervate droplets with an atto488 and atto532 FRET pair were prepared by first mixing unlabelled and fluorescently labelled nt44 oligonucleotides to get a fraction of labelled chains α of 0.06. Half of the fluorescent labels was atto488 and the other half of fluorescent labels was atto532. Subsequently, concentrated PBS solution and poly(L-lysine) were added to get a final monomer cationic and anionic monomer concentration of 2.5 mM (corresponding to a charge ratio of 1:1) in a 1X PBS solution. To determine the fluorescence lifetime of the atto488 donor in absence of the atto532 acceptor, a similar sample preparation protocol was used, but in this case the label fraction α was 0.03 and all fluorescent labels were atto488. In all cases, the samples were prepared directly at microscopy glass slides coated with a 5 wt % poly(vinyl alcohol) solution, sealed by gluing a cover slip on top of the slide and measured 1 h to 3 h after preparation (Subsection 5.2.6). All FRET-FLIM samples were prepared and measured *in duplo*.

5.2.6 FLIM measurements

Fluorescence lifetime image microscopy (FLIM) measurements of both the fluorescence of sulfo-BODIPY molecular rotors in the complex coacervate samples (Section 5.2.4) and the fluorescence of atto488 donors in complex coacervate samples (Section 5.2.5) were performed on Leica TCS SP8 inverted scanning confocal microscope coupled with a Becker-Hickl SPC830 time-correlated single photon counting (TCSPC) module. A 63x 1.2 NA water immersion object was used for imaging. Images of 256x256 pixels were recorded at a line scanning speed of 400 Hz. The acquisition time was set to 80 s for each image. The samples were excited at 488 nm by a pulsed white light laser with a frequency of 40 MHz. The emission was collected using a spectral window of 20 nm centered on 510 nm (atto488) or 525 nm (sulfo-BODIPY) onto a Leica HyD SMD hybrid photodetector. For each sample, a FLIM image was recorded at three different positions in the sample.

After image acquisition SPCImage 8.4 software (Becker & Hickl) was used to fit the fluorescence decay curves in each pixel. A two-component exponential decay was used to determine the average fluorescence lifetime in each pixel. A false colour scale was used to report lifetime values and yield the fluorescence lifetime images.

The majority of the sulfo-BODIPY partitioned inside the complex coacervate. Yet, a small fraction of the sulfo-BODIPY remained free in solution. To exclude the fluorescence lifetime of these free sulfo-BODIPY molecular rotors from the lifetime comparison, the lifetimes of pixels with a fluorescence intensity 2.5 times smaller than the average image intensity were excluded from the lifetime histograms. No atto488 fluorescence was detected outside the complex coacervate droplets and therefore the fluorescence lifetime histograms of the atto488 dye could be directly obtained from the FLIM images.

5.2.7 Micelle preparation

Micelles were prepared based on the thermal annealing protocol of Lueckheide *et al.*.[13] For the micelles with fluorescently labelled DNA, stock solutions of fluorescently labelled oligonucleotides and unlabelled oligonucleotides of the same length were mixed with nuclease free water and concentrated PBS solution to get the desired fraction of labelled chains α and to give the desired final PBS concentration. Subsequently, the PEG-pLL diblock copolymer stock solution was added to give a charge unit concentration of 1 mM for both the oligonucleotides and the PEG-pLL diblock copolymers (charge ratio is 1:1). The samples were immediately vortexed for 20 s and subsequently heated at 75 °C for 2 h. Samples were cooled to room temperature and measured after being at least 1 h at room temperature. Unless otherwise indicated, a label fraction of $\alpha = 0.03$ was used for the nt22/PEG-pLL micelles and $\alpha = 0.06$ was used for the nt44/PEG-pLL micelles. We note that at this label fraction, already some self-quenching occurs for the micelles labelled with atto488 or atto532 (Fig. 5.A.4). However, a lower label fraction resulted in a low FRET efficiency where the FRET was difficult to distinguish from the direct acceptor excitation, especially for the micelles in 1X PBS, and therefore this lower label fraction was not used.

For the micelles with fluorescently labelled PEG-5k-pLL47 the same preparation protocol was used. The only difference is that labelled and unlabelled PEG-5k-pLL47 diblock copolymers were first mixed in the desired ratio and that afterwards the oligonucleotides were added. In this case, 10% of the PEG-5k-pLL47 polymers was coming from the fluorescently labelled PEG-5k-pLL47 stock solution and the other 90% was coming from the unlabelled PEG-5k-pLL47 stock solution with the same monomer concentration. The exact label fraction corresponding to this mix ratio is not known because we do not know the coupling efficiency of the PEG-pLL labelling reaction, but it is lower than 0.10 since the maximum average amount of fluorescent labels per polymer chain is 1 for this reaction.

The ssDNA/PEG-pLL micelles in 0.2X PBS solution were also prepared following the same thermal annealing protocol. For these micelles, only unlabelled ssDNA and PEG-pLL were added and no fluorescently labelled polymers were used.

5.2.8 Light scattering measurements

Static light scattering measurements of the ssDNA/PEG-pLL micelles were performed on an ALV instrument equipped with a 660 nm laser over a detection angle range from to 46° to 146° in intervals of 2°. Five runs of 30 s were performed at every detection angle. The Rayleigh ratio R at each detection angle θ was calculated by:

$$R(\theta) = \frac{I_{\text{sample}}(\theta) - I_0(\theta)}{I_{\text{ref}}(\theta)} R_{\text{ref}} \left(\frac{n_0}{n_{\text{ref}}} \right)^2 \tag{5.3}$$

Here $I_{\text{sample}}(\theta)$, $I_0(\theta)$ and $I_{\text{ref}}(\theta)$ are the sample, solvent and reference scattering intensities respectively, n_0 and n_{ref} are the refractive index of the solvent and reference respectively and R_{ref} is the Rayleigh ratio of the reference. The refractive index of the solvent is $n_0 = 1.3332$. We have used toluene as reference with $n_{\text{ref}} = 1.496$ and $R_{\text{ref}} = 8.56 \times 10^{-4}\,\text{m}^{-1}$.[26] The micelle molar mass was estimated based on both Zimm analysis and Guinier analysis of the measured Rayleigh ratio at different scattering angles. According to the Zimm approximation, the Rayleigh ratio is given by:

$$\frac{KC}{R(\theta, C)} \approx \frac{1}{M_w} \left(1 + \frac{1}{3} R_g^2 q^2 \right) \tag{5.4}$$

where C is the mass concentration, M_w is the molar mass of the scattering particle, R_g is its radius of gyration, $q = (4\pi n_0/\lambda)\sin(\theta/2)$ is the scattering vector with λ the laser wavelength and K is an optical constant given by:

$$K = \frac{4\pi^2 n_0^2 (dn/dC)^2}{\lambda^4 N_{av}} \tag{5.5}$$

where N_{av} is Avogadro's number and dn/dC is the specific refractive index increment of the micelles, for which we have used a weighted average of the refractive index increments of PEG, poly(L-lysine) and DNA, which are $0.135\,\text{mL g}^{-1}$, $0.17\,\text{mL g}^{-1}$ and $0.17\,\text{mL g}^{-1}$ respectively.[27,28] In the Guinier approximation, the Rayleigh ratio is given by:

$$\frac{KC}{R(\theta, C)} \approx \frac{1}{M_w} \exp\left(\frac{1}{3} R_g^2 q^2 \right) \tag{5.6}$$

Both the Zimm and Guinier approximation can thus be used to obtain the molar mass of the micelle and therefore the micelle aggregation number. Data points measured at scattering angles below 70° and above 120° deviated from the linear dependence in both the Zimm and Guinier plot (Fig. 5.A.3) and were therefore excluded from the data analysis, like we also did in Chapter 4.

5.2.9 Fluorescence spectroscopy measurements

Fluorescence spectroscopy measurements were performed on an Agilent Cary Eclipse fluorescence spectrophotometer connected to a PCB-150 circulating water bath. All measurements were performed at 20 °C. We note that the temperature control is essential because the dye quantum yield can depend strongly on the temperature[29] and in that case small temperature fluctuations can cause significant fluctuations in FRET efficiency.

An excitation wavelength of 490 nm was used to excite the (sulfo-)cyanine 3 donor dye. At this wavelength, the direct excitation of the (sulfo-)cyanine 5 acceptor dye is negligible. An excitation wavelength of 470 nm was used to excite the atto488 dye. To calculate the FRET efficiency, the emission of the atto532 acceptor dye was corrected for direct acceptor excitation at this wavelength. The degree of self-quenching of the atto532 acceptor dyes in the micelles was determined by using an excitation wavelength of 510 nm.

For the measurements of the equilibrated micelles, a single emission spectrum of the equilibrated sample was recorded. For the micelle exchange measurements, the equilibrated donor and acceptor micelles solutions were added to the cuvette in a 1 to 1 concentration ratio and mixed and placed in the spectrophotometer. Every minute an emission spectrum was recorded.

To determine the FRET efficiency, the spectrum (after correction for direct acceptor excitation for the atto488/atto532 FRET pair) was fitted with a linear combination of fixed log normal functions to determine the relative contribution of the donor and acceptor emission to the overall emission spectrum (appendix Section 5.A.3). Finally, the FRET efficiency E was calculated by:

$$E = \frac{I_A}{I_A + I_D} \tag{5.7}$$

where the donor intensity I_D and acceptor intensity I_A follow from integration of the donor and acceptor part of the emission spectrum respectively.

5.2.10 Fit of the FRET-based C3M exchange experiments to analytical model

To explain the shape of the FRET-based exchange experiment curve for ssDNA/PEG-pLL micelles with atto488/atto532 labels in 0.2X PBS solution, we have fitted the exchange experiment data with the analytical FRET model that we have developed in Chapter 4. Briefly, we have first determined the micelle geometric constant ν by fitting the FRET efficiency at different fractions of labelled chains (Fig. 5.A.4) to the function:

$$E = \frac{\nu n_A}{1 + \nu n_A} \tag{5.8}$$

where n_A is the average number of acceptor fluorophores per micelle, which can be calculated by $n_A = 0.5N\alpha$ where N is the total number of ssDNA chains in the micelle, which is measured by static light scattering experiments (Section 5.2.8), and α is the fraction of labelled chains (half of the labelled chains were acceptors and therefore α is multiplied by 0.5).

Subsequently, the data of the C3M exchange experiments is fitted to the following function:

$$\frac{< E(t) >}{E(\infty)} = \frac{1}{E(\infty)} \frac{f_D < n_D(t) >< E_D(t) > +(1 - f_D) < m_D(t) >< E_A(t) >}{f_D N_D} \tag{5.9}$$

Here, $E(\infty)$ is the FRET efficiency of the completely mixed micelles and is for the right hand side of the equation given by Equation 5.8 with $n_A(\infty) = (1 - f_D)N\alpha$ where f_D is the fraction of micelles containing only donors at the start of the mixing experiments ($f_D = 0.5$ in all mix experiments in this chapter) and α is the label fraction used in the mix experiment. We have divided by $E(\infty)$ at both sides of Equation 5.9 because experimental variations can result in a slightly different final FRET efficiency compared to the theoretical FRET efficiency. If the experimental FRET efficiency is slightly lower than the theoretical FRET efficiency of the completely mixed micelles, this will introduce an artificially low exchange time in the fit when directly comparing the FRET efficiency $E(t)$ and therefore we compare the normalised FRET efficiencies $E(t)/E(\infty)$ instead. $< n_D >$ is the average number of donors in micelles that contained only donors at the start of the mixing experiment (the donor micelles) and $< m_D >$ is the average number of donors in micelles that contained only acceptors at the start of the mixing experiments (the acceptor micelles). The average number of donors in donor micelles at a certain time t is is given by:

$$< n_D(t) >= N_D \sum_i x_i (f_D + (1 - f_D)e^{-k_i t}) \tag{5.10}$$

where N_D is the average number of donors in donor micelles at the start of the mixing experiment, k_i is the exchange rate of donor species i and x_i indicates the fraction of this species compared to all donor species, such that $\sum_i x_i = 1$.

The average number of donors in acceptor micelles at a certain time t is given by:

$$< m_D(t) >= N_D f_D \sum_i x_i(1 - e^{-k_i t}) \tag{5.11}$$

$< E_D(t) >$ and $< E_A(t) >$ in Equation 5.9 are the average FRET efficiency at a time t in the donor micelles and acceptor micelles respectively. They are given by:

$$< E_D(t) >= \sum_{n_A} P(n_A, t) \frac{\nu n_A}{1 + \nu n_A} \tag{5.12}$$

and

$$< E_A(t) >= \sum_{m_A} P(m_A, t) \frac{\nu m_A}{1 + \nu m_A} \tag{5.13}$$

where $P(n_A, t)$ is the probability to have n_A acceptors in donor micelles at time t and $P(m_A, t)$ is the probability to have m_A acceptors in acceptor micelles at time t. $P(n_A, t)$ is given by:

$$P(n_A, t) = e^{-\lambda(t)} \frac{\lambda(t)^n}{n!} \tag{5.14}$$

where n is the shortened notation of n_A and $\lambda(t)$ is given by:

$$\lambda(t) = N_A(1 - f_D) \sum_i x_i(1 - e^{-k_i t}) \tag{5.15}$$

where N_A is the average number of acceptors in acceptor micelles at the start of the mixing experiment, k_i is the exchange rate of acceptor species i and x_i indicates the fraction of this species compared to all acceptor species, such that $\sum_i x_i = 1$. $P(m_A, t)$ is given by:

$$P(n, t) = e^{-\mu(t)} \frac{\mu(t)^m}{m!} \tag{5.16}$$

where m is the shortened notation of m_A and $\mu(t)$ is given by:

$$\mu(t) = N_A \sum_i x_i(1 - f_D + f_D e^{-k_i t}) \tag{5.17}$$

In this case, we have used two different exchange rates for both the donor and acceptor exchange. We imposed that the fraction of fast exchanging fluorophores x_{fast} was the same for the donors and acceptors. In addition, we required that the fast exchange rate k_{fast} was the same for the donor and the acceptor, while the slow exchange rate of the donor and acceptor could be different. This resulted in four different fit parameters: x_{fast}, k_{fast}, k_D and k_A, where k_D and k_A indicate the slow exchange rate of the donor and acceptor respectively. The fits were performed by using a nonlinear least-square fit algorithm, as implemented in the python software package SciPy, with the following boundaries for the fit parameters: $x_{\text{fast}} = [0, 0.2]$, $k_{\text{fast}} = [10\,\text{h}^{-1}, 1000\,\text{h}^{-1}]$, $k_D = [0\,\text{h}^{-1}, 100\,\text{h}^{-1}]$ and $k_A = [0\,\text{h}^{-1}, 100\,\text{h}^{-1}]$. For the initial guess of k_D we have used a value twice as large as the initial guess of k_A (in all cases, $k_D = 0.02\,\text{h}^{-1}$ and $k_A = 0.01\,\text{h}^{-1}$) since the use of $k_D = k_A$ as initial guess decreased the quality of the fit with $E(t) = E(\infty)$ being reached too early.

5.2.11 Langevin dynamics simulations

Langevin dynamics simulations were based on the same approach as described in Chapter 3: the Kremer-Grest bead-spring model in combination with Coulomb interactions was used to simulate

coarse-grained cationic-neutral diblock copolymers and negatively charged homopolymers. Counter ions were modelled as beads with the same size of the monomers. No additional salt ions were added. All beads have a size σ_s and a mass m_s. The Bjerrum length l_B in the Coulomb potential was set to $l_B = 2.5\sigma_s$. The polymer bonds are modelled with a finitely extensible nonlinear elastic (FENE) potential with a bond stiffness k_{bond} of $30k_BT/\sigma_s^2$ and a maximum bond extension distance r_{bond} of $1.5\sigma_s$. The non-electrostatic interactions between equally and oppositely charged monomers was modelled with a Lennard-Jones potential with a cutoff distance of $2.5\sigma_s$ and a Lennard-Jones minimum ε_{LJ} of $0.05k_BT$. The non-electrostatic interaction between all other monomer–monomer, monomer–ion, and ion–ion combinations was purely repulsive. For this repulsive interaction we used the Weeks–Chandler–Andersen (WCA) potential with an interaction strength $\varepsilon = 1k_BT$.

For all 223 diblock copolymers in the simulation a neutral block length of 50 monomers was used. The cationic block was polydisperse and 48 diblock copolymers had a cationic block length of $N_{\text{pos}} = 14$, for 47 diblock copolymers $N_{\text{pos}} = 16$, for 40 diblock copolymers $N_{\text{pos}} = 18$, for 40 diblock copolymers $N_{\text{pos}} = 20$ and for 48 diblock copolymers $N_{\text{pos}} = 22$. The polyanion was monodisperse. Two different simulations were performed: one with 400 polyanions with a length of $N_{\text{neg}} = 10$ and one with 200 polyanions with $N_{\text{neg}} = 20$. In both cases, the periodic box size was $L_s = 163\sigma_s$.

We started the simulations by placing the homopolymers, diblocks, and counterions randomly in the simulation box and used the GPU-optimized molecular dynamcis software package HOOMD-blue [30–33] to perform the Langevin dynamic simulations. The Coulomb interactions were calculated by using the particle-particle particle-mesh (PPPM) Ewald summation method [32] with a real space cut off distance of $2.5\sigma_s$. The neighbour lists were generated by using the linear bounding volumes hierarchies (LBVHs) method. [33] We used $\gamma = 1m_s/\tau_s$ as drag coefficient and $\Delta t = 0.005\tau_s$ as simulation time step where τ_s is the time unit in the system. We saved the configuration of the simulation every 2500 steps. The total simulation time was $2 \times 10^7\tau_s$.

To determine the number of split events per polymer chain, the composition of the micelle clusters was followed over time. The micelle cluster identification was performed in the same way as described in Chapter 3. Every time a polymer was part of the smallest cluster formed after a splitting event of a micelle cluster, this was counted as a split event for this polymer. To reduce the effect of micelle growth on the split events analysis, the split events at a simulation time shorter than $2 \times 10^6\tau_s$ were excluded from the analysis.

5.3 Results and discussion

5.3.1 DNA diffusion in complex coacervate droplets

The strength of the electrostatic bonds in complex coacervates is often on the order of the thermal energy and thermal fluctuations can thus continuously break and reform these electrostatic bonds. The transient nature of the electrostatic bonds makes the complex coacervate dynamic systems. In active coacervate droplets like membraneless organelles, this dynamic effect is even further increased by covalent changes of the phase separating molecules in time, but also in passive complex coacervate droplets dynamics already plays a large role. For example, the dynamics of a complex coacervate material determines its response to deformation. The complex coacervate dynamics is affected by the polyelectrolyte chain length. In general, increasing the chain length results in more ionic bonds per polyelectrolyte chain and therefore the relaxation of the complex coacervate becomes slower. [18,34,35] Yet, more complex effects can occur when the oppositely charged polyelectrolytes have different lengths and their lengths are varied independently from each other: in some cases, only one of the two polyelectrolyte species determines the dynamic response. [18] At the moment it is difficult to identify the origin of this asymmetric response because there are only a few studies that have quantitatively

determined the chain length effects on the dynamics in complex coacervates with mismatched chain lengths. [18,35]

Here we have used fluorescence recovery after photo-bleaching (FRAP) to systematically study the chain length effect on the diffusion of fluorescently labelled ssDNA in ssDNA/pLL coacervates (Fig. 5.1). We have varied both the pLL length and the ssDNA length independently from each other. The increase in FRAP recovery time for increasing chain lengths, shows that the DNA diffusion is not only affected by its own length (Fig. 5.1b), but also by the length of the oppositely charged poly(L-lysine) (Fig. 5.1c) . This indicates that the relaxation time of a polyelectrolyte in a complex coacervate is not only determined by its own length and the ionic strength of the solution, as shown earlier, [18,19,36] but that also other complex coacervate properties can affect the dynamics.

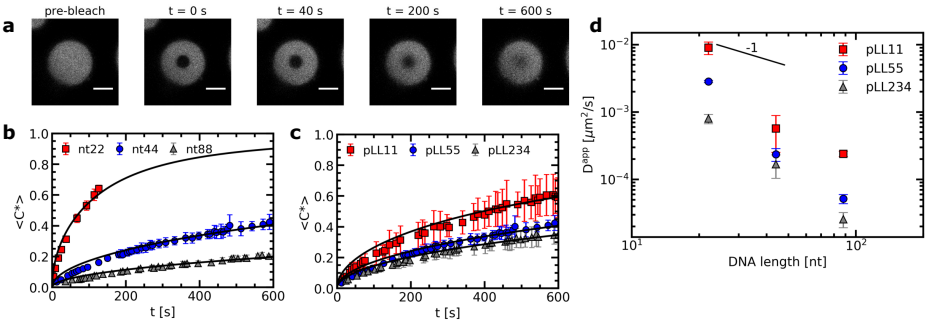

Figure 5.1. FRAP experiments of ssDNA/pLL complex coacervate droplets with fluorescently labelled ssDNA. a) Example images at different time points of a FRAP experiment of a nt44/pLL55 complex coacervate droplet. Size scale bars correspond to 5 μm. b) Comparison of the normalised fluorescence recovery curve for complex coacervates with pLL55 and different ssDNA lengths (nt22,nt44 and nt88) averaged over 5 different positions in the sample. For nt22, the data of the recovery curve stops after 150 s because from this point the contrast between the bleach spot and its surroundings becomes too low to track the center of the bleach spot. c) Comparison of the average normalised fluorescence recovery curve for complex coacervates with nt44 and different pLL lengths (pLL11, pLL55 and pLL234) averaged over 5 different positions in the sample. Solid lines in b) and c) indicate the recovery curves calculated from the average diffusion coefficients obtained from fitting the individual recovery curves. d) The average apparent diffusion coefficient D_{app}, obtained from fitting the fluorescence recovery curves, as function of the ssDNA length.

From the recovery curves the diffusion coefficient of the DNA in the complex coacervate droplets can be determined. Here, we have used the 3D diffusion model developed by Taylor *et al.* [24] to obtain the apparent DNA diffusion coefficients, as explained in the materials and methods (Section 5.2.3). The DNA diffusion coefficient strongly decreases with increasing DNA length N (Fig. 5.1d). In fact, it decreases more strongly than the $D \propto N^{-1}$ dependence predicted by the sticky Rouse model, which is the model that is often used to describe polyelectrolyte dynamics in coacervates. A possible explanation for this stronger decrease is that the density of the complex coacervate also increases with increasing DNA length and that this increase in density slows down the dynamics in the complex coacervate. This increase in density is predicted by multiple coacervation models [37,38] and has been mentioned as explanation why the viscosity depends more strongly on the polyelectrolyte length than predicted by the sticky Rouse model. [18] This density increase has also been mentioned to explain why the relaxation time in coarse-grained simulations of salt-free polyelectrolyte complexes of equal length showed a stronger dependence on the polyelectrolyte length than the sticky Rouse model. [39] In the latter case, the increase in complex density was also confirmed by the same simulations. For the ssDNA/pLL complex coacervate droplets, an increase in density with increasing chain length might not only explain the stronger dependence of DNA diffusion coefficient on the DNA length, but it might also explain why the pLL chain length affects the DNA diffusion coefficient in the complex.

5.3.2 Chain length effect on the complex coacervate density

We have used a sulfonated boron-dipyrromethene (sulfo-BODIPY) molecular rotor[25] to probe the changes in local coacervate density for different ssDNA and poly(L-lysine) chain lengths. This sulfo-BODIPY molecule is a rigidochromic sensor: its fluorescence lifetime depends on its rate of intramolecular rotation and this rate of intramolecular rotation depends on the mechanics of its surroundings. A higher intramolecular rotation rate makes the non-radiative fluorescence decay pathway more favourable and therefore the fluorescence lifetime of the molecular rotor is shorter. An increase the microviscosity can slow down the intramolecular rotation rate and thus can be observed by an increase in the fluorescence lifetime. Since the fluorescence lifetime is determined by rotations on the molecular scale, the molecular rotor will mainly probe changes in microviscosity caused by changes in the mesh size of the complex coacervate. These changes in microviscosity can be different from the macroscopic viscosity changes. Fist, the macroscopic viscosity is governed by the overall polymer relaxation rather than changes on the smaller mesh size scale. In addition, the macroscopic viscosity averages over all changes on the microscopic scale while with the molecular rotors inhomogeneities on the microscopic scale can still be distinguished.

Increasing the DNA chain length results in an increase of fluorescence lifetime of the sulfo-BODIPY molecular rotor (Fig. 5.2), especially for the longest ssDNA length (nt88). This increase in lifetime indicates that the intramolecular rotation of the molecular rotor becomes more hindered and that the local complex coacervate density thus increases for longer ssDNA lengths. This shows that the deviations from the expected $D \propto N^{-1}$ dependence might indeed (partly) be explained by changes in the complex coacervate density.

In contrast, changes of the pLL chain length do not affect the lifetime of the rotor (Fig. 5.2m,n,o), even though the changes in the pLL lengths are larger than the changes in ssDNA length. This is unexpected because in theoretical descriptions of complex coacervation,[37,38] longer chain lengths increase both the complex coacervate density and the critical salt concentration of the complex coacervates. This critical salt concentration is the salt concentration at which the complex coacervates fall apart and where the system transitions from a two phase system (below the critical salt concentration), consisting of a polymer rich phase (the coacervate) and a diluted phase, to a one phase system (above the critical salt concentration). Earlier measurements have shown that the critical salt concentration of ssDNA/pLL coacervates increases both by increasing the ssDNA length or by increasing the pLL length.[40] Still, we do not observe any change in fluorescence lifetime of the molecular rotor in coacervate complexes with increasing pLL length. This might mean that the pLL length has no effect at all on the complex coacervate density or that the effect of the pLL length is too small to be observed by using the sulfo-BODIPY molecular rotor. In any case, the effect of pLL chain length is different from ssDNA length effect, where the molecular rotor fluorescence lifetime increase with longer DNA length. Similar asymmetric length effects on the complex coacervate density have been observed earlier in rheology measurements, where changing the length of one of the polyelectrolytes left the storage and loss modulus nearly unaffected, while increasing the length of the oppositely charged polyelectrolyte increased the both the storage and loss modulus.[18] A higher modulus reflects a larger crosslink density and thus an increase in coacervate density.

To verify whether only minor changes in complex coacervate density occur when the pLL length is changed, we have performed FRET-FLIM measurements of nt44/pLL complex coacervates containing both nt44 labelled with a donor fluorophore and nt44 labelled with an acceptor fluorophore. In FRET-FLIM measurements, the lifetime of the donor fluorophore is measured, which will become shorter when the energy transfer from the donor to the acceptor is faster. This energy transfer becomes faster when the donor and acceptor are closer to each other. An increase in complex coacervate density will decrease the average distance between the donors and acceptors and therefore will result in a decrease of the average donor fluorescence lifetime. Comparison of the fluorescence lifetime histograms for the different pLL chain lengths (Fig. 5.3) shows that the pLL length only has little effect on the fluorescence

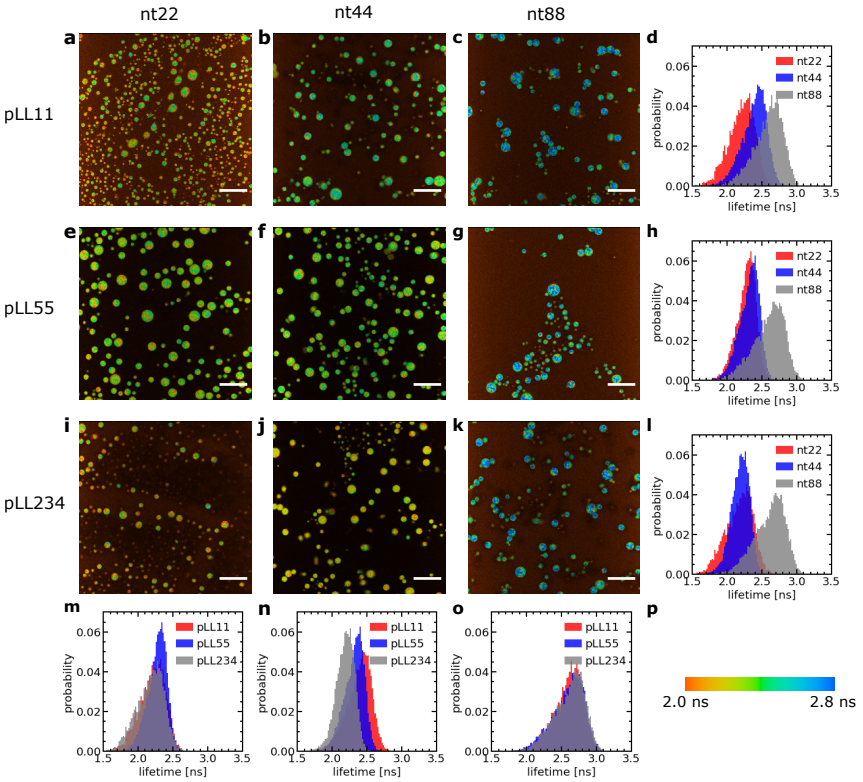

Figure 5.2. Fluorescence lifetime image microscopy (FLIM) measurements of a sulfo-BODIPY molecular rotor in ssDNA/pLL complex coacervate droplets. a-c, e-g, i-k) Example FLIM images of the complex coacervate droplets for different ssDNA and pLL lengths. The size scale bar corresponds to 30 μm. The colour scale in p) translates the colours in the images to fluorescence lifetimes. d,h,l,m,n,o) Probability distribution of the sulfo-BODIPY fluorescence lifetime obtained by combining the fluorescence lifetimes from the FLIM images at 3 different positions in the sample. The pLL length is 11 (a,b,c,d), 55 (e,f,g,h) or 234 (i,j,k,l). The ssDNA length is 22 (a,e,i,m), 44 (b,f,j,n) or 88 (c,g,k,o).

lifetime of the donor, suggesting that the changes in complex coacervate density are indeed small. In fact, we can use the changes in donor fluorescence lifetime to roughly estimate the density changes: the average measured fluorescence lifetime of the donor $< \tau_F >$ is given by $< \tau_F >= 1/(k_A + k_D)$ where k_A is the energy transfer rate to the acceptor and k_D is the rate of photon emission from the donor in absence of the acceptor. The ratio between k_D and k_A depends on the distance r between the donor and acceptor fluorophore: $k_D/k_A = (r/R_F)^6$ where R_F is the Förster radius. The ratio of transfer rate to the acceptor k_A can thus be used to calculate the changes in average distance between the donor and acceptor fluorophore: $r_2/r_1 = (k_{A,1}/k_{A,2})^{1/6}$. Since the coacervate density $\phi \propto r^{-3}$, we get $\phi_2/\phi_1 = (k_{A,1}/k_{A,2})^{-0.5}$. With an average donor fluorescence lifetime in complex coacervates without acceptor of $< \tau_F >_{\text{donor}}$= 2.1 ns (and therefore $k_D = 1/< \tau_F >_{\text{donor}} \approx 0.5\,\text{ns}^{-1}$), an average donor fluorescence lifetime in a nt44/pLL11 complex coacervate of $< \tau_F >_{\text{pLL11}}$= 1.4 ns and an average donor fluorescence lifetime in a nt44/pLL234 complex coacervate of $< \tau_F >_{\text{pLL234}}$ = 1.2 ns , we get $\phi_{\text{pLL234}}/\phi_{\text{pLL11}} \approx 1.2$. This factor is comparable to the density changes predicted in theoretical models for complex coacervation [37,38] and might indicate that still minor changes in complex coacervate density

occur with increasing pLL length, but that they are too small to be observed with the sulfo-BODIPY molecular rotor.

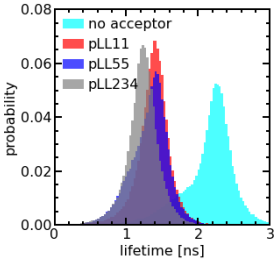

Figure 5.3. Probability distributions of the fluorescence lifetime of nt44-atto488 in ssDNA/pLL complex coacervate droplets in the presence of nt44-atto532 for different pLL lengths (pLL11, pLL55 and pLL234) and the probability distribution of the fluorescence lifetime of nt44-atto488 in ssDNA/pLL55 complex coacervate droplets in the absence of nt44-atto532 (no acceptor).

The effect of the pLL chain length on the complex coacervate density is relatively small compared to its effect on the DNA diffusion coefficient (Fig. 5.1): for nt44, the apparent diffusion coefficient decreased by a factor ~ 3.4 when changing from pLL11 to pLL234, while the estimated density increase is only a factor ~ 1.2. If changes in density are the only cause for the change in DNA diffusion coefficient with increasing pLL length, this would mean that the dynamics has to depend strongly on the complex coacervate density. In the classical model for the dynamics of associating polymers,[21] there are two scenarios were the dynamics depends strongly on the concentration. The first scenario occurs in the sticky Rouse regime and corresponds to a transition from intramolecular to intermolecular bonds with increasing concentration. The second scenario occurs in the reptation regime, where an increase in concentration decreases the reptation tube diameter. Both scenarios do not apply to the ssDNA/pLL complex coacervates studied here. First, the reptation regime is only relevant when there are significant entanglements, which only occurs for long polyelectrolyte lengths.[39] Here, we also see a strong length dependence for the short pLL and DNA lengths, which are too short for the reptation regime. In addition, the ionic bonds in (homo)polyelectrolyte complexes are always intermolecular since they are based on the attraction between oppositely charged species and therefore no intramolecular to intermolecular bond transition will occur. The probability of ionic bond formation can also increase with increasing concentration, but this probability p scales only weakly with the density ($p \propto \phi$ for a theta solvent and $p \propto \phi^{1.59}$ for a good solvent)[21] and is therefore not enough to explain the relatively large change in DNA diffusion coefficient for small concentration changes. Our results thus seem to suggest that pLL length also affects the dynamics in a different way than by only changing the density. These other effects have not been discussed earlier for strongly charged polyelectrolyte complexes, but in a scaling model for weakly charged complexes a more complex length dependence has already been predicted for certain cases.[41] Yet, we can also not exclude that the observed large difference between the density change and diffusion coefficient change is caused by experimental uncertainty. For example, there is a quite large variation in the donor fluorescence lifetime measured in the same complex coacervate (Fig. 5.3) and therefore the real density variation might be different from the estimated factor of 1.2. Therefore, it would be interesting to see in future research whether these small changes in density and relatively large changes in dynamics can also observed with other techniques, for example by using small angle X-ray scattering (SAXS) or small-angle neutron scattering (SANS) experiments to measure the correlation length[42] or mesh size[43] of the complex coacervate or rheology measurements to probe both the complex coacervate dynamics and its concentration.[18,19]

In conclusion, the chain length can have a complex effect on the density and dynamics of ssDNA/pLL complex coacervates. Changing the ssDNA chain length has a stronger effect on the coacervate density than changing the pLL length. The changes in complex cocaervate density might (partly) explain the effect of the chain length on the dynamics in the complex coacervates. Yet, we cannot exclude that also other factors play a role, since the estimated changes in complex coacervate density seem relatively small compared to the observed changes in ssDNA diffusion coefficient.

5.3.3 C3Ms: monodisperse DNA exchange

The ssDNA dynamics is not only important for complex coacervate droplets, but also for complex coacervate core micelles: the ssDNA molecular exchange rate can affect the encapsulating efficiency of the C3Ms, where a slower exchange might correspond to better protected DNA and hence a better encapsulator. Therefore, we have also measured the molecular exchange of DNA between C3Ms. For this, we have used Förster resonance energy transfer (FRET). We have mixed C3Ms with part of the ssDNA fluorescently labelled with donor fluorophores and C3Ms with part of the ssDNA fluorescently labelled with acceptor fluorophores. At the start of the mixing experiment, the donors and acceptor are part of different micelle cores and are too far away from each other for FRET to occur. However, when the micelles start to exchange, the donors and acceptors can become part of the same micelle core and are close enough to each other for FRET to occur. Therefore, exchange of the micelles will result in an increase in FRET efficiency E in time, until the final FRET efficiency $E(\infty)$ is reached where the donor and acceptor micelle components are completely mixed.

Both the ssDNA length and the PEG-pLL diblock copolymer length seem to affect the molecular exchange rate of DNA between C3Ms (Fig. 5.4a,b): for shorter chain lengths, the observed increase in FRET efficiency is faster, which indicates a faster molecular exchange rate. To better observe the differences in exchange rate for the fast exchanging C3Ms, we have also performed the exchange measurements in a 0.2X PBS solution (Fig. 5.4c,d) instead of a 1X PBS solution. The lower ionic strength in the 0.2X PBS solution increases the strength of the electrostatic interactions in the C3M core and therefore decreases the exchange rate.

We observe similar trends for the chain length effects on the exchange rate in both 1X PBS and 0.2X PBS solution, but we also observe very large variations between repetitions of the same experiment, as indicated by the shaded regions in Fig. 5.4. Because of this large uncertainty, we can conclude only that most likely both the ssDNA length and the PEG-pLL diblock copolymer length have a substantial effect on the DNA exchange rate, but we cannot exactly quantify this effect. The large variations between repetitions were unexpected: the formation of these ssDNA/PEG-pLL C3Ms is well-studied and the use of the thermal annealing protocol makes the formation of unlabelled ssDNA/PEG-pLL micelles well reproducible.[13] Still, we expect that the origin of these large variations lies in differences in micelle preparation since the variations are much smaller for repetitions of the exchange experiments from the same micelle stock solutions (Fig. 5.A.5, 5.A.6 and 5.A.7). A possible explanation is that differences in dye concentrations result in different exchange rates: when we compared the repetitions of the same mix experiment, we observed differences in dye concentration, in particular in the acceptor concentration (Fig. 5.A.5, 5.A.6 and 5.A.7), which might be caused by concentration inhomogeneities in the fluorescently labelled DNA stock solutions. We will come back to this presumed relation between uncertainty in the molecular exchange rate and dye concentration in the next section.

In some cases, the effect of the diblock copolymer length on the DNA exchange rate seems much larger than the effect of the polycation length on the DNA diffusion in complex coacervates: for ssDNA with a length of 44 nucleotides the measured exchange rates differ two orders of magnitude or more between PEG-5k-pLL47 and PEG-20k-pLL212 (Fig. 5.4b,d), while the average nt44 diffusion coefficient for pLL55 and pLL234 only differs a factor ~1.4 (Fig. 5.1). This could suggest that the DNA exchange rate is not governed only by relaxation processes in the core since in that case the poly(L-lysine) length should have a similar effect on the DNA exchange rate and the DNA diffusion. Yet, for the ssDNA with

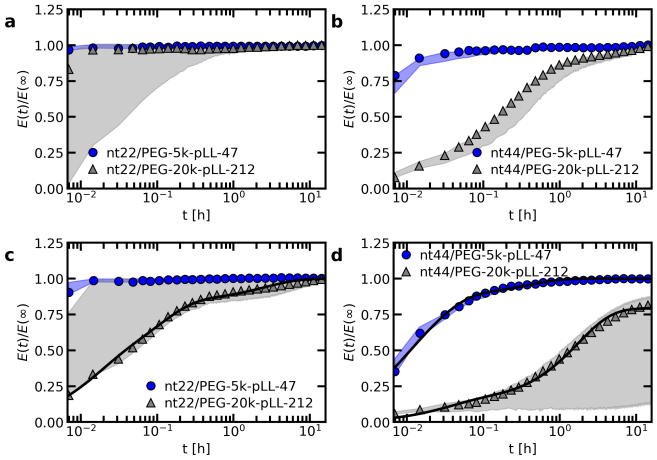

Figure 5.4. FRET-based exchange experiments of C3Ms with fluorescently labelled monodisperse DNA for different diblock copolymer lengths. In all cases, the donor fluorophore is atto488 and the acceptor fluorophore is atto532. The ssDNA length is 22 (a,c) or 44 (b,d) and the micelles are dissolved in a 1X PBS solution (a,b) or a 0.2X PBS solution (c,d). Shaded regions are an indication of the uncertainty in the exchange measurements with the region borders given by the minimum and maximum $E(t)/E(\infty)$ of three repetitions of the same exchange experiment. Symbols indicate an example of one of these three repetitions and solid black lines in (c) and (d) indicate fits of the data of this example exchange experiment to the analytical FRET model. The corresponding input parameters and the fit results are given in Table 5.1.

a length of 22 nucleotides, the measured diblock copolymer effect is less pronounced and the variations of the exchange measurements for the different diblock copolymer are closer to each other. Therefore, to be entirely sure that the pLL chain length indeed has a much stronger effect on the molecular exchange rate than on the DNA diffusion, the uncertainty in the exchange rate determination first has to be decreased.

The measured DNA exchange rate is relatively fast compared to earlier measurements of the molecular exchange of C3Ms: the nt22/PEG-pLL47 micelles exchanged within 2 minutes, which is much faster than the exchange rate that we measured for C3Ms with poly(3-sulfopropyl methacrylate) (PSPMA) and poly(ethylene glycol)-poly(2-trimethylammonioethyl methacrylate) (PEG-PTMAEMA) at similar salt concentrations (Chapter 4), where after 40 h the micelles were still not completely exchanged. The measured exchange rate of the nt22/PEG-pLL47 micelles is even faster than exchange rate of C3Ms with fluorescent proteins,[44] while the protein exchange measurements were performed very close to the critical salt concentration at which the C3Ms disassemble and the nt22/PEG-pLL47 micelles are performed far away from the critical salt concentration (their critical salt concentration is ~ 0.6 M NaCl[45] and 1X PBS contains 0.137 M NaCl). In fact, the critical salt concentration is more comparable to the PSPMA/PEG-PTMAEMA micelles (~ 0.79 M KCl), while the exchange rate is much faster than for the PSPMA/PEG-PTMAEMA micelles. Also for differences between the ssDNA/PEG-pLL micelles themselves, the exchange rate does not correlate with the critical salt concentration: an increase in diblock length seems to decrease the molecular exchange rates (Fig. 5.4), while it seems to leave the critical salt concentration unaffected.[45] Together these observations show that the critical salt concentration is not a good predictor for the molecular exchange rate of the C3Ms.

Not only the exchange rates of the ssDNA/PEG-pLL micelles are different from the PSPMA/PEG-PTMAEMA micelles, but also the shape of exchange curve: the PSPMA/PEG-PTMAEMA showed a slow, gradual increase of the FRET efficiency as function of time plotted on logarithmic axes, while

for the DNA exchange the increase is much steeper. A gradual increase on a double logarithmic scale corresponds to a broad distribution of exchange times. For the PSPMA/PEG-PTMAEMA measurements, we hypothesised that the broad range of exchange times was the result of chain polydispersity. The steeper increase for the monodisperse ssDNA exchange could support this hypothesis. Yet, we still observe different time scales for the C3Ms with slow monodisperse ssDNA exchange: there is an initial increase that is too fast to be measured and afterwards a second exchange time scale seems to occur. Subsequently, we observe a quasi-plateau and then the FRET efficiency increases again at longer logarithmic time scales. The initial fast exchange might correspond to a small population of unstable micelles, for example because these micelles are destabilised by the shear of mixing of donor and acceptor micelle solutions. A possible explanation for the two other time scales is that the ssDNA labelled with donor fluorophores have a different exchange rate than the ssDNA labelled with acceptor fluorophores.

As a first check of this explanation for the different time scales in the monodisperse ssDNA exchange, we have fitted the C3M exchange experiments with an analytical model for FRET-based micelle exchange experiments, which we developed in Chapter 4. In this case, both the donor and acceptor fluorophores consisted of two different species, where the exchange rate of the fast exchanging species was the same for the donor and acceptor, while the exchange rate of the slow exchanging species could be different for the donor and acceptor. Further details of this fit procedure given in the materials and methods (Section 5.2.10). We note that the purpose of this fit is to explain the shape of the DNA exchange experiments curves and not to exactly determine the rate constants because the experimental uncertainty is too large for this. The precise values of the rate constants obtained from the fit (Table 5.1) are therefore not that relevant. The fits can describe the exchange experiments well (Fig. 5.4c,d), which suggests that the ssDNA exchange indeed occurs with only three different exchange rates instead of a broad distribution.

Table 5.1. Fit input parameters (N, α and ν) and fit results (x_{fast}, k_D and k_A) of fluorescently labelled ssDNA exchange for C3Ms in a 0.2X PBS solution with atto488 as donor fluorophore label and atto532 as acceptor fluorophore label. The exchange of nt22/PEG-5k-pLL47 was too fast to fit the data and therefore no fit results are given for this sample.

sample	N	α	ν	x_{fast}	k_{fast} [h^{-1}]	k_D [h^{-1}]	k_A [h^{-1}]
nt22/PEG-5k-pLL47	2454	0.03	0.01	-	-	-	-
nt22/PEG-20k-pLL212	3835	0.03	0.01	0.2	62	9	0.2
nt44/PEG-5k-pLL47	1079	0.06	0.01	0.2	133	41	1
nt44/PEG-20k-pLL212	1702	0.06	0.01	0.07	30	0.6	0.001

5.3.4 Dye effect on the molecular exchange of C3Ms

To verify that the fluorophore label can indeed affect the exchange rate of the ssDNA between C3Ms, we have performed the exchange experiment with a cyanine3/cyanine5 (Cy3/Cy5) FRET pair instead of the atto488/atto532 FRET pair. We indeed observe a change in the exchange rate of nt44/PEG-5k-pLL47 micelle, with a slower exchange for the Cy3/Cy5 FRET pair (Fig. 5.5a). Similar effects occur for the exchange of nt44/PEG-20k-pLL212 micelles (Fig. 5.A.8). The Cy3/Cy5 pair is more hydrophobic: the partition coefficient of cyanine5 in anionic lipids is more than 1×10^4 times higher than for atto532 and more than 3×10^4 times higher than for atto488.[46] This suggests that the use of a more hydrophobic dye decreases the exchange rate. This could also explain why the acceptor rate would be lower than the donor exchange rate, as suggested by the fits (Table 5.1), since atto532 might be slightly more hydrophobic than atto488.

To further study the dye effect, we have also increased the dye concentration by a factor 2. A larger dye concentration results in a slower exchange (Fig. 5.5b). This shows that variations in dye concentration can indeed affect the exchange rate, as we suggested in the previous section to explain the large variations in exchange rate between repetitions of the same measurements. However, for the

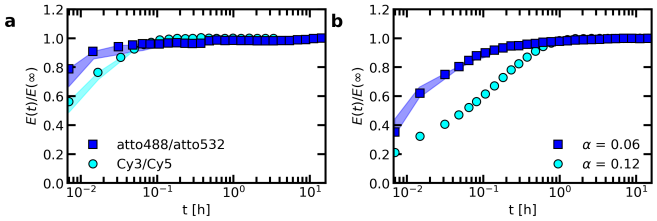

Figure 5.5. Effect of the fluorescent dye on the exchange rate of nt44/PEG-5k-pLL47 C3Ms with fluorescently labelled DNA. (a) Effect of the dye type: FRET-based exchange experiments of nt44/PEG-5k-pLL47 C3Ms in 1X PBS solution with an atto488/atto532 FRET-pair or an cyanine3/cyanine5 (Cy3/Cy5) FRET-pair. In both cases, the fraction of labelled chains α is 0.06 (b) Effect of the dye concentration: FRET-based exchange experiments of nt44/PEG-5k-pLL47 C3Ms in 0.2X PBS solution with an atto488/atto532 FRET-pair and a fraction of labelled chains α of $\alpha = 0.06$ or $\alpha = 0.12$. Shaded regions in both (a) and (b) are an indication of the uncertainty in the exchange measurements with the region borders given by the minimum and maximum $E(t)/E(\infty)$ of three (for atto488/atto532, $\alpha = 0.06$, 1X PBS and 0.2X PBS) or two (for Cy3/Cy5) repetitions of the same exchange experiment. Symbols indicate an example of one of these repetitions. The exchange experiment with a label fraction $\alpha = 0.12$ in (b) was performed only once and therefore the uncertainty is not indicated.

repetitions of the same exchange experiments the dye concentration effect seems to be reversed and the micelles with a lower acceptor concentration seem to exchange more slowly (Fig. 5.A.5, 5.A.6 and 5.A.7). This could point to a complex dye effect where for example the acceptor concentration has a different effect on the exchange rate than the donor concentration. Alternatively, except from the dyes, also other variations in micelle preparation might have played a role. To test whether other factors than the dyes play a role in the large variations in exchange experiments, the ssDNA/PEG-pLL exchange could be measured also by using small angle neutron scattering (SANS) since for these measurements no dyes are needed.

The large effects of the dyes on the molecular exchange rates of C3Ms show that one has to be careful with interpreting the results of FRET-based micelle exchange experiments and that in general SANS measurements are a better option to measure the exchange: SANS measurements are based on neutron scattering contrast and the introduction of deuterated protons will have a much smaller effect on the exchange rate than the introduction of dyes. Although the dye effect is a large disadvantage for fundamental studies to the molecular exchange of C3Ms, it shows that the molecular exchange can be tuned by just introducing an additional hydrophobic group. It was already shown earlier that additional hydrophobicity can affect the static properties of both complex coacervates[47] and complex coacervate core micelles.[48] In addition, by simulating the C3M exchange with Langevin dynamics simulations, we showed that the non-electrostatic attraction (like hydrophobic interactions) between the oppositely charged polyelectrolytes, can largely affect the exchange rate (Chapter 3). These simulations also suggested that the non-electrostatic interactions between only one of the core species might not be enough to reduce the exchange rate. In that respect, it would be interesting to see whether the dyes have similar effects on the molecular exchange of other C3Ms systems or that also specific interactions with the poly(L-lysine) and/or the ssDNA have played a role in the large dye effect that we observed here.

5.3.5 C3Ms: polydisperse diblock exchange

So far, we have focused on the molecular exchange of DNA. We have shown that the monodisperse ssDNA exchanges with only a few different rates, which we explained by the DNA being monodisperse and the different rates being caused by differences between the donor and acceptor exchange (and by a small fraction of unstable C3Ms). Apart from the ssDNA chains, the C3Ms also consists of oppositely

charged PEG-pLL diblock copolymers, which are polydisperse. If the low number of exchange rates observed for ssDNA is indeed the result of the DNA being monodisperse, we should observe a broader distribution of exchange rates for the PEG-pLL diblock copolymer. To verify this, we have fluorescently labelled the PEG-pLL diblock copolymer and measured their molecular exchange (Fig. 5.6). In this case, we did not divide by the FRET efficiency of the completely mixed micelles because the FRET efficiency that we measured by directly preparing micelles with donor and acceptor fluorophores in their core, was lower than we measured at the end of the exchange experiments. This uncertainty in end FRET efficiency determination can be explained by the fact that the overall FRET efficiency of these fluorescently labelled PEG-pLL micelles is relatively low.

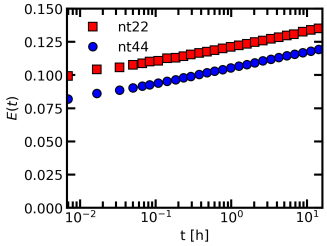

Figure 5.6. FRET-based exchange experiments of C3Ms with fluorescently labelled polydisperse PEG-5k-pLL47 diblock copolymers for two different ssDNA lengths. Sulfo-cyanine 3 is used as the donor fluorophore and sulfo-cyanine 5 is used as the acceptor fluorophore. The micelles are dissolved in a 1X PBS solution.

We indeed observe a gradual increase in FRET efficiency for the C3Ms with fluorescently labelled PEG-pLL diblock copolymers, similar to what we observed earlier for the PSPMA exchange of PSPMA/PEG-PTMAEMA micelles (Chapter 4). This further supports that chain polydispersity is the main cause for a broad distribution of exchange rates. The difference between the ssDNA and PEG-pLL exchange also shows that the exchange of one of the core species cannot be used as a direct measure for the exchange of the oppositely charged core species.

The differences between the shape in the monodisperse ssDNA and polydisperse diblock copolymer exchange curves can be explained in two ways. In the first explanation, the ssDNA and the diblock copolymer exchange independently from each other. This explanation is unlikely because this does not agree with the combined exchange that we observed earlier in Langevin dynamics simulations in Chapter 3. In addition, the diblock copolymer length seems to have a substantial effect on the ssDNA exchange rate (Fig. 5.4), which we do not expect for independent exchange. In the second explanation, the ssDNA and diblock copolymer exchange together, but the exchange of neutrally charged complexes is preferred and therefore the ssDNA exchanges mainly with polydiblock copolymers with a polycationic block length that is the same as (a multiple of) the ssDNA length. These diblock copolymers therefore have the largest exchange rate. Diblock copolymers with polycationic block lengths that result in the formation of complexes with a net charge will exchange less often and therefore have a lower exchange rate. In this way, the average exchange rate of all monodisperse DNA molecules can be the same, while the exchange rates of the polydisperse PEG-pLL diblock copolymers can differ depending on their polycationic length.

5.3.6 Molecular exchange mechanism of C3Ms

To verify that polydispersity of the diblock copolymers can result in different diblock copolymer exchange rates even when the oppositely charged polyelectrolyte is monodisperse, we have performed Langevin dynamics of C3Ms consisting of monodisperse polyanions and diblock copolymers with different polycation lengths. Indeed, the exchange rate differs for the different cationic block lengths N_{pos}, with the highest exchange rates for the diblock copolymers that can form neutrally charged

complexes with the oppositely charged homopolymer (Fig. 5.7a,b). This is also reflected by the probability distribution of the net charge of the complexes that split off during the simulations, with the highest probability for neutrally charged complexes (Fig. 5.7d). The charge probability distribution also shows that all exchange events involve at least one polycation and polyanion and that no independent exchange of the polycations or polyanions occurs. Besides the charge ratio between the polycationic block and the polyanion(s), the absolute polyanion length also has a large effect on the exchange rate: an increase of the polyanion length N_{neg} from 10 to 20 results in a much lower exchange rate (Fig. 5.7a,b,c). This agrees with the observed decrease in exchange rate when doubling the ssDNA length in ssDNA exchange experiments (Fig. 5.4).

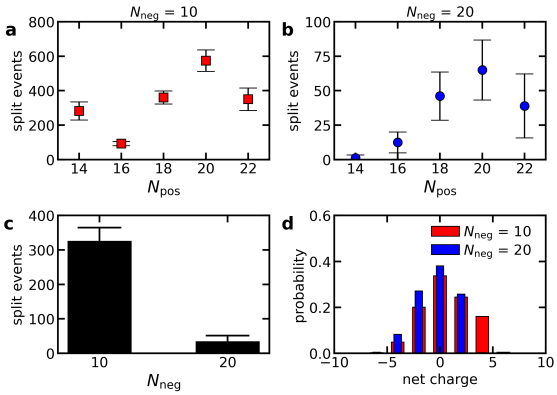

Figure 5.7. Langevin dynamics simulations of the exchange of C3Ms consisting of monodisperse anionic homopolymers and cationic-neutral diblock copolymers with a polydisperse cationic block. (a,b) Average number of split events per diblock copolymer in the time range $2 \times 10^6 \tau_s$ to $2 \times 10^7 \tau_s$ as function of the cationic block length N_{pos} for an anionic homopolymer length $N_{\text{neg}} = 10$ (a) or $N_{\text{neg}} = 20$ (b). Error bars indicate the standard deviation of the average. (c) The average number of split events per anionic homopolymer in the time range $2 \times 10^6 \tau_s$ to $2 \times 10^7 \tau_s$ for simulations with $N_{\text{neg}} = 10$ and simulations with $N_{\text{neg}} = 20$. Error bars again indicate the standard deviation of the average. (d) Probability distribution of the net charge of the complexes that split off in the time range $2 \times 10^6 \tau_s$ to $2 \times 10^7 \tau_s$.

The fact that the charge ratio between the cationic block and the polyanion(s) has a larger impact on the diblock copolymer exchange rate than the cationic block length itself (Fig. 5.7a,b) indicates that the exchange rate is not only governed by the polyelectrolyte movements in the C3M core: inside a complex coacervate, the oppositely charged polyelectrolytes do not move simultaneously, as shown by different diffusion coefficients of oppositely charged polyelectrolytes in the same complex,[49] and therefore for movements inside the C3M core, the absolute length of the polyelectrolytes should be more important than the charge ratio. Instead, the large dependence on the charge ratio suggests that also an activated process is involved in the exchange where the height of the energy barrier is mainly determined by the number of uncompensated charges in the expelled complex.

In contrast, the strong dependence of the exchange rate on the polyanion length, shows that the exchange rate is also not only governed by an activated process. For example, the same number of monomers is involved in the exchange of a polycationic block with $N_{\text{pos}} = 20$ with the oppositely charged polyanion(s) with length $N_{\text{neg}} = 10$ or $N_{\text{neg}} = 20$. Therefore, the energy barrier is the same for both polyanion lengths. Still, we observe a much larger exchange rate for the shorter polyanion (Fig. 5.7a and b). Similar effects occur for other cationic block lengths and we have also observed the same effects in exchange experiments with fluorescently labelled ssDNA (Fig. 5.4). This indicates that relaxation processes in the C3M core also affect the exchange rate.

The chain length effect on the core relaxation part of the C3M exchange cannot be described by a simple (sticky) Rouse relaxation: for the polyanion, the average number of split events with a cationic

block with length N_{pos} = 20 decreases by a factor ~8.8 when increasing the polyanion length from N_{neg} = 10 to N_{neg} = 20, which is larger than the $\tau \propto N^2$ dependence of the sticky Rouse model. In contrast, increasing the cationic block length from N_{pos} = 18 to N_{pos} = 22, decreases the number of split events only by a factor of ~1.03 (N_{neg} = 10) or ~1.3 (N_{neg} = 20), while in the sticky Rouse model this should be a factor 1.5 and this factor can even become larger when also the effect of non-electrostatic interactions on the energy barrier is taken into account. At the moment, we cannot exactly explain this complex effect of the chain length on the core relaxation part of the exchange. Possibly, the average number of chains to which a polyelectrolyte binds partly determines the exchange rate. Shorter chains have a smaller radius of gyration and therefore bind to less chains on average, which might increase the expulsion rate. In that case, density effects might have further enhanced the effect of the polyanion length since a lower density could further decrease the average number of chains to which a polyelectrolyte binds. This density effect did not occur in the comparison of the cationic block length effect because here we compared cationic block lengths that are part of the same C3Ms and therefore the density is the same for both polycation lengths.

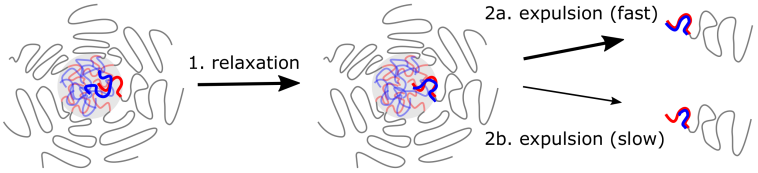

Figure 5.8. Schematic overview of the C3M exchange mechanism: 1. Relaxation processes in the C3M core are required to form a separate small polyelectrolyte complex inside the core. 2. This separate small complex can subsequently be expelled from the core. This is an activated process and the expulsion probability is large when the complex is neutrally charged (2a) and small when the complex has a large net charge (2b).

In summary, both an activated process and relaxation processes in the core determine the C3M exchange rate (Fig. 5.8), as was also suggested for the exchange of amphiphilic diblock copolymers micelles.[50] However, the underlying mechanism of the C3M exchange are different than for the amphiphilic diblock copolymer micelles: for the C3M exchange, the exchange rate of a core species depends also on the length of the oppositely charged core species, while the exchange of an amphiphilic diblock copolymer only depends on its own length because there is only one core species. As a result, the energy barrier of the activated process in C3M exchange might not always increase with increasing polyelectrolyte length and the charge ratio can be more important than the absolute polyelectrolyte length. In addition, the contribution of the relaxation in the core to the exchange rate deviates from the Rouse relaxation suggested for amphiphilic diblock copolymer micelles. These differences between C3Ms and amphiphilic diblock copolymer micelles can explain why we could not use the amphiphilic diblock copolymer model to describe the exchange of PSPMA/PEG-PTMAEMA micelles (Chapter 4) and why in a recent SANS study of C3M exchange a lower polydispersity was needed than measured to obtain a good fit between the exchange data and the amphiphilic diblock copolymer model.[23] Furthermore, these differences stress the importance of specifically studying C3Ms to further unravel the effect of chain lengths and other parameters on the C3M exchange rate.

5.4 Conclusions

In conclusion, both the length of the oppositely charged poly(L-lysine) and the DNA length itself affect the DNA dynamics in both ssDNA/pLL complex coacervate droplets and ssDNA/PEG-pLL complex coacervate core micelles. For the complex coacervate droplets, the DNA diffusion coefficient showed a stronger dependence on its chain length than predicted by the sticky Rouse model. We have shown

that this stronger dependence can be (partly) explained by an increase in complex coacervate density with increasing DNA length, but also other factors might have played a role.

For complex coacervate core micelles, the chain length effects were more difficult to quantify because we observed large variations in C3M exchange rates between repetitions of the same experiment. We hypothesise that these large variations are caused by dye concentration variations and we have shown that changing the dye concentration can indeed affect the C3M exchange rate. In addition, we have shown that the dye type can also affect the exchange rate and we have hypothesised that the different exchange rates observed for the exchange of monodisperse DNA are mainly caused by a differences in exchange rate for DNA labelled with a donor fluorophore and DNA labelled with an acceptor fluorophore. Measuring the exchange of ssDNA/PEG-pLL micelles with small angle neutron scattering (SANS) could be used to test our hypotheses on the dye effects.

Although the determination of the exact values of the C3M exchange rate constants was hindered by the large uncertainty of the measurements, the shape of the FRET-based C3M exchange curve still provided information on the exchange mechanisms: the broader distribution of exchange rates for the polydisperse PEG-pLL diblock copolymer than the monodisperse ssDNA suggests that chain length polydispersity is the main cause for a broad distribution of exchange times. The different exchange rates for ssDNA and PEG-pLL can be explained by a preferred exchange of ssDNA with PEG-pLL with a cationic block length that is the same as (a multiple of) the ssDNA length, which results in a lower exchange rate for PEG-pLL polymers with mismatched cationic block lengths. We have supported this explanation by performing Langevin dynamics simulations and we have shown that both relaxation processes in the core and an activated process determine the C3M exchange rate. Furthermore, we have concluded that the chain length effect on the C3M exchange is different from the chain length effect on the exchange of amphiphilic diblock copolymers. For C3Ms, the expulsion of neutral complexes is preferred and as a result the length ratio of the oppositely charged core species might play a larger role than the absolute chain length. Therefore, the length ratio of the oppositely charged polyelectrolytes might be used to tune exchange rate. However, the presence of polydisperse polymers make it more difficult to use this length ratio as tuning parameter since a mismatch in only the average chain length is not enough to prevent fast exchange, as was illustrated here by the fast ssDNA exchange in the presence of polydisperse PEG-pLL. Apart from the length ratio with the oppositely charged cationic block, the ssDNA length itself can also be used to adapt the exchange rate, with a lower exchange rate for longer ssDNA lengths.

5.A Appendix

5.A.1 Oligonucleotide sequences

Table 5.A.1. The oligonucleotide sequences used in this study.

Name	Sequence (5′-3′)
nt22	TCAACATCAGTCTGATAAGCTA
nt44	TCAACATCAGTCTGATAAGCTATGGATACTCGTCTGGACTACTT
nt88	TCAACATCAGTCTGATAAGCTATGGATACTCGTCTGGACTACTT ACTCACTCATTCATCACTATCTACCGTCGCATTCAGCATTCATG

5.A.2 FRAP bleach profile

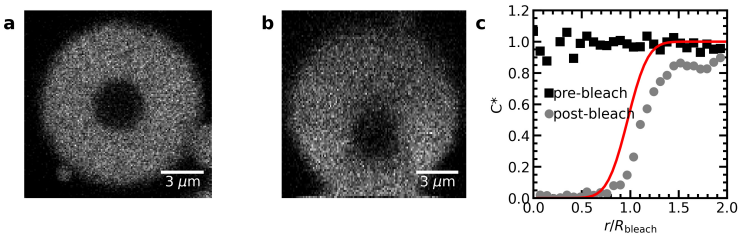

Figure 5.A.1. Profile of the bleach spot in a FRAP measurement of a nt88/pLL234 complex coacervate sample. a) xy-image of the droplet with the bleach spot b) xz-image of the droplet and bleach spot. c) Comparison of the radially averaged intensity in the xy-plane before and directly after bleaching as function of distance r from the center of the bleach spot. The red solid line shows the best fit of the post-bleach profile to the radial profile of the 3D infinite model.[24] The fit parameter is the normalised time $t^* = t/\tau$. This t^* is 0 for a perfect step bleach profile without any diffusion during the bleaching. In this case, $t^* = 0.01$.

5.A.3 Deconvolution of the emission spectra

To determine the relative contributions of the donor emission and acceptor emission to the total emission spectrum, we have used the same approach as in Chapter 4 and we have fit the total spectrum with a weighted sum of the separate donor and acceptor spectra:

$$I_{\text{tot}}(\lambda) = dI_D(\lambda) + aI_A(\lambda) \tag{5.A.1}$$

Here $I_{\text{tot}}(\lambda)$ it the total intensity at a wavelength λ and $I_D(\lambda)$ and $I_A(\lambda)$ are the intensity of the donor and acceptor spectrum at this wavelength respectively. The prefactors d and a give the relative contribution of the donor and acceptor. These prefactors are the fit parameters. To perform this fit, we have first approximated both the donor and acceptor emission spectrum with a sum of a two log normal functions:

$$I(\lambda) = \frac{x}{\lambda\sigma_1\sqrt{2\pi}} \exp\left(-\frac{(\ln(\lambda)-\mu_1)^2}{2\sigma_1^2}\right) + \frac{1-x}{\lambda\sigma_2\sqrt{2\pi}} \exp\left(-\frac{(\ln(\lambda)-\mu_2)^2}{2\sigma_2^2}\right) \tag{5.A.2}$$

here $I(\lambda)$ is the intensity of the donor or acceptor. Every dye has its own specific values for x, σ_1, μ_1, σ_2 and μ_2, which are given in Table 5.A.2. These values were obtained by fitting Equation 5.A.2 to the donor or acceptor emission spectrum using a Monte Carlo fit algorithm.

Table 5.A.2. Overview of the parameters used to describe the dye emission spectrum with Equation 5.A.2.

dye	x	μ_1	σ_1	μ_2	σ_2
atto488	0.58	6.26	0.026	6.31	0.046
atto532	0.50	6.32	0.021	6.37	0.050
cyanine3	0.53	6.34	0.019	6.39	0.040
cyanine5	0.68	6.51	0.022	6.55	0.053
sulfo-cyanine3	0.54	6.35	0.020	6.41	0.039
sulfo-cyanine5	0.36	6.51	0.019	6.52	0.042

To fit Equation 5.A.1 to the measured emission spectra, we have used the non-linear least square fit algorithm as implemented in the python package SciPy. An example fit for every FRET pair is given in Fig. 5.A.2. After fitting the data, the total donor intensity and total acceptor intensity, needed to calculate the FRET efficiency, were obtained by integrating $dI_D(\lambda)$ and $aI_A(\lambda)$ over the wavelength range

$\lambda = 400\,\text{nm}$ to $\lambda = 700\,\text{nm}$ (atto488/atto532 dyes) or $\lambda = 500\,\text{nm}$ to $\lambda = 800\,\text{nm}$ (cyanine3/cynanine5 and sulfo-cyanine3/sulfo-cyanine5 dyes).

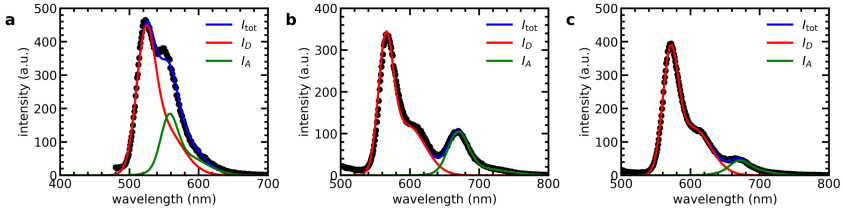

Figure 5.A.2. Example of fluorescence emission spectra of nt44/PEG-5k-pLL47 micelles with (a) part of the nt44 labelled with atto488 dye and a part of the nt44 labelled with atto532 dye, (b) part of the nt44 labelled with cyanine 3 dye and a part of the nt44 labelled with cyanine 5 dye and (c) part of the PEG-5k-pLL47 labelled with sulfo-cyanine 3 dye and a part of the PEG-5k-pLL47 labelled with sulfo-cyanine 5 dye. Solid lines indicate fits of the spectra to Equation 5.A.1 where $I_D(\lambda)$ and $I_A(\lambda)$ are defined by Equation 5.A.2 with the parameters given in Table 5.A.2.

5.A.4 Light scattering measurements

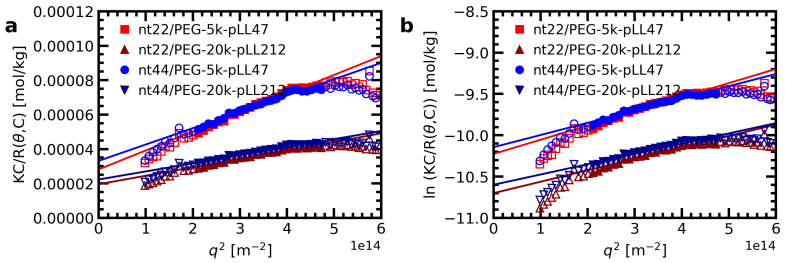

Figure 5.A.3. (a) Zimm plot and (b) Guinier plot for light scattering data of ssDNA/pegpLL micelles in a 0.2X PBS solution. The solid lines indicate the linear fit of the data from which the intercept and thus the micelle molar mass was estimated. For this fit, only the data points marked with solid symbols are used. The micelle aggregation numbers N calculated from the molar mass obtained from these fits are given in Table 5.1 of the main text. For this, the average of the molar mass obtained from the Zimm analysis and the molar mass obtained from the Guinier analysis is used.

5.A.5 Estimation of the geometric constant ν

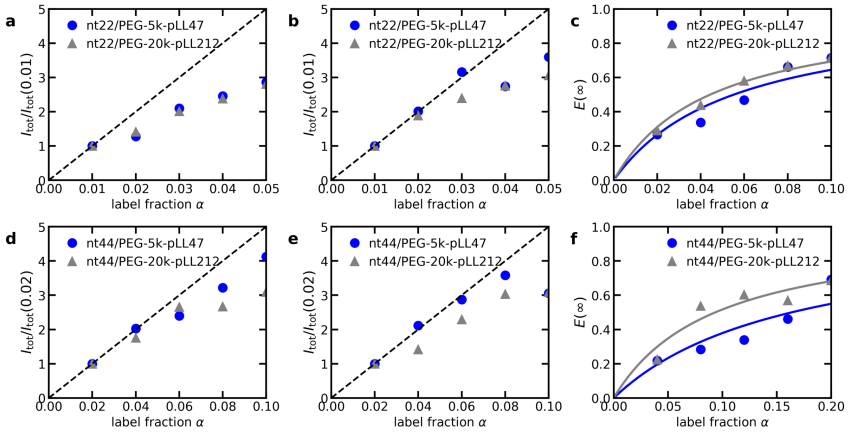

Figure 5.A.4. Fluorescence of the equilibrated ssDNA/pegpLL micelles at different label fractions in a 0.2X PBS solution. (a,b,d,e) Fluorescence intensity of the donor micelles (a,d) and acceptor micelles (b,e) with nt22 (a,b) or nt44 (d,e) at different label fractions α normalised to the intensity at a label fraction $\alpha = 0.01$ (a,b) or $\alpha = 0.02$ (d,e). The dashed lines indicate the theoretical intensity without self-quenching. (c,f) FRET efficiency of the mixed micelles with nt22 (c) or nt44 (f) as a function of label fraction. FRET efficiencies are corrected for differences in donor and acceptor self-quenching. Solid lines indicate fits with Equation 5.8 of the main text to obtain the geometric constant ν. The used values for the micellel aggregation number N (needed to calculate $n_A = 0.5N\alpha$) and the obtained values for the geometric constant ν are indicated in Table 5.1 of the main text.

5.A.6 Comparison of repetitions of C3Ms exchange experiments

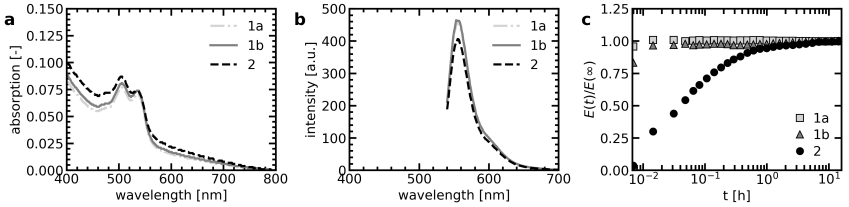

Figure 5.A.5. Comparison of three repetitions of the mix experiment of nt22/PEG-20k-pLL212 micelles in 1X PBS with part of the ssDNA fluorescently labelled with atto488 and atto532. For the 1a and 1b mix experiments the same micelle stock solutions are used, while for mix experiment 2 other micelle stock solutions are used than in 1a and 1b. (a) Absorption spectra of the micelles after the mix experiments. The background absorbance that increases with decreasing wavelength is probably the result of light scattering by the micelles. (b) Acceptor emission spectra after the mix experiments (excitation wavelength: 530 nm). (c) The mix experiments: the FRET efficiency E at time t divided by the FRET efficiency of completely mixed micelles $E(\infty)$.

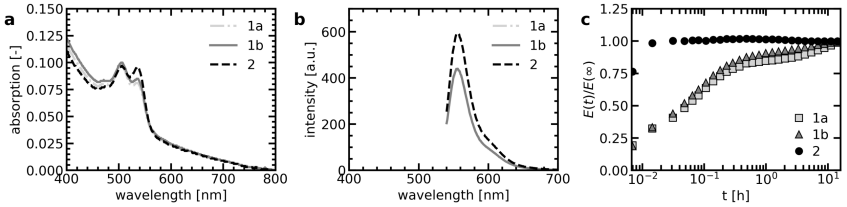

Figure 5.A.6. Comparison of three repetitions of the mix experiment of nt22/PEG-20k-pLL212 micelles in 0.2X PBS with part of the ssDNA fluorescently labelled with atto488 and atto532. For the 1a and 1b mix experiments the same micelle stock solutions are used, while for mix experiment 2 other micelle stock solutions are used than in 1a and 1b. (a) Absorption spectra of the micelles after the mix experiments. The background absorbance that increases with decreasing wavelength is probably the result of light scattering by the micelles. (b) Acceptor emission spectra after the mix experiments (excitation wavelength: 530 nm). (c) The mix experiments: the FRET efficiency E at time t divided by the FRET efficiency of completely mixed micelles $E(\infty)$.

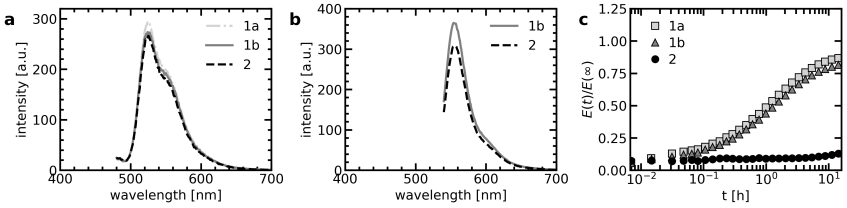

Figure 5.A.7. Comparison of three repetitions of the mix experiment of nt44/PEG-20k-pLL212 micelles in 0.2X PBS with part of the ssDNA fluorescently labelled with atto488 and atto532. For the 1a and 1b mix experiments the same micelle stock solutions are used, while for mix experiment 2 other micelle stock solutions are used than in 1a and 1b. (a) Emission spectra at the start of the mixing experiment ($t \approx 25$ s). (b) Acceptor emission spectra after the mix experiments (excitation wavelength: 530 nm). (c) The mix experiments: the FRET efficiency E at time t divided by the FRET efficiency of completely mixed micelles $E(\infty)$ where $E(\infty)$ was obtained from a separate measurement of the FRET efficiency of nt44/PEG-20k-pLL212 C3Ms that were prepared to have the donor and acceptor fluorophores completely mixed in their core.

5.A.7 Dye effect on the exchange of nt44/PEG-20k-pLL212 micelles

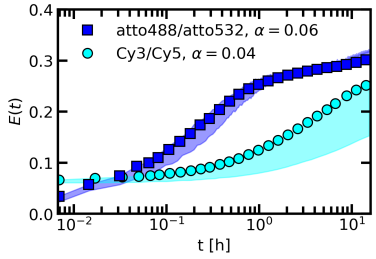

Figure 5.A.8. Effect of the fluorescent dye type on the exchange rate of nt44/PEG-20k-pLL212 C3Ms with fluorescently labelled DNA: comparison of the FRET efficiency E as function of time after mixing t for an atto488/atto532 FRET-pair (label fraction $\alpha = 0.06$) and a cyanine3/cyanine5 (Cy3/Cy5) FRET-pair (label fraction $\alpha = 0.04$). In both cases, the micelles are dissolved in 1X PBS solution. Shaded regions are an indication of the uncertainty in the exchange measurements with the region borders given by the minimum and maximum $E(t)/E(\infty)$ of three (for atto488/atto532) or two (for Cy3/Cy5) repetitions of the same exchange experiment. Symbols indicate an example of one of these repetitions.

References

[1] Perico, A.; La Penna, G.; Arcesi, L. Electrostatic interactions with histone tails may bend linker DNA in chromatin. *Biopolymers* **2006**, *81*, 20–28.

[2] Arcesi, L.; Penna, G. L.; Perico, A. Generalized electrostatic model of the wrapping of DNA around oppositely charged proteins. *Biopolymers* **2007**, *86*, 127–135.

[3] Feric, M.; Vaidya, N.; Harmon, T. S.; Mitrea, D. M.; Zhu, L.; Richardson, T. M.; Kriwacki, R. W.; Pappu, R. V.; Brangwynne, C. P. Coexisting liquid phases underlie nucleolar subcompartments. *Cell* **2016**, *165*, 1686–1697.

[4] Banani, S. F.; Lee, H. O.; Hyman, A. A.; Rosen, M. K. Biomolecular condensates: organizers of cellular biochemistry. *Nat. Rev. Mol. Cell Biol.* **2017**, *18*, 285–298.

[5] Yewdall, N. A.; André, A. A.; Lu, T.; Spruijt, E. Coacervates as models of membraneless organelles. *Curr. Opin. Colloid Interface Sci.* **2020**, 101416.

[6] Drobot, B.; Iglesias-Artola, J. M.; Le Vay, K.; Mayr, V.; Kar, M.; Kreysing, M.; Mutschler, H.; Tang, T. D. Compartmentalised RNA catalysis in membrane-free coacervate protocells. *Nat. Commun.* **2018**, *9*, 1–9.

[7] Poudyal, R. R.; Guth-Metzler, R. M.; Veenis, A. J.; Frankel, E. A.; Keating, C. D.; Bevilacqua, P. C. Template-directed RNA polymerization and enhanced ribozyme catalysis inside membraneless compartments formed by coacervates. *Nat. Commun.* **2019**, *10*, 1–13.

[8] Mountain, G. A.; Keating, C. D. Formation of multiphase complex coacervates and partitioning of biomolecules within them. *Biomacromolecules* **2019**, *21*, 630–640.

[9] Lu, T.; Spruijt, E. Multiphase complex coacervate droplets. *J. Am. Chem. Soc.* **2020**, *142*, 2905–2914.

[10] Wu, H.; Ting, J. M.; Weiss, T. M.; Tirrell, M. V. Interparticle interactions in dilute solutions of polyelectrolyte complex micelles. *ACS Macro Lett.* **2019**, *8*, 819–825.

[11] Voets, I. K.; De Keizer, A.; Cohen Stuart, M. A. Complex coacervate core micelles. *Adv. Colloid Interface Sci.* **2009**, *147*, 300–318.

[12] Marras, A. E.; Campagna, T. R.; Vieregg, J. R.; Tirrell, M. V. Physical property scaling relationships for polyelectrolyte complex micelles. *Macromolecules* **2021**, *54*, 6585–6594.

[13] Lueckheide, M.; Vieregg, J. R.; Bologna, A. J.; Leon, L.; Tirrell, M. V. Structure–property relationships of oligonucleotide polyelectrolyte complex micelles. *Nano Lett.* **2018**, *18*, 7111–7117.

[14] Kakizawa, Y.; Kataoka, K. Block copolymer micelles for delivery of gene and related compounds. *Adv. Drug Deliv. Rev.* **2002**, *54*, 203–222.

[15] Lee, Y.; Kataoka, K. Biosignal-sensitive polyion complex micelles for the delivery of biopharmaceuticals. *Soft Matter* **2009**, *5*, 3810–3817.

[16] Cabral, H.; Miyata, K.; Osada, K.; Kataoka, K. Block copolymer micelles in nanomedicine applications. *Chem. Rev.* **2018**, *118*, 6844–6892.

[17] Kim, Y. H.; Lee, K.; Li, S. Nucleic Acids Based Polyelectrolyte Complexes: Their Complexation Mechanism, Morphology, and Stability. *Chem. Mater.* **2021**, *33*, 7923–7943.

[18] Spruijt, E.; Cohen Stuart, M. A.; van der Gucht, J. Linear viscoelasticity of polyelectrolyte complex coacervates. *Macromolecules* **2013**, *46*, 1633–1641.

[19] Liu, Y.; Winter, H. H.; Perry, S. L. Linear viscoelasticity of complex coacervates. *Adv. Colloid Interface Sci.* **2017**, *239*, 46–60.

[20] Späth, F.; Donau, C.; Bergmann, A. M.; Kränzlein, M.; Synatschke, C. V.; Rieger, B.; Boekhoven, J. Molecular Design of Chemically Fueled Peptide–Polyelectrolyte Coacervate-Based Assemblies. *J. Am. Chem. Soc.* **2021**, *143*, 4782–4789.

[21] Rubinstein, M.; Semenov, A. N. Dynamics of entangled solutions of associating polymers. *Macromolecules* **2001**, *34*, 1058–1068.

[22] Holappa, S.; Kantonen, L.; Andersson, T.; Winnik, F.; Tenhu, H. Overcharging of polyelectrolyte complexes by the guest polyelectrolyte studied by fluorescence spectroscopy. *Langmuir* **2005**, *21*, 11431–11438.

[23] Heo, T.-Y.; Kim, S.; Chen, L.; Sokolova, A.; Lee, S.; Choi, S.-H. Molecular Exchange Kinetics in Complex Coacervate Core Micelles: Role of Associative Interaction. *ACS Macro Lett.* **2021**, *10*, 1138–1144.

[24] Taylor, N. O.; Wei, M.-T.; Stone, H. A.; Brangwynne, C. P. Quantifying dynamics in phase-separated condensates using fluorescence recovery after photobleaching. *Biophys. J.* **2019**, *117*, 1285–1300.

[25] Michels, L.; Gorelova, V.; Harnvanichvech, Y.; Borst, J. W.; Albada, B.; Weijers, D.; Sprakel, J. Complete microviscosity maps of living plant cells and tissues with a toolbox of targeting mechanoprobes. *Proc. Nat. Acad. Sci. U.S.A.* **2020**, *117*, 18110–18118.

[26] Wu, H. Correlations between the Rayleigh ratio and the wavelength for toluene and benzene. *Chemical Physics* **2010**, *367*, 44–47.

[27] Polik, W. F.; Burchard, W. Static light scattering from aqueous poly (ethylene oxide) solutions in the temperature range 20-90 C. *Macromolecules* **1983**, *16*, 978–982.

[28] Lai, E.; Van Zanten, J. H. Monitoring DNA/poly-L-lysine polyplex formation with time-resolved multiangle laser light scattering. *Biophysical journal* **2001**, *80*, 864–873.

[29] Sanborn, M. E.; Connolly, B. K.; Gurunathan, K.; Levitus, M. Fluorescence properties and photophysics of the sulfoindocyanine Cy3 linked covalently to DNA. *J. Phys. Chem. B* **2007**, *111*, 11064–11074.

[30] Anderson, J. A.; Lorenz, C. D.; Travesset, A. General purpose molecular dynamics simulations fully implemented on graphics processing units. *J. Comput. Phys.* **2008**, *227*, 5342–5359.

[31] Glaser, J.; Nguyen, T. D.; Anderson, J. A.; Lui, P.; Spiga, F.; Millan, J. A.; Morse, D. C.; Glotzer, S. C. Strong scaling of general-purpose molecular dynamics simulations on GPUs. *Comput. Phys. Commun.* **2015**, *192*, 97–107.

[32] LeBard, D. N.; Levine, B. G.; Mertmann, P.; Barr, S. A.; Jusufi, A.; Sanders, S.; Klein, M. L.; Panagiotopoulos, A. Z. Self-assembly of coarse-grained ionic surfactants accelerated by graphics processing units. *Soft Matter* **2012**, *8*, 2385–2397.

[33] Howard, M. P.; Anderson, J. A.; Nikoubashman, A.; Glotzer, S. C.; Panagiotopoulos, A. Z. Efficient neighbor list calculation for molecular simulation of colloidal systems using graphics processing units. *Comput. Phys. Commun.* **2016**, *203*, 45–52.

[34] Andreev, M.; Prabhu, V. M.; Douglas, J. F.; Tirrell, M.; de Pablo, J. J. Complex coacervation in polyelectrolytes from a coarse-grained model. *Macromolecules* **2018**, *51*, 6717–6723.

[35] Liu, Y.; Santa Chalarca, C. F.; Carmean, R. N.; Olson, R. A.; Madinya, J.; Sumerlin, B. S.; Sing, C. E.; Emrick, T.; Perry, S. L. Effect of polymer chemistry on the linear viscoelasticity of complex coacervates. *Macromolecules* **2020**, *53*, 7851–7864.

[36] Spruijt, E.; Sprakel, J.; Lemmers, M.; Cohen Stuart, M. A.; Van Der Gucht, J. Relaxation dynamics at different time scales in electrostatic complexes: time-salt superposition. *Phys. Rev. Lett.* **2010**, *105*, 208301.

[37] Spruijt, E.; Westphal, A. H.; Borst, J. W.; Cohen Stuart, M. A.; van der Gucht, J. Binodal compositions of polyelectrolyte complexes. *Macromolecules* **2010**, *43*, 6476–6484.

[38] Lytle, T. K.; Sing, C. E. Transfer matrix theory of polymer complex coacervation. *Soft Matter* **2017**, *13*, 7001–7012.

[39] Yu, B.; Rauscher, P. M.; Jackson, N. E.; Rumyantsev, A. M.; De Pablo, J. J. Crossover from Rouse to reptation dynamics in salt-free polyelectrolyte complex coacervates. *ACS Macro Lett.* **2020**, *9*, 1318–1324.

[40] Vieregg, J. R.; Lueckheide, M.; Marciel, A. B.; Leon, L.; Bologna, A. J.; Rivera, J. R.; Tirrell, M. V. Oligonucleotide–peptide complexes: phase control by hybridization. *J. Am. Chem. Soc.* **2018**, *140*, 1632–1638.

[41] Aponte-Rivera, C.; Rubinstein, M. Dynamic coupling in unentangled liquid coacervates formed by oppositely charged polyelectrolytes. *Macromolecules* **2021**, *54*, 1783–1800.

[42] Marciel, A. B.; Srivastava, S.; Tirrell, M. V. Structure and rheology of polyelectrolyte complex coacervates. *Soft Matter* **2018**, *14*, 2454–2464.

[43] Spruijt, E.; Leermakers, F. A.; Fokkink, R.; Schweins, R.; van Well, A. A.; Cohen Stuart, M. A.; van der Gucht, J. Structure and dynamics of polyelectrolyte complex coacervates studied by scattering of neutrons, X-rays, and light. *Macromolecules* **2013**, *46*, 4596–4605.

[44] Nolles, A.; Hooiveld, E.; Westphal, A. H.; van Berkel, W. J.; Kleijn, J. M.; Borst, J. W. FRET reveals the formation and exchange dynamics of protein-containing complex coacervate core micelles. *Langmuir* **2018**, *34*, 12083–12092.

[45] Marras, A. E.; Vieregg, J. R.; Ting, J. M.; Rubien, J. D.; Tirrell, M. V. Polyelectrolyte complexation of oligonucleotides by charged hydrophobic—neutral hydrophilic block copolymers. *Polymers* **2019**, *11*, 83.

[46] Zhang, Z.; Yomo, D.; Gradinaru, C. Choosing the right fluorophore for single-molecule fluorescence studies in a lipid environment. *Biochim. Biophys. Acta - Biomembr.* **2017**, *1859*, 1242–1253.

[47] Tabandeh, S.; Leon, L. Engineering peptide-based polyelectrolyte complexes with increased hydrophobicity. *Molecules* **2019**, *24*, 868.

[48] Voets, I. K.; de Keizer, A.; Cohen Stuart, M. A.; Justynska, J.; Schlaad, H. Irreversible structural transitions in mixed micelles of oppositely charged diblock copolymers in aqueous solution. *Macromolecules* **2007**, *40*, 2158–2164.

[49] Weinbreck, F.; Rollema, H. S.; Tromp, R. H.; de Kruif, C. G. Diffusivity of whey protein and gum arabic in their coacervates. *Langmuir* **2004**, *20*, 6389–6395.

[50] Choi, S.-H.; Lodge, T. P.; Bates, F. S. Mechanism of molecular exchange in diblock copolymer micelles: hypersensitivity to core chain length. *Phys. Rev. Lett.* **2010**, *104*, 047802.

Chapter 6

Towards a probe of the sub-chain dynamics in a polyelectrolyte complex

Polyelectrolyte complexes are dynamic systems. Although their average macroscopic dynamics has been widely studied and also the average dynamics of microscopic complexes has regularly been investigated (for example in the previous chapters), the individual (sub-)molecule dynamics of these polyelectrolyte complexes is less well-known. In this chapter, we aim to zoom in to the dynamics at this nanoscopic scale and try to follow the sub-chain dynamics in a polyelectrolyte complex by using a single stranded DNA chain that is labelled with a single donor and acceptor fluorophore. We use coarse-grained molecular dynamics DNA simulations in combination with dye accessible volume calculations to find the optimal label positions and to show how the fluctuations in Förster resonance energy transfer (FRET) can be analysed to infer the sub-chain dynamics. Subsequently, we conclude based on fluorescence recovery after photo-bleaching measurements that increasing the DNA length can help to slow the dynamics in the complex such that the dynamics at small length scales can be measured. Therefore, we use an asymmetric polymerase chain reaction (PCR) to synthesise long single stranded DNA from a short fluorescently labelled single stranded DNA primer and show how this fluorescent long single stranded DNA can be purified and incorporated in a polyelectrolyte complex. Unfortunately, among others due to irreproducibility of the PCR, we have not yet been able to use this fluorescently labelled DNA to probe the sub-chain dynamics. We therefore end with some recommendations on how to continue on this approach in order to measure the sub-chain dynamics and advance the understanding of the polyelectrolyte complex dynamics.

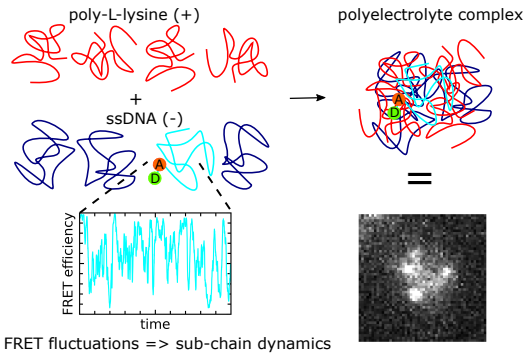

6.1 Introduction

Polyelectrolyte complexes can form when oppositely charged polyelectrolytes are mixed. The driving force for this complexation is often a combination of an increase in entropy due to the release of counter-ions and a decrease in enthalpy due to formation of electrostatic bonds or other favourable enthalpic interactions. The strength of the electrostatic bonds in these polyelectrolyte complexes are on the order of the thermal energy and thermal fluctuations can thus continuously break and reform these electrostatic bonds. The transient nature of the electrostatic bonds makes the complexes dynamic systems. This dynamic nature is important for many of their applications. For example, the dynamics largely determines the material response to deformation, which is important for both liquid like[1,2] and solid like[3] polyelectrolyte complex materials. In addition, inside cells, polyelectrolyte complex-based membraneless organelles continuously need to form and dissociate again.[4,5] Recently, this dynamic behaviour of the membraneless organelles has also been mimicked in artificial systems.[6,7] Furthermore, the dynamics of polyelectrolyte complex micelles can affect their encapsulation efficiency, as extensively discussed in the other chapters of this thesis.

Because of its broad importance, the dynamics of polyelectrolyte complexes has been widely studied. Many of these studies have focused on the ensemble-averaged movement of the complete polymers. For example, fluorescence recovery after photo-bleaching experiments measure the average diffusion coefficient of the polymers.[8–10] In addition, linear viscoelasticity measurements mainly probe the terminal relaxation time of the polymers:[1,11–13] the zero-shear viscosity is proportional to this terminal relaxation time[14] and also in small amplitude oscillatory shear measurements this terminal relaxation time is often determined from the observed transition between the terminal regime and the rubbery plateau.

Although a lot has been learnt already from just focusing on the ensemble-averaged dynamics of the complete polymers, the individual sub-chain dynamics is also important: measurements of the dynamics of individual polymers provides information on the heterogeneity of the dynamics and the comparison of the sub-chain dynamics to the complete polymer dynamics can be used to verify theoretical models since these models describe the relaxation time for different (sub-)chain lengths. For example, the sticky Rouse model, that is commonly used to describe the polyelectrolyte dynamics,[1,11,13] predicts that the relaxation time scales with the square of the polyelectrolyte length. This relation is difficult to verify by studying only the total polyelectrolyte relaxation time because changing the polyelectrolyte length also changes other properties of the complex like its density.[15,16] Verifying and fine-tuning the theoretical models can help to better predict the mechanical properties of polyelectrolyte complex-based materials and in this way help to improve the design of materials for a broad variety of applications. Another reason to study the sub-chain dynamics is that in some systems the local polyelectrolyte movements compete with other processes. For example, in reaction-assembly networks the local chain movements compete with monomer association and dissociation (Chapter 2) and in complex coacervate core micelles the local chain movements in the core compete with chain expulsion (Chapter 5). The outcome of these competing processes can be better predicted when the time scales of all processes are known.

Unfortunately, this sub-chain dynamics is more difficult to directly obtain from experiments. In principle, the dynamics at shorter length and time scales are probed by the higher frequencies in linear viscoelasticity measurements. Yet, interpretation of these measurements at short times already requires the use of the theoretical models, making it difficult to independently verify these models and directly determine the relaxation time of specific parts of the total polyelectrolyte chain. Other measurements are thus needed to complement the linear viscoealisticity measurements. A few studies have already attempted this. For example, single-molecule force spectroscopy measurements have been used to estimate the strength and the lifetime of a single ionic bond of a polyelectrolyte pair.[17] However, this measurement was done for one polyelectrolyte pair, while differences in polymer chemistry

might affect the bond lifetime.[18] In addition, this type of measurement only probes the lifetime of a single bond of a single polyelectrolyte pair and does not measure the local relaxation time of a few monomers in a unperturbed complex, while the bulk polyelectrolyte complex environment and the possibility to form bonds with multiple chains might also change the dynamics compared to the dynamics of these single ionic bonds. To learn more about this local chain dynamics in a generalised polyelectrolyte complex, coarse-grained polyelectrolyte simulations can be used.[19–21] These simulations can for example reproduce the experimentally observed length effects.[21] However, at the moment, the coarse-grained simulations are not able to capture all experimentally observed features. For example, the simulated polymer dynamics did not depend on the amount of salt ions,[21] while in experiments the salt concentration has a huge effect on the dynamics in the polyelectrolyte complex.[11,22–26]

Here, we aim to measure the sub-chain dynamics in a polyelectrolyte complex by making use of Förster resoncance energy transfer (FRET). FRET is a type of non-radiative energy transfer between a donor fluorophore and a nearby acceptor fluorophore. This energy transfer is strongly distance dependent with the FRET efficiency E given by:

$$E = \frac{1}{1 + (r/R_F)^6} \tag{6.1}$$

where r is the distance between the donor and acceptor fluorophore and R_F is the Förster radius, which depends on the fluorophore pair and is typically a few nanometers. A simple argument can illustrate that the fluctuations in FRET efficiency correspond to chain density fluctuations on the length scale of this Förster radius, as discussed earlier by van de Laar *et al.*:[27] in a first order approximation of the strong distance dependency of the FRET efficiency, the donor fluorophores within a distance R_F of an acceptor fluorophore have a FRET efficiency of 1, while donor fluorophores at distance larger than the R_F from the acceptor have a FRET efficiency of 0. An increase in FRET efficiency thus corresponds to an increase in the number of donor fluorophores n_D within a distance R_F of the acceptor fluorophore and therefore to an increase in the local density n_D/R_F^3. The Förster radius is typically smaller than or comparable to the typical gyration radii of polyelectrolytes in a complex.[28] For polyelectrolyte complexes, fluctuations in FRET efficiency will therefore mainly correspond to monomer density fluctuations on a sub-chain length scale and can thus be used to probe the sub-chain movements in a polyelectrolyte complex.

The fluctuations in FRET efficiency will be averaged out when the FRET signals of different FRET pairs are combined. To minimise this averaging, we will use single-molecule spectroscopy in combination with specific labelling of DNA polyelectrolytes. Single-molecule spectroscopy allows to follow the FRET of individual polyelectrolytes. Recent advances in DNA technology make it possible to incorporate the functional groups at specific positions in a DNA molecule. Because of this specific labelling, the number of FRET pairs per DNA molecule can be limited to one, while the FRET efficiency is still large enough to be measured (Fig. 6.1). Another advantage of this specific labelling is that variations in FRET efficiency between different polymers always correspond to variations in polymer configurations and are not the result of variations in label positions.

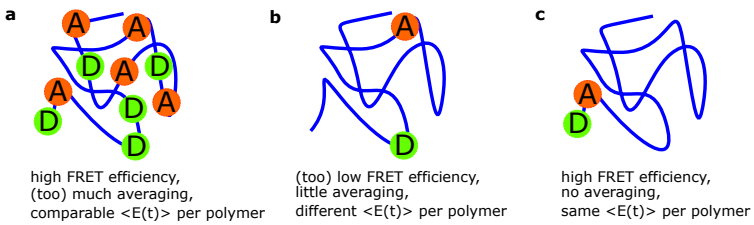

Figure 6.1. Comparison of the different polymer labelling strategies with donor (D) and acceptor (A) fluorophores. a) Non-specific labelling with a high label degree b) Non-specific labelling with a low degree and c) Specific labelling.

In this chapter, we elaborate on the design of this single-molecule FRET probe. We use coarse-grained DNA simulations to find the best label positions and to illustrate how the fluctuations in FRET efficiency can be analysed to infer the polymer dynamics. In addition, we use fluorescence recovery after photo-bleaching (FRAP) to estimate the polymer diffusion coefficient in polyelectrolyte complexes varying in single stranded DNA lengths. From these FRAP measurements we conclude that long polyelectrolytes can help to sufficiently slow down the dynamics to measure the local chain movements. Hence, we use an asymmetric polymerase chain reaction (PCR) to synthesise long single stranded DNA from a short fluorescently labelled single stranded DNA primer. Unfortunately, mainly due to problems with the reproducibility of the asymmetric PCR results, we have not succeeded yet to measure the local dynamics in a polyelectrolyte complex based on FRET fluctuations. Therefore, we will end this chapter with some recommendations to further improve on this system. Hopefully, this will enable to follow the local chain movements in a polyelectrolyte complex in the future.

6.2 Materials and methods

6.2.1 DNA and poly(L-lysine)

DNA primers were purchased from Integrated DNA Technologies. An overview of all primers is given in the appendix (Table 6.A.1). The long, circular, single stranded Type p7249 DNA (identical base sequence as M13mp18 DNA) was purchased from Tilibit Nanosystems as a 400 nM solution containing 10 mM TRIS base and 1 mM EDTA. poly(L-lysine hydrobromide), Mw = 15 000 - 30 000 g/mol (by viscosity), and FITC labelled poly(L-lysine hydrobromide), Mw = 15 000 - 30 000 g/mol (by viscosity), were purchased from Sigma Aldrich.

6.2.2 DNA simulations and FRET efficiency calculations

Coarse-grained molecular dynamics DNA simulations were based on the oxDNA model.[29] Brownian dynamics was realised by using the default oxDNA simulations thermostat that is based on an Anderson-like algorithm. The simulation temperature was set to $T = 0.110T_s$, the integration time step was set to $\mathrm{dt} = 0.005\tau_s$ and the diffusion coefficient was set to $D = 2.5b_s^2/\tau_s$. Here, T_s, τ_s and b_s are the simulation temperature unit, time unit and distance unit respectively. A simulation temperature unit corresponds to 3000 K and a distance unit corresponds to 8.518 Å.[30] Direct conversion from the simulation time unit to experimental times is difficult because of the coarse-grained nature of the simulations and the fact that hydrodynamic interactions are neglected. The DNA configurations were analysed after an equilibration period of 200000 integration steps. For the simulation data shown in this chapter, we have taken the first 100 nucleotides of the ssDNA that is formed in the asymmetric PCR (Section 6.2.7) as DNA sequence, which is: 5' GTC TGC GTG CTA CTT CTG TCT GAT TTC CGT ATG TTT CAA CGA GCA TGT CTG GAA TGG TTT TTA CTG AGA ACG TCA TGC GGC CTC ACT TCT GCT ATT TCG C '3.

After obtaining different DNA configurations with the molecular dynamcis simulations, we have used accessible volume simulations software[31] to calculate the FRET efficiency of these DNA configurations for different dye attachment points. For this, we have first converted the DNA configuration from the oxDNA file format to the Protein Data Bank (PDB) file format using the TacoxDNA software[32] because the accessible volume simulations software uses the PDB file format. In the accessible volume simulations, the dye is approximated by a sphere that is connected to a specific position at the DNA with a flexible linkage. To account for the different sizes of the dye in the different dimensions, the software performs the accessible volume calculation three times, with every time a different radius based on the dye dimensions, and then superimposes the results of these three calculations to give the dye accessible volume. In this case, we have used the atto550-NHS ester as donor dye with a linker length of 20.5 Å, a linker width of 4.5 Å and dye radii of 7.8 Å, 4.5 Å and

1.5 Å, and atto647-NHS ester as acceptor dye with a linker length of 20.5 Å, a linker width of 4.5 Å and dye radii of 7.15 Å, 4.5 Å and 1.5 Å. The Förster radius of this FRET pair is 65 Å, as given by the manufacturer of the atto-dyes. With this Förster radius, the FRET efficiency can be calculated for a given donor-acceptor distance (Equation 6.1). The average FRET efficiency for a specific DNA configuration and specific dye attachment points, follows from the average FRET efficiency of all possible donor and acceptor dye position combinations. Due to the fine mesh size of the calculated accessible volume, averaging over all possible donor and acceptor positions combinations would take too long. Instead, we have obtained the average FRET efficiency by averaging the FRET efficiency for 1×10^6 donor and acceptor positions randomly sampled from their accessible volume.

6.2.3 FRAP measurements

Complex coacervate samples for fluorescence recovery after photo-bleaching (FRAP) measurements were prepared by mixing the ssDNA and a 1/9 poly(L-lysine-FITC)/poly(L-lysine) solution to give a positive and negative monomer concentration of 1.5 mM in 1X phosphate buffered saline (PBS). The samples were prepared directly at microscopy glass slides coated with a ~2 wt % poly(vinyl alcohol) solution, sealed by gluing a cover slip on top of the slide and measured 16 h to 24 h after preparation. The FRAP measurements were performed on a Nikon C2 laser scanning confocal microscope with a 60X 1.4 NA oil-immersion objective. A 488 nm laser was used for both imaging and bleaching. The images were recorded at a 4X digital zoom and consisted of 512x512 pixels. Bleaching of a spherical region with a 3 μm diameter was performed in the middle of a coacervate droplet. Two images were recorded before bleaching and 51 images were recorded after bleaching to follow the recovery. All images were recorded at a time interval of 2 s.

Image analysis of the FRAP data was based on the method described by Taylor *et al.*[33] The fluorescence intensity concentration C inside the bleach spot was normalised according to:

$$< C > (t) = \frac{< C(r,t) > - < C(r,0) >}{< C_{\text{ref}} > - < C(r,0) >} \tag{6.2}$$

where $< C(r,t) >$ is the average fluorescence intensity in the bleach spot at a time t after bleaching and C_{ref} is the average reference intensity in the bleach spot before bleaching. During the recovery, some additional bleaching occurred. Corrections for this bleaching were calculated from the intensity of a coacervate region in the image outside the bleached spot.

To obtain the characteristic diffusion τ, the bleaching corrected data was fitted with a 3D diffusion model in an infinite medium:[33]

$$< C > (t) = 1 - \text{erf}\left(\sqrt{\frac{\tau}{t}}\right) + \sqrt{\frac{t}{\pi\tau}}\left[3 - \exp\left(-\frac{\tau}{t}\right)\right] + 2\sqrt{\frac{t^3}{\pi\tau^3}}\left[\exp\left(-\frac{\tau}{t}\right) - 1\right] \tag{6.3}$$

The diffusion coefficient D was calculated from the obtained characteristic time τ by $D = R^2/\tau$ where R is the radius of the bleach region. The reported diffusion coefficients are the average of the diffusion coefficient of FRAP measurements at five different positions in the sample.

6.2.4 Primer design

We have used multiple selection steps to find a suitable primer set to obtain long ssDNA with a FRET pair at one of its ends. For the first selection round, we have made use of the aPrime software, which is specifically developed to select primers for the synthesis of long ssDNA by asymmetric PCR.[34] In this step, we selected primers that could form a ssDNA strand of 7200 to 7300 nucleotides from a lambda DNA template, with primer lengths between 20 and 30 nucleotides, a forward primer melting temperature between 60 °C and 63 °C and a reverse primer melting temperature that was 3 °C to 5 °C

degrees lower than the forward primer. The last two requirements are adapted compared to the original aPrime software to account for a possible decrease of the melting temperature by the dyes with ~ 3 °C per dye, as was observed earlier for cyanine dyes.[35] Subsequently, we have used Blast software[36] to discard the primers pairs that had alternative possible priming sites (similarity of 9 or more nucleotides). In addition, to prevent that the observed dynamics is affected by DNA hybridisation interactions, we have used the Blast software to check that the first 40 nucleotides of the formed strand did not partly hybridise with part of the p7249 DNA that is used as unlabelled ssDNA in the sample (hybridisation of 9 or more nucleotides). Next, we selected the primers that had a thymine base at its second and second-last position since these are the positions we aimed to use for the dye attachment and thymines might cause the least quenching of the dyes.[37] Finally, from the remaining selection of primers, we selected the primer pair with the weakest secondary structures since these secondary structures will interfere the primer annealing in the PCR. The forward primer sequence that we obtained in this way is: 5' GTC TGC GTG CTA CTT CTG TCT GAT TT '3 and the corresponding reverse primer sequence is: 5' GGT ATC ATG TAG CCG CTT ATG C '3. This primer set forms DNA of 7200 nucleotides from a lambda DNA template.

6.2.5 Primer labelling

Two slightly different procedures were used to obtain the fluorescently labelled primer. Both protocols are based on NHS coupling between the NHS ester dyes and the C6 amino modified thymines at the second and second last position of the primer sequence (Section 6.2.4). In both cases, the NHS coupling was performed in a 100 mM phosphate buffer, pH = 7.2, at an atto550-NHS ester and atto647N-NHS ester concentration of 2.5 mM and a primer concentration of 50 μM. For the first protocol, resulting in forward primer 1A, the reaction time was 2 h and the reaction mixture was subsequently dialysed against miliQ. For the second protocol, resulting in forward primer 1B, the reaction time was increased to 4 h. In addition, the reaction mixture was first dialysed against phosphate buffer and 1 M NaCl solution to remove any dyes that are bound to the DNA by electrostatic interactions only. Afterwards, the reaction mixture was dialysed against miliQ.

The clean-up procedure of forward primer 1A consisted only of dialysis. Subsequently, forward primer 1A was concentrated by freeze-drying and dissolved in nuclease free water. Forward primer 1B was further purified by HPLC (Agilent 1220 Infinity system) on a C18 column with a linear gradient from solvent A to solvent B in 0-20 min and from solvent B to A in 20-40 min, with solvent A: 100 mM triethyl ammonium acetate in miliQ, pH = 7.0 and solvent B: acetonitrile. The retention time of the labelled primer was ~ 19.5 min. After HPLC purification, the forward primer 1B sample was shortly dialysed to remove the HPLC solvents, freeze-dried and dissolved in nuclease free water.

6.2.6 Primer characterisation

Steady state fluorescence spectra of the fluorescently labelled forward primers were recorded with an Agilent Cary Eclipse fluorescence spectrometer. All measurements were performed in a 50 mM NaCl solution.

DNA melting and annealing experiments were performed with a Shimadzu UV-2600 spectrophotometer. The temperature was controlled by a CPS-100 unit and was changed in steps of 2 °C at a time interval of ~ 3 min. The samples consisted of 0.5 μM forward primer (forward primer 1B or unmodified forward primer) and 0.5 μM of the complementary strand of the forward primer in a 10 mM phosphate buffer.

6.2.7 PCR and gel purification

The synthesis and purification of long ssDNA by asymmetric PCR was based on a method described by Veneziano *et al*..[34] The required LongAmp Taq polymerase PCR kit was purchased from New England Biolabs Inc. A standard PCR reaction mixture contained 1 μM forward primer, 20 nM reverse primer, 0.3 mM dNTPs, 100 μg/μL lambda DNA template and 0.1 units/μL LongAmp Taq polymerase in 1X LongAmp buffer. All components were mixed on ice and transferred to a pre-heated PCR thermocycler. Thermocycled reactions were initiated for 30 s at 94 °C, cycled 31 times for 20 s at 94 °C, 45 s at 56.5 °C and 11 min at 65 °C. In the last cycle, the 65 °C period was extended with 5 min. Samples were run on a 0.9 % low-melt agarose gel stained with SybrSafe for 1 h at 100 V.

The ssDNA and dsDNA bands were purified from the agarose gels by using the ZymoClean Gel DNA Recovery Kit (Zymo Research) following the protocol provided by the manufacturer. Briefly, the excised agarose gel bands were dissolved in 3 volumes binding buffer and melted for 10 min at 45 °C. The resulting solution was transferred to a spin column and centrifuged for 60 s at 11,000 RPM. The flow-through was discarded. Subsequently, the columns were washed two times by adding 250 μL of washing buffer, centrifuging at 11,000 RPM for 60 s and discarding the flow-through. Finally, the purified DNA was obtained by adding 6 μL of elution buffer to the column, centrifuging at 11,000 RPM for 60 s and collecting the flow-through.

6.2.8 TIRF microscopy

Total internal reflection fluorescence (TIRF) measurements of the polyelectrolyte complexes were performed on a home-built single-molecule TIRF setup as described in detail elsewhere.[38] This setup uses alternating laser excitation (ALEX) to alternately excite the donor and acceptor fluorophores. The emitted light is spectrally split in a donor and acceptor emission channel and the resulting light beams are focused next to each other on a CCD camera. In this case, we have used a 561 nm laser with a power of 3.5 mW to excite the donors and a 642 nm laser with a power of 2.6 mW to excite the acceptor. The frequency of alternating the laser was set to 20 Hz. The camera acquisition rate was also set to 20 Hz and was synchronised to the alternating of the lasers. The polyelectrolyte complexes were imaged for 50 s at the same sample position.

The polyelectrolyte complexes were prepared by first mixing 1 μL of the fluorescently labelled ssDNA obtained from asymmetric PCR (Section 6.2.7) with 29 μL of p7249 solution. Subsequently, part of the ssDNA solution was mixed with 10X PBS solution, nuclease free water and poly(L-lysine) stock solution to obtain a solution with an average positive and negative monomer concentration of 1 mM in 1X PBS. Samples were prepared directly a microscopy glass slide coated with 3 wt % poly(vinyl alcohol) solution and measured shortly after preparation.

6.3 Results and discussion

6.3.1 Simulations of the FRET signal

The first step to develop a FRET-based probe for the dynamics in the polyelectrolyte complex is to determine the best label strategy. As already mentioned in the introduction, we aim to use specific labelling of DNA to prevent averaging of the FRET signal and to allow for direct comparison of the FRET signal of different polymers. To find the optimal dye attachment positions in the DNA, we have generated 1000 different DNA configurations, both for ssDNA and dsDNA, and have used accessible volume simulations to calculate for each DNA configuration the FRET efficiency for different dye attachment points (Fig. 6.2).

The ssDNA strands have a higher FRET efficiency and show more variations in FRET efficiency between different strands than the dsDNA strands (Fig. 6.2b) and thus have a larger configurational

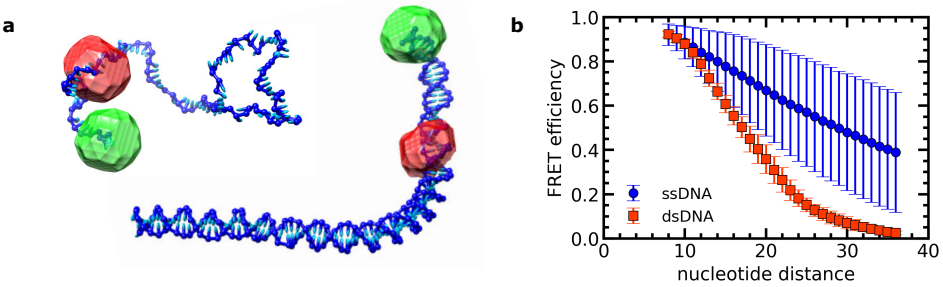

Figure 6.2. Determination of the FRET efficiency of ssDNA and dsDNA based on coarse-grained molecular dynamics simulations followed by accessible volume calculations with atto550-NHS ester as donor dye and atto647N-NHS ester as acceptor dye. a) Example of a simulated ssDNA (left) and dsDNA (right) configuration including the calculated accessible volume of the donor dye (green) and acceptor dye (red). b) Average FRET efficiency and standard deviation of thousand independent DNA configurations as function of the number of nucleotides between the donor and acceptor attachment points. In all cases, the donor dye is attached to the second nucleotide from the 5′ end.

entropy than the dsDNA strands. These differences reflect the lower stiffness of ssDNA compared to dsDNA: the persistence length of ssDNA ($\sim 2\,\mathrm{nm}$)[39] is much lower compared to the persistence length of dsDNA ($\sim 44\,\mathrm{nm}$)[40] at similar ion concentrations. The example DNA configurations (Fig. 6.2a) also illustrate this difference in persistence length with the ssDNA strand showing much more turns than the dsDNA strand.

In this case, we want the variations in FRET efficiency between the different DNA configurations to be large. Since all DNA configurations have been generated for the same DNA sequence, these large variations in FRET efficiency should also occur in a single strand if this strand is followed over a sufficient amount of time. The large FRET fluctuations imply that both significant changes in the DNA configuration occur and that these changes are on a length scale that can be probed by the FRET efficiency. The ssDNA shows much larger variations in FRET efficiency than the dsDNA and is therefore more suited to use as a FRET-based probe of the sub-chain dynamics. For short distances between the dye attachment points, fewer variations in FRET efficiency occur (Fig. 6.2b), while for large distances between the attachment points, the FRET efficiency might become too low to be measured. The optimum FRET efficiency is thus in between and roughly corresponds to a distance of 18-40 nucleotides (Fig. 6.2b).

To verify that the FRET fluctuations of ssDNA with appropriate dye attachment points can indeed be used as a probe for the sub-chain dynamics, we have simulated the movements of ssDNA in time and subsequently calculated the corresponding FRET efficiency. The FRET efficiency calculations were again based on accessible volume calculations for the dyes. This approach requires that the movement of the dye and the linker itself are much faster than the movement of the DNA. Although this is not the case for the free DNA simulated here, we expect that this requirement is fulfilled in polyelectrolyte complexes as the electrostatic interactions will slow down the DNA movements, while the movements of the uncharged linker will be less affected.

The relative sub-chain dynamics of the simulated DNA starts from the ballistic regime ($\Delta r^2 \sim t^2$) and gradually levels of to reach a plateau (Fig. 6.3a). The plateau occurs because the connectivity of the two monomers imposes a minimum and a maximum of the distance between the two monomers and therefore the relative mean-squared displacement cannot increase further beyond a certain point. The plateau of dsDNA is lower because its larger stiffness allows fewer relative movements. For both the ssDNA and dsDNA, we do not observe the sub-diffusive regime ($\Delta r^2 \sim t^{0.5}$) predicted for Rouse polymers[14] and observed in simulations of coarse-grained bead-spring polymers.[41] Probably this

is because the ballistic regime is relatively large for the used oxDNA simulation settings: a closer inspection of the mean-squared displacement of the the middle monomer shows that the ballistic regime continues beyond the point where the mean square displacement equals the monomer size b (Fig. 6.A.1), while the sub-diffusive regime should start here. As a result, the plateau in the relative sub-chain dynamics is already reached before the sub-diffusive regime can be observed. A change in thermostat settings and diffusion coefficient might help to ensure that the sub-diffusive regime starts when $< \Delta R^2 >= b^2$. In this case, we are mainly interested in the comparison between the FRET efficiency fluctuations and sub-chain dynamics and not in the precise sub-chain dynamics itself, as this will also change when the DNA polymer is incorporated in the polyelectrolyte complex. Therefore we have just used the default oxDNA model simulation settings.

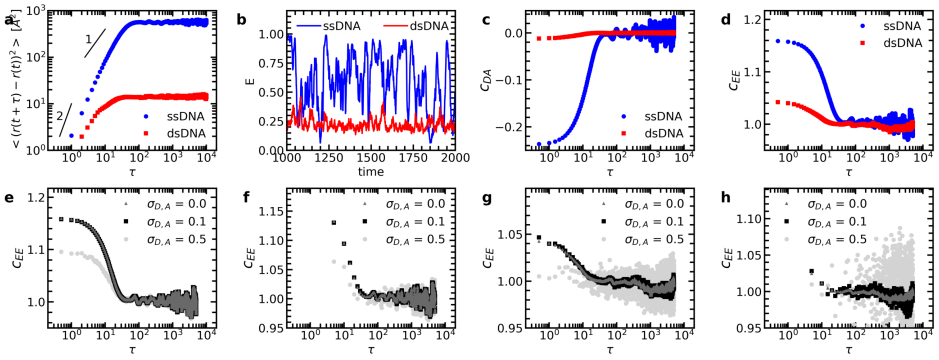

Figure 6.3. Simulations of the DNA dynamics and the corresponding FRET efficiency. The donor dye is attached to nucleotide 2 and the acceptor dye is attached to nucleotide 25 counted from the 5′ end. a) Relative mean squared displacement of nucleotide 2 compared to nucleotide 25. b) Comparison of the FRET fluctuations in time for ssDNA and dsDNA. c) Comparison of the donor and acceptor cross correlation c_{DA} curve for ssDNA and dsDNA. d) Comparison of FRET efficiency auto correlation c_{EE} curve for ssDNA and dsDNA. e,f) The FRET efficiency auto correlation for ssDNA for different degrees of noise ($\sigma_{D,A}$) for a time resolution $1/\Delta t$ with $\Delta t = 0.5\tau_s$ (e) and $\Delta t = 5\tau_s$ (f). g,h) The FRET efficiency auto correlation for dsDNA for different degrees of noise ($\sigma_{D,A}$) for a time resolution $1/\Delta t$ with $\Delta t = 0.5\tau_s$ (g) and $t = 5\tau_s$ (h).

The corresponding FRET efficiency fluctuations in time are much larger for ssDNA than for dsDNA (Fig. 6.3b), as we expected based on calculations of independently generated DNA configurations (Fig. 6.2). A way to obtain the characteristic of the FRET fluctuations is to calculate the cross correlation c_{DA} of the FRET signal:

$$c_{DA}(\tau) = \frac{< I_D(t+\tau) I_A(t) >}{< I_D(t+\tau) >< I_A(t) >} - 1 \tag{6.4}$$

Here, I_D is the donor intensity and I_A is the acceptor intensity. These are related to the FRET efficiency:

$$E = \frac{I_A}{I_A + I_D} \tag{6.5}$$

To calculate the cross correlation (Equation 6.4) from the simulated FRET signal, we have set $I_D + I_A = 1$ and used $I_A = E$ and $I_D = 1 - E$.

The characteristic time of the FRET fluctuations can also be obtained by calculating the auto correlation function c_{EE} of the FRET signal itself:

$$c_{EE}(\tau) = \frac{< E(t+\tau) E(t) >}{< E(t >^2} \tag{6.6}$$

Both the cross correlation and auto correlation approach give similar results (Fig. 6.3c,d), but comparison of the dsDNA correlation results suggests that the autocorrelation might perform slightly better for samples with low FRET efficiencies.

The characteristic decay time that we observe in the correlation functions (Fig. 6.3) agrees well with the relative mean squared displacement (Fig. 6.3a), although the correlation functions seem to decay slightly earlier than the relative mean squared displacement reaches its plateau. This small difference might be the result of the relatively large variation in dye positions because of the flexible linker. The relatively good agreement between the relative mean squared displacement and the correlation functions supports the use of FRET correlation to probe the sub-chain dynamics. It might be tempting to try to convert the FRET efficiency directly to the distance between the nucleotide by using the Förster radius (Equation 6.1) and from this calculate the relative mean squared displacement. However, due to the flexible linker between the dye and the nucleotide attachment point, the FRET efficiency cannot be directly converted to nucleotide distances (Fig. 6.A.2). As a result, this conversion will not give any additional information compared to the correlation function.

In experiments the time resolution can be limited and the FRET signal will contain experimental noise. To study the effects of these factors, we have calculated the auto correlation for different degrees of experimental noise in the donor and acceptor intensity $\sigma_{D,A}$ and different time resolutions $1/\Delta t$ (Fig. 6.3d-i). Here $\sigma_{D,A}$ is the standard deviation introduced in the donor and acceptor signal separately (in the cases where the intensity became negative, an intensity of 1×10^{-4} was used instead) and Δt is the time interval over which the FRET signal is averaged. If the time resolution becomes too low compared to the characteristic correlation time, the dynamics cannot be measured anymore (Fig. 6.3f,h). This point occurs earlier when the experimental noise is very large, as illustrated by the case where $\sigma_{D,A} = 0.5$ (Fig. 6.3g). We expect that the experimental noise will be lower than this large value of $\sigma_{D,A} = 0.5$. For example, for a system with an average FRET efficiency of $< E >= 0.55$ measured a camera-based TIRF single-molecule setup, the minimal noise was estimated to be $\sigma_E \approx 0.06$.[42]

In conclusion, the simulations show that the auto correlation of the labelled ssDNA FRET signal can indeed provide information about the sub-chain dynamics as long as the time resolution is high enough. For dsDNA, fluctuations on FRET length scale are much smaller, resulting in lower fluctuations in FRET and an auto correlation that is more difficult to measure due to the shorter decorrelation time and the lower FRET efficiency.

6.3.2 Diffusion in polyelectrolyte complexes with different DNA lengths

In the previous section, we concluded that the DNA dynamics has to be sufficiently slow compared to the experimental time resolution. To be able to predict whether this can be accomplished for polyelectrolyte complexes with ssDNA, we have performed FRAP measurements on ssDNA/poly(L-lysine) complexes with fluorescently labelled poly(L-lysine) (Fig. 6.4).

Increasing the length of the ssDNA slows down the movement of the poly(L-lysine) as shown by the slower recovery in the FRAP measurements (Fig. 6.4). This effect of varying the length of the oppositely charged polymer is similar to what we observed in Chapter 5 and might be partly explained by changes in coacervate density with increasing polyelectrolyte length. This different poly(L-lysine) diffusion for the two different ssDNA lengths also suggests that increasing the overall ssDNA length might help to slow down the local polymer dynamics.

The FRAP recovery curves can be fitted with an infinite medium 3D diffusion model (Methods section 6.2.3) to estimate the diffusion coefficient (Fig. 6.4c). The systematic deviation between the fit and the data at the start of the short ssDNA recovery curve is probably the result of imperfect bleaching: the model assumes that bleaching occurs only in the bleach spot region, but comparison of the radial intensity profile directly before and after bleaching showed that also part of the fluorophores outside the bleach region are bleached. As a result, the initial recovery is slightly slower than for the perfect stepwise bleach profile assumed in the model. The pLL diffusion coefficients that we obtain from the

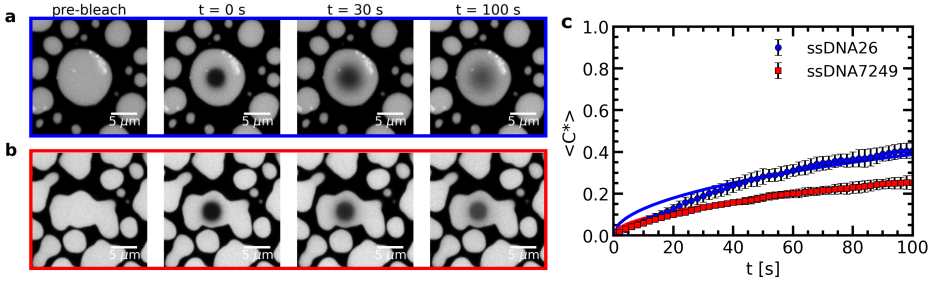

Figure 6.4. FRAP experiments with polyelectrolyte complexes consisting of ssDNA and fluorescently labelled poly(L-lysine). a-b) Example images at different time points during the FRAP experiment for polyelectrolyte complexes with short (a) and long (b) ssDNA. We note that the non-spherical shape of the coacervate droplets is probably the result of the coacervate droplets heterogeneously wetting the microscopy glass slide due to insufficient coating with PVA. c) Comparison of the average normalised fluorescence recovery curve for complexes with short (ssDNA26) and long (ssDNA7249) single stranded DNA. Solid lines indicate the recovery curves calculated from the average diffusion coefficients $D = 1 \times 10^{-3} \mu m^2/s$ (ssDNA26) and $D = 5 \times 10^{-4} \mu m^2/s$ (ssDNA7249) obtained from fitting the individual recovery curves.

fit are $D = 1 \times 10^{-3} \mu m^2/s$ and $D = 5 \times 10^{-4} \mu m^2/s$ for the polyelectrolyte complexes with short ssDNA (ssDNA26) and long ssDNA (ssDNA7249) respectively. These diffusion coefficients are larger than for example the ssDNA diffusion coefficient in the nt88/pLL50 complexes. This might be explained by the presence of some free fluorescently labelled pLL polymers that increased the FRAP recovery in Fig. 6.4.

In a first approximation, the monomer diffusion time can be estimated from the overall polymer diffusion coefficient by assuming that the dynamics follows the sticky Rouse model and by neglecting any numerical prefactors. In that case, the monomer diffusion coefficient D_{mon} is given by:

$$D_{mon} = DN \tag{6.7}$$

where N is the length of the poly(L-lysine) chain. In this case, the polyelectrolyte length is in the range of ~72 to ~143 monomers. Subsequently, the monomer relaxation time τ_0 can be estimated from

$$\tau_0 = b^2/D_{mon} \tag{6.8}$$

where b is the size of the monomer. By taking a monomer size in the range of 0.3 nm to 1 nm and a poly(L-lysine) length in the range of 72-143 monomers, we obtain a monomer relaxation time in the range ~0.6 μs to ~14 μs for the complexes with ssDNA consisting of 7249 nucleotides. This is shorter than earlier estimations on the monomer relaxation time based on rheology and force spectroscopy measurements, although these earlier estimations also largely vary from ~0.1 ms at 0.03 M salt concentration,[12,23] to ~200 ms at 0.6 M.[11,17] These differences might be partly explained by differences in salt and polyelectrolyte concentration and the neglecting of prefactors. However, inaccuracy in some of these estimations can also not be excluded yet, like the presence of freely diffusing poly(L-lysine) in the case of our FRAP measurements.

The typical decorrelation time for the single-molecule measurements can also be estimated from the FRAP measurements by using the same assumptions as for the monomer relaxation time. For example, for a donor-acceptor distance of 20 nucleotides, the decorrelation time would roughly be on the order of 0.3 ms to 6 ms based on $\tau(N) = \tau_0 N^2$ with $N = 20$ and $\tau_0 = 0.6$ μs to 14 μs. This suggests that the dynamics of these polyelectrolyte complexes might be slightly too fast to be measured on a camera based single-molecule set up which has a minimal time resolution of ~10 ms.[38] To further slow down the dynamics, the salt concentration can be decreased. In this case, we measured the complexes in

1X PBS, corresponding to a salt concentration of 140 mM. The salt concentration can thus be further decreased by diluting the PBS solution.

6.3.3 Primer labelling

The FRAP measurements show that the dynamics can be slowed down by increasing the ssDNA length. Yet, the length of ssDNA synthesised by solid phase chemical synthesis is restricted to ~ 200 nucleotides. Therefore, we take a different approach to obtain long, specifically labelled ssDNA: we use asymmetric PCR to start from short, fluorescently labelled ssDNA to make long ssDNA with a FRET pair at its end (Fig. 6.7a). We decided to attach the dyes to the second and second-last nucleotide of the short ssDNA primer. To reduce chain-end effects, it would have been better if we could attach the first dye further away from the chain end. However, since the primer length is limited to ~ 30 nucleotides and the simulations show that a distance of ≥ 18 nucleotides is optimal for the FRET signal, attaching the dye much further away from the 5′ end is not possible. The other dye is attached to the second-last nucleotide since a dye at the last nucleotide position might interfere with the chain extension. To ensure that the distance between the dyes is sufficiently large, we searched for forward primers with a minimum length of 20 nucleotides. The other selection criteria that we used to find the primer set are given in the materials and methods (Section 6.2.4).

The label reaction was based on a NHS coupling reaction between the NHS ester of the dye and the amino group of the C6 modified thymine. Since we used the same reaction for both dyes, four different combinations of dye pairs could be formed: D-D, D-A, A-D and A-A. Only the ones with a donor and acceptor attached to the same primer will be selected for analysis in the single-molecule FRET experiments.

We have performed the label reaction two times. Although, initially the first attempt seemed to have worked well, dilution of the primer showed that a substantial part of the FRET was caused by intermolecular interactions and not the intramolecular interactions that we aimed for (Fig. 6.5a). In the second attempt, we increased the reaction time. We also performed HPLC purification to remove the last part of the unreacted dye. After this HPLC purification, the primer:donor:acceptor ratio was 1:1:0.9 as measured by UV-VIS absorption. Compared to the first attempt, this forward primer 1B showed a larger FRET efficiency, which was caused only by intramolecular interactions (Fig. 6.5b). In fact, the FRET efficiency was higher than we expected. Based on the simulations, we expected that a donor-acceptor pair has a FRET efficiency of ~ 0.61. For completely random labelling, we would expect that about half of the donors is attached to a primer that also has an acceptor attached. This would give a FRET efficiency ~ 0.30, while we measure a FRET efficiency of ~ 0.55. A possible explanation is that differences in quantum efficiency and deviations of the Förster radius have resulted in a different apparent FRET efficiency. In addition, interactions between the dyes themselves or the DNA and the dye might have occurred. These interactions might have resulted in slightly different conformations than calculated in the simulations, where these interactions are not taken into account. Furthermore, favourable interactions between the donor and acceptor pairs might have resulted in a larger fraction of donor-acceptor pairs than the 0.5 expected from random labelling.

As an additional check of the labelling of forward primer 1B, we have added its complementary strand to obtain dsDNA. The hybridisation should lower the FRET efficiency (Fig. 6.2b). Indeed, the FRET efficiency decreases by adding is complementary strand (Fig. 6.5c). Adding a 10x excess of complementary strand, decreases the FRET efficiency even further, while the FRET efficiency remains the same when increasing this excess to 20x. This suggests that at a 10x excess already all fluorescently labelled primers are double stranded. Again, the FRET efficiency was larger than we expected for random labelling. In fact, the FRET efficiency that we estimated from the emission spectrum ($E \approx 0.25$) was even larger than the FRET efficiency of a dsDNA donor-acceptor pair that we estimated from the simulations ($E \approx 0.22$). This might point at specific dye-dye or dye-DNA interactions. Alternatively, the

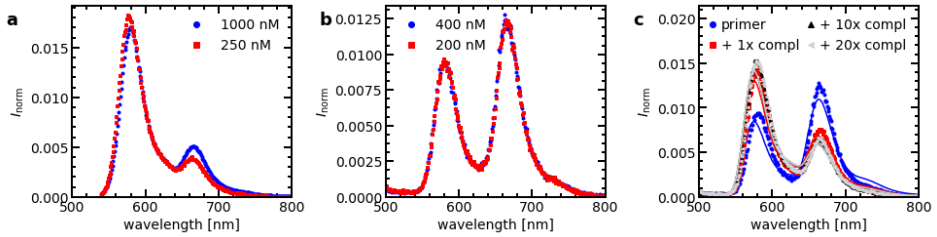

Figure 6.5. Normalised fluorescence emission spectra of of the fluorescently labelled forward primer 1A and 1B a) Concentration effect on the FRET efficiency of forward primer 1A. b) Concentration effect on the FRET efficiency of forward primer 1B. c) Effect of the addition complementary DNA strands to forward primer 1B. Solid lines indicate fits with a linear combination of the atto550 and the atto647N emission spectrum.

larger FRET efficiency might also be caused by a somewhat different Förster radius or some inaccuracy of the fit of the emission spectrum (Fig. 6.5c).

For the selection of the primers, we assumed that each dye lowers the melting temperature by ~ 3 °C based on a study for cyanine dyes.[35] With the fluorescently labelled forward primer 1B we can check whether atto dyes indeed have the same effect as the cyanine dyes. For this, we measured the DNA melting and annealing curves of unmodified forward primer 1 and the fluorescently labelled forward primer 1B. Both show hysteresis between the heating and cooling, indicating that kinetic effects play a role.[43] Their real melting temperature will be in between the apparent melting temperature of the heating and cooling curves. For both primers, this is around ~ 52 °C. In contrast to the cyanine dyes, the atto dyes thus seem to have nearly no effect on the melting temperature. We thus overcorrected for the dye temperature effect in our primer design.

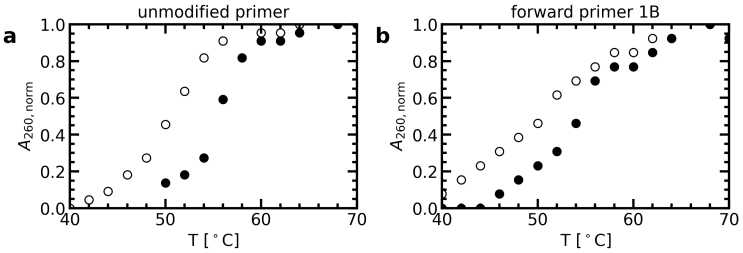

Figure 6.6. DNA melting (filled symbols) and annealing (open symbols) curves of the unmodified primer (a) and the fluorescently labelled forward primer 1B (b).

6.3.4 Asymmetric PCR

Even though the primer selection might be sub-optimal due to overcorrection for the dye effect on the melting temperature, the selected primers set still could form both ssDNA and dsDNA (Fig. 6.7b). The ssDNA and dsDNA bands are separated by gel electrophoresis, with the ssDNA bands migrating more quickly through the gel. Both the dsDNA and ssDNA band correspond well to the expected size of 7200 nucleotides: the dsDNA band is in between 6000 and 8000 base pair bands of the dsDNA marker (lane M) and the ssDNA band is at the same height as circular p7249 ssDNA (lane p), which consist of 7249 nucleotides. Although we aim to use the ssDNA to probe the sub-chain dynamics, the dsDNA byproduct can also be purified from the gel to serve as a control to check whether it indeed gives a different result in the auto correlation compared to the ssDNA FRET signal (Fig. 6.3)

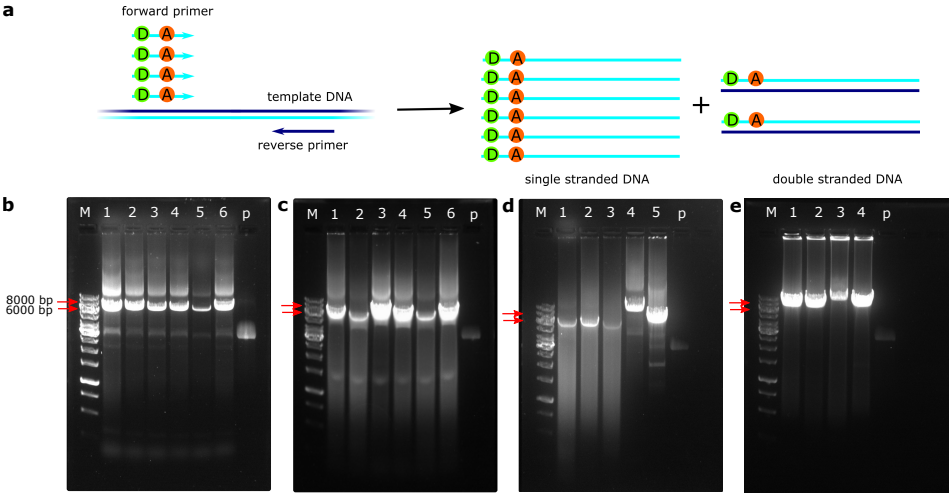

Figure 6.7. Asymmetric PCR to synthesize long ssDNA with a FRET pair at its end. a) Schematic overview of the reaction. By adding an excess of the fluorescently labelled forward primer, the forward primer strand is formed more often, resulting in a mixture of fluorescently labelled ssDNA and dsDNA instead of only dsDNA. b-d) Agarose gel electrophoresis of the asymmetric PCR products. Red arrows indicate the double stranded DNA markers with a size of 8000 basepairs (top arrow) and 6000 basepairs (bottom arrow). M = dsDNA size marker, p = type p7249 circular ssDNA. b) Six repetitions (1-6) of the same PCR experiment with forward primer 1A. c) PCR experiments with different forward primer 1A (F): reverse primer 1 (R) ratios. 1. F:R = 50, 2. F:R = 100, 3. F:R = 25, 4. F:R = 200, 5. F:R = 400, 6. F:R = 2. d) PCR experiments with different primer sets. 1. forward primer 1A, 2. forward primer 1B, 3. unmodified forward primer, 4. literature primer set for a ~10 kb DNA fragment,[34] 5. literature primer set for a ~6.8 kb DNA fragment using p7249 ssDNA as template.[34]. e) PCR experiments with different primer sets. 1. forward primer 1B, 2. unmodified forward primer, 3. literature primer set for a ~10 kb DNA fragment,[34] 4. forward primer 2. An overview of the used primer sets in d) and e) is given in the appendix (Table 6.A.1).

Unfortunately, at certain moment, the asymmetric PCR reaction with the fluorescently labelled primer started to yield only dsDNA and no ssDNA. Changing the forward and reverse primer ratio did also not result in the formation of ssDNA (Fig. 6.7c). So far, we have not yet found the cause for the absence of ssDNA. It might be related to the LongAmp Taq polymerase batch as it started to occur when we changed to a new batch. In addition, also other primer sets sometimes did not yield ssDNA (Fig. 6.7e) with this batch of LongAmp Taq polymerase: it occurred both for a primer set from literature[34] and a primer set that was selected in a similar way as forward primer 1, but then without correcting the forward primer melting temperature with 6 °C. However, in other cases, we could observe some ssDNA bands for literature primers with this batch (Fig. 6.7d). In addition, trying another new batch of LongAmp Taq polymerase also did not result in the formation of ssDNA. Therefore, also other factors, like a decrease in primer quality over time, might have hindered the ssDNA formation.

6.3.5 Single-molecule measurements

Because of the irreproducibility of the asymmetric PCR results, we were only able to obtain fluorescently labelled ssDNA formed from forward primer 1A and not from forward primer 1B. Although the FRET efficiency of forward primer 1A is too low to use it as a FRET-based probe of the sub-chain dynamics in polyelectrolyte complexes, we can still use it as a first check of the proposed strategy to measure this sub-chain dynamics.

We have mixed the fluorescently labelled ssDNA with p7249 ssDNA and subsequently mixed it with oppositely charged poly(L-lysine) to obtain fluorescent polyelectrolyte complexes (Fig. 6.8a,b). The acceptor fluorescence upon direct acceptor excitation is significantly higher than for the control sample (Fig. 6.8f and Fig. 6.8b versus Fig. 6.A.3). This shows that the fluorescently labelled ssDNA is successfully purified and incorporated in the polyelectrolyte complex. Yet, for donor excitation, the amount of donor fluorescence is comparable to the amount of donor fluorescence of the control sample (Fig. 6.8d and Fig. 6.8b versus Fig. 6.A.3). The fluorescence of the unlabelled polyelectrolytes is thus too high to easily distinguish the donors from the background fluorescence. This background fluorescence might be the result of a small amount of fluorescent groups introduced during the synthesis of the poly(L-lysine). Even though the fluorescence of these groups is very weak, still a significant amount of background is observed because the local concentration of the unlabelled poly(L-lysine) is high. The background fluorescence might be reduced by using poly(L-lysine) that is specifically synthesised for microscopy experiments and therefore might have less fluorescent groups. Alternatively, the difference in photo-stability might be used to distinguish between the background fluorescence and the donor dyes as the atto-dyes are more stable against bleaching.

The amount of acceptor fluorescence upon donor excitation seemed somewhat higher than in the control sample (Fig. 6.8e), but this is probably the result of differences in the amount of background signal: no clear fluorescent acceptor emission spots were observed upon donor excitation of the complexes with fluorescently labelled ssDNA, while these spots are observed upon acceptor excitation. In addition, the positions of the highest acceptor intensity upon donor excitation did not correspond to the ones upon acceptor excitation, while this should be the case for FRET. In fact, we also did not expect a high acceptor emission upon donor excitation because of the low FRET efficiency of forward primer 1A (Fig. 6.5a).

Although complexes with ssDNA from forward primer 1A cannot be used as a FRET-based probe of the sub-chain polyelectrolyte dynamics, they still give a first indication on the overall polymer movement. The position of the acceptor emission spots upon acceptor excitation remained the same over time (Fig. 6.8c), indicating that the polyelectrolyte movement is at least sufficiently slowed down to keep the fluorescently labelled ssDNA at the same position during the single-molecule measurements. Yet, to test whether the dynamics is also sufficiently slow enough to resolve the FRET fluctuations caused by the sub-chain movements, a probe with a higher FRET efficiency is needed.

6.4 Conclusions and outlook

In conclusion, specific labelling of long single stranded DNA molecules with a single FRET-pair might be a good strategy to probe the sub-chain dynamics in a polyelectrolyte complex. Our simulations have illustrated how from the FRET fluctuations of specifically labelled ssDNA, the sub-chain dynamics of the ssDNA chain can be inferred, provided that the experimental time resolution is high enough. In addition, we have shown that in principle ssDNA with a FRET pair at its end can be synthesised by using a coupling reaction between the FRET dyes and a short ssDNA strand followed by the extension of this short ssDNA by asymmetric PCR. The long specifically labelled ssDNA that is formed in this way can be incorporated in a polyelectrolyte complex. Its presence can be observed in TIRF microscopy and the overall ssDNA strand shows little movement over longer times.

Unfortunately, irreproducibility of the asymmetric PCR results prevented the synthesis of a sufficient amount of long ssDNA with a FRET pair at its end. Therefore, to reach our goal of probing the sub-chain dynamics in a polyelectrolyte complex, first the reproducibility of the synthesis of long, specifically labelled single stranded DNA has to be improved. For the synthesis by asymmetric PCR, the LongAmp Taq polymerase batch, the primer batches and the other PCR reaction mixture components have to be systematically varied to find the origin of the absence of ssDNA. The type of polymerase enzyme might also be varied, since also other Taq polymerases have been reported to form long ssDNA.[34]

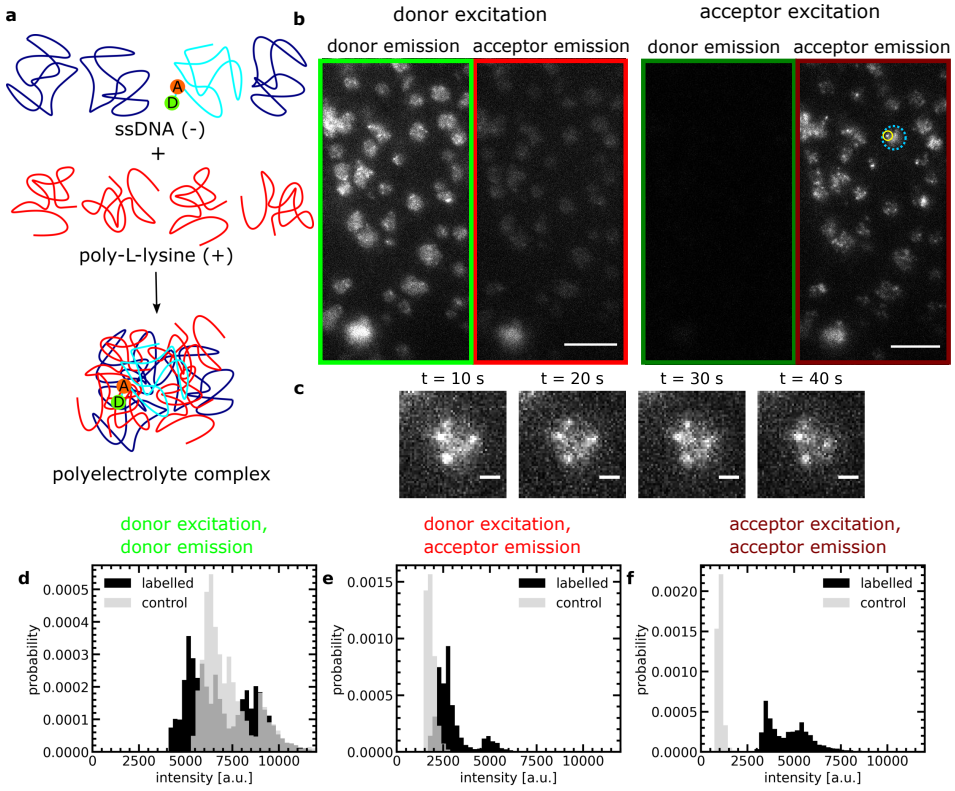

Figure 6.8. Camera-based TIRF microscopy measurements of ssDNA and poly(L-lysine) polyelectrolyte complexes containing a small amount of fluorescently labelled ssDNA formed by asymmetric PCR with forward primer 1A. a) Schematic overview of the complex formation: the fluorescently labelled ssDNA is mixed with circular p7249 ssDNA. Subsequently, the ssDNA mixture is mixed with poly(L-lysine) to form the polyelectrolyte complexes. b) Examples of a camera frame after donor (left) and acceptor (right) excitation. In both cases, the right hand side of the frame corresponds to the donor emission channel and the left hand side of the frame corresponds to the acceptor emission channel. Scale bars correspond to 10 μm. The cyan dotted circle in the acceptor channel after acceptor excitation indicates an example of a polyelectrolyte complex region and the small yellow circle indicates an example of a single-molecule fluorescence spot. c) Close-up of a part of the acceptor channel after acceptor excitation at different time points during the a measurement. Scale bars correspond to 1 μm. d -f) Histogram of the intensity of the 0.5 % brightest pixels of the channel for polyelectrolyte complexes with fluorescently labelled ssDNA (labelled) and without fluorescently labelled ssDNA added (control). d) Histogram for the donor channel after donor excitation. e) Histogram for the acceptor channel after donor excitation and f) Histogram for the acceptor channel after acceptor excitation.

Alternatively, other methods for the synthesis of long labelled ssDNA can be considered. For example, rolling circle amplification can be used to form long ssDNA from a fluorescently labelled primer.[44] However, in this case the overall DNA length is different for every formed strand, which will make the interpretation of the dynamics more difficult. Another strategy might be to just use the longest possible length of solid phase synthesised DNA (~ 200 nucleotides) and try to adapt the other parameters such that its dynamics is still slow enough to be measured. An advantage of this chemically synthesised DNA is that the fluorophores can also be placed slightly further away from each other since in this case the dye distance is not limited by a maximum primer length. In addition, chain end effects can be

prevented by attaching the FRET pair to nucleotides in the middle of the chemically synthesised DNA chain.

Once specifically labelled single stranded DNA has been obtained, the sub-chain dynamics of the DNA molecule can be followed by single-molecule fluorescence spectroscopy measurements. Hopefully, the dynamics is slow enough to be measured by using a camera-based single-molecule TIRF setup, which has a minimal time resolution of ~ 10 ms.[38] Otherwise, other methods with a higher time resolution can be used. For example, sub-millisecond resolutions can be obtained by diffusion-based single-molecule measurements with a confocal microscope setup with alternating laser excitation integrated in the setup.[45] However, since this method is based on confocal microscopy and not on TIRF microscopy, it is more sensitive to background fluorescence. This might be a problem because of the high background fluorescence of the polyelectrolyte complexes.

Finally, the obtained sub-chain dynamics could be compared to the overall chain dynamics. For example, the local DNA dynamics can be compared to the overall DNA diffusion coefficient. This diffusion coefficient can be obtained by single-molecule mean squared displacement tracking[46] or by using FRAP measurements. Alternatively, the dynamics of the DNA containing polyelectrolyte complexes can be probed by micro-rheology measurements.[47] By comparing the diffusion or rheology measurements to the single-molecule FRET measurements, the overall dynamics can be directly related to the local dynamics, which could considerably advance our understanding of the dynamics in polyelectrolyte complexes.

Acknowledgements

We would like to thank Johannes Hohlbein and Mattia Fontana for useful discussions on the FRET probe design and for the use of their TIRF-based single-molecule setup. In addition, we would like to thank Bauke Albada for his help with the HPLC purification of the primer and Rob de Haas and Nicolò Alvisi for their help with the PCR and gel purification.

6.A Appendix

6.A.1 Primer sequences

Table 6.A.1. Overview of the PCR primers used in this chapter, F = forward primer and R = reverse primer. A bold **T** indicates a thymidine modified with a C6 amino linker that can react with a NHS ester dye.

forward primer name	**primer sequences**	**fragment length (bp)**
unmodified forward primer	F: 5′ GTC TGC GTG CTA CTT CTG TCT GAT TT ′3 R: 5′ GGT ATC ATG TAG CCG CTT ATG C 3′	7200
forward primer 1A	F: 5′ G**T**C TGC GTG CTA CTT CTG TCT GAT **T**T ′3 R: 5′ GGT ATC ATG TAG CCG CTT ATG C 3′	7200
forward primer 1B	F: 5′ G**T**C TGC GTG CTA CTT CTG TCT GAT **T**T ′3 R: 5′ GGT ATC ATG TAG CCG CTT ATG C 3′	7200
forward primer 2	F: 5′ CTG TTG CCC CTA AGA CCT TTA ATA ′3 R: 5′ GCC TTC TCC CTG TAC CTG AAT C ′3	7298
literature forward primer 10kb	F: 5′ CAG TGC AGT GCT TGA TAA CAG G ′3 R: 5′ GTA GTG CGC GTT TGA TTT CC ′3	10 033
literature forward primer 6.8kb	F: 5′ GCGA CGA TTT ACA GAA GCA A ′3 R: 5′ GGC ATT TTC GAG CCA GTA AT ′3	6812

6.A.2 Monomer mean squared displacement

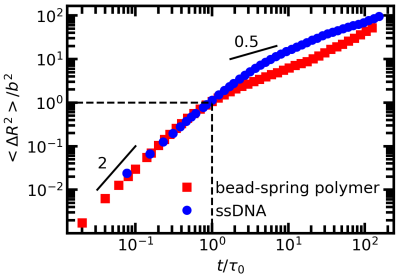

Figure 6.A.1. Mean squared displacement $< \Delta R^2 >$ of the middle monomer of the coarse-grained ssDNA polymer based on the oxDNA model and a polymer of 100 monomers modelled by the bead-spring model of Kremer and Grest.[41] The monomer size is indicated with b and τ_0 is the time at with $< \Delta R^2 >= b^2$.

6.A.3 FRET efficiency versus distance between the nucleotides

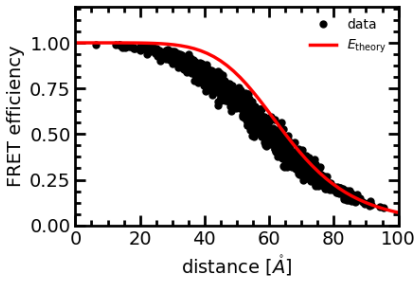

Figure 6.A.2. Overview of the simulated FRET efficiency versus distance between the labelled nucleotides for the 1000 different DNA configurations. The donor dye is attached to nucleotide 2 and the acceptor dye is attached to nucleotide 25 counted from the 5′ end. The red line (E_{theory}) shows the theoretical FRET efficiency (Equation 6.1) for a Förster radius of 65 Å as function of the distance between the dyes.

6.A.4 TIRF microscopy of the control sample

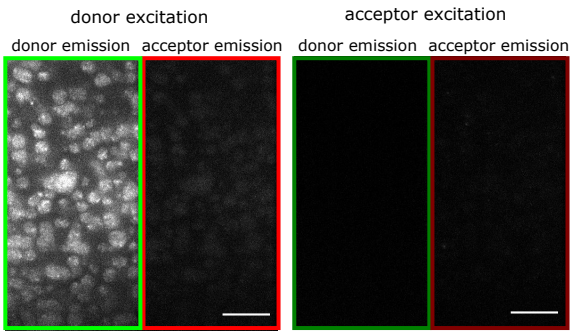

Figure 6.A.3. Camera-based TIRF microscopy measurements of ssDNA and poly(L-lysine) polyelectrolyte complexes without fluorescently labelled ssDNA added (control): examples of a camera frame after donor (left) and acceptor (right) excitation. In both cases, the right hand side of the frame corresponds to the donor emission channel and the left hand side of the frame corresponds to the acceptor emission channel. Scale bars correspond to 10 μm.

References

[1] Liu, Y.; Winter, H. H.; Perry, S. L. Linear viscoelasticity of complex coacervates. *Adv. Colloid Interface Sci.* **2017**, *239*, 46–60.

[2] Schmitt, C.; Turgeon, S. L. Protein/polysaccharide complexes and coacervates in food systems. *Adv. Colloid Interface Sci.* **2011**, *167*, 63–70.

[3] Reisch, A.; Tirado, P.; Roger, E.; Boulmedais, F.; Collin, D.; Voegel, J.-C.; Frisch, B.; Schaaf, P.; Schlenoff, J. B. Compact saloplastic poly (acrylic acid)/poly (allylamine) complexes: kinetic control over composition, microstructure, and mechanical properties. *Adv. Funct. Mater.* **2013**, *23*, 673–682.

[4] Rai, A. K.; Chen, J.-X.; Selbach, M.; Pelkmans, L. Kinase-controlled phase transition of membraneless organelles in mitosis. *Nature* **2018**, *559*, 211–216.

[5] Brangwynne, C. P.; Eckmann, C. R.; Courson, D. S.; Rybarska, A.; Hoege, C.; Gharakhani, J.; Jülicher, F.; Hyman, A. A. Germline P granules are liquid droplets that localize by controlled dissolution/condensation. *Science* **2009**, *324*, 1729–1732.

[6] Nakashima, K. K.; Baaij, J. F.; Spruijt, E. Reversible generation of coacervate droplets in an enzymatic network. *Soft Matter* **2018**, *14*, 361–367.

[7] Donau, C.; Späth, F.; Sosson, M.; Kriebisch, B. A.; Schnitter, F.; Tena-Solsona, M.; Kang, H.-S.; Salibi, E.; Sattler, M.; Mutschler, H., et al. Active coacervate droplets as a model for membraneless organelles and protocells. *Nat. Commun.* **2020**, *11*, 1–10.

[8] Xu, L.; Selin, V.; Zhuk, A.; Ankner, J. F.; Sukhishvili, S. A. Molecular weight dependence of polymer chain mobility within multilayer films. *ACS Macro Lett.* **2013**, *2*, 865–868.

[9] Aumiller Jr, W. M.; Pir Cakmak, F.; Davis, B. W.; Keating, C. D. RNA-based coacervates as a model for membraneless organelles: formation, properties, and interfacial liposome assembly. *Langmuir* **2016**, *32*, 10042–10053.

[10] Spoelstra, W. K.; Van Der Sluis, E. O.; Dogterom, M.; Reese, L. Nonspherical coacervate shapes in an enzyme-driven active system. *Langmuir* **2020**, *36*, 1956–1964.

[11] Spruijt, E.; Cohen Stuart, M. A.; van der Gucht, J. Linear viscoelasticity of polyelectrolyte complex coacervates. *Macromolecules* **2013**, *46*, 1633–1641.

[12] Yang, M.; Shi, J.; Schlenoff, J. B. Control of dynamics in polyelectrolyte complexes by temperature and salt. *Macromolecules* **2019**, *52*, 1930–1941.

[13] Larson, R. G.; Liu, Y.; Li, H. Linear viscoelasticity and time-temperature-salt and other superpositions in polyelectrolyte coacervates. *J. Rheol.* **2021**, *65*, 77–102.

[14] Rubinstein, M.; Colby, R. H. *Polymer Physics*; Oxford University Press New York, 2003.

[15] Spruijt, E.; Westphal, A. H.; Borst, J. W.; Cohen Stuart, M. A.; van der Gucht, J. Binodal compositions of polyelectrolyte complexes. *Macromolecules* **2010**, *43*, 6476–6484.

[16] Li, L.; Srivastava, S.; Andreev, M.; Marciel, A. B.; de Pablo, J. J.; Tirrell, M. V. Phase behavior and salt partitioning in polyelectrolyte complex coacervates. *Macromolecules* **2018**, *51*, 2988–2995.

[17] Spruijt, E.; van den Berg, S. A.; Cohen Stuart, M. A.; van der Gucht, J. Direct measurement of the strength of single ionic bonds between hydrated charges. *ACS Nano* **2012**, *6*, 5297–5303.

[18] Liu, Y.; Santa Chalarca, C. F.; Carmean, R. N.; Olson, R. A.; Madinya, J.; Sumerlin, B. S.; Sing, C. E.; Emrick, T.; Perry, S. L. Effect of polymer chemistry on the linear viscoelasticity of complex coacervates. *Macromolecules* **2020**, *53*, 7851–7864.

[19] Shen, K.-H.; Fan, M.; Hall, L. M. Molecular Dynamics Simulations of Ion-Containing Polymers Using Generic Coarse-Grained Models. *Macromolecules* **2021**, *54*, 2031–2052.

[20] Yu, B.; Rauscher, P. M.; Jackson, N. E.; Rumyantsev, A. M.; De Pablo, J. J. Crossover from Rouse to reptation dynamics in salt-free polyelectrolyte complex coacervates. *ACS Macro Lett.* **2020**, *9*, 1318–1324.

[21] Andreev, M.; Prabhu, V. M.; Douglas, J. F.; Tirrell, M.; de Pablo, J. J. Complex coacervation in polyelectrolytes from a coarse-grained model. *Macromolecules* **2018**, *51*, 6717–6723.

[22] Spruijt, E.; Sprakel, J.; Lemmers, M.; Cohen Stuart, M. A.; Van Der Gucht, J. Relaxation dynamics at different time scales in electrostatic complexes: time-salt superposition. *Phys. Rev. Lett.* **2010**, *105*, 208301.

[23] Hamad, F. G.; Chen, Q.; Colby, R. H. Linear viscoelasticity and swelling of polyelectrolyte complex coacervates. *Macromolecules* **2018**, *51*, 5547–5555.

[24] Syed, V. M.; Srivastava, S. Time–ionic strength superposition: A unified description of chain relaxation dynamics in polyelectrolyte complexes. *ACS Macro Lett.* **2020**, *9*, 1067–1073.

[25] Morin, F. J.; Puppo, M. L.; Laaser, J. E. Decoupling salt-and polymer-dependent dynamics in polyelectrolyte complex coacervates via salt addition. *Soft Matter* **2021**, *17*, 1223–1231.

[26] Marciel, A. B.; Srivastava, S.; Tirrell, M. V. Structure and rheology of polyelectrolyte complex coacervates. *Soft Matter* **2018**, *14*, 2454–2464.

[27] van de Laar, T.; Schuurman, H.; van der Scheer, P.; van Doorn, J. M.; van der Gucht, J.; Sprakel, J. Light from within: Sensing weak strains and femtoNewton forces in single molecules. *Chem* **2018**, *4*, 269–284.

[28] Spruijt, E.; Leermakers, F. A.; Fokkink, R.; Schweins, R.; van Well, A. A.; Cohen Stuart, M. A.; van der Gucht, J. Structure and dynamics of polyelectrolyte complex coacervates studied by scattering of neutrons, X-rays, and light. *Macromolecules* **2013**, *46*, 4596–4605.

[29] Ouldridge, T. E.; Louis, A. A.; Doye, J. P. Structural, mechanical, and thermodynamic properties of a coarse-grained DNA model. *J. Chem. Phys.* **2011**, *134*, 02B627.

[30] Sengar, A.; Ouldridge, T. E.; Henrich, O.; Rovigatti, L.; Šulc, P. A Primer on the oxDNA Model of DNA: When to Use it, How to Simulate it and How to Interpret the Results. *Front. Mol. Biosci.* **2021**, *8*, 551.

[31] Sindbert, S.; Kalinin, S.; Nguyen, H.; Kienzler, A.; Clima, L.; Bannwarth, W.; Appel, B.; Müller, S.; Seidel, C. A. Accurate distance determination of nucleic acids via Forster resonance energy transfer: implications of dye linker length and rigidity. *J. Am. Chem. Soc.* **2011**, *133*, 2463–2480.

[32] Suma, A.; Poppleton, E.; Matthies, M.; Šulc, P.; Romano, F.; Louis, A. A.; Doye, J. P.; Micheletti, C.; Rovigatti, L. TacoxDNA: A user-friendly web server for simulations of complex DNA structures, from single strands to origami. *J. Comput. Chem.* **2019**, *40*, 2586–2595.

[33] Taylor, N. O.; Wei, M.-T.; Stone, H. A.; Brangwynne, C. P. Quantifying dynamics in phase-separated condensates using fluorescence recovery after photobleaching. *Biophys. J.* **2019**, *117*, 1285–1300.

[34] Veneziano, R.; Shepherd, T. R.; Ratanalert, S.; Bellou, L.; Tao, C.; Bathe, M. In vitro synthesis of gene-length single-stranded DNA. *Sci. Rep.* **2018**, *8*, 1–7.

[35] Hall, L. M.; Gerowska, M.; Brown, T. A highly fluorescent DNA toolkit: synthesis and properties of oligonucleotides containing new Cy3, Cy5 and Cy3B monomers. *Nucleic Acids Res.* **2012**, *40*, e108–e108.

[36] Altschul, S. F.; Gish, W.; Miller, W.; Myers, E. W.; Lipman, D. J. Basic local alignment search tool. *J. Mol. Biol.* **1990**, *215*, 403–410.

[37] Seidel, C. A.; Schulz, A.; Sauer, M. H. Nucleobase-specific quenching of fluorescent dyes. 1. Nucleobase one-electron redox potentials and their correlation with static and dynamic quenching efficiencies. *J. Phys. Chem.* **1996**, *100*, 5541–5553.

[38] Fontana, M.; Fijen, C.; Lemay, S. G.; Mathwig, K.; Hohlbein, J. High-throughput, non-equilibrium studies of single biomolecules using glass-made nanofluidic devices. *Lab Chip* **2019**, *19*, 79–86.

[39] Roth, E.; Glick Azaria, A.; Girshevitz, O.; Bitler, A.; Garini, Y. Measuring the conformation and persistence length of single-stranded DNA using a DNA origami structure. *Nano Lett.* **2018**, *18*, 6703–6709.

[40] Porschke, D. Persistence length and bending dynamics of DNA from electrooptical measurements at high salt concentrations. *Biophys. Chem.* **1991**, *40*, 169–179.

[41] Grest, G. S.; Kremer, K. Molecular dynamics simulation for polymers in the presence of a heat bath. *Phys. Rev. A* **1986**, *33*, 3628.

[42] Farooq, S.; Hohlbein, J. Camera-based single-molecule FRET detection with improved time resolution. *Phys. Chem. Chem. Phys.* **2015**, *17*, 27862–27872.

[43] Mergny, J.-L.; Lacroix, L. Analysis of thermal melting curves. *Oligonucleotides* **2003**, *13*, 515–537.

[44] Ali, M. M.; Li, F.; Zhang, Z.; Zhang, K.; Kang, D.-K.; Ankrum, J. A.; Le, X. C.; Zhao, W. Rolling circle amplification: a versatile tool for chemical biology, materials science and medicine. *Chem. Soc. Rev.* **2014**, *43*, 3324–3341.

[45] Kim, J.-Y.; Kim, C.; Lee, N. K. Real-time submillisecond single-molecule FRET dynamics of freely diffusing molecules with liposome tethering. *Nat. Commun.* **2015**, *6*, 1–9.

[46] Kienle, D. F.; Schwartz, D. K. Complex salt dependence of polymer diffusion in polyelectrolyte multilayers. *J. Phys. Chem. Lett.* **2019**, *10*, 987–992.

[47] Robertson-Anderson, R. M. Optical tweezers microrheology: from the basics to advanced techniques and applications. *ACS Macro Lett.* **2018**, *7*, 968 – 975.

Chapter 7

General discussion

7.1 Introduction

This thesis aimed to further unravel the dynamics of complex coacervate core micelles (C3Ms). The previous chapters not only provide new insights into this C3M dynamics, but also further emphasize the need to study the dynamics of C3Ms specifically. For example, the reaction-assembly network of Chapter 2 showed once again that the formation dynamics can affect the final structure of the C3Ms. In addition, the differences in exchange of the diblock copolymer and the DNA homopolymer in Chapter 5 demonstrated that an additional species in the micelle core introduces additional complexity to its exchange. As a result, the exchange models developed for amphiphilic diblock copolymer micelles are insufficient to describe the exchange of C3Ms. Furthermore, the length of the oppositely charged polyelectrolyte seemed to have a different effect on the DNA diffusion in coacervate droplets than on the DNA exchange in C3Ms, which suggests that also models for the dynamics in polyelectrolyte complexes are not enough to completely understand the C3M dynamics. Finally, the large differences in exchange times between the C3Ms of Chapter 4 and 5 showed that only the static micelle properties, like their critical salt concentration, are not sufficient to predict the micelle performance as encapsulator of its core components.

In this final chapter, we combine the insights obtained in the previous chapters to formulate design strategies that minimise the molecular exchange of C3Ms. This set of strategies can be further refined if more details of the C3M exchange are known. Hence, after outlining the design strategies, we discuss how the research in this thesis can be continued to further unravel the C3M exchange mechanisms. While trying to unveil the C3M dynamics, we did not only identify further research directions to study the polyelectrolyte complex dynamics in the micelle cores, but also to study the polyelectrolyte complex dynamics in general, which we will also briefly discuss. This polyelectrolyte complex dynamics is important not only for a wide variety of synthetic polyelectrolyte complex-based materials, but also to understand what happens in biological systems like membraneless organelles. Finally, we will elaborate on how the obtained insights on the dynamics of C3Ms can also be applied to other dynamic systems like vesicles, viruses and reaction-assembly networks.

7.2 C3M design strategies

The molecular exchange of complex coacervate core micelles occurs mainly via expulsion and insertion, as was shown in Chapter 3 and 4 of this thesis. The Langevin dynamics simulations in Chapter 3 showed that during the initial micelle formation the expulsion/insertion mechanism is dominant as long as the homopolymer is not too long. In addition, in Chapter 4, the exchange rate of equilibrated

micelles did not depend on the micelle concentration, which is also supported by a recent small-angle neutron scattering (SANS) based C3M exchange study (Fig. 7.1).[1] This demonstrates that the splitting step is the rate-limiting step in the C3M exchange and not the concentration dependent merging step. Furthermore, the exchange of the fluorescently labelled homopolymers in Chapter 4 did not depend on the length of the unlabelled homopolymers. This indicates that the homopolymers exchange independently from each other and that the splitting takes place by expulsion, where only one or two polymers split off, and not by fission, where multiple polymers split off simultaneously. Therefore, the molecular exchange of C3Ms cannot be reduced by adding additional core components as long as these new core components do not have permanent bonds with the other parts of the core.

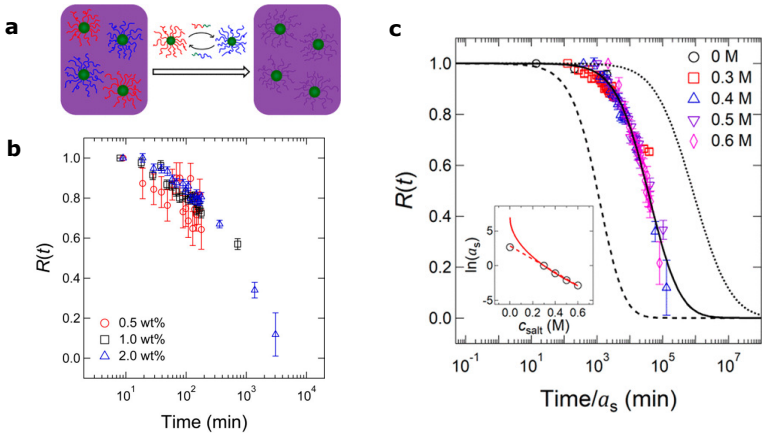

Figure 7.1. Small angle neutron scattering (SANS) measurements of the exchange of complex coacervate core micelles consisting of PEO-b-guanidium diblock copolymers and PEO-b-sulfonate diblock copolymers. a) Principle of the SANS measurement: micelles with deuterium-labelled PEO blocks are mixed with micelles with normal PEO blocks. Exchange of the micelles results in a decrease in neutron scattering contrast. b) The relaxation function $R(t) = \sqrt{\frac{I(t)-I(\infty)}{I(0)-I(\infty)}}$ with I the neutron scattering intensity for C3M exchange experiments at different polymer concentrations. c) The relaxation function for C3M exchange experiments at different salt concentrations after time-salt superposition. The used shift factors a_s are shown in the inset. The red solid line is the fit with a square root dependence of $\ln a_s$ on the salt concentration and the red dashed line a fit with a linear dependence. All three sub figures are reprinted with permission from Ref. 1. Copyright 2021 American Chemical Society.

The expulsion of polymers from the C3M core requires the breaking of ionic bonds and therefore the electrostatic interactions largely determine the C3M exchange rate. As a result, the exchange can be regulated by the ionic strength, although for some applications, like medicine delivery, the ionic strength is set by the physiological environment and cannot be tuned. The exact dependence on the ionic strength is not known yet. In Chapter 4, the best fits of the micelle exchange data were based on simple activated processes and the corresponding energy barriers decreased linearly with the square root of the salt concentration. However, when comparing the characteristic exchange times at different salt concentrations, the time obtained from extrapolating the exchange data at the lowest salt concentration seemed to deviate from this square root salt dependence. Also in the recent SANS study the shift factors used for the time-salt superposition suggested a deviation from the square root salt dependence and instead a linear dependence of the energy barrier on the salt concentration was suggested (Fig. 7.1c).[1]

Although the electrostatic interactions play a major role in determining the C3M exchange rate, the non-electrostatic effects are also important. In Chapter 3, we observed that a small increase in the non-electrostatic interactions between the oppositely charged polymers can reduce the exchange rate more than an order of magnitude. In addition, in Chapter 5 the hydrophobic dyes could largely

change the micelle exchange rates. This demonstrates that the exchange rate can be tuned by the non-electrostatic interactions between the core components and that polyelectrolytes with identical charge properties can still show different exchange rates because of differences in hydrophobicity, van der Waals interactions or hydrogen bonding. However, because of the complex interplay between the electrostatic and different types of non-electrostatic interactions, it is not possible yet to precisely predict the effect of the non-electrostatic interactions differences.

The polyelectrolyte length also largely affects the C3M exchange rate and polyelectrolyte polydispersity results in a very broad range of exchange times (Chapter 4 and 5). We have shown that the polyelectrolyte length can alter the exchange in two ways. First, an increase in overall polyelectrolyte length can reduce the exchange rate, as was shown both by changing the length of both polyelectrolytes in Chapter 3 and by changing only the length of the positive block in Chapter 5. Second, the length ratio between the oppositely charged polymers has a large impact on the C3M exchange: a mismatch in chain length with its oppositely charged polymer, largely reduces the exchange rate of a polymer, both for C3Ms consisting of only monodisperse polymers (Chapter 3) and for C3Ms with polydisperse core blocks (Chapter 5). In the latter case, only the exchange of the core components with a length mismatch is reduced. Core components that have the same length as (one of) the oppositely charged species still exchange quickly.

In some cases, the overall polyelectrolyte length can be increased by just increasing the degree of polymerisation of the core blocks, but this is not always possible. For example, for the encapsulation of proteins and specific DNA sequences, the length of the macro-ion is fixed. In addition, changing the length of the polyelectrolytes can also affect the micelle size and structure,[2–4] which might affect their applications.[5,6] In that case, other strategies can used: the core components can be covalently linked to new core components to increase their number of charges. Alternatively, the diblock core blocks can be cross-linked after the micelle formation.[7,8] In this way, the effective length of the diblock is increased and therefore the molecular exchange will be reduced. In the limit of strong cross-linking, the exchange might completely disappear. However, in case of normal cross-links, this also removes the C3M responsivity to environmental triggers which is important for many applications. To keep this responsivity, environmental sensitive cross-links could be used, like disulfide bonds that are cleaved in the reducing environment inside the cell.[7,8]

A mismatch in oppositely charged polyelectrolyte length is difficult to accomplish when polydisperse polymers are involved. For example, in Chapter 5 we observed rapid DNA exchange even though the length of the DNA was not the same as the average positive block length. We explained this rapid exchange by assuming that the DNA exchanges mainly with the few positive blocks with (nearly) the same length as the DNA length or a multiple of the DNA length. To prevent this rapid exchange, the positive blocks with similar length as the DNA need to be absent. This requires the synthesis of diblock copolymers that have a monodisperse charged block. We can think of two different strategies to make these diblock copolymers. First, genetic engineering can be used to obtain proteins consisting of a neutral block and a charged block, similar to what has been done earlier by Hernandez-Garcia *et al.*.[9] Since proteins consist of a specific amino acid sequence, all charged blocks will have the same length. Alternatively, solid phase peptide synthesis can be used to obtain monodisperse charged peptides that can be reacted with a neutral polymer with a carboxylic end group to give a diblock copolymer. This coupling reaction has been used earlier by Van Domeslaar *et al.* to synthesize various PEO-*b*-peptide diblock copolymers.[10] In both cases, we expect that the DNA exchange rate can be largely reduced by selecting a charged block length with a clear length mismatch compared to the DNA length. In addition, we expect that this strategy might also help to reduce the exchange rate for other C3Ms with monodisperse core components like enzymes.

Finally, we note that in some cases the formation dynamics can be used to regulate the final structure of the C3Ms and in this way might affect their molecular exchange. For example, in Chapter 2 the structure of the C3Ms depended on the speed at which the point of equal charge stoichiometry was

reached. At the moment, the exact effect on the C3M structure on its exchange dynamics is not known. Yet, we expect that the structure has a minor effect because expulsion is the rate-limiting step. For the expulsion, the core interactions are most important, although a study on amphiphilic diblock copolymers suggested that still the structure of the micelle corona might have some effect.[11] Even though the micelle structure might not largely affect the molecular exchange, tuning this structure is still important for many applications. For example, the micelle size can affect its distribution in the body[5] and its toxicity.[6] In any case, the C3M formation dynamics will thus play a significant role in the future design of C3Ms.

7.3 Further elucidating the C3M exchange

In the previous section we have described the general design strategies to minimise the C3M exchange. To refine this description, the precise effect of certain parameters on the C3M exchange needs to be further elucidated. In particular, further systematic studies on the effect of the polyelectrolyte length are required. The broad range of exchange times for polydisperse polymers shows that the polyelectrolyte length has a large effect, but the exact relation between the polyelectrolyte length and the exchange rate is not known yet. In Chapter 5, we have found indications that the polyelectrolyte length affects the exchange by changing both the relaxation in the core and the expulsion energy barrier. However, because the fluorescent dye concentration also affected the exchange, no quantitative relations could be derived. We have used Langevin dynamics simulations to complement the observations from the fluorescent DNA exchange experiments, but also here full quantitative relations over a large range of chain lengths are difficult to obtain because it takes too long to simulate enough slow exchange events for sufficient statistics. Therefore, we recommend to use time resolved small-angle neutron scattering (TR-SANS) measurements to systematically study the polyelectrolyte length effect on the exchange. Since these measurements are based on neutron scattering contrast, only some protons have to be replaced by deuterium isotopes and no additional compounds like dyes have to be introduced. TR-SANS measurements have often been used to study amphiphilic diblock copolymer micelle exchange[12–15] and have recently also been used to study the exchange of C3Ms (Fig. 7.1).[1] In this study, the length effect was also discussed, but only in the context of polyelectrolyte polydispersity. To develop a full description of the polyelectrolyte length effect on the exchange, new TR-SANS measurements have to be performed where the polyelectrolyte length is systematically varied. The DNA micelles that we studied in Chapter 5 are a good system for this because DNA is monodisperse and its length can be easily adapted.

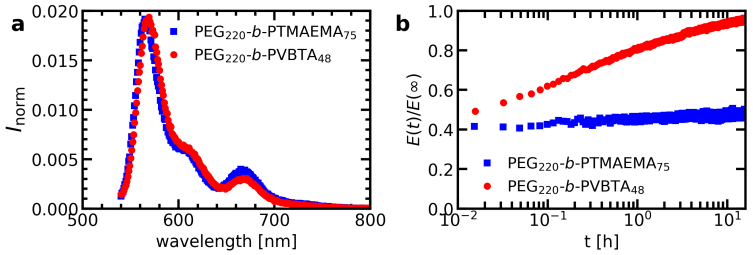

Figure 7.2. Preliminary results on the effect of the positive block chemistry on the micelle exchange. In both cases, the negative homopolymer is PSPMA, the fraction of fluorescently labelled PSPMA polymers is 0.2 and the salt concentration is 100 mM KCl. a) Normalised fluorescence spectra of mixed micelles with PEG$_{220}$-*b*-PTMAEMA$_{75}$ or PEG$_{220}$-*b*-PVBTA$_{48}$ diblock copolymers. b) Normalised FRET efficiency $E(t)/E(\infty)$ as a function of time after mixing t for the two different diblock copolymers.

Not only the polyelectrolyte lengths, but also the non-electrostatic interactions have a complex effect on the C3M exchange. For example, we observed that an increase in non-electrostatic interactions between both polyelectrolytes can decrease the exchange rate, but that non-electrostatic interactions for only one of the polyelectrolyte species have the opposite effect (Chapter 3). In addition, in Chapter 5, the donor dye concentration might have had a different effect than the acceptor dye concentration. To better understand these effects, the non-electrostatic interactions have to be varied more often. For example, the C3M exchange rate can be measured for different polymers. As a first test, we have measured the exchange of fluorescently labelled PSPMA polymers in C3Ms with poly(ethylene glycol)-*b*-poly((vinylbenzyl)trimethylammonium) (PEG-*b*-PVBTA) diblock copolymers instead of the PEG-*b*-PTMAEMA diblock copolymers used in Chapter 4. Because of their benzene rings, the VBTAC monomers might have non-electrostatic interactions mainly with themselves and not with the oppositely charged KSPMA monomers. This could destabilise the micelles and increase their exchange rate, like we observed in the simulations. The micelles with PEG-*b*-PVBTA indeed showed a faster increase in FRET efficiency (Fig. 7.2). However, the PVBTA block is shorter than the PTMAEMA block, which also increases the exchange rate. To exclude these length effects, first PVBTA and PTMAEMA diblock copolymers with the same length have to be synthesised. In addition, for FRET exchange measurements a full characterisation of the average number of fluorophores per micelles and the geometric constant ν is required to compare the data instead of only the first quick check of comparing the FRET efficiency of the mixed micelles that we used here (Fig. 7.2a).

Some parameters have been neglected up to now and their effect on the C3M exchange still needs to be determined. Among others, differences in polymer chemistry were so far mainly discussed as a non-electrostatic interaction effect, but differences in charge density and polymer stiffness can also affect the complex coacervation.[16,17] In some cases, it might be difficult to isolate the effect of a certain parameter because it also affects other factors like the micelle structure.[3,4,18] As already mentioned in previous section, the effect of the micelle structure itself is also not known yet. Finally, for some C3Ms, additional parameters are introduced that can affect their exchange dynamics. For example, micelles based on metal coordination polymers[19] are not only dynamic in their exchange, but also in their coordination polymer length. This makes their polyelectrolyte length effect even more complex. The effect of these additional parameters could be further elucidated once the general effects of polyelectrolyte length and (non)-electrostatic interactions are known.

7.4 Dynamics of polyelectrolyte complexes

Although this thesis focused mainly on the dynamics in complex coacervate core micelles, we have also paid some attention to the dynamics in (macroscopic) polyelectrolyte complexes, especially in Chapter 5 and 6. The chain length has an intricate effect on this polyelectrolyte complex dynamics because it can affect the overall polyelectrolyte relaxation time by increasing the number of monomers but also by changing the local environment of the polyelectrolyte (sub-)chain. In Chapter 5, we have started to discriminate between these two effects by measuring for different chain lengths both the changes in complex cocaervate density and DNA diffusion. In Chapter 6, we have tried to measure the sub-chain dynamics of a single chain in a polyelectrolyte complex. This would allow to study how the polyelectrolyte length alters the dynamics of a fixed sub-chain length. Unfortunately, we have not yet succeeded to measure this sub-chain dynamics and instead have discussed how our approach might be continued to be able to measure the sub-chain dynamics in the future. In Chapter 5, we were able to observe some aspects of the complex chain length effects and found indications that the poly(L-lysine) chain length affects the complex coacervate density differently than the DNA length. Similar asymmetric effects have been observed earlier in rheology measurements.[20] At this moment, the origin of this asymmetric effect of changing the chain length and the way it affects the polyelectrolyte complex dynamics is not known.

More research is required to fully understand these asymmetric length effects in polyelectrolyte complexes. As a first step, coarse-grained simulations could be used. These simulations have already been used for symmetric oppositely charged polyelectrolytes to study both the phase behaviour[21] and the polyelectrolyte dynamics[22,23] and can relatively easily be adapted to study asymmetric polyelectrolytes with different lengths, charge density and/or non-electrostatic interactions. The simulations might not capture all effects because they lack molecular detail, but they can be used to obtain some first insights into the effect of asymmetric non-electrostatic interactions and charge density. To obtain a full picture of the asymmetric length effects, the simulations need to be complemented with experiments. Preferentially, the same polyelectrolyte pair will be used to measure the (asymmetric) chain length effects on the overall polyelectrolyte complex dynamics, the separate dynamics of the polyelectrolytes and the complex coacervate density. For the overall polyelectrolyte dynamics, (micro-)rheology measurements can be used.[24] For the separate polyelectrolyte dynamics, FRAP measurements or other (single-molecule) diffusion measurements[25,26] could be used. Finally, for the changes in complex coacervate density, the molecular rotors could be used, like we did in Chapter 5. Alternatively, SANS or SAXS measurements[27] could be used to study the changes in complex coacervate structure for different chain lengths. With this combination of experiments, both the macroscopic and microscopic response to changes in polyelectrolyte length could be described and related to each other. In the end, these descriptions might also be used for the dynamics inside the C3M core.

7.5 Vesicle and virus dynamics

The methods and results that we obtained by studying the dynamics of C3Ms can also be expanded to related systems. In the previous section, we have already discussed polyelectrolyte complexes, but there exist also other systems with similar interactions as the C3Ms. For example, in some specific cases, charged-neutral diblock copolymers and oppositely charged polymers can form vesicles instead of micelles.[28–30] Another example is the formation of artificial virus-like particles.[31] Here, the DNA-coating strategy of the tobacco mosaic virus was mimicked by designing proteins consisting of a DNA binding domain, a cooperative binding domain that favours the dense packing of proteins and a stabilising domain. These proteins encapsulate the DNA and form rod-like structures. The main differences with C3Ms is that these virus-like particles have an additional cooperativity block instead of only the electrostatic blocks and the neutral stabilising block.

The formation of polyion complex vesicles is based on the same interactions as C3Ms, but they differ in their geometry and their neutral to charged block ratio. Because of the similarity in interactions, we would expect that most descriptions of the C3Ms exchange can also be applied to the vesicle exchange, although some differences might occur because of the different geometry and block ratio. It has been suggested that precisely matching the chain length of the oppositely charged polyelectrolytes is essential for vesicle formation.[28,29] If this is indeed the case, the vesicle wall components might exchange rapidly because neutral complexes can easily be formed. Similar strategies as for the C3Ms (Section 7.2) might be used to reduce this large exchange rate. For example, the wall components could be covalently cross-linked after the vesicle formation. Alternatively, the non-electrostatic attraction might be increased. In fact, this has already been used recently and polyion complex vesicles have been stabilised by additional hydrogen bonds.[30]

For the virus-like particles, we expect that the molecular exchange is relatively slow. First, the DNA or RNA that is encapsulated by the virus proteins is relatively long. In Chapter 3 we concluded that for long homopolymer lengths, the exchange rate is highly decreased because no small neutral complexes can be formed. For virus-like particles, the number of charge interactions might be even further increased compared to C3Ms as shown by the use of a mechanochromic sensor to study the virus-like particle assembly:[32] binding of the virus proteins to the anionic homopolymer induces stretching of the homopolymer, which can increase the number of electrostatic interactions between the cationic binding

blocks and the anionic homopolymer. Another factor that slows down the molecular exchange of the virus is the cooperative binding domains of the virus proteins. These domains effectively increase the multivalency of the DNA binding block. In fact, in models for virus assembly it is often assumed that the exchange of this cooperatively bound blocks is so small that it can be neglected.[32,33]

To further study both the vesicle and virus exchange, FRET experiments might be used. These FRET-based exchange measurements can also be analysed by using the model developed in Chapter 4. Only in some cases, the geometry constant needs to be adapted to account for the different dimensionality (Fig. 7.3a-c): we described the micelle cores as 3-dimensional spherical objects. For vesicles with a low curvature and a thin outer fluorescently labelled layer, the geometry might be better described by a 2-dimensional circle. For the rod-like structures formed by virus-like particles, a 1-dimensional line is probably the best description.

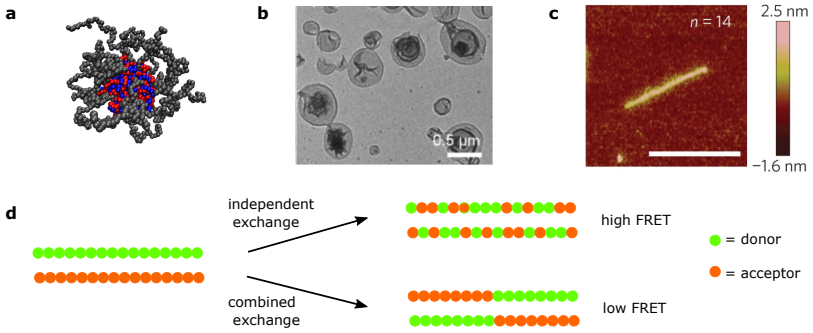

Figure 7.3. Complex coacervate core micelles (a), polyion complex vesicles (b) and virus-like particles (c) differ in their geometry as shown by an image rendered from Langevin dynamics simulations, a transmission electron microscopy image and an atomic force microscopy image (scale bar is 300 nm)respectively. Sub figure b) is reprinted with permission of the Royal Society of Chemistry, from Ref. 30 and c) is reprinted by permission from Springer Nature: Nature Nanotechnology. Ref. 31. Copyright 2014. d) For objects with a line geometry, the independent exchange of fluorophores can result in a different FRET efficiency than the combined exchange of fluorophores, while the fraction of exchanged fluorophores is the same.

The starting point remains the same for all three different geometries: a donor fluorophore can transfer its energy to all acceptor fluorophores in the same object and the FRET energy per donor is given by:

$$E = \frac{\sum_j n_{A,j} \left(\frac{R_F}{r_j}\right)^6}{1 + \sum_j n_{A,j} \left(\frac{R_F}{r_j}\right)^6} \tag{7.1}$$

where $n_{A,j}$ is the number of acceptors that have a distance r_j to the donor and R_F is the Förster radius.

The differences between the three geometries occur in the next step, where we replace the summation by an integral over all possible acceptor distances. For a 3-dimensional sphere, the number of acceptors at a distance r from the donor is given by: $n_A = \rho_A 4\pi r^2 dr$. For a 2-dimensional circle applies: $n_A = \rho_A 2\pi r dr$ and for a 1-dimensional line applies: $n_A = \rho_A dr$. Substituting this in Equation 7.1 gives for the 3-dimensional sphere:

$$E = \frac{4/3\pi\rho_A R_F^6 R_0^{-3}}{1 + 4/3\pi\rho_A R_F^6 R_0^{-3}} = \frac{\nu_S n_A}{1 + \nu_S n_A} \tag{7.2}$$

where $\rho_A = n_A/(4/3\pi R_S^3)$ and $\nu_S = R_F^6/(R_0^3 R_S^3)$ with R_S the radius of the spherical object and R_0 the (effective) size of the fluorophore. This is the same equation as used in Chapter 4, but here we have replaced the radius of the micelle core R_m with the more general description R_S.

For a 2-dimensional circle we obtain:

$$E = \frac{1/2\pi\rho_A R_F^6 R_0^{-4}}{1 + 1/2\pi\rho_A R_F^6 R_0^{-4}} = \frac{\nu_C n_A}{1 + \nu_C n_A} \tag{7.3}$$

where $\rho_A = n_A/(\pi R_C^2)$ and $\nu_C = R_F^6/(2R_0^4 R_C^2)$ with R_C the radius of the circular object.

Finally, for a 1-dimensional line, the FRET efficiency per donor is given by:

$$E = \frac{1/5\rho_A R_F^6 R_0^{-5}}{1 + 1/5\rho_A R_F^6 R_0^{-5}} = \frac{\nu_L n_A}{1 + \nu_L n_A} \tag{7.4}$$

where $\rho_A = n_A/R_L$ and $\nu_L = R_F^6/(5R_0^5 R_L)$ with R_L the length of the line object.

Although the values of the geometric constants are different, all three geometries still show the same dependence of the FRET efficiency on this geometric constant and on the number of acceptors. The remaining part of the model, that describes the changes in the number of donor and acceptor per object in time, is also the same in all three cases. The only requirement is that the fluorophores exchange independently from each other, since this independent exchange assumption was used to derive the equations in Chapter 4. We note that this requirement might not be met for virus-like particles. The cooperative binding of the coat proteins might favour the exchange of clusters containing multiple fluorophores, especially because for these one-dimensional structures the degree of fluorescent labelling has to be relatively high. For this combined exchange, the increase in FRET efficiency will be relatively slow compared to the fraction of molecules that have exchanged because the donor-acceptor contacts only occur at the edges of exchanged clusters (Fig. 7.3d). Also for SANS the decrease in the scattering intensity will be relatively slow because the separate clusters in one object still provide scattering contrast. Therefore, for a combined exchange with little rearrangements of the molecules within a object, the FRET efficiency or the neutron scattering intensity is mainly a measure for the degree of mixing of the differently labelled molecules in one object rather than a measure for the fraction of exchanged molecules.

7.6 Reaction-assembly networks

In the previous sections, we have focused mainly on the equilibrium dynamics of complex coacervates and complex coacervate core micelles. However, the dynamics does not only determine their equilibrium properties, but can also affect their formation. In Chapter 2 we have further illustrated the importance of the formation dynamics and shown how the formation pathway can affect the final structure of the C3Ms. In particular, we have introduced new formation pathways by combining the polymerisation reaction and the micelle assembly together in one network and shown that this might be used to prevent kinetic trapping. Apart from providing important insights into the C3M formation itself, our findings can also be applied to reaction-assembly networks in general, as we will discuss in this section. We will start with some remarks on the use of NMR relaxation measurements to study these networks and subsequently compare our systems to other reaction-assembly networks.

7.6.1 T_1 and T_2 relaxation

In Chapter 2, we have introduced the use of ^{1}H NMR relaxation measurements to study reaction-assembly networks. Specifically, we have used a combination of longitudinal relaxation time (T_1) and transverse relaxation time (T_2) measurements to follow the assembly and the monomer partitioning.

Together, T_1 and T_2 can probe a wide range of molecule mobility times because they depend differently on the rotational correlation time of the molecule.[34,35] This different dependence was also illustrated in Chapter 2 by the different response of the T_1 and T_2 of the neutral block protons to the micelle assembly.

The assembly decreases the mobility of the molecules in the reaction-assembly network and therefore decrease the T_2 of the protons. This decrease in T_2 results in peak broadening in the ^{1}H NMR spectrum. To reduce the resulting spectral overlap, we have introduced a short T_2 filter in the T_1 measurements. For both the T_2 measurements and the T_2 filter in the T_1 measurement, we made use of the PROJECT sequence[36] to correct for the J-coupling effects (Fig. 7.4a). In this way, we could follow the T_1 and T_2 changes even in the complex environment of the reaction-assembly network.

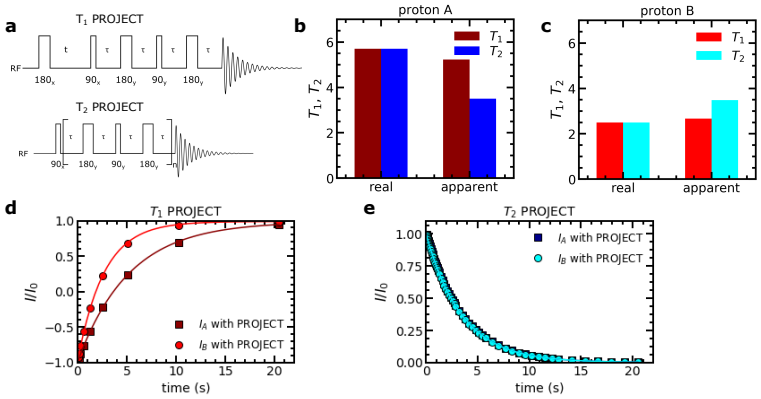

Figure 7.4. Effect of the use of the PROJECT sequence on the apparent T_1 and T_2. a) Pulse sequences used to measure the PROJECT-filtered T_1 and the PROJECT-based T_2. In this case, the 90_y pulses result in coherence transfer between the coupled protons. b and c) Comparison of the real and apparent T_1 and T_2 calculated (Equation 7.5 and 7.6) for protons A and B with $T_{1,A} = T_{2,A} = 5.7$ s, $T_{1,B} = T_{2,B} = 2.5$ s, a coupling constant J_{AB} of 10 Hz and an inter-pulse delay τ of 5 ms. d) The corresponding calculated intensity for a PROJECT-filtered inversion recovery experiment and e) for a T_2 PROJECT experiment. Solid lines indicate the fits used to determine the apparent T_1 and T_2 respectively.

The use of the PROJECT sequence was essential for both T_1 and T_2 measurements in the reaction-assembly network, but it also introduced the mixing of signals of J-coupled protons (as illustrated in the appendix of Chapter 2). This has to be taken into account when interpreting the results. For example, when we measured the apparent T_1 and T_2 of the separate components of the network with the PROJECT based sequences of Fig. 7.4a, we were initially surprised to observe that for some of the monomer protons the apparent T_1 was shorter than the apparent T_2. A T_1 shorter than T_2 is impossible because all processes that result T_1 relaxation, also affect the T_2 relaxation at least as much.[34,35] To explain this apparent shorter T_1, we calculated the theoretical intensities for our T_1 and T_2 relaxation experiments by taking into account that during the PROJECT sequence coherence transfer takes place. Coherence transfer results in the transfer of magnetisation from proton spin A to its coupled proton spin B. For our T_2-filtered T_1 measurement, the PROJECT sequence was only applied at the end of the sequence and the resulting intensity I of a proton A, coupled to proton B with a coupling constant J_{AB} is given by:

$$\begin{aligned} I_A = &\cos^2(2\pi J_{AB}\tau) I_A(0) \left[1 - 2\exp\left(-\frac{t}{T_{1,A}}\right)\right] \exp\left(-\frac{4\tau}{T_{2,A}}\right) + \\ &\sin^2(2\pi J_{AB}\tau) I_B(0) \left[1 - 2\exp\left(-\frac{t}{T_{1,B}}\right)\right] \exp\left(-\frac{2\tau}{T_{2,A}}\right) \exp\left(-\frac{2\tau}{T_{2,B}}\right) \end{aligned} \tag{7.5}$$

where t is the variable delay time and τ is the inter-pulse delay time in the PROJECT sequence. For the T_2 measurement, the PROJECT sequence was repeated n times and the intensity I after a certain loop n

can be calculated recursively based on the intensity of the previous loops:

$$I_A(n) = \cos^2(2\pi J_{AB}\tau) I_A(n-1) \exp\left(-\frac{4\tau}{T_{2,A}}\right) + \sin^2(2\pi J_{AB}\tau) I_B(n-1) \exp\left(-\frac{2\tau}{T_{2,A}}\right) \exp\left(-\frac{2\tau}{T_{2,B}}\right) \tag{7.6}$$

By calculating the intensity for several coupling constants and ^{1}H NMR relaxation times and fitting the calculated intensities to obtain the apparent relaxation time, we could show that in some cases the apparent T_1 can indeed be shorter than the apparent T_2 (Fig. 7.4b-e) as result of the different degree of mixing of the proton signals in the T_1 and T_2 measurement sequences.

Although it is important to keep the coherence transfer induced mixing of proton signals in mind, we do not expect that this mixing will impede the use of T_1 and T_2 to study reaction-assembly networks. In most cases, it is possible to select one proton without J-coupling, which will not show this mixing effect. In addition, mainly the relative changes in relaxation time of the complete molecule are needed to understand the underlying pathways of the networks. Even when the signals of the different protons of the molecule are mixed, these relative changes can still be followed, as long as the used acquisition sequences are not changed during a reaction-assembly process. In fact, we expect that in many cases no quantitative measurement of the relaxation time will be performed and only relative changes will be measured: in our case, the reaction was relatively slow and therefore we could perform full T_1 measurements during the reaction-assembly process. In many cases, the reaction will be too fast for this full T_1 measurement during the reaction. Instead, the signal ratio at two different delay times can be measured, similar to what we used to follow the changes in T_2. In this way, the relative changes in T_1 can still be used the elucidate the pathways in faster reaction-assembly networks, especially when these relative changes are combined with full T_1 characterisations at the start and end of the reaction-assembly process.

7.6.2 Polymerisation-induced electrostatic self-assembly (PIESA)

The templated reaction-assembly network of Chapter 2 is a specific case of what is known as polymerisation-induced electrostatic self-assembly (PIESA). In PIESA, the polymerisation of a polyelectrolyte occurs in the presence of oppositely charged macro-ions resulting in assembly. This combination of the polymerisation reaction and assembly has been used to form specific structures.[30,37–40] As already mentioned in the general introduction, so far the studies on PIESA mainly focused on the end structures and not on the underlying pathways. Our approach helps to better understand the underlying pathways and has shown that the relative reaction rate can be regulated by tuning the fraction of monomers that bind to the template. Yet, not all observations made for the PIESA networks can be explained by our approach. For example, in some cases a decrease in reaction rate was observed when adding the template,[38] while we observed an increase in reaction rate. In Chapter 2 we acscribed this diffrence to the higher concentration used in these cases, resulting in an increase in viscosity of the sample. Viscosity measurements in combination with NMR relaxation measurements of these systems can be used to verify this and adapt our kinetic model to account for the larger concentrations. We note that because of the larger concentrations, the reaction will proceed faster and therefore a full quantitative measurement of T_1 during the reaction is probably not possible. Instead, the relative changes in T_1 can be measured by measuring the intensity ratio for two different delay times, as suggested in the previous section.

To directly link the reaction kinetics to the structure formation, the formed structures have to be analysed simultaneously with the reaction. In Chapter 2, we have used light scattering to probe the structure formation. Yet, our network was already a bit too concentrated to unambiguously interpret the light scattering data. The PIESA systems with higher concentration are thus definitely too concentrated

to be directly followed by light scattering measurements. Therefore, we recommend to use SAXS or SANS to follow the assembly since these methods are more suited for higher concentrations and also can obtain sufficiently large time resolutions as illustrated by their use in micelle formation [41,42] and micelle exchange studies [1,12] respectively.

The combined NMR and SAXS/SANS approach might not only be used to study already existing PIESA networks, but also to elucidate the underlying pathways in new PIESA networks. For example, it would be interesting to study the effect of the polymer chemistry on the assembly pathways since for C3M formation from pre-synthesised polymers different pathways have been observed for different polymers. For C3Ms containing poly(ethylene oxide)-block-poly((vinylbenzyl)trimethylammonium chloride) (PEO-*b*-PVBTA) and poly(sodium 4-styrenesulfonate) (PSSS) polymers, first larger structures were formed that subsequently rearranged to smaller micelles. [41] However, for C3Ms formed from PE0-*b*-PVBTA and sodium poly(acrylate) (PAA) polymers, only a gradual increase in micelle size was observed. [42] By changing the polymers in our templated reaction-assembly network, it can be tested whether the rearrangement and kinetic trapping effects that we observed in Chapter 2 are specific for the polymers that we used or that other polymers show the same effect.

7.6.3 Biomimetic reaction-assembly networks

Reaction-assembly networks are not only used to obtain new synthetic materials, but are also common in nature. For example, the assembly and disassembly of membraneless organelles is probably largely regulated by phosphorylation reactions. [43,44] In order to better understand nature and to increase the potential of synthetic systems, multiple research groups have tried to mimic the dissipative nature of these natural reaction-assembly networks. Most of these mimicking networks were based on enzyme-catalysed reactions, [45–50] although recently also some purely synthetic reaction-assembly networks have been developed, [51,52] in one case showing strong similarities to PIESA. [51]

Although the used reactions differ, in all these systems the reaction induced assembly, like in our templated reaction-assembly network the polymerisation reaction resulted in micelle assembly. Some of the biomimetic reaction-assembly systems even show additional similarities to our templated reaction-assembly network. For example, in an enzymatic network, the growth of coacervate droplets could be regulated by the ADP partitioning (Fig. 7.5a,b). [48] A lower amount of ADP in the droplets resulted a lower droplet growth rate. This is a similar effect as observed in our reaction-assembly network, where the partitioning of the monomer between a free and template-bound state could be regulated by changing the salt concentration and in this way the polymerisation rate could be tuned. Another example of a system that showed additional similarities with our templated reaction-assembly network is the EDC-fuelled oligomerisation of isophtalic acid monomers (Fig. 7.5c-e). [52] In this network, assembly of the larger oligomers decreased their dissocation rate. Also in our templated reaction-assembly network, we observed that the assembly affected the reaction: the association of polymers to the template resulted in expulsion of the monomers from the template and therefore in a decrease of the polymerisation reaction rate. Although the mechanisms are different in these systems, they both show chemical feedback between the reaction and the assembly and illustrate the additional complexity that can emerge when two different processes are combined.

Because of these similarities, the approaches that we used to study the templated reaction-assembly network might also be useful for these biomimetic reaction-assembly networks. For example, NMR relaxation measurements could be used to follow the partitioning of ADP and ATP or other reaction components during the reaction-assembly process. So far, the partitioning of ADP has been determined only in equilibrium by first inducing macroscopic phase separation and subsequently measuring the concentration in the coacervate phase and dilute phase by HPLC. [48] With the NMR relaxation measurements this partitioning can be measured directly in the network and even changes in partitioning during the reaction-assembly process might be observed. We note that in some cases, it might be difficult to accomplish this latter part because the process can be too fast to be followed by NMR

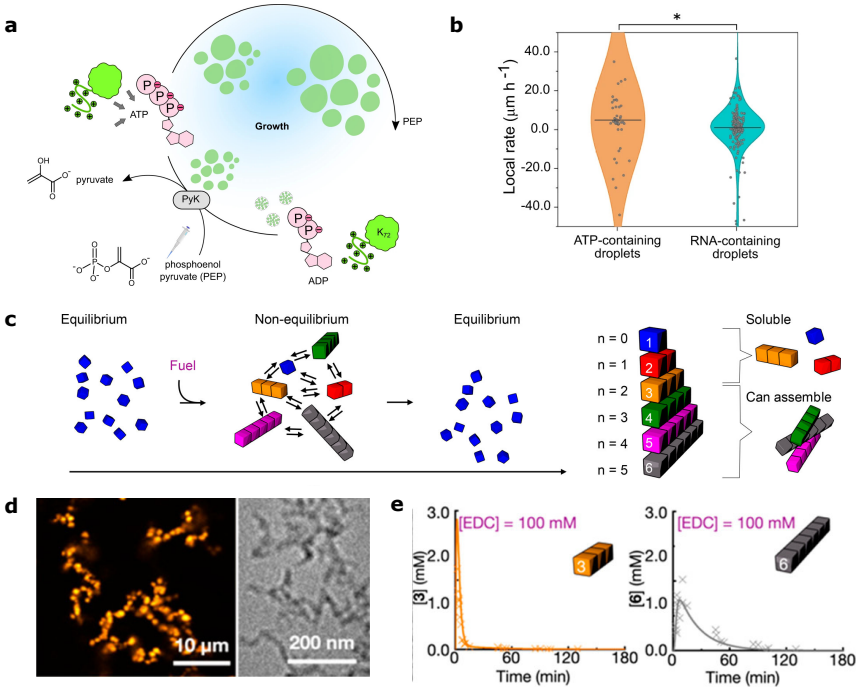

Figure 7.5. Examples of other reaction-assembly networks. a) Enzymatic network where the conversion from ADP to ATP by pyruvate kinase (PyK) in the presence of the lysine-rich protein K_{72} induces the formation and growth of complex coacervate droplets. b) Effect of ADP partitioning in this network: seed droplets with RNA contain a lower amount of ADP than seed droplets with ATP and therefore show a lower droplet growth rate. Figure a) and b) are reprinted from Ref. 48. c) Synthetic reaction-assembly network where EDC act as fuel to chemically grow oligomers from isophthalic acid monomers. The formed oligomers dissociate in smaller oligomers and monomers by hydrolysis and transacylation reactions. d) The larger oligomers ($n > 3$) can assemble into larger structures as shown here by fluoresence microscopy (left) and cryogenic transmission electron microscopy (right). e) The dissociation rates of the larger oligomers (right) are lower compared to the smaller oligomers (left) which might be explained by the assembly of the larger oligomers. Figure c-e) are reprinted (adapted) with permission from Ref. 52 Copyright 2021 American Chemical Society

relaxation measurements. To obtain the highest time resolution, again only the intensity ratio at different two delay times can be measured instead of performing of full quantitative T_1 or T_2 relaxation measurements. For the highest time resolution, the use of ^{1}H NMR is also preferred over ^{31}P NMR, even though the ^{31}P NMR provides a better spectral resolution between ADP and ATP.[53] The reason for this is that ^{31}P NMR has a lower sensitivity and therefore more scans need to be recorded to get a sufficient signal to noise ratio.

Finally we note that for a thorough understanding of these reaction-assembly networks, it is essential to not only unravel the reaction kinetics, but also have a detailed view on the dynamics of the assembled structures. In this respect, the insights that we obtained on the molecular exchange dynamics of C3Ms and the polyelectrolyte complex dynamics might also help to further unveil the complex mechanisms in these reaction-assembly networks.

7.7 Conclusion and outlook

Dynamics plays an important role for C3Ms. In this thesis, we have provided some new insights into this C3M dynamics, but still a large part of the underlying mechanisms needs to be further unravelled. To explain our observations, we have often relied on what is known from the extensive research on their static equilibrium properties. Yet, we have also observed that the dynamics might introduce additional complexity that cannot be predicted from their static equilibrium properties alone. This emphasises the importance of studying both the fundamental static properties and the complexity that emerges because of the dynamics. Together this will help to improve the rational design of C3Ms, but also to understand the dynamics in other systems. We believe that this dynamics will become more and more important now the static properties of many systems are getting better and better understood.

References

[1] Heo, T.-Y.; Kim, S.; Chen, L.; Sokolova, A.; Lee, S.; Choi, S.-H. Molecular Exchange Kinetics in Complex Coacervate Core Micelles: Role of Associative Interaction. *ACS Macro Lett.* **2021**, *10*, 1138–1144.

[2] van der Kooij, H. M.; Spruijt, E.; Voets, I. K.; Fokkink, R.; Cohen Stuart, M. A.; van der Gucht, J. On the stability and morphology of complex coacervate core micelles: From spherical to wormlike micelles. *Langmuir* **2012**, *28*, 14180–14191.

[3] Lueckheide, M.; Vieregg, J. R.; Bologna, A. J.; Leon, L.; Tirrell, M. V. Structure–property relationships of oligonucleotide polyelectrolyte complex micelles. *Nano Lett.* **2018**, *18*, 7111–7117.

[4] Marras, A. E.; Campagna, T. R.; Vieregg, J. R.; Tirrell, M. V. Physical property scaling relationships for polyelectrolyte complex micelles. *Macromolecules* **2021**, *54*, 6585–6594.

[5] Seymour, L.; Duncan, R.; Strohalm, J.; Kopeček, J. Effect of molecular weight (Mw) of N-(2-hydroxypropyl) methacrylamide copolymers on body distribution and rate of excretion after subcutaneous, intraperitoneal, and intravenous administration to rats. *J. Biomed. Mater. Res.* **1987**, *21*, 1341–1358.

[6] Ogris, M.; Brunner, S.; Schüller, S.; Kircheis, R.; Wagner, E. PEGylated DNA/transferrin–PEI complexes: reduced interaction with blood components, extended circulation in blood and potential for systemic gene delivery. *Gene Ther.* **1999**, *6*, 595–605.

[7] Dirisala, A.; Uchida, S.; Tockary, T. A.; Yoshinaga, N.; Li, J.; Osawa, S.; Gorantla, L.; Fukushima, S.; Osada, K.; Kataoka, K. Precise tuning of disulphide crosslinking in mRNA polyplex micelles for optimising extracellular and intracellular nuclease tolerability. *J. Drug. Target.* **2019**, *27*, 670–680.

[8] Kakizawa, Y.; Harada, A.; Kataoka, K. Environment-sensitive stabilization of core- shell structured polyion complex micelle by reversible cross-linking of the core through disulfide bond. *J. Am. Chem. Soc.* **1999**, *121*, 11247–11248.

[9] Hernandez-Garcia, A.; Werten, M. W.; Cohen Stuart, M.; de Wolf, F. A.; de Vries, R. Coating of single DNA molecules by genetically engineered protein diblock copolymers. *Small* **2012**, *8*, 3491–3501.

[10] Van Domeselaar, G. H.; Kwon, G. S.; Andrew, L. C.; Wishart, D. S. Application of solid phase peptide synthesis to engineering PEO–peptide block copolymers for drug delivery. *Colloids Surf. B: Biointerfaces* **2003**, *30*, 323–334.

[11] Wang, E.; Lu, J.; Bates, F. S.; Lodge, T. P. Effect of corona block length on the structure and chain exchange kinetics of block copolymer micelles. *Macromolecules* **2018**, *51*, 3563–3571.

[12] Lund, R.; Willner, L.; Richter, D.; Dormidontova, E. E. Equilibrium chain exchange kinetics of diblock copolymer micelles: Tuning and logarithmic relaxation. *Macromolecules* **2006**, *39*, 4566–4575.

[13] Choi, S.-H.; Lodge, T. P.; Bates, F. S. Mechanism of molecular exchange in diblock copolymer micelles: hypersensitivity to core chain length. *Phys. Rev. Lett.* **2010**, *104*, 047802.

[14] Choi, S.-H.; Bates, F. S.; Lodge, T. P. Molecular exchange in ordered diblock copolymer micelles. *Macromolecules* **2011**, *44*, 3594–3604.

[15] Lu, J.; Bates, F.; Lodge, T. Chain exchange in binary copolymer micelles at equilibrium: confirmation of the independent chain hypothesis. *ACS Macro Lett.* **2013**, *2*, 451–455.

[16] Huang, J.; Morin, F. J.; Laaser, J. E. Charge-density-dominated phase behavior and viscoelasticity of polyelectrolyte complex coacervates. *Macromolecules* **2019**, *52*, 4957–4967.

[17] Shakya, A.; King, J. T. DNA local-flexibility-dependent assembly of phase-separated liquid droplets. *Biophys. J.* **2018**, *115*, 1840–1847.

[18] Rumyantsev, A. M.; Zhulina, E. B.; Borisov, O. V. Scaling theory of complex coacervate core micelles. *Acs Macro Lett.* **2018**, *7*, 811–816.

[19] Yan, Y.; de Keizer, A.; Cohen Stuart, M. A.; Drechsler, M.; Besseling, N. A. Stability of complex coacervate core micelles containing metal coordination polymer. *J. Phys. Chem. B* **2008**, *112*, 10908–10914.

[20] Spruijt, E.; Cohen Stuart, M. A.; van der Gucht, J. Linear viscoelasticity of polyelectrolyte complex coacervates. *Macromolecules* **2013**, *46*, 1633–1641.

[21] Li, L.; Srivastava, S.; Andreev, M.; Marciel, A. B.; de Pablo, J. J.; Tirrell, M. V. Phase behavior and salt partitioning in polyelectrolyte complex coacervates. *Macromolecules* **2018**, *51*, 2988–2995.

[22] Andreev, M.; Prabhu, V. M.; Douglas, J. F.; Tirrell, M.; de Pablo, J. J. Complex coacervation in polyelectrolytes from a coarse-grained model. *Macromolecules* **2018**, *51*, 6717–6723.

[23] Yu, B.; Rauscher, P. M.; Jackson, N. E.; Rumyantsev, A. M.; De Pablo, J. J. Crossover from Rouse to reptation dynamics in salt-free polyelectrolyte complex coacervates. *ACS Macro Lett.* **2020**, *9*, 1318–1324.

[24] Liu, Y.; Winter, H. H.; Perry, S. L. Linear viscoelasticity of complex coacervates. *Adv. Colloid Interface Sci.* **2017**, *239*, 46–60.

[25] Jomaa, H. W.; Schlenoff, J. B. Salt-induced polyelectrolyte interdiffusion in multilayered films: A neutron reflectivity study. *Macromolecules* **2005**, *38*, 8473–8480.

[26] Kienle, D. F.; Schwartz, D. K. Complex salt dependence of polymer diffusion in polyelectrolyte multilayers. *J. Phys. Chem. Lett.* **2019**, *10*, 987–992.

[27] Spruijt, E.; Leermakers, F. A.; Fokkink, R.; Schweins, R.; van Well, A. A.; Cohen Stuart, M. A.; van der Gucht, J. Structure and dynamics of polyelectrolyte complex coacervates studied by scattering of neutrons, X-rays, and light. *Macromolecules* **2013**, *46*, 4596–4605.

[28] Koide, A.; Kishimura, A.; Osada, K.; Jang, W.-D.; Yamasaki, Y.; Kataoka, K. Semipermeable polymer vesicle (PICsome) self-assembled in aqueous medium from a pair of oppositely charged block copolymers: physiologically stable micro-/nanocontainers of water-soluble macromolecules. *J. Am. Chem. Soc.* **2006**, *128*, 5988–5989.

[29] Zhou, W.; Wang, J.; Ding, P.; Guo, X.; Cohen Stuart, M. A.; Wang, J. Functional polyion complex vesicles enabled by supramolecular reversible coordination polyelectrolytes. *Angew. Chem.* **2019**, *131*, 8582–8586.

[30] Zhao, Q.; Liu, Q.; Li, C.; Cao, L.; Ma, L.; Wang, X.; Cai, Y. Noncovalent structural locking of thermoresponsive polyion complex micelles, nanowires, and vesicles via polymerization-induced electrostatic self-assembly using an arginine-like monomer. *Chem. Commun.* **2020**, *56*, 4954–4957.

[31] Hernandez-Garcia, A.; Kraft, D. J.; Janssen, A. F.; Bomans, P. H.; Sommerdijk, N. A.; Thies-Weesie, D. M.; Favretto, M. E.; Brock, R.; De Wolf, F. A.; Werten, M. W., et al. Design and self-assembly of simple coat proteins for artificial viruses. *Nat. Nanotechnol.* **2014**, *9*, 698–702.

[32] Cingil, H. E.; Boz, E. B.; Biondaro, G.; De Vries, R.; Cohen Stuart, M. A.; Kraft, D. J.; Van der Schoot, P.; Sprakel, J. Illuminating the reaction pathways of viromimetic assembly. *J. Am. Chem. Soc.* **2017**, *139*, 4962–4968.

[33] Van Galen, M.; Higler, R.; Sprakel, J. Allosteric pathway selection in templated assembly. *Sci. Adv.* **2019**, *5*, eaaw3353.

[34] Bloembergen, N.; Purcell, E. M.; Pound, R. V. Relaxation effects in nuclear magnetic resonance absorption. *Phys. Rev.* **1948**, *73*, 679.

[35] Levitt, M. H. *Spin Dynamics: Basics of Nuclear Magnetic Resonance*; John Wiley & Sons, 2013.

[36] Aguilar, J. A.; Nilsson, M.; Bodenhausen, G.; Morris, G. A. Spin echo NMR spectra without J modulation. *Chem. Commun.* **2012**, *48*, 811–813.

[37] Yu, Q.; Ding, Y.; Cao, H.; Lu, X.; Cai, Y. Use of polyion complexation for polymerization-induced self-assembly in water under visible light irradiation at 25 C. *ACS Macro Lett.* **2015**, *4*, 1293–1296.

[38] Ding, Y.; Zhao, Q.; Wang, L.; Huang, L.; Liu, Q.; Lu, X.; Cai, Y. Polymerization-Induced Self-Assembly Promoted by Liquid–Liquid Phase Separation. *ACS Macro Lett.* **2019**, *8*, 943–946.

[39] Liu, Q.; Wang, X.; Ma, L.; Yu, K.; Xiong, W.; Lu, X.; Cai, Y. Polymerization-Induced Hierarchical Electrostatic Self-Assembly: Scalable Synthesis of Multicompartment Polyion Complex Micelles and Their Monolayer Colloidal Nanosheets and Nanocages. *ACS Macro Lett.* **2020**, *9*, 454–458.

[40] Shen, L.; Li, Y.; Lu, Q.; Qi, X.; Wu, X.; Zhou, Z.; Shen, J. Directed arrangement of siRNA via polymerization-induced electrostatic self-assembly. *Chem. Commun.* **2020**, *56*, 2411–2414.

[41] Amann, M.; Diget, J. S.; Lyngsø, J.; Pedersen, J. S.; Narayanan, T.; Lund, R. Kinetic pathways for polyelectrolyte coacervate micelle formation revealed by time-resolved synchrotron SAXS. *Macromolecules* **2019**, *52*, 8227–8237.

[42] Wu, H.; Ting, J. M.; Yu, B.; Jackson, N. E.; Meng, S.; de Pablo, J. J.; Tirrell, M. V. Spatiotemporal Formation and Growth Kinetics of Polyelectrolyte Complex Micelles with Millisecond Resolution. *ACS Macro Lett.* **2020**, *9*, 1674–1680.

[43] Li, P.; Banjade, S.; Cheng, H.-C.; Kim, S.; Chen, B.; Guo, L.; Llaguno, M.; Hollingsworth, J. V.; King, D. S.; Banani, S. F., et al. Phase transitions in the assembly of multivalent signalling proteins. *Nature* **2012**, *483*, 336–340.

[44] Yewdall, N. A.; André, A. A.; Lu, T.; Spruijt, E. Coacervates as models of membraneless organelles. *Curr. Opin. Colloid Interface Sci.* **2020**, 101416.

[45] Semenov, S. N.; Wong, A. S.; Van Der Made, R. M.; Postma, S. G.; Groen, J.; Van Roekel, H. W.; De Greef, T. F.; Huck, W. T. Rational design of functional and tunable oscillating enzymatic networks. *Nat. Chem.* **2015**, *7*, 160–165.

[46] Aumiller, W. M.; Keating, C. D. Phosphorylation-mediated RNA/peptide complex coacervation as a model for intracellular liquid organelles. *Nat. Chem.* **2016**, *8*, 129–137.

[47] Nakashima, K. K.; Baaij, J. F.; Spruijt, E. Reversible generation of coacervate droplets in an enzymatic network. *Soft Matter* **2018**, *14*, 361–367.

[48] Nakashima, K. K.; van Haren, M. H.; André, A. A.; Robu, I.; Spruijt, E. Active coacervate droplets are protocells that grow and resist Ostwald ripening. *Nat. Commun.* **2021**, *12*, 1–11.

[49] Spoelstra, W. K.; Van Der Sluis, E. O.; Dogterom, M.; Reese, L. Nonspherical coacervate shapes in an enzyme-driven active system. *Langmuir* **2020**, *36*, 1956–1964.

[50] Donau, C.; Späth, F.; Sosson, M.; Kriebisch, B. A.; Schnitter, F.; Tena-Solsona, M.; Kang, H.-S.; Salibi, E.; Sattler, M.; Mutschler, H., et al. Active coacervate droplets as a model for membraneless organelles and protocells. *Nat. Commun.* **2020**, *11*, 1–10.

[51] Späth, F.; Donau, C.; Bergmann, A. M.; Kränzlein, M.; Synatschke, C. V.; Rieger, B.; Boekhoven, J. Molecular Design of Chemically Fueled Peptide–Polyelectrolyte Coacervate-Based Assemblies. *J. Am. Chem. Soc.* **2021**, *143*, 4782–4789.

[52] Kriebisch, C. M. E.; Bergmann, A. M.; Boekhoven, J. Fuel-Driven Dynamic Combinatorial Libraries. *J. Am. Chem. Soc.* **2021**, *143*, 7719–7725.

[53] Lian, Y.; Jiang, H.; Feng, J.; Wang, X.; Hou, X.; Deng, P. Direct and simultaneous quantification of ATP, ADP and AMP by 1H and 31P Nuclear Magnetic Resonance spectroscopy. *Talanta* **2016**, *150*, 485–492.

Summary

Complex coacervate core micelles (C3Ms) form when charged-neutral diblock copolymers are mixed with oppositely charged macro-ions. The charged species form the core of the micelle. The macro-ion rich liquid-like phase formed by phase separation of oppositely charged macro-ions from the rest of the aqueous solution is often called a complex coacervate. Hence the name complex coacervate core micelles. Sometimes also other names are used to describe these micelles like polyelectrolyte complex micelles (PCMs), polyion complex (PIC) micelles, block ionomer complexes (BIC) and inter polyelectrolyte complex (IPEC) micelles. The formation of the complex coacervate phase is based on electrostatic attraction. As a result, the C3Ms can respond to environmental changes like changes in salt concentration or pH. The neutral blocks form the micelle corona around the complex coacervate core. They prevent coalescence of the micelles and can protect the core components against external elements. Because of their small well-defined size, their protective properties and their ability to respond to environmental triggers, C3Ms are promising encapsulators for a wide variety of compounds. They have for example been used for encapsulation of DNA, proteins, small charged drugs and imaging contrast agents and in this way can among others be used as medicine or gene delivery tools.

The dynamics of C3Ms plays a large role in their application as encapsulators. First, their molecular exchange determines how often core components are exposed to their surroundings and thus the level of protection that the C3M offers. In addition, in some cases, the C3M formation dynamics can affect their structure.

In this thesis we aimed to further unravel the C3M dynamics. After a general introduction (Chapter 1), we started with focusing on the dynamics of C3M formation. In Chapter 2, we studied how the assembly of the C3Ms can be altered by coupling a covalent polymerisation reaction of one of the micellar building blocks with the supramolecular assembly with the other pre-synthesised micellar building block, which acts as macromolecular template. We have unveiled the underlying pathways in this templated reaction-assembly network by using a combination of time-resolved ^{1}H NMR spectroscopy, time- and spectrally-resolved ^{1}H NMR relaxation spectroscopy and time-resolved light scattering measurements. In particular, we observed chemical feedback between the reaction and assembly process: the polymerisation rate could be increased by pre-assembly of the monomers at the template and the polymerisation rate in its turn could affect the supramolecular micelle assembly. We quantitatively captured the reaction kinetics of the templated reaction-assembly network in a kinetic model and in this way identified the parameters that can be used to tune this templated reaction-assembly network and thus the C3M formation.

In Chapter 3, we also focused on the micelle formation stage and used Langevin dynamics simulations to study the molecular exchange mechanisms during the initial micellisation of charged-neutral diblock copolymers and oppositely charged homopolymers. We observed that the molecular exchange occurred mainly via expulsion and insertion, where one or two polymers split off and are inserted in another micelle. The fission and fusion exchange mechanism, where the micelle splits in two parts of both substantial sizes and subsequently merge with other micelles, occurred much less often. In addition, we showed that the exchange of neutrally charged complexes is highly preferred. Therefore, the exchange rate of oppositely charged polyelectrolytes with matched chain lengths occurred much faster than the exchange of polyelectrolyte with a length mismatch. Apart from the polyelectrolyte length ratio, the absolute polyelectrolyte lenght also affected the exchange rate, with the longer polyelectrolytes exchanging more slowly. The large preference for neutrally charged complexes demonstrates that the electrotstatic interactions play a large role in the C3M exchange, but we showed that the non-electrostatic interactions can also be important: a slight increase in the non-electrostatic attraction between the oppositely charged polyelectrolytes could significantly reduce the exchange rate, especially for polyelectrolytes with matched chain lengths.

We continued to study this molecular exchange of C3Ms in Chapter 4, but this time we focused on the exchange of equilibrated micelles instead of the exchange of micelles during their formation. To follow this exchange, we made use of Förster resonance energy transfer (FRET). FRET is a type of non-radiative energy transfer between a donor and a nearby acceptor. We mixed C3Ms with donor fluorophores in their core with micelles with acceptor fluorophores in their core. When the micelles exchange, the donor and acceptor fluorophores become part of the same core and are close enough to each other for FRET to occur. We developed an analytical model to convert the observed increase in FRET efficiency as function of time to the molecular exchange rates of the micelles. We showed that the micelle exchange rate was strongly affected by the salt concentration. In contrast, the exchange of fluorescently labelled homopolymer was not affected by changing the length of the unlabelled homopolymers. In addition, only at low micelle concentrations the rate of FRET efficiency increase was affected by the concentration, while this rate was unaffected at higher concentrations. Together these results suggest that the C3M exchange occurs mainly by an expulsion and insertion mechanism and that the breaking of electrostatic bonds in the expulsion step is the rate-limiting step for the exchange. We also observed that the C3Ms have a very broad range of exchange rate and hypothesised that this is the result of chain length polydispersity with every chain length having its own exchange rate.

We tested this polydispersity hypothesis in Chapter 5, where we studied the molecular exchange of C3Ms consisting of monodisperse single stranded DNA (ssDNA) and polydisperse poly(ethyleneglycol)–poly(L-lysine) (PEG–pLL) diblock copolymers. By fluorescently labelling either the ssDNA or the PEG-pLL we could follow the exchange of both C3M components separately. The monodisperse ssDNA showed only two or three exchange rates, while the polydipserse PEG-pLL again showed a broad distribution of exchange rates. This suggests that chain length polydispersity is indeed the main cause of the broad distribution of exchange times. To further study this chain length effect, we measured the molecular exchange rates for different ssDNA and PEG-pLL lengths and showed that both the ssDNA and the pLL length can affect the exchange rate. We also compared the chain lengths effects on the C3M dynamics to the chain lengths effects on the dynamics in ssDNA/pLL complex coacervate droplets. Here, we used the ssDNA diffusion as measure for the dynamics in the complex coacervates and found that this ssDNA diffusion also depended on both the DNA length and the pLL length. However, the quantitative effects of changing the chain lengths seemed different for C3M exchange and ssDNA diffusion in complex coacervate droplets, suggesting that the C3M exchange rate is not solely governed by the polyelectrolyte movements in the core. This was confirmed by Langevin dynamics simulations of the micelle exchange, where the large effect of the length ratio of the oppositely charged core species indicated that also an activated process is involved in the C3M exchange. We also observed that the diffusion coefficient of the ssDNA depended more strongly on the ssDNA chain length than predicted by the sticky Rouse model, which is the model that is usually used to describe the complex coacervate dynamics. This stronger dependence might be explained by an increase in complex coacervate density with increasing chain length, but we cannot exclude yet that other factors also play a role.

In Chapter 6, we aimed to measure the sub-chain dynamics of a single ssDNA molecule in a polyelectrolyte complexes. In this way, we hoped to learn more about the sub-chain relaxation mechanisms, which might also help to better understand the dynamics inside the C3M core. We aimed to probe the sub-chain dynamics by labelling ssDNA with a single donor and acceptor fluorophore and to use the fluctuations in FRET efficiency in time as a measure for the ssDNA sub-chain dynamics. First, we performed coarse-grained molecular dynamics simulations of the DNA in combination with dye accessible volume calculations to find the optimal label positions. Subsequently, we illustrated how the measured fluctuations in FRET efficiency can be analysed to obtain the sub-chain dynamics. We decided to use an asymmetric polymerase chain reaction (PCR) to obtain long ssDNA with a single FRET pair at its end. We took this approach because fluorescence recovery after photo-bleaching (FRAP) measurements showed that increasing the ssDNA length can help to slow down the dynamics in the complex and therefore long ssDNA might help to make the sub-chain fluctuations slow enough

to be measured in experiments. We showed that asymmetric PCR can indeed be used to obtain long ssDNA with a fluorescent label at its end and that this fluorescently labelled long ssDNA can be incorporated in the polyelectrolyte complex. However, among others due to irreproducibility of the asymmetric PCR, we did not obtain a sufficient amount of long ssDNA with a single FRET pair to measure the sub-chain dynamics. Therefore, we ended this chapter with some recommendations on how to continue on our approach to be able to measure the sub-chain dynamics in a polyelectrolyte complex.

Finally, in Chapter 7, we combined the insights obtained in the previous chapters to outline the C3Ms design rules that minimise the molecular exchange. In addition, we discussed possible future research directions, not only to study specifically the C3M dynamics, but also to study the dynamics in other systems that might benefit from the insights that we obtained on the C3M dynamics.

Samenvatting

Complex coacervaat kern micellen (in het Engels: complex coacervate core micelles en daarom afgekort als C3Ms) zijn kleine structuren van meestal 10 tot 100 nanometer en bestaan uit een kern van tegenovergesteld geladen moleculen met daaromheen een schil van lange, neutraal geladen moleculen. Voor de vorming van de C3Ms zijn minimaal twee verschillende soorten moleculen nodig, namelijk diblok copolymeren, die bestaan uit een neutraal geladen deel en een deel met veel ladingen, en tegenovergesteld geladen moleculen, die per molecuul meerdere ladingen hebben. Dit tegenovergesteld geladen molecuul kan ook een diblok copolymeer zijn, maar het kan ook een homopolymeer zijn. Een (homo)polymeer bestaat uit een keten dat een herhaling is van steeds hetzelfde stuk, een monomeer. Als dit monomeer geladen is, wordt het polymeer ook wel polyelektroliet genoemd. Bij een diblok copolymeer bestaat het molecuul uit twee verschillende polymeerblokken aan elkaar, elk met hun eigen monomeer.

De vorming van de C3Ms is gebaseerd op elektrostatische aantrekkingskracht tussen de tegenovergesteld geladen moleculen in de kern. Als deze elektrostatische aantrekkingskracht niet sterk genoeg meer is, vallen de micellen uit elkaar. De sterkte van de elektrostatische interacties kan onder andere beïnvloed worden door de zoutconcentratie en de pH van de oplossing: de zoutionen schermen de lading van de moleculen af en daardoor is de aantrekkingskracht minder sterk bij hoge zoutconcentratie. De pH van de oplossing kan het aantal geladen groepen per molecuul veranderen en op die manier de elektrostatische aantrekkingskracht veranderen. De C3Ms kunnen dus reageren op pH en zoutconcentratie veranderingen in hun omgeving.

De neutrale schil om de C3Ms zorgt voor afstoting tussen de micellen onderling en voorkomt zo dat de micellen samenvoegen tot veel grotere structuren. Daardoor hebben de micellen hun karakteristieke grootte van meestal 10 tot 100 nanometer. Daarnaast zorgt de neutrale schil ervoor dat grotere moleculen niet bij de moleculen in de kern kunnen komen en op die manier vormt de neutrale schil een beschermende laag om de moleculen in de kern.

De beschermende eigenschappen van de C3M schil, de kleine afmetingen van de C3Ms en hun vermogen om te reageren op veranderingen in de omgeving samen maken de C3Ms veelbelovende verpakkingsmaterialen voor bijvoorbeeld de levering van medicijnen in het lichaam. Onder andere geladen medicijnen kunnen worden verpakt in de C3M kern en worden dan door de neutral schil van de C3M beschermd tegen bijvoorbeeld enzymen die de medicijnen kunnen afbreken. De kleine afmetingen van de C3Ms zorgen ervoor dat de C3Ms naar verschillende plekken in het lichaam vervoerd kunnen worden. Tenslotte kan de gevoeligheid van C3Ms voor bijvoorbeeld pH- en zoutconcentratieveranderingen worden gebruikt om ervoor te zorgen dat de C3Ms uit elkaar vallen als ze op de plaats van bestemming zijn aangekomen, zodat de medicijnen vrijkomen.

De dynamische eigenschappen zijn erg belangrijk voor het gebruik van C3Ms als verpakkingsmateriaal. Zelfs als gemiddeld het overgrote merendeel van de moleculen onderdeel is van een C3M, kan de bescherming nog niet goed werken als er steeds delen van de C3M afsplitsen en samenvoegen met andere C3Ms. Op het moment dat er een deel afsplitst, is dit deel namelijk minder goed beschermd door de neutral schil en in sommige gevallen is er zelfs helemaal geen schil meer om de kerncomponenten te beschermen. Daarom is het belangrijk om de uitwisseling van de C3Ms zo veel mogelijk te beperken. Naast de uitwisselingsdynamica is ook de vormingsdynamica belangrijk voor het gebruik van C3Ms als verpakkingsmateriaal. In sommige gevallen kan de manier waarop de C3Ms worden gevormd namelijk de uiteindelijke C3M structuur bepalen.

In dit proefschrift hebben we geprobeerd de dynamica van de C3Ms beter te begrijpen. Na een algemene inleiding (hoofdstuk 1), hebben we in hoofdstuk 2 gekeken naar de vorming van C3Ms. In dit geval bestudeerden we wat er gebeurt als je de reactie waarbij het geladen blok van een diblok copolymeer wordt gevormd, laat plaatsvinden in aanwezigheid van een tegenovergesteld geladen

homopolymeer. Naarmate de reactie vordert, wordt het geladen blok lang genoeg om sterk te binden aan het tegenovergestelde geladen homopolymeer en op die manier worden C3Ms gevormd. De vorming van structuren op basis van andere interacties dan chemische bindingen wordt ook wel assemblage genoemd en de vorming van C3Ms valt dus ook onder assemblage. Daarom hebben we het in hoofdstuk 2 over een reactie-assemblage netwerk. We hebben een combinatie van experimentiële technieken (kernspinresonantie en lichtverstrooiing) gebruikt om erachter te komen wat er precies in dit reactie-assemblage netwerk gebeurt. Zo hebben we laten zien dat er terugkoppeling is tussen de reactie en de assemblage en dat de reactiesnelheid kan worden gebruikt om de C3M assemblage te regelen. Daarnaast hebben we laten zien hoe de reactiesnelheid kan worden geregeld.

In hoofdstuk 3 hebben we computersimulaties gebruikt om meer te weten te komen over de uitwisselingsmechanismen tijdens de vorming van de C3Ms vanuit diblok copolymeren en tegenovergesteld geladen homopolymeren. We hebben laten zien dat de micellen vooral uitwisselden via een expulsie en insertie mechanisme. Bij dit mechanisme splitsen één of twee polymeren af van een micel en voegen vervolgens samen met een andere micel. Het andere mechanisme (fissie en fusie), waarbij de micel splitst in twee micellen van ongeveer gelijke grootte en de nieuw gevormde micellen weer samenvoegen met andere micellen, kwam veel minder vaak voor. We hebben ook laten zien dat vooral neutraal geladen combinaties van polymeren snel uitwisselden. Dit zorgt ervoor dat tegenovergesteld geladen polyelektrolieten met gelijke lengte veel sneller uitwisselen dan polyelektrolieten met ongelijke lengtes. Naast de lengte ratio van de polyelektrolieten is ook de absolute lengte belangrijk: langere polyelektrolieten wisselden langzamer uit. Verder bleek ook de niet-elektrostatische aantrekkingskrachten (zoals Van der Waals interactie, hydrofobe interacties of waterstofbruggen) tussen de polyelektrolieten een grote rol te kunnen spelen in de uitwisseling van C3Ms, waarbij een kleine toename van de niet-elektrostatische aantrekkingskracht de C3M uitwisseling sterk kon laten afnemen.

In hoofdstuk 4 hebben we ook gekeken naar de uitwisseling van C3Ms, maar dit keer bestudeerden we de uitwisseling als de C3Ms al helemaal gevormd zijn en dus een evenwicht hebben bereikt waarbij hun gemiddelde grootte niet meer verandert. Hiervoor maakten we gebruik van Förster resonantie energie overdracht (in het Engels: Förster resonance energy transfer (FRET)). FRET vindt plaats tussen twee verschillende fluorescente kleurstoffen: de donor kleurstof draagt zijn energie over aan de acceptor kleurstof en daardoor zie je fluorescentie van de acceptor in plaats van de donor. FRET kan alleen plaatsvinden als de donor en acceptor heel dicht bij elkaar in de buurt zijn (meestal dichterbij dan 10 nanometer). Om de uitwisseling van C3Ms te meten, hebben we C3Ms met donor kleurstoffen in hun kern gemengd met C3Ms met acceptor kleurstoffen in de kern. Aan het begin van het mixexperiment zijn de donor en acceptor te ver weg van elkaar om FRET te laten plaatsvinden. Maar als de micellen beginnen uit te wisselen, kunnen de donor en acceptor onderdeel worden van dezelfde micelkern en dan kan er wel FRET plaatsvinden. Door de verandering in FRET efficiëntie te volgen in de tijd, konden we dus iets zeggen over de miceluitwisselingssnelheid. Door de mixexperimenten uit te voeren bij verschillende micelconcentraties, verschillende lengtes van ongelabelde polymeren en verschillende zoutconcentraties hebben we laten zien dat ook hier de uitwisseling waarschijnlijk vooral plaatsvindt via een expulsie en insertie mechanisme en dat het afsplitsen van polymeren uit de micel de langzaamste stap is in de uitwisseling. Daarnaast zagen we een brede verdeling van uitwisselingssnelheden. Soms waren de eerste polymeren al binnen een minuut uitgewisseld en nam de uitwisseling van de overige polymeren slechts heel geleidelijk toe, waardoor een deel van de polymeren na meer dan 40 uur nog steeds niet uitgewisseld was. Onze hypothese was dat dit verklaard kan worden doordat de polymeren polydispers zijn (dat wil zeggen dat de polymeren verschillende lengtes hebben) en dat de uitwisselingssnelheid sterk afhangt van de polymeerlengte.

Om deze hypothese te testen, hebben we in hoofdstuk 5 gekeken naar de uitwisseling van C3Ms die bestaan uit DNA moleculen en diblok copolymeren met een positief en een neutraal geladen blok. DNA zelf is een negatief geladen polyelektroliet en het is tegenwoordig mogelijk om DNA moleculen met allemaal precies dezelfde lengte te maken (in dat geval noemen we het DNA monodispers). We zagen

dat dit monodisperse DNA inderdaad veel minder verschillende uitwisselingssnelheden had, terwijl het polydisperse diblok copolymeer wel weer een brede verdeling van uitwisselingssnelheden vertoonde. Dat suggereert dat polydispersiteit in polymeerlengte inderdaad de belangrijkste oorzaak is van de brede verdeling in uitwisselingssnelheden. Om meer te weten te komen over dit lengte effect op de dynamica, hebben we zowel de lengte van het DNA als de lengte van het diblok copolymer gevarieeërd en het effect hiervan op de C3M uitwisselingssnelheid bestudeerd. Daarnaast hebben we DNA gemixt met positief geladen homopolymeren, dus zonder een neutraal geladen blok. Door de afwezigheid van de neutrale blokken konden de tegenovergesteld geladen polymeren in grotere hoeveelheden bij elkaar komen en zo druppels vormen waarin de concentratie van beide polyelektrolieten verhoogd was ten opzichte van de rest van de oplossing. Zo'n vloeistof fase die wordt gevormd door de fasescheiding van tegenovergesteld geladen polyelektrolieten van de rest van de wateroplossing wordt een complex coacervaat genoemd. (Hier komt ook de naam complex coacervaat kern micellen vandaan). Ook bij de complex coacervaat druppels hebben we gekeken naar het effect van het variëren van lengte van het DNA en het positief geladen polymeer op de dynamica. Zo hebben we ook een eerste indicatie gekregen van hoeveel de dynamica in de C3M kern bijdraagt aan de uiteindelijke uitwisselingssnelheid van de C3Ms.

In hoofdstuk 6 hebben we geprobeerd de lokale dynamica van een deel van een enkel DNA molecuul in een complex coacervaat te meten. Dit kan ook nuttig zijn om de dynamica in de kern van de C3Ms beter te begrijpen. We hebben geprobeerd deze lokale dynamica te meten door het DNA te labellen met één donor kleurstof en één acceptor kleurstof en dan de fluctuaties in FRET efficiëntie in de tijd te gebruiken als maat voor de lokale bewegingen van het DNA molecuul. De FRET efficiëntie is immers sterk afhankelijk van de afstand tussen de donor en acceptor en veranderingen in de DNA configuratie leiden dus tot veranderingen in FRET efficiëntie. We hebben computersimulaties gebruikt om de optimale posities voor de donor en acceptor op het DNA te vinden en om te laten zien hoe de fluctuaties in FRET efficiëntie geanalyseerd kunnen worden om de lokale DNA dynamica te bepalen. Vervolgens hebben we geprobeerd een lang DNA molecuul te maken met één donor-acceptor paar aan één uiteinde. We hebben ervoor gekozen om lang DNA te maken omdat een langere DNA lengte zou kunnen helpen om de lokale DNA bewegingen langzaam genoeg te maken om te meten in experimenten. Hoewel we wel hebben laten zien dat het mogelijk is om lang DNA te maken met een donor-acceptor paar aan één uiteinde en dat dit DNA onderdeel kan worden van een complex coacervaat, is het ons nog niet gelukt om de lokale dynamica van een deel van het DNA molecuul te meten. Dit kwam onder andere door problemen met de reproduceerbaarheid van de reactie om het lange DNA te maken. Daarom hebben we dit hoofdstuk afgesloten met enkele aanbevelingen hoe dit project kan worden vervolgd zodat uiteindelijk deze lokale dynamica in een complex coacervaat wel kan worden gemeten.

In de algemene discussie (hoofdstuk 7) hebben we de belangrijkste resultaten uit de andere hoofdstukken gecombineerd en zijn zo tot een paar algemene richtlijnen gekomen om de uitwisseling van C3Ms te beperken. Daarnaast hebben we besproken hoe het onderzoek in dit proefschrift kan worden voortgezet, niet alleen om meer te weten te komen over de dynamica van C3Ms, maar ook over de dynamica van andere systemen.

List of publications

This thesis

- Inge Bos, Camilla Terenzi and Joris Sprakel. Chemical Feedback in Templated Reaction-Assembly Networks. *Macromolecules* **2020** *53*(23), 10675–10685. (Chapter 2)
- Inge Bos and Joris Sprakel. Langevin Dynamics Simulations of the Exchange of Complex Coacervate Core Micelles: The Role of Nonelectrostatic Attraction and Polyelectrolyte Length. *Macromolecules* **2019** *52*(22), 8923–8931. (Chapter 3)
- Inge Bos, Marga Timmerman and Joris Sprakel. FRET-Based Determination of the Exchange Dynamics of Complex Coacervate Core Micelles. *Macromolecules* **2021** *54*(1), 398–411. (Chapter 4)
- Inge Bos, Eline Brink, Lucile Michels and Joris Sprakel. DNA dynamics in complex coacervate droplets and micelles. *Soft Matter* **2022** *18*(10), 2012-2027. (Chapter 5)

Other work

- Inge Bos, Pieter van der Scheer, Wouter G. Ellenbroek and Joris Sprakel. Two-dimensional crystals of star polymers: a tale of tails. *Soft Matter* **2019** *15*(4), 615-622.
- Inge Bos, Holger Merlitz, Alice Rosenthal, Petra Uhlmann and Jens-Uwe Sommer. Design of binary polymer brushes with tuneable functionality. *Soft Matter* **2018** *14*(35), 7237-7245.
- Inge Bos, Kaitlyn M. Bland, Lijin Tian, Roberta Croce, Laurie K. Frankel, Herbert van Amerongen, Terry M. Bricker, Emilie Wientjes. Multiple LHCII antennae can transfer energy efficiently to a single Photosystem I. *Biochim. Biophys. Acta - Bioenerg.* **2017** *1858*(5), 371-378.
- Juan Yang, Inge Bos, Wim Pranger, Anthonie Stuiver, Aldrik H. Velders, Martien A. Cohen Stuart, Marleen Kamperman. A clear coat from a water soluble precursor: a bioinspired paint concept. *J. Mater. Chem. A* **2016** *4*(18), 6868-6877.

Acknowledgements

The past four years, I have spent quite some time on trying to do research (and to end up with something that looks like a PhD thesis) and I quite enjoyed it. For this, I would like to start to thank everyone of PCC. Thank you all for the nice atmosphere, the nice conversations during the lunch breaks, in the lab, or just in the corridor, and the help with all kind of things.

Joris, bedankt dat je me deze PhD hebt laten doen en de moeite die je steeds nam om er een project van te makend dat bij mij paste. Ik heb veel bewondering voor je oneindige stroom van nieuwe ideeën en hoe je altijd een alternatief plan weet te bedenken als iets niet lukt. Bedankt voor al je ideeën, hulp en supersnelle feedback.

Camilla, thank you for all your help with designing the experiments of Chapter 2 and in the meantime learning me a lot about NMR. Johannes and Mattia, thank you for letting me use the single-molecule set-up. Unfortunately, I did not manage to do real single-molecule experiments in the end, but your help and suggestions definitely took the project a step further. Bauke, bedankt voor je hulp met de HPLC. Jasper, bedankt voor je goede vragen en suggesties bij presentaties en bedankt dat je tijd vrijmaakte om commentaar te geven op hoofdstuk 6. Frans, bedankt voor je uitgebreide instructies voor het soft matter practicum en voor de interesse die je toonde in mijn onderzoek. Hanne, dankzij jouw template was de opmaak van mijn thesis zo geregeld. Dankjewel daarvoor en voor al je positieve aanmoedigen tijdens mijn hele PhD.

Joran, Inge, Marga en Eline, bedankt dat ik betrokken mocht zijn bij jullie BSc of MSc thesis. Joran, je kon enthousiast en met het nodige gevoel voor humor over je nieuwe resultaten vertellen. Jouw simulaties maakten het effect van ladingsstoichiometrie in hoofdstuk 2 eenvoudiger te begrijpen. Dankjewel hiervoor. Inge, bedankt voor al die keren dat je het gewoon ging proberen. Door jouw doorzettingsvermogen hebben we uiteindelijk toch een werkend protocol voor het fluorescent labellen van de polymeren gevonden. Marga, bedankt voor al je handigheid en nauwkeurigheid op het lab. Dankzij jouw goed gedocumenteerde syntheses heb ik veel micel uitwisselingsexperimenten kunnen doen. Eline, jij pikte alles heel snel op en hebt zo in korte tijd een belangrijke basis gelegd voor de experimenten van hoofdstuk 5. Bedankt voor je bijdrage.

Remco, Diane en Raoul, jullie regelen superveel en staan altijd klaar om te helpen, van hulp bij meetinstrumenten en computers tot het regelen van practica. Zonder jullie ondersteuning was onderzoek doen een stuk ingewikkelder geweest. Bedankt voor al jullie hulp.

Mara, Leonie en Marioes, bedankt voor het regelen van alle administratieve onderdelen en van alle bestellingen van chemicaliën. Het was heel fijn dat jullie dit elke keer weer goed en ook nog eens erg snel konden regelen.

Ilse, Anton, Lucile, Jessica, Joanne, Chuanbao, Sophie, Kasper and Maarten, thank you for sharing office 7071 for a longer or shorter time. It was always nice to be there, talking about research and sharing the occasional frustrations, or just discussing the weekend or getting distracted by the nice view.

Lucile, thank you for your help with the measurements with the molecular rotors in Chapter 5.

Sophie en Martijn, bedankt voor de leuke gesprekken over verschillende experimenten en bedankt dat jullie de rol van paranimf op jullie wilden nemen.

De afgelopen 4 jaar heb ik vrij veel tijd besteed aan proberen onderzoek te doen, maar ik had het nooit volgehouden om alleen maar hiermee bezig te zijn. Daarom wil ik hier ook degenen bedanken die ervoor hebben gezorgd dat er meer was dan (en genoeg afleiding van) onderzoek.

Ik wil graag mijn trainingsmaatjes van STW en iedereen van 'een rondje doen' bedanken voor alle schaats-, fiets-, skeeler- en warme chocolademelk rondjes.

Evelien, Gea, Ilona, Piet, Steven, Tess, Vincent en Willem-Jane, bedankt voor alle gezelligheid tijdens de (online) spelletjesavonden. Ik hoop dat we hier nog lang mee door kunnen gaan.

Eva, Jacqueline, Marijke en Martine, het is fijn om zo lang al vriendinnen te zijn. Bedankt hiervoor.

Papa, mama, Thijs en Meike, bedankt voor jullie interesse in wat ik doe (ook al snap ik soms zelf niet eens wat ik aan het doen ben). Bedankt dat jullie er voor me waren op de momenten dat de cursus omgaan met teleurstellingen toch wel door dreigde te gaan. En vooral bedankt dat het gewoon altijd gezellig is om bij jullie te zijn.

Dirk, ik ben erg gelukkig dat ik zo'n lief iemand ontmoet heb. Bedankt voor alle fijne momenten samen. Ik kijk uit naar nog heel veel jaren samen met jou.

Inge

Overview of completed training activities

Discipline-specific activities

- Han-sur-Lesse Winterschool, Han-sur-Lesse (BE), 2018.
- International Symposium on Polyelectrolytes, VLAG, Wageningen, 2018.
- CHAINS, NWO, Veldhoven, 2018.
- RPK-B Polymer Physics, PTN, Utrecht, 2018.
- Dutch Polymer Days, PTN, Lunteren, 2019.‡
- CHAINS, NWO, Veldhoven, 2019.
- Physics@Veldhoven, NWO, online, 2021.
- SoftComp Annual Meeting, SoftComp, online, 2021.†

General courses

- Presenting with Impact, WGS, Wageningen, 2018.
- Posters and Pitching, WGS, Wageningen, 2018.
- Scientific Writing, WGS, Wageningen, 2019.
- Scientific art work - Vector graphics and images, WGS, Wageningen, 2019.
- Start to teach, WGS, Wageningen, 2020.
- Brain training, WGS, Wageningen, 2020.
- Scientific publishing, WGS, Wageningen, 2020.

Other activities

- Preparation of research proposal, PCC, Wageningen, 2018.
- Group meetings, PCC, Wageningen, 2017–2021.†
- Simulation meetings, PCC, Wageningen, 2017–2021.†
- Journal Club, PCC, Wageningen, 2017–2021.

---

† oral presentation

‡ poster presentation

Printed by ProefschriftMaken || www.proefschriftmaken.nl

The research described in this thesis was financially supported by the Netherlands Organisation for Scientific Research (NWO) through the VIDI programme 'Light from Within' (project number: 723.016.001)